# Assessing roof vulnerability to collapse from tephra fall loading, with relevance to Ascension Island

## Sara Jane Osman

Submitted in accordance with the requirements for the degree of

Doctor of Philosophy

The University of Leeds

School of Earth and Environment

December 2023

# Declaration

The candidate confirms that the work submitted is her own, except where work has been included which has formed part of jointly authored publications. The contribution of the candidate and the other authors to this work has been explicitly indicated below. The candidate confirms that appropriate credit has been given within the thesis where reference has been made to work of others.

This thesis is submitted as an alternative style of doctoral thesis including published material. This format is appropriate as the research consists of different strands which are best presented as separate papers because the sections are of importance to different groups. The results are then brought together in a fourth paper detailing a new GIS tool that enables roofs that are susceptible to collapse under tephra fall loading to be identified for given eruption scenarios. The thesis also includes an introduction giving the context and rationale for the work and an extended discussion section which draws the strands together.

The material in Chapter 2 has been published in:

Osman S, Thomas M, Crummy J, Carver S (2022) Investigation of geomechanical properties of tephra relevant to roof loading for application in vulnerability analyses. Journal of Applied Volcanology 11:9. https://doi.org/10.1186/s13617-022-00121-2

I undertook all the laboratory work, data collection and data analysis. I produced all the figures, authored the initial version of the manuscript and edited it following suggestions from my co-authors. The manuscript went through British Geological Survey (BGS) internal review as it was published with the permission of the executive director of BGS. I also edited it following comments from one anonymous reviewer from the Journal of Applied Volcanology and the journal editor, Tom Wilson.

Data published as an Appendix to this article are included in Appendix A1. Appendix A2 shows rate of change of shear stress with time for the small shear box tests with Ascension ash, referred to in Fig. 2-7.

The material in Chapter 3 has been published in:

Osman S, Thomas M, Crummy J, Sharp, A, Carver S (2023) Laboratory tests to understand tephra sliding behaviour on roofs. Journal of Applied Volcanology 12:11. https://doi.org/10.1186/ s13617-023-00137-2

I undertook the laboratory work, assisted for one set of tests by AS, an MSc student, who worked under my guidance. I did all the data analysis and produced all the figures. I authored the initial version of the manuscript and edited it following suggestions from my co-authors. The manuscript went through BGS internal review as it was published with the permission of their executive director. I also edited it following comments from two anonymous reviewers from the Journal of Applied Volcanology and the journal editor, Emma Hudson-Doyle.

Data published as Supplementary material to this article are included in Appendix B1. Appendix B2 shows details of calculations on the volume of corrugations of the metal and fibre cement sheets used for the sliding tests (referred to in Methods – Sliding tests).


The material in Chapter 4 has been submitted to Bulletin of Volcanology:

Osman S, Crummy J, Thomas M, Carver S (submitted) Probabilistic hazard analysis for a small island: quantifying tephra fall hazard and appraising the possible impact on Ascension Island. Bulletin of Volcanology

I calibrated the model and ran all model simulations. I did all the data analysis and produced all the figures. I authored the initial version of the manuscript and edited it following suggestions from my co-authors. The manuscript went through BGS internal review as it was submitted with the permission of their executive director.

Figures and tables submitted as Supplementary material to this article are included in Appendix C1. Details of the model calibration are given in Appendix C2.

The material in Chapter 5 has been prepared for submission to Natural Hazards:

Osman S, Crummy J, Carver S, Thomas M (in prep.) From probabilistic tephra load modelling to vulnerability assessment: a GIS tool to identify buildings susceptible to roof collapse.

I created the GIS tool, did all the data analysis and produced all the figures. I authored the initial version of the manuscript and edited it following suggestions from my co-authors.

Appendix D contains supplementary material for this paper.

# Acknowledgements

# Abstract

Tephra fall can significantly increase loading on roofs and by better understanding the factors that influence roof vulnerability to collapse, mitigations can be more appropriately targeted. My research assessed tephra sliding behaviour, modelled tephra loads and developed a GIS tool to estimate how vulnerable individual buildings are to roof collapse.

In the laboratory I confirmed the geomechanical properties of synthetic tephra that influence deposit sliding behaviour (bulk density, grain size distribution, internal angle of friction) match well to natural samples. I then used synthetic samples to characterise how tephra slides on roofs and validated my results with field observations during the 2021 Cumbre Vieja eruption (La Palma, Canary Islands). Grain size, roof material and pitch were the key factors influencing sliding. I compiled initial sliding coefficients for three roof materials on simply pitched roofs, based on the Eurocode approach for snow loads. These coefficients estimate the fraction of tephra load on the ground that is expected to remain on a roof.

I conducted a probabilistic tephra fall hazard analysis for Ascension Island, using knowledge from the geological record and data from analogous eruptions on São Miguel, Azores. I modelled possible future eruption scenarios and provided probabilities of tephra fall loads exceeding threshold values for roof failure. There was a 50 % probability that three basaltic events, each with a 6–10 km plume height could produce proximal tephra loads sufficient to cause roof collapse if roofs were not cleared between eruptive phases.

Finally, I combined my results to develop a GIS tool that assesses susceptibility to roof collapse at a building level. The tool takes model output tephra loading, data on individual buildings, my tephra sliding coefficients and published estimates of collapse loads to identify buildings where tephra loads may exceed the roof failure load for a given eruption scenario.

# Contents

# Contents

# Contents

# Contents

# Contents

# List of Figures

# List of figures

# List of figures

# List of Tables

# List of tables

# List of Abbreviations and symbols

## Abbreviations

| | | | | |
|---|---|---|---|---|
| BGS | British Geological Survey | | MER | Mass eruption rate |
| DC | Diffusion coefficient | | PDC | Pyroclastic density current |
| ESP | Eruption source parameter | | RSF | Roof shape factor |
| FTT | Fall-time threshold | | SiO₂ % | Weight percent silica |
| GSD | Grain size distribution | | TTDM | Tephra transport and dispersal models |
| GIS | Geographic information systems | | | |
| IGME | Instituto Geológico y Minero de España | | UNDRR | United Nations Office for Disaster Risk Reduction |
| LVDT | Linear Variable Differential Transformers | | VEI | Volcanic explosivity index |

## Symbols

| | | | | |
|---|---|---|---|---|
| $c$ | Cohesion | | $\mu$ | Roof shape coefficient for deposit sliding |
| $F$ | Fail fraction | | | |
| $l$ | Modelled tephra load | | $\rho$ | Density |
| $\mathrm{Md}_\phi$ | Median grain size (Phi scale) | | $\sigma$ | Normal stress |
| | | | $\sigma_\phi$ | Standard deviation of grain size distribution (Phi scale) |
| $N$ | Number of model runs | | | |
| $P$ | Probability | | | |
| $T$ | Modelled tephra mass loading threshold | | $\tau$ | Shear stress at failure along a plane |
| $v$ | Model vent | | $\varphi_f$ | Internal angle of friction |
| | | | $\phi_g / \phi$ | Grain size in Phi scale (Chapter 2/ Chapter 3) |
| $\alpha$ | Roof pitch | | | |

# Chapter 1

## Introduction

During explosive volcanic eruptions, tephra fall deposits can increase loading on roofs and pose a significant problem to the structural integrity of buildings. The additional roof load due to tephra (the term for ejected particles of all sizes) depends on a complex interplay of factors which must be considered when assessing possible impacts on buildings. These include eruption parameters (vent location, eruption size and intensity), deposit properties (grain size distribution, bulk density), atmospheric conditions (wind velocity, precipitation) and building features (proximity to the source, roof material, pitch).

Observations after eruptions provide valuable data on conditions that may lead to roof damage. However, large eruptions that produce tephra deposits sufficient to cause roof collapse are relatively infrequent and field observations are therefore limited. In addition, surveys need to be conducted as soon as possible after deposits are emplaced, but this must be balanced with the risks of entering areas while there is still a danger of further explosive activity and sensitivities regarding affected communities and emergency response.

Experimental studies and model simulations can help to fill in knowledge gaps by exploring a wider range of conditions than is easily encountered in the field. In this project I use these methods to investigate tephra fall loading and sliding on roofs.

# Chapter 1: Introduction

## Aim of the project

The overall aim of this project is to better understand the factors influencing roof vulnerability to collapse under tephra fall loading using laboratory tests validated with field data and numerical modelling. A secondary aim is to combine my results with building data, using geographic information systems (GIS) to identify buildings where tephra loading may lead to roof collapse so they can be prioritised for roof clearing or other mitigations.

To achieve these aims, my specific objectives are to:

- Confirm the geomechanical properties of synthetic tephra, made from crushing and grading volcanic aggregates, match those of natural samples when considering deposit sliding behaviour, enabling synthetic samples to be used for sliding tests.
- Characterise tephra sliding behaviour on roofs using laboratory tests to investigate how grain size and density, roof material and pitch impact sliding, and ground-truth the results with field observations taken during the Cumbre Vieja 2021 eruption, La Palma, Canary Islands.
- Compile an initial set of tephra sliding coefficients from the laboratory results, applicable to simply pitched roofs, using an approach based on the Eurocode building standard for snow loads.
- Conduct a probabilistic tephra fall hazard analysis for Ascension Island and assess possible impacts to buildings, focusing on eruptions large enough to potentially cause roof collapse and taking account of knowledge gaps in the island's eruptive history because of poor deposit preservation.
- Develop a GIS tool that combines the tephra sliding coefficients with published roof collapse load estimates and data on individual buildings to identify buildings where tephra loading may exceed the roof failure load for a given eruption scenario.

## Thesis outline

The remainder of this first thesis chapter provides background and context for the later chapters. I discuss tephra hazards, focusing on tephra fall, and introduce tephra transport and dispersal modelling. I review exposure data and assess existing knowledge on tephra fall impacts on buildings, based on field observations and laboratory studies. Finally, I consider mitigation measures and summarise the Eurocode building standard approach for

assessing roof loads. Chapters 2 to 5 present the laboratory tests, modelling and GIS analysis that make up this project (Fig. 1-1).
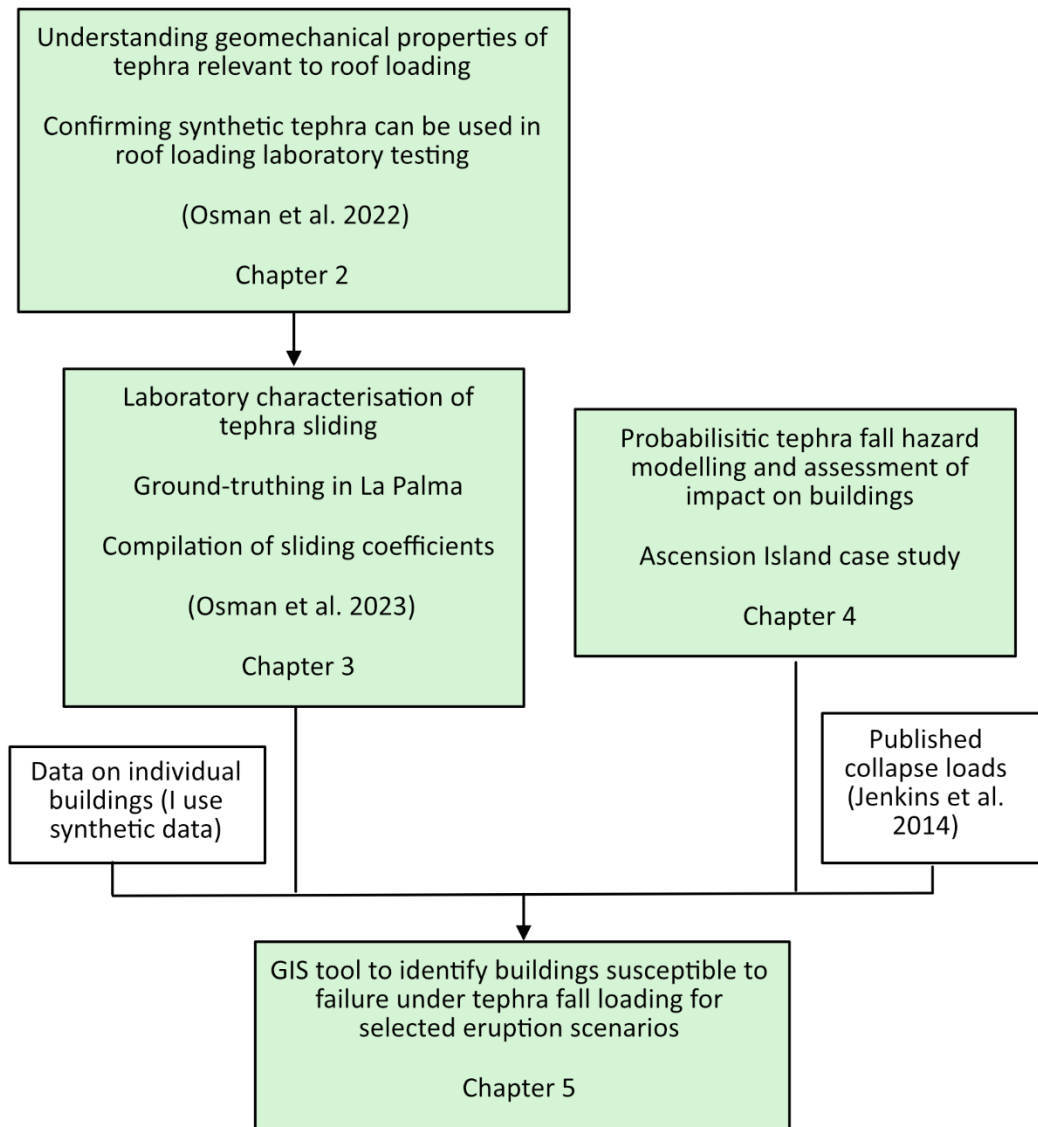


**Fig. 1-1** Outline of thesis science chapters

In Chapter 2, I detail my investigation on the geomechanical properties of tephra relevant to roof loading for application in vulnerability analyses. I compare bulk density, grain size distribution and internal angle of friction for natural and synthetic tephra deposits using a combination of published data and new experimental results from sieving, Camsizer analyses and shear box tests. I show that synthetic samples match well to the natural tephra deposits, an important finding confirming that we can use synthetic samples in

# Chapter 1: Introduction

experiments relating to tephra loading of roofs. The work in this chapter has been published in the peer-reviewed Journal of Applied Volcanology (Osman et al. 2022).

Chapter 3 presents small-scale laboratory tilt-table tests to investigate how tephra sliding on a roof is affected by the roof material and pitch, as well as the density and grain size distribution of the deposit. From the results, ground-truthed by field observations in La Palma during the 2021 eruption of Cumbre Vieja, I develop a preliminary set of sliding coefficients for simply pitched roofs using methodology adapted from the Eurocode standard for snow loading. This work has been published in the peer-reviewed Journal of Applied Volcanology (Osman et al. 2023).

Chapter 4 describes a probabilistic hazard analysis for Ascension Island which quantifies tephra fall hazard and appraises the possible impact on buildings. I model a range of felsic and mafic scenarios, for explosive events that could lead to tephra deposition sufficient to cause roof collapse. Because Ascension's eruptive history is poorly constrained, I combine data from the geological record on Ascension with analogue eruptions from São Miguel, Azores to calibrate the model and identify eruption source parameters for the simulations. There are insufficient data to assess vent opening probabilities and so I use a novel grid of possible source locations to account for uncertainty in vent location for eruptions from the monogenetic field. The work in this chapter has been submitted to the peer-reviewed Bulletin of Volcanology, with an abstract that has already been accepted for a special issue on Uncertainty quantification.

In Chapter 5 I present a new GIS tool (available for ArcGIS Pro and QGIS) to enable roofs susceptible to failure under tephra fall loading to be identified. As inputs, the tool takes a spatial tephra load distribution (I use an example from Ascension Island (Chapter 4)), tephra sliding coefficients (detailed in Chapter 3), published roof collapse load estimates and building characteristics (location, roof material, pitch and building condition). The output is a map highlighting buildings for which the tephra load on the roof is greater than the estimated roof collapse load for that building, given the event being considered. The tool could assist emergency managers to identify buildings most vulnerable to collapse for different eruption scenarios, enabling them to prioritise roof clearing or other mitigation measures. The work in this chapter is being prepared for submission to the peer-reviewed journal Natural Hazards.

Finally, Chapter 6 provides a critical discussion of the whole project, presents conclusions from the work and recommends directions for future research.

## Tephra hazards

Explosive volcanic eruptions are a major global hazard with the potential to impact ~ 800 million people who live within 100 km of an active volcano (Brown et al. 2015). The United Nations Office for Disaster Risk Reduction (UNDRR) defines a hazard as a phenomenon that has the potential to cause damage or disruption (2016) and volcanic hazards vary with eruption size and distance from the eruptive vent. They include blocks ejected ballistically or falling from the plume, which can travel hundreds of metres (e.g. Tsunematsu et al. 2016; Osman et al. 2019; Waythomas and Mastin 2020), pyroclastic density currents (PDCs) with hot and fast-moving, gravity-driven mixtures of tephra and gas extending to tens of kilometres from the source (e.g. Jenkins et al. 2013; Baxter et al. 2017; Risica et al. 2022) and tephra dispersed by the wind, where the finest particles can travel hundreds or even thousands of kilometres (e.g. Watson et al. 2017; Cashman and Rust 2020; Buckland et al. 2022).

When in the air, the finest tephra can pose a hazard to aircraft, as ingested particles can melt at the high temperatures found in jet engines, leading to engine failure (Song et al. 2019; Pearson and Brooker 2020; Lokachari et al. 2020). Airborne tephra can also impact human health with respiratory problems reported due to inhalation of the finest ash, particularly when particles are fragmented by wind or traffic after deposition (e.g. Horwell et al. 2017; Zabert et al. 2019; Eychenne et al. 2022).

After deposition, tephra accumulations of just a few millimetres can severely impact critical infrastructure by causing electrical flashovers, clogging water filters and corroding metal components (e.g. Jenkins et al. 2015; Wilson et al. 2017; Deligne et al. 2022). When deposits reach a few centimetres thickness, crops can be damaged if a tephra blanket prevents photosynthesis or abrades leaves or fruit, and livestock can be lost as a result of fluorosis (e.g. Craig et al. 2016; Flueck 2016; Ligot et al. 2022). Thicker deposits (tens of centimetres) can cause buildings to fail due to increased roof loading (e.g. Jenkins et al. 2014; Blong et al. 2017; Williams et al. 2020) and this is the focus of my project.

# Chapter 1: Introduction

Hot particles can also start fires (Wardman, et al. 2012; Jenkins et al. 2013; Day et al. 2022) and if the deposit remains in place long-term, metal roofs can corrode, as was reported in Montserrat (Sword-Daniels et al. 2014) and Rabaul, Papua New Guinea (Blong 2003).

Populations of small volcanically active islands can be particularly susceptible to disruption from tephra fall because of their proximity to the source and logistical difficulties in arranging prompt evacuations (e.g. Hicks et al. 2014; Sword-Daniels et al. 2014; Miller et al. 2022). However, better understanding of potential future hazards through modelling a range of eruption scenarios enables mitigations to be considered, both prior to an eruption and during events. This project models a range of eruption scenarios for Ascension Island, focusing on events where tephra fall deposits could be sufficient to cause roof collapse.

## Modelling tephra fall hazard

Tephra transport and dispersal models (TTDM) can be used to reconstruct past events by matching outputs to field observations (inverse mode), to provide short-term tephra hazard forecasts during eruptions (forward mode) and to generate probabilistic hazard analyses that can assist in longer-term planning for potential future events (Folch 2012). Scenarios can be used to assess the impact on current infrastructure of eruptions similar to those in the historic or geological record (e.g. Barsotti et al. 2018; Wild et al. 2019; Aravena et al. 2023) The modelling work in this project underpins probabilistic analysis of tephra fall hazard and related impacts on buildings, focusing on Ascension Island.

TTDMs that focus on deposit hazards usually simplify the physics of the rising plume and use empirical scaling relationships to relate plume height to mass eruption rate (MER), which provides a time-averaged MER as variations in plume height during an eruptive phase are rarely recorded (Aubry et al. 2023; Dürig et al. 2023). The models then solve advection-diffusion-sedimentation equations to simulate diffusion of particles in the plume, advection by wind and sedimentation under gravity (Folch 2012). Near source processes such as aggregation and gravitational settling are usually accounted for through selection of appropriate input parameters (Kavanagh et al. 2018).

Models are calibrated using observations from past eruptions to optimise the model parameters for the volcano of interest (e.g. those defining diffusion of particles within the plume). Where possible, calibration and selection of eruption source parameters (ESPs) should be based on the historic or geological record at that volcano, but gaps in our knowledge of past eruptions may make this impossible. This can occur when tephra is

deposited over inaccessible terrain or over the sea and when erosion rates are high because of wind or rain, making it difficult to constrain previous eruptive events (e.g. Cole et al. 2019; Preece et al. 2021; Burgos et al. 2023). We must then use well-studied volcanoes or eruptions with similar characteristics as analogues, as we assume that 'common processes [occur] at unique volcanoes' (Cashman and Biggs 2014). Criteria for selection of analogues include tectonic setting, eruption size and style, repose intervals, magma composition and deposit geochemistry (Tierz et al. 2019). In this project, I used eruptions on São Miguel, Azores as analogues for poorly-constrained explosive events on Ascension Island, with selection criteria described in detail in Chapter 4.

Modelling of future tephra fall hazard must take account of both the intrinsic variability in volcanic processes and atmospheric conditions, that together influence plume dispersal and tephra deposition (aleatory uncertainty) as well as uncertainties arising from our incomplete knowledge of those processes (epistemic uncertainty) (Beven et al. 2018; Marzocchi et al. 2021). As an example, selection of eruption source parameters based on deposit data introduces uncertainty as many combinations of ESPs may produce tephra deposits that match observed values (Constantinescu et al. 2022). To attempt to quantify these uncertainties, probabilistic hazard analysis uses a large number of simulations, with input parameters for each simulation (e.g. plume height, eruption duration, erupted mass and wind fields) sampled from a range of possible values (Bonadonna et al. 2015; Connor et al. 2015). This allows the probabilities of different outcomes to be assessed, a feature I discuss in detail in Chapter 4.

## Exposure and impacts

Exposure can be defined as the people and infrastructure located in areas affected by a hazard, while vulnerability considers their susceptibility to the impacts of that hazard (UNDRR 2016). Over the past ~ 500 years, over 2400 fatalities resulting from tephra-induced roof collapse have been recorded (Table 1-1). The largest loss of life (2000 deaths) occurred in Guatemala following the VEI 6 eruption of Santa María in 1902. However, even small eruptions can have devastating local impact, with the VEI 3 eruptions of Cerro Negro (1992) and Mayon (1886) leading to 9 and 15 deaths respectively (Brown et al. 2017). In addition, tephra clean-up can result in injury or death, with 17 major injuries reported after the Shinmoedake 2013 eruption due to falls from roofs or ladders (Magill et al. 2013).

# Chapter 1: Introduction

Tephra deposits sufficient to cause roof collapse can extend tens of kilometres from source for even relatively small eruptions, and global population growth means that increasing numbers of people are exposed to volcanic hazard. In 2015, around 59 million people were estimated to live within 10 km of a Holocene volcano (active within the last ~ 11 ka) up from 29 million in 1975 (Freire et al. 2019).

**Table 1-1** Fatalities resulting from building or roof collapse due to tephra fall (Brown et al. 2017)

| Volcano | Date | Eruption size (VEI) | Fatalities |
|---|---|---|---|
| Santa María, Guatemala | 1902 | 6 | 2000 |
| Pinatubo, Philippines | 1991 | 6 | > 300 |
| El Chichón, Mexico | 1982 | 5 | 100 |
| Kelut, Indonesia | 1990 | 4 | 35 |
| Mayon, Philippines | 1886 | 3 | 15 |
| Cerro Negro, Nicaragua | 1992 | 3 | 9 |
| Taal, Philippines | 1754 | 4 | 6 |

The number of people potentially exposed to tephra fall hazard is particularly large because one of the key controls on tephra deposition is wind velocity, with the plume spread depending on the wind direction during an eruption. Using Fuego Volcano in Guatemala and Cerro Negro in Nicaragua as examples, we can estimate current population exposure if eruptions similar to ones in recent decades were to occur, using LandScan global population data (Sims et al. 2023). Fuego's VEI 4 eruption in October 1974 deposited 25 cm thickness of tephra up to 15 km from the source, as shown in Fig. 1-2a (Rose et al. 1978). The current population living in the area bounded by the 25 cm isopach is ~ 7000, but ~ 197 000 people who live within 15 km of Fuego may experience roof collapse from a similar future eruption (Sims et al. 2023). Of course, tephra fall would need to be considered alongside other volcanic hazards such as PDCs which occur on the steep slopes of the volcano and tragically resulted in at least 300 deaths and over 5000 people made homeless following paroxysms in June 2018 (Naismith et al. 2020).

At Cerro Negro in Nicaragua, VEI 3 eruptions in 1971 and 1992 resulted in tephra deposits ~ 20 cm thick ~ 10 km from source (Fig. 1-2b) with roof collapse from tephra loading leading
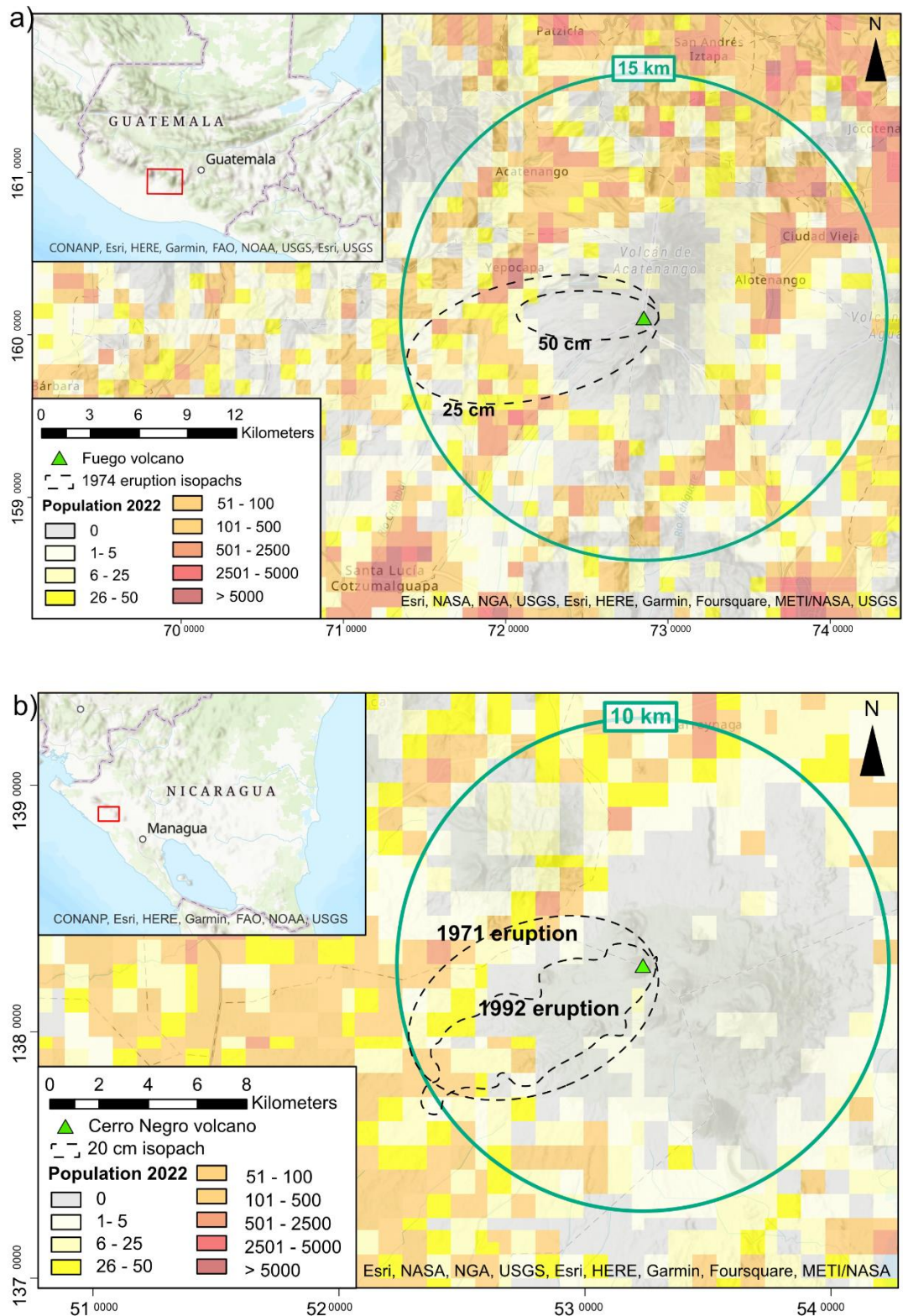
**Fig. 1-2** Area impacted by tephra fall > 20 cm thick following a) 1974 eruption of Fuego, Guatemala (Rose et al. 1978), b) 1971 and 1992 eruptions of Cerro Negro, Nicaragua (Rose et al. 1973; Courtland et al. 2012). Maps show 2022 population (Sims et al. 2023)

to 9 fatalities in 1992  (Rose et al. 1973; Courtland et al. 2012; Brown et al. 2017). The area within the 20 cm isopach has a current population of ~ 1000, but ~ 10 000 people live within 10 km of the volcano and so may potentially be impacted (Sims et al. 2023). A VEI 2 eruption in 1995 also deposited 30 cm of tephra 2 km from source, but this was in a virtually uninhabited area (Hill et al. 1998; Sims et al. 2023).

## Impacts on buildings

In volcanic regions, it is important to understand which buildings are most vulnerable to tephra fall hazard so that mitigations can be considered, but data on building damage from tephra fall are limited. Post-eruption surveys in Olangapo City and Castillejos, Philippines in 1991 (Spence et al. 1996) and Rabaul, Papua New Guinea in 1994 (Blong 2003) provided estimates of collapse loads for a range of building types. Jenkins et al. (2014) combined field data with theoretical and experimental results to identify the range of failure loads expected for different roof types. Surveys of buildings in Chile impacted by the Calbuco 2015 eruption (Hayes et al. 2019) and a remote survey of buildings within ~ 10 km of Kelud volcano in Indonesia following the 2015 eruption (Williams et al. 2020) provided further data on damage to timber- and bamboo-framed buildings. These observations indicate that roofs can collapse at tephra loads of ~ 1–10 kPa depending on the roof material, with the quality of construction and the condition of the building being key factors in determining the failure load. More recently, following an estimated VEI 4 eruption of Taal volcano, Philippines in 2020, deposition of wet andesitic ash led to collapse of low-strength roofs in the proximal towns of Agoncillo and Laurel, with deposit thickness of 11 cm measured in Agoncillo ~ 8 km from source (Balangue-Tarriela et al. 2022). This suggests collapse at a load of 1–2 kPa (assuming dry andesite bulk density of 500–1500 kg m$^{-3}$ and water increasing load by ~ 50 % (Hayes et al. 2019; Osman et al. 2022)).

Long-lasting eruptions present additional challenges as tephra deposits can build up over the course of days or weeks when eruptions consist of multiple explosive pulses. The 2021 eruptions of Soufrière, St Vincent and Cumbre Vieja, La Palma, Canary Islands showed that this increase in tephra fall loading on roofs could lead to roof collapse, highlighting the importance of clearing tephra when it is safe to do so (Bonadonna et al. 2022; Miller et al. 2022; Martí et al. 2022; Cole et al. 2024).

Expanding the dataset of field observations is difficult as tephra fall sufficient to cause building failure usually occurs proximal to the source and it may not be possible to access

buildings within exclusion zones before clean-up has begun or the deposit has been altered by wind or rain. Remotely sensed data can complement fieldwork (Thouret et al. 2022) and laboratory tests allow a wider range of conditions to be explored than is easily encountered in the field. Detailed building surveys supplemented with strength testing of structural components enabled failure loads to be estimated for typical tiled-roof buildings in the Azores (Pomonis et al. 1999). Experimental results have also shown how rainfall and deposit sliding can affect roof loads, although to date only a limited set of conditions has been tested.

Large-scale testing of ash sliding on metal sheet roofing and its impact on guttering found sliding of a dry deposit occurred on roof pitches ≥ 15 ° with substantial ash build up in guttering when the roof pitch was ≥ 30 ° (Hampton et al. 2015). For dry loads, most of the ash was shed from roofs steeper than 35 °, while wet deposits were stable on roofs with pitches ≤ 45 ° (Hampton et al. 2015). Small-scale testing on the impact of post-depositional rainfall on ash found grain size distribution and rainfall intensity affected the depth to which water could infiltrate a deposit, with surface crusting limiting rainfall penetration (Jones et al. 2017; Tarasenko et al. 2019; Williams et al. 2021). On low pitched roofs (15 °) rainfall increased deposit density by 18–30 % (Williams et al. 2021), much lower than theoretical values assuming deposit saturation (Macedonio and Costa 2012). This project expands the range of parameters tested in the laboratory by assessing the geomechanical properties of tephra that are relevant to roof loading (Chapter 2) and identifying their influence on deposit sliding. Small and large shear box tests are used to measure internal angle of friction of fine- and coarse-grained deposits respectively. The test set-up is shown in Fig 1-3 and the method is detailed in Chapter 2. Small-scale sliding tests on a tilt table (Fig 1-4) are used to quantify the impact of grain size and density, roof type and pitch on sliding and assess the resulting reduction in tephra fall loading on a roof (Chapter 3).

## Mitigation actions

During and immediately after eruptions, clearing tephra from roofs and gutters can reduce the likelihood of building failure loads being reached. This requires careful planning for long-lasting eruptions where deposits can build up in evacuated areas (Leonard et al. 2005) and the costs of repeated clean-up must be balanced against timely intervention to minimise building damage (Hayes et al. 2015). In addition, it is important to follow best
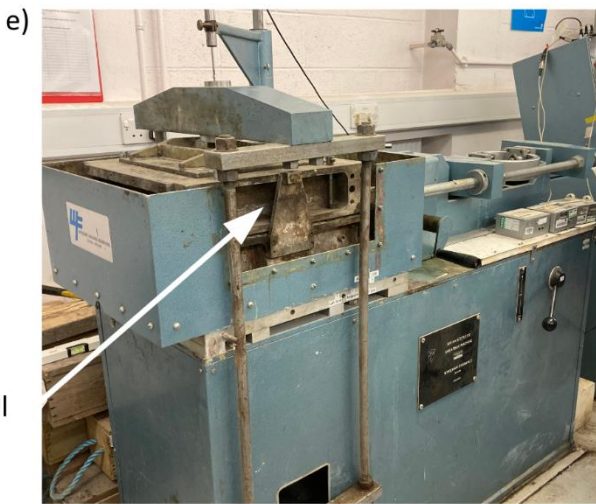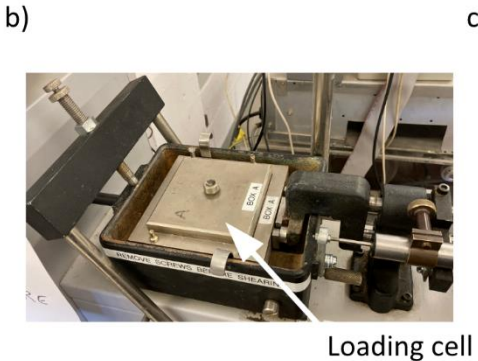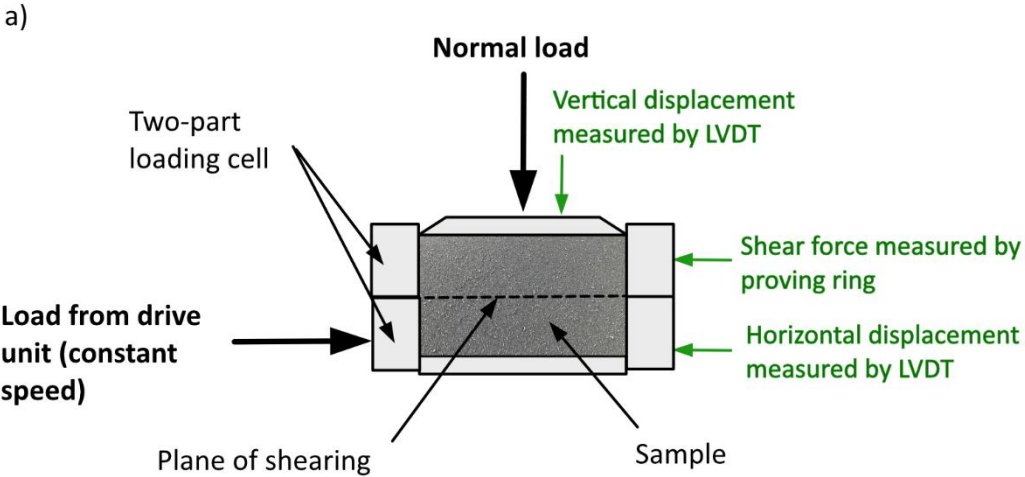
**Fig. 1-3** Shear box equipment. a) Schematic diagram amended from BS 1377-7 (British Standards Institution 1990). LVDT = linear variable differential transformer, b) Loading sample (10 x 10 x 2 cm) in small shear box, (c) Small shear box set-up, d) Loading sample (30 x 30 x 16 cm) in large shear box, e) Large shear box set-up
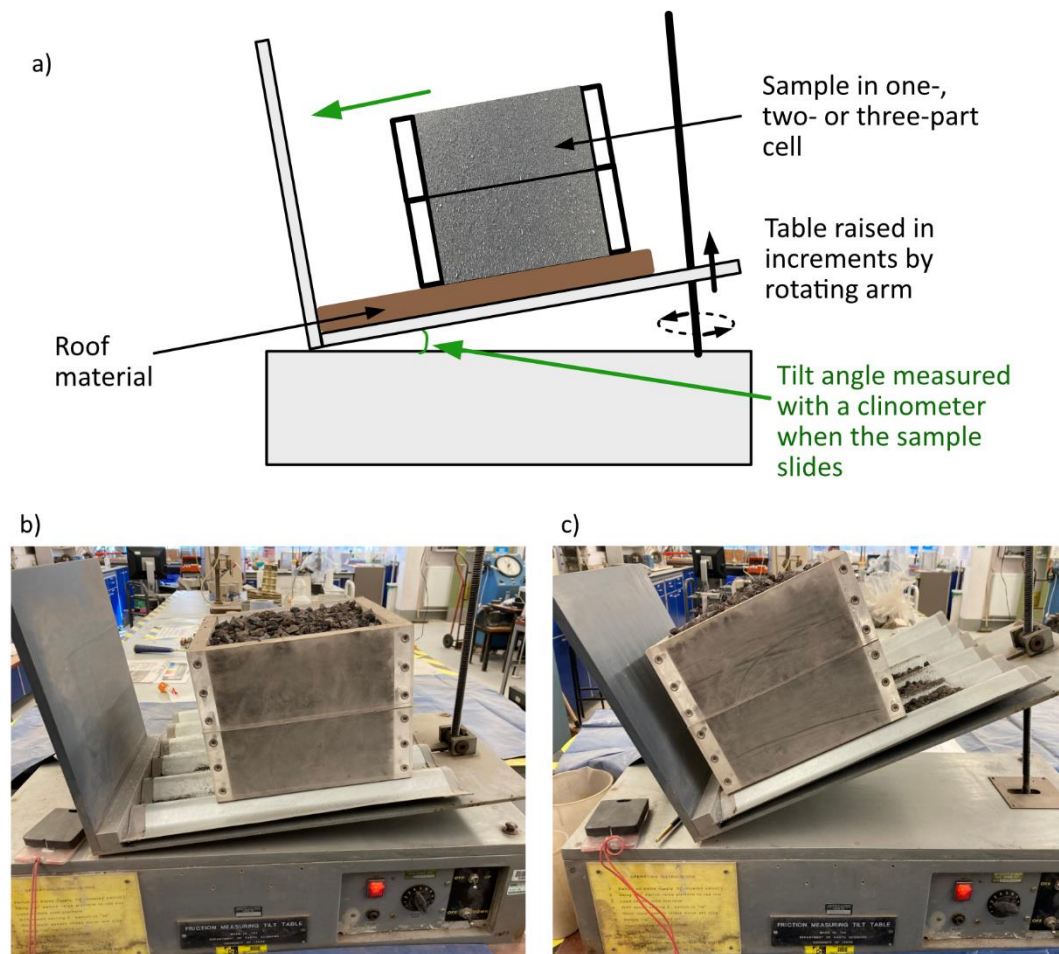
**Fig. 1-4** Tilt table equipment. a) Schematic diagram, b) Scoria sample on metal sheet roofing during test, c) Scoria on metal sheet after sliding. Sample size 22 x 22 x 10 cm per cell

practice guidelines (IVHHN 2021), as injuries during clean-up activities, including falling from roofs, are common (Leonard et al. 2005; Magill et al. 2013) and sweeping away abrasive deposits can damage waterproof roof coatings creating additional structural issues (Wardman, et al. 2012).

In the longer term, constructing buildings to withstand tephra loading could reduce vulnerability if an eruption occurs. This approach is common for snow or wind loads where building standards specify design thresholds that structures must meet. These design codes are based on expected maximum loads that may occur during a building's design life. They do not routinely consider tephra fall, but the methodology for designing for snow loads can provide a useful model when considering how tephra load standards could be compiled as they are both air-fall deposits (Leder et al. 2017).

# Chapter 1: Introduction

## Building design standards

The Structural Eurocodes, used in the UK, throughout Europe and more widely, take a limit state approach to design, where expected loads on a building and its components must never exceed the specified design values that would lead to failure or loss of function (British Standards Institution 2010).

The Eurocode dealing with snow loads (Eurocode 1, part 1-3, enacted in the UK as BS EN 1991-1-3) first defines characteristic values for snow loading on the ground and then uses roof shape coefficients to quantify the fraction of that load that is expected to remain on a roof (British Standards Institution 2009). The characteristic value for snow load on the ground is the load with an expected 50-year return period, calculated using empirical equations which take account of local conditions (British Standards Institution 2009, 2018). These best-fit equations were obtained from statistical analyses of historical snow depth measurements across the EU (Sanpaolesi et al. 1998).

A 50-year timeframe is not appropriate for tephra loading, where repose periods between eruptions may be decades to millennia. It may be more helpful to consider the probabilistic approach to earthquake hazard taken in Eurocode 8 (BS EN 1998). This bases the size and frequency of possible events on previous occurrences at the design location, compiled from earthquake catalogues, historical records and geological investigations (McGuire 1995; British Standards Institution 2013). For buildings with a design life of 50 years, Eurocode 8 requires buildings to sustain no more than light structural damage during events with an expected 225-year return period, and to avoid collapse during events expected once every 2475 years (British Standards Institution 2004).

The impact of a fall deposit on a roof depends in part on the roof shape.  Eurocode 1 defines a shape coefficient ($\mu$) which takes account of roof shape and pitch. Shape coefficients were empirically derived from measurements of ground and roof snow loads collected for 81 buildings over the 1998-99 winter season (Sanpaolesi et al. 1999). Values of $\mu$ for undrifted snow depend on the roof pitch ($\alpha$) as shown in equations 1-1 – 1-3, with steeply pitched roofs (≥ 60 °) assumed to shed all snow.

For $\alpha \leq 30\,°$ $\qquad\qquad \mu = 0.8$ $\qquad\qquad$ (1-1)

For $30\,° < \alpha < 60\,°$ $\qquad \mu = 0.8(60 - \alpha)/30$ $\qquad$ (1-2)

For $\alpha \geq 60\,°$ $\qquad\qquad \mu = 0$ $\qquad\qquad\qquad$ (1-3)

A single shape coefficient is used on the simplest monopitch or symmetrically pitched roofs (Fig. 1-5a), with two values used for a roof with different pitch angles (Fig. 1-5b). The standard also provides equations to take account of drifting and more complex roof shapes (British Standards Institution 2009).
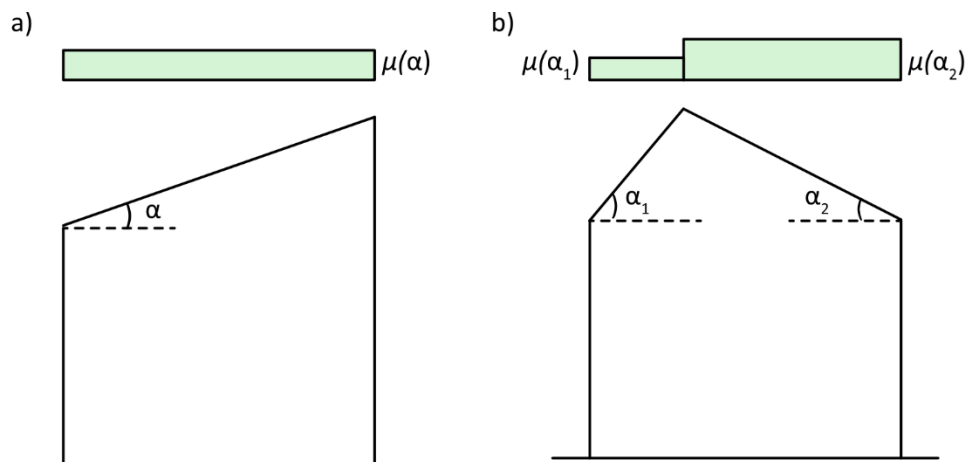


**Fig. 1-5** Roof shape coefficients ($\mu$) used in snow load calculations for a) monopitch roof, b) pitched roof. Values of $\mu$ are defined in equations 1–3 (based on British Standards Institution 2009).

In this research I follow the Eurocode approach, using laboratory sliding tests on analogue simply pitched roofs to define preliminary roof shape coefficients that can be used to calculate tephra load on a roof as a fraction of tephra ground load (Chapter 3). Characteristic values of ground loads for a range of possible eruption scenarios are obtained by probabilistic hazards analyses, as I show in my case study of Ascension Island (Chapter 4).

## Building scale assessment

The impact of tephra fall on an individual roof depends not only on its distance from the source (which influences the tephra load) but also on the type of construction and condition of the building (which control the failure load for the roof). In the final part of this project, I develop a GIS tool that assesses susceptibility to roof collapse at a building scale, enabling mitigation measures to be most appropriately targeted (Chapter 5). The tool combines tephra load maps with my experimental sliding results, published typical collapse loads and data on individual buildings to estimate the probability of roof failure for the eruption scenario being considered.

## References

Aravena A, Bevilacqua A, Neri A, et al (2023) Scenario-based probabilistic hazard assessment for explosive events at the San Salvador volcanic complex, El Salvador. J Volcanol Geotherm Res 438:107809. https://doi.org/10.1016/j.jvolgeores.2023.107809

Aubry TJ, Engwell SL, Bonadonna C, et al (2023) New insights into the relationship between mass eruption rate and volcanic column height based on the IVESPA data set. Geophys Res Lett 50:102633. https://doi.org/10.1029/2022GL102633

Balangue-Tarriela MIR, Lagmay AMF, Sarmiento DM, et al (2022) Analysis of the 2020 Taal Volcano tephra fall deposits from crowdsourced information and field dat. Bull Volcanol 84:35. https://doi.org/10.1007/s00445-022-01534-y

Barsotti S, Di Rienzo DI, Thordarson T, et al (2018) Assessing impact to infrastructures due to tephra fallout from Öræfajökull volcano (Iceland) by using a scenario-based approach and a numerical model. Front Earth Sci 6:196. https://doi.org/10.3389/feart.2018.00196

Baxter PJ, Jenkins S, Seswandhana R, et al (2017) Human survival in volcanic eruptions: thermal injuries in pyroclastic surges, their causes, prognosis and emergency management. Burns 43:1051–1069. https://doi.org/10.1016/j.burns.2017.01.025

Beven KJ, Almeida S, Aspinall WP, et al (2018) Epistemic uncertainties and natural hazard risk assessment – Part 1: A review of different natural hazard areas. Nat Hazards Earth Syst Sci 18:2741–2768. https://doi.org/10.5194/nhess-18-2741-2018

Blong R (2003) Building damage in Rabaul, Papua New Guinea, 1994. Bull Volcanol 65:43–54. https://doi.org/10.1007/s00445-002-0238-x

Blong RJ, Grasso P, Jenkins SF, et al (2017) Estimating building vulnerability to volcanic ash fall for insurance and other purposes. J Appl Volcanology 6:2. https://doi.org/10.1186/s13617-017-0054-9

Bonadonna C, Costa A, Folch A, Koyaguchi T (2015) Tephra dispersal and sedimentation. In: Sigurdsson H, Houghton B, McNutt S, Rymer H (eds) The encyclopedia of volcanoes. Elsevier, Oxford, pp 587–597

Bonadonna C, Pistolesi M, Biass S, et al (2022) Physical characterization of long-lasting hybrid eruptions: the 2021 Tajogaite eruption of Cumbre Vieja (La Palma, Canary Islands). J Geophys Res Solid Earth 127:e2022JB025302. https://doi.org/10.1029/2022JB025302

British Standards Institution (1990) BS 1377–7:1990. Methods of test for soils for civil engineering purposes. Shear strength tests (total stress). BSI, London

British Standards Institution (2010) BS EN 1990:2002+A1:2005: Eurocode - basis of structural design. BSI, London

British Standards Institution (2009) BS EN 1991-1-3: 2003 + A1:2015. Eurocode 1 – actions on structures. Part 1-3: general actions – snow loads. BSI, London

British Standards Institution (2018) NA+A2:2018 to BS EN 1991-1-3: 2003+A1:2015. UK national annex to Eurocode 1: actions on structures. Part 1-3: general actions — snow loads. BSI, London

British Standards Institution (2013) BS EN 1998-3: 2004 + A1:2013. Eurocode 8 — design of structures for earthquake resistance. Part 3: assessment and retrofitting of buildings. BSI, London

British Standards Institution (2004) NA to BS EN 1998-1: 2004. UK National Annex to Eurocode 8 — design of structures for earthquake resistance. Part 1: general rules, seismic actions and rules for buildings. BSI, London

Brown SK, Jenkins SF, Sparks RSJ, et al (2017) Volcanic fatalities database: analysis of volcanic threat with distance and victim classification. J Appl Volcanology 6:15. https://doi.org/10.1186/s13617-017-0067-4

Brown SK, Loughlin SC, Sparks RSJ, et al (2015) Global volcanic hazard and risk. In: Global Volcanic Hazards and Risk. Cambridge University Press, pp 81–172

Buckland HM, Mastin LG, Engwell SL (2022) Modelling the transport and deposition of ash following a magnitude 7 eruption: the distal Mazama tephra. Bull Volcanol 84:87. https://doi.org/10.1007/s00445-022-01593-1

# Chapter 1: Introduction

Burgos V, Jenkins SF, Bono Troncoso L, et al (2023) Identifying analogues for data-limited volcanoes using hierarchical clustering and expert knowledge: a case study of Melimoyu (Chile). Front Earth Sci 11:1144386. https://doi.org/10.3389/feart.2023.1144386

Cashman K, Biggs J (2014) Common processes at unique volcanoes - a volcanological conundrum. Front Earth Sci 2:28. https://doi.org/10.3389/feart.2014.00028

Cashman K V., Rust AC (2020) Far-travelled ash in past and future eruptions: combining tephrochronology with volcanic studies. J Quat Sci 35:11–22. https://doi.org/10.1002/jqs.3159

Cole PD, Barclay J, Robertson REA, et al (2024) Explosive sequence of La Soufrière, St Vincent, April 2021: insights into drivers and consequences via eruptive products. Geological Society, London, Special Publications 539. https://doi.org/10.1144/SP539-2022-292

Cole PD, Robertson REA, Fedele L, Scarpati C (2019) Explosive activity of the last 1000 years at La Soufrière, St Vincent, Lesser Antilles. J Volcanol Geotherm Res 371:86–100. https://doi.org/10.1016/j.jvolgeores.2019.01.002

Connor C, Bebbington M, Marzocchi W (2015) Probabilistic volcanic hazard assessment. In: Sigurdsson H, Houghton B, McNutt S, Rymer H (eds) The encyclopedia of volcanoes, 2nd edn. Elsevier, Oxford, pp 897–910

Constantinescu R, White JT, Connor CB, et al (2022) Uncertainty quantification of eruption source parameters estimated from tephra fall deposits. Geophys Res Lett 49: e2021GL097425. https://doi.org/10.1029/2021GL097425

Courtland LM, Kruse SE, Connor CB, et al (2012) GPR investigation of tephra fallout, Cerro Negro volcano, Nicaragua: a method for constraining parameters used in tephra sedimentation models. Bull Volcanol 74:1409–1424. https://doi.org/10.1007/s00445-012-0603-3

Craig H, Wilson T, Stewart C, et al (2016) Agricultural impact assessment and management after three widespread tephra falls in Patagonia, South America. Nat Hazards 82:1167–1229. https://doi.org/10.1007/s11069-016-2240-1

Day JMD, Geiger H, Troll VR, et al (2022) Bouncing spallation bombs during the 2021 La Palma eruption, Canary Islands, Spain. Earth Sci Syst Soc 2:10063. https://doi.org/10.3389/esss.2022.10063

Deligne NI, Jenkins SF, Meredith ES, et al (2022) From anecdotes to quantification: advances in characterizing volcanic eruption impacts on the built environment. Bull Volcanol 84:7. https://doi.org/10.1007/S00445-021-01506-8

Dürig T, Schmidt LS, Dioguardi F (2023) Optimizing mass eruption rate estimates by combining simple plume models. Front Earth Sci 11:1250686. https://doi.org/10.3389/feart.2023.1250686

Eychenne J, Gurioli L, Damby D, et al (2022) Spatial distribution and physicochemical properties of respirable volcanic ash from the 16–17 August 2006 Tungurahua eruption (Ecuador), and alveolar epithelium response in-vitro. Geohealth 6:e2022GH000680. https://doi.org/10.1029/2022GH000680

Flueck WT (2016) Brief communication: extended chronology of the Cordón Caulle volcanic eruption beyond 2011 reveals toxic impacts. Nat Hazards Earth Syst Sci 16:2351–2355. https://doi.org/10.5194/nhess-16-2351-2016

Folch A (2012) A review of tephra transport and dispersal models: Evolution, current status, and future perspectives. J Volcanol Geotherm Res 235–236:96–115. https://doi.org/10.1016/j.jvolgeores.2012.05.020

Freire S, Florczyk AJ, Pesaresi M, Sliuzas R (2019) An improved global analysis of population distribution in proximity to active volcanoes, 1975-2015. ISPRS Int J Geoinf 8:341. https://doi.org/10.3390/ijgi8080341

Hampton SJ, Cole JW, Wilson G, et al (2015) Volcanic ashfall accumulation and loading on gutters and pitched roofs from laboratory empirical experiments: implications for risk assessment. J Volcanol Geotherm Res 304:237–252. https://doi.org/10.1016/j.jvolgeores.2015.08.012

Hayes JL, Calderón R, Deligne NI, et al (2019) Timber-framed building damage from tephra fall and lahar: 2015 Calbuco eruption, Chile. J Volcanol Geotherm Res 374:142–159. https://doi.org/10.1016/j.jvolgeores.2019.02.017

# Chapter 1: Introduction

Hayes JL, Wilson TM, Magill C (2015) Tephra fall clean-up in urban environments. J Volcanol Geotherm Res 304:359–377. https://doi.org/10.1016/j.jvolgeores.2015.09.014

Hicks A, Barclay J, Simmons P, Loughlin S (2014) An interdisciplinary approach to volcanic risk reduction under conditions of uncertainty: a case study of Tristan da Cunha. Nat Hazards Earth Syst Sci 14:1871–1887. https://doi.org/10.5194/nhess-14-1871-2014

Hill BE, Connor CB, Jarzemba MS, et al (1998) 1995 eruptions of Cerro Negro volcano, Nicaragua, and risk assessment for future eruptions. GSA Bull 110:1231–1241. https://doi.org/10.1130/0016-7606(1998)110<1231:eocnvn>2.3.co;2

Horwell CJ, Sargent P, Andronico D, et al (2017) The iron-catalysed surface reactivity and health-pertinent physical characteristics of explosive volcanic ash from Mt. Etna, Italy. J Appl Volcanology 6:12. https://doi.org/10.1186/s13617-017-0063-8

IVHHN (2021) Health and safety considerations for ashfall clean-up: briefing note. https://www.ivhhn.org/uploads/IVHHN_briefing_note_clean-up_health_safety.pdf. Accessed 29 Mar 2023

Jenkins S, Komorowski JC, Baxter PJ, et al (2013) The Merapi 2010 eruption: an interdisciplinary impact assessment methodology for studying pyroclastic density current dynamics. J Volcanol Geotherm Res 261:316–329. https://doi.org/10.1016/j.jvolgeores.2013.02.012

Jenkins SF, Spence RJS, Fonseca JFBD, et al (2014) Volcanic risk assessment: quantifying physical vulnerability in the built environment. J Volcanol Geotherm Res 276:105–120. https://doi.org/10.1016/j.jvolgeores.2014.03.002

Jenkins SF, Wilson T, Magill C, et al (2015) Volcanic ash fall hazard and risk. In: Loughlin SC, Sparks RSJ, Brown SK, et al. (eds) Global volcanic hazards and risk. Cambridge University Press, Cambridge, pp 173–221

Jones R, Thomas RE, Peakall J, Manville V (2017) Rainfall-runoff properties of tephra: simulated effects of grain-size and antecedent rainfall. Geomorphology 282:39–51. https://doi.org/10.1016/j.geomorph.2016.12.023

Kavanagh JL, Engwell SL, Martin SA (2018) A review of laboratory and numerical modelling in volcanology. Solid Earth 9:531–571. https://doi.org/10.5194/se-9-531-2018

Leder J, Wenzel F, Daniell JE, Gottschämmer E (2017) Loss of residential buildings in the event of a re-awakening of the Laacher See Volcano (Germany). J Volcanol Geotherm Res 337:111–123. https://doi.org/10.1016/j.jvolgeores.2017.02.019

Leonard GS, Williams S, Finnis K, et al (2005) Impacts and management of recent volcanic eruptions in Ecuador: lessons for New Zealand. GNS Science report 2005/20. https://shop.gns.cri.nz/publications/science-reports/2001-to-2005/2005/. Accessed 21 Nov 2019

Ligot N, Guevara A, Delmelle P (2022) Drivers of crop impacts from tephra fallout: insights from interviews with farming communities around Tungurahua volcano, Ecuador. Volcanica 5:163–181. https://doi.org/10.30909/vol.05.01.163181

Lokachari S, Song W, Yuan J, et al (2020) Influence of molten volcanic ash infiltration on the friability of APS thermal barrier coatings. Ceram Int 46:11364–11371. https://doi.org/10.1016/j.ceramint.2020.01.166

Macedonio G, Costa A (2012) Brief communication: rain effect on the load of tephra deposits. Nat Hazards Earth Syst Sci 12:1229–1233. https://doi.org/10.5194/nhess-12-1229-2012

Magill C, Wilson T, Okada T (2013) Observations of tephra fall impacts from the 2011 Shinmoedake eruption, Japan. Earth, Planets Space 65:677–698. https://doi.org/10.5047/eps.2013.05.010

Martí J, Becerril L, Rodríguez A (2022) How long-term hazard assessment may help to anticipate volcanic eruptions: the case of La Palma eruption 2021 (Canary Islands). J Volcanol Geotherm Res 431:107699. https://doi.org/10.1016/j.jvolgeores.2022.107669

Marzocchi W, Selva J, Jordan TH (2021) A unified probabilistic framework for volcanic hazard and eruption forecasting. Nat Hazards Earth Syst Sci 21:3509–3517. https://doi.org/10.5194/nhess-21-3509-2021

McGuire RK (1995) Probabilistic seismic hazard analysis and design earthquakes: closing the loop. Bull Seismol Soc Am 85:1275–1284. https://doi.org/10.1785/BSSA0850051275

Miller VL, Joseph EP, Sapkota N, Szarzynski J (2022) Challenges and opportunities for risk management of volcanic hazards in small-island developing states. Mt Res Dev 42:D22–D31. https://doi.org/10.1659/MRD-JOURNAL-D-22-00001.1

# Chapter 1: Introduction

Naismith A, Armijos MT, Barrios Escobar EA, et al (2020) Fireside tales: understanding experiences of previous eruptions among other factors that influence the decision to evacuate from eruptive activity of Volcán de Fuego. Volcanica 3:205–226. https://doi.org/10.30909/vol.03.02.205226

Osman S, Rossi E, Bonadonna C, et al (2019) Exposure-based risk assessment and emergency management associated with the fallout of large clasts at Mount Etna. Nat Hazards Earth Syst Sci 19:589–610. https://doi.org/10.5194/nhess-19-589-2019

Osman S, Thomas M, Crummy J, et al (2023) Laboratory tests to understand tephra sliding behaviour on roofs. J Appl Volcanology 12:11. https://doi.org/10.1186/ s13617-023-00137-2

Osman S, Thomas M, Crummy J, Carver S (2022) Investigation of geomechanical properties of tephra relevant to roof loading for application in vulnerability analyses. J Appl Volcanology 11:9. https://doi.org/10.1186/s13617-022-00121-2

Pearson D, Brooker R (2020) The accumulation of molten volcanic ash in jet engines; simulating the role of magma composition, ash particle size and thermal barrier coatings. J Volcanol Geotherm Res 389:106707. https://doi.org/10.1016/ j.jvolgeores.2019.106707

Pomonis A, Spence R, Baxter P (1999) Risk assessment of residential buildings for an eruption of Furnas Volcano, São Miguel, the Azores. J Volcanol Geotherm Res 92:107–131. https://doi.org/10.1016/S0377-0273(99)00071-2

Preece K, Barclay J, Brown RJ, et al (2021) Explosive felsic eruptions on ocean islands: a case study from Ascension Island (South Atlantic). J Volcanol Geotherm Res 416:107284. https://doi.org/10.1016/j.jvolgeores.2021.107284

Risica G, Rosi M, Pistolesi M, et al (2022) Deposit-derived block-and-ash flows: the hazard posed by perched temporary tephra accumulations on volcanoes; 2018 Fuego disaster, Guatemala. J Geophys Res Solid Earth 127:e2021JB023699. https://doi.org/10.1029/ 2021JB023699

Rose WI, Anderson AT, Woodruff LG, Bonis SB (1978) The October 1974 basaltic tephra from Fuego volcano: description and history of the magma body. J Volcanol Geotherm Res 4:3–53. https://doi.org/10.1016/0377-0273(78)90027-6

Rose WI, Bonis S, Stoiber RE, et al (1973) Studies of volcanic ash from two recent Central American eruptions. Bull Volcanologique 37:338–364. https://doi.org/10.1007/BF02597633

Sanpaolesi L, Brettle M, Currie D, et al (1999) Scientific support activity in the field of structural stability of civil engineering works: snow loads. Final Report Phase II. www2.ing.unipi.it/dic/snowloads/Final Report II.pdf. Accessed 28 Oct 2022

Sanpaolesi L, Currie D, Sims P, et al (1998) Scientific support activity in the field of structural stability of civil engineering works: snow loads. Final Report Phase I. www2.ing.unipi.it/dic/snowloads/Final Report I.pdf. Accessed 28 Oct 2022

Sims K, Reith A, Bright E, et al (2023) LandScan global 2022. landscan.ornl.gov. Accessed 15 Aug 2023

Song W, Yang S, Fukumoto M, et al (2019) Impact interaction of in-flight high-energy molten volcanic ash droplets with jet engines. Acta Mater 171:119–131. https://doi.org/10.1016/j.actamat.2019.04.011

Spence RJS, Pomonis A, Baxter PJ, et al (1996) Building damage caused by the Mount Pinatubo eruption of June 15, 1991. In: Newhall CG, Punongbayan RS (eds) Fire and mud: eruptions and lahars of Mount Pinatubo, Philippines. University of Washington Press, Seattle, pp 1055–1061

Sword-Daniels V, Wilson TM, Sargeant S, et al (2014) Consequences of long-term volcanic activity for essential services in Montserrat: challenges, adaptations and resilience. In: Wadge G, Robertson REA, Voight B (eds) The eruption of Soufrière Hills Volcano, Montserrat from 2000 to 2010. Geological Society, London, pp 471–488

Tarasenko I, Bielders CL, Guevara A, Delmelle P (2019) Surface crusting of volcanic ash deposits under simulated rainfall. Bull Volcanol 81:30. https://doi.org/10.1007/S00445-019-1289-6

Thouret J-C, Arapa E, Charbonnier S, et al (2022) Modeling tephra fall and sediment-water flows to assess their impacts on a vulnerable building stock in the city of Arequipa, Peru. Front Earth Sci 10:865989. https://doi.org/10.3389/feart.2022.865989

# Chapter 1: Introduction

Tierz P, Loughlin SC, Calder ES (2019) VOLCANS: an objective, structured and reproducible method for identifying sets of analogue volcanoes. Bull Volcanol 81:76. https://doi.org/10.1007/s00445-019-1336-3

Tsunematsu K, Ishimine Y, Kaneko T, et al (2016) Estimation of ballistic block landing energy during 2014 Mount Ontake eruption. Earth Planets Space 68:1–11. https://doi.org/10.1186/s40623-016-0463-8

United Nations Office for Disaster Risk Reduction (2016) Report of the open-ended Intergovernmental Expert Working Group on indicators and terminology relating to disaster risk reduction. https://www.undrr.org/publication/report-open-ended-intergovernmental-expert-working-group-indicators-and-terminology. Accessed 4 Jul 2023

Wardman, J, Sword-Daniels V, Stewart C, Wilson T (2012) Impact assessment of the May 2010 eruption of Pacaya volcano, Guatemala. GNS Science report 2012/09. https://ir.canterbury.ac.nz/handle/10092/10563. Accessed 5 Jul 2023

Watson EJ, Swindles GT, Savov IP, et al (2017) Estimating the frequency of volcanic ash clouds over northern Europe. Earth Planet Sci Lett 460:41–49. https://doi.org/10.1016/j.epsl.2016.11.054

Waythomas CF, Mastin LG (2020) Mechanisms for ballistic block ejection during the 2016–2017 shallow submarine eruption of Bogoslof volcano, Alaska. Bull Volcanol 82:13. https://doi.org/10.1007/s00445-019-1351-4

Wild AJ, Wilson TM, Bebbington MS, et al (2019) Probabilistic volcanic impact assessment and cost-benefit analysis on network infrastructure for secondary evacuation of farm livestock: a case study from the dairy industry, Taranaki, New Zealand. J Volcanol Geotherm Res 387:106670. https://doi.org/10.1016/j.jvolgeores.2019.106670

Williams GT, Jenkins SF, Biass S, et al (2020) Remotely assessing tephra fall building damage and vulnerability: Kelud Volcano, Indonesia. J Appl Volcanology 9:10. https://doi.org/10.1186/s13617-020-00100-5

Williams GT, Jenkins SF, Lee DWJ, Wee SJ (2021) How rainfall influences tephra fall loading - an experimental approach. Bull Volcanol 83:42. https://doi.org/10.1007/s00445-021-01465-0

Wilson G, Wilson TM, Deligne NI, et al (2017) Framework for developing volcanic fragility and vulnerability functions for critical infrastructure. J Appl Volcanology 6:14. https://doi.org/10.1186/s13617-017-0065-6

Zabert I, Benítez S, Zabert G (2019) Impact on the respiratory airways of acute exposure to volcanic ash in the Patagonia: cross-sectional study. Rev Am Med Resp 19:119–124

# Chapter 2

# Investigation of geomechanical properties of tephra relevant to roof loading for application in vulnerability analyses

Sara Osman[1], Mark Thomas[1], Julia Crummy[2] and Stephen Carver[3]

[1] University of Leeds, School of Earth and Environment, Woodhouse, Leeds LS2 9JT, UK

[2] British Geological Survey, The Lyell Centre, Research Avenue South, Edinburgh EH14 4AP, UK

[3] University of Leeds, School of Geography, Woodhouse, Leeds LS2 9JT, UK

Material published in the appendix of this paper is presented in Appendix A.

# Chapter 2: Geomechanical properties of tephra

## Abstract

Tephra fall can lead to significant additional loading on roofs. Understanding the relevant geomechanical properties of tephra is critical when assessing the vulnerability of buildings to tephra fall and designing buildings to withstand tephra loads. Through analysis of published data and new experimental results on dry tephra (both natural samples from Ascension Island, South Atlantic and synthetic tephra made from crushed aggregates), we discuss the geomechanical properties of tephra relevant to roof loading, which include bulk density, grain size distribution and internal angle of friction. Compiled published data for deposits from 64 global eruptions reveal no clear trend in deposit densities based on magma composition or eruption size. The global data show a wide range of values within single eruptions and between eruptions of similar compositions. Published grain size distributions near to source (≤ 10 km) vary widely but again there are no clear trends relating to magma composition. We used laboratory tests to investigate the internal angle of friction, which influences deposit sliding behaviour. For dry tephra, at the low normal stresses likely to be experienced in roof loads (≤ 35 kPa), we found similar values across all our tests (35.8°– 36.5°) suggesting that any internal sliding will be consistent across a variety of deposits. By considering different magma compositions, densities and grain size distributions, we have provided an envelope of values for deposit parameters relevant to roof loading, in which future eruptions are likely to sit. Finally, we created synthetic tephra (fine- and coarse-grained pumice and scoria) by crushing volcanic aggregates and compared it to samples from Ascension and published data. Our results reveal that synthetic tephra successfully replicated the properties relevant to loading, potentially reducing the need to collect and transport natural samples.

## Introduction

During an explosive volcanic eruption, the fall out of tephra (ejected particles of all sizes) from the eruptive plume can lead to significant additional loading on roofs. Buildings close to an eruptive vent can sustain substantial damage or even collapse (e.g. Blong 2003; Jenkins et al. 2014; Hayes et al. 2019). Most recently, roof collapses occurred following the April 2021 eruption of La Soufrière on St Vincent (Lesser Antilles).

The key factors that are thought to influence the load transferred to the roof by a tephra deposit, are magma composition and vesicularity, the size distribution and shape of the grains, and properties of the roof (Fig. 2-1). Magma properties influence the density of

individual grains, while their size distribution and shape influence packing (Estrada 2016; Landauer et al. 2020).
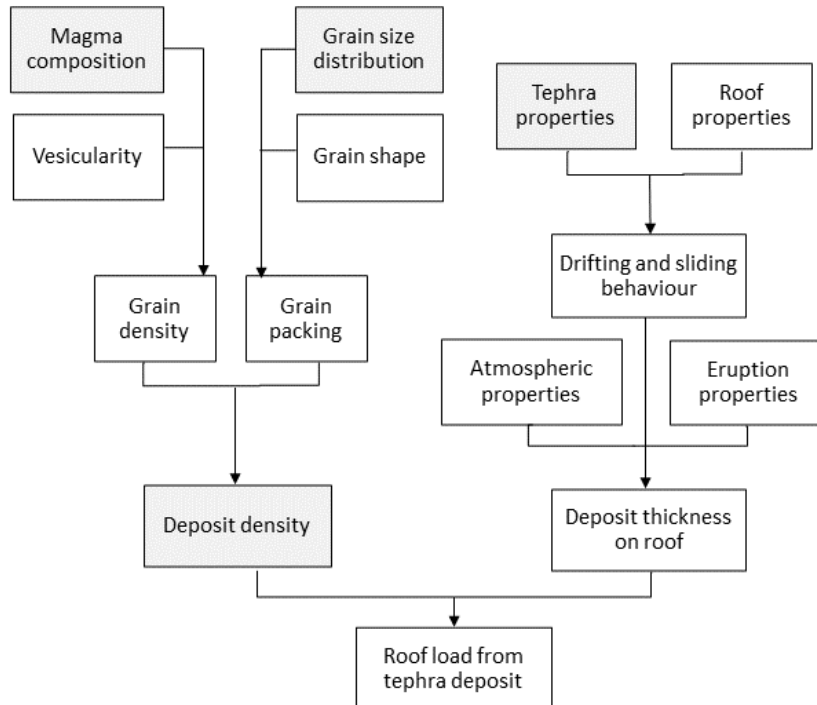


**Fig. 2-1** Key factors influencing the load transferred to the roof by a tephra deposit. Shaded factors are the focus of this study

Deposit density depends on both grain density and packing and can also increase substantially if the deposit is wet (e.g. Blong 1981; Macedonio and Costa 2012; Hayes et al. 2019; Williams et al. 2021). The size and intensity of the eruption impact the height of the volcanic plume (e.g. Bonadonna and Costa 2013; Suzuki et al. 2016; Cassidy et al. 2018) and atmospheric processes, including wind velocity and precipitation, influence the transport and deposition of particles (e.g. Petersen et al. 2012; Bonadonna et al. 2015; Poulidis et al. 2018). In turn, these factors affect the amount of tephra deposited at any location. The load on the roof depends on the bulk density and thickness of the deposit, but tephra thickness can be altered after deposition by drifting and sliding. These processes are influenced by tephra properties, such as the internal angle of friction and grain size distribution, as well as the material, shape and pitch of the roof and the coefficient of friction between the tephra and the roof (e.g. Hampton et al. 2015).

# Chapter 2: Geomechanical properties of tephra

The aim of this study is to discuss and present the geomechanical properties of tephra relevant to roof loading. Understanding these properties is critical when assessing the vulnerability of buildings in areas susceptible to tephra fall as they influence the additional load that is transferred to a roof and hence its likelihood of collapse. Estimating this additional loading is also important for building design, where building codes use a combination of historic records and experimental results to assess loads likely to occur within a building's lifespan. Snow loading, which is fundamentally similar to loading from tephra in that it a granular air-fall deposit, is well characterised and routinely included in international design standards (e.g. British Standards Institution 2009; International Standards Organization 2013; American Society of Civil Engineers and Structural Engineering Institute 2017), but tephra fall is not routinely taken into account, and at the time of writing is not specifically considered in any international design standards or building codes.

This study forms part of a wider body of research investigating the potential of roof collapse by tephra loading with relevance to Ascension Island and the development of standards to account for tephra loads in building design. Ascension is a volcanically active UK Overseas Territory in the south Atlantic with an area of 98 km$^2$ and ~ 780 residents. Because of Ascension's remote location and exposure to potential volcanic hazards, buildings could be vulnerable to collapse from any future explosive activity. In addition, Ascension tephra deposits vary widely in grain size and composition (e.g. Winstanley 2020; Preece et al. 2021), making it an ideal location to investigate any variation in the geomechanical properties of tephra, and whether synthetic tephra can be used in lieu of natural material.

In order to undertake the required laboratory tests, large volumes of tephra are required, and these are not always easily obtained from natural sources due to the hazards associated with near-source sampling following an eruption and the costs of transporting large volumes of samples. We therefore investigated whether synthetic tephra (of unknown composition, made from crushing and sieving commercially available volcanic aggregates) could be used to model the properties of naturally occurring deposits that are relevant when considering roof loads (bulk density, grain size distribution and internal angle of friction). By comparing synthetic tephra of a non-specific composition to published data and the results from tests conducted as part of this study on Ascension tephra, the possibility of using commercially available aggregate to generate the volumes of material required for large scale testing can be assessed.

We compiled published density and grain size data for deposits from 64 global eruptions, measured the grain size distributions (GSDs) of samples of pumice, scoria and ash from Ascension and selected representative GSDs for our synthetic samples. We then used shear box tests to measure the internal angle of friction of dry samples of both natural and synthetic material. The tests undertaken in this study were only performed on dry tephra and do not consider the saturated state of the deposit. Results for our synthetic samples matched well with both Ascension samples and published data from a wide range of eruptions; we can therefore be confident in using synthetic tephra to investigate the properties that control loading and sliding.

## Methods

To ensure our test samples were representative of natural deposits, we compared them to published GSDs from global mafic, intermediate and silicic eruptions (listed in Table 2-1), focusing on proximal samples ($\leq$ 10 km from source) to enable comparison with GSDs of samples from Ascension. The Ascension samples were sieved to 4 $\phi_g$ (63 µm) diameter, with smaller particles analysed by dynamic image analysis (British Standards Institution 2006) using a Microtrac CAMSIZER® X2. These samples comprised trachytic ash, lithic-rich and lithic-poor trachytic pumice (Preece et al. 2021) and coarse-grained and fine-grained basaltic scoria (Winstanley 2020) from five locations shown in Fig. 2-2.

Bulk densities for dry deposits were compiled from published data for 61 eruptions at 33 volcanoes (detailed in the Appendix). These cover small to large eruptions (VEI 2–7), with mafic to silicic magma compositions, and include both proximal-medial (< 50 km from source) and distal ($\geq$ 50 km from source) values.

Test samples were created by crushing commercially available volcanic material using a Proctor compactor to obtain a range of grain sizes. The aggregates comprised mafic 'volcanic lava filtration gravel' and silicic 'pumice gravel' and 'pumice crush' from Specialist Aggregates Ltd. Samples were then sieved to 4 $\phi_g$ (63 µm) and finer grain sizes were analysed using the CAMSIZER® X2. The coarse ($\geq$ − 4 $\phi_g$, $\leq$ 16 mm) and fine ($\geq$ 1 $\phi_g$, $\leq$ 2 mm) test GSDs were selected to be consistent with published global data and the Ascension deposits. For each test, samples were oven dried and the sample mass and volume were measured, and density calculated to ensure that test densities were consistent with our dataset of published values.

# Chapter 2: Geomechanical properties of tephra

**Table 2-1** Published grain size distribution (GSD), size and magma composition for eruptions with published GSDs ≤ 10 km from source, used in Fig. 2-3

| Eruption | VEI | Composition | GSD distance from source (km) | Reference |
|---|---|---|---|---|
| Askja 1875 Unit D | 5* | Rhyolite | 1–7 | (Sparks et al. 1981) |
| Fogo A | 5 | Trachyte | ~ 3–8 | (Walker and Croasdale 1970; Pensa et al. 2015) |
| Eyjafjallajökull 2010 | 4 | Trachyte | 2–9.6 | (Bonadonna et al. 2011) |
| Quizapu 1932 | 6 | Dacite | 2.5–7.4 | (Hildreth and Drake 1992) |
| Agung 1963 | 5 | Andesite | 7 | (Self and Rampino 2012) |
| Ruapehu 1996 | 3 | Andesite | 0.4 | (Bonadonna et al. 2005) |
| Hekla 1991 | 3 | Basaltic andesite | 5 | (Gudnason et al. 2017) |
| Calbuco 2015 | 4 | Basaltic andesite | 5–6 | (Castruccio et al. 2016; Romero et al. 2016) |
| Etna 2002-3 | 3 | Basalt | 3.7–10 | (Andronico et al. 2008) |
| Grimsvötn 2004 | 3 | Basalt | 5–10 | (Oddsson 2007) |
| Kilauea Iki 1959 | 2 | Basalt | ~ 0.5–4 | (Mueller et al. 2019) |

Shear box tests were used to measure the internal angle of friction of the test samples. These tests represent stress along a shear plane, as described in BS 1377–7 (British Standards Institution 1990) and use the Mohr-Coulomb equation. For dry samples (with no fluid pore pressure) the equation can be written as:

$$\tau = \sigma \tan \varphi_f + c \qquad (2\text{-}1)$$

where $\tau$ is the shear stress at failure along a plane, $\sigma$ is normal stress, $\varphi_f$ is the internal angle of friction, and $c$ is cohesion.

For each test, the sample was loaded into the shear box and a normal force applied via a load plate. For the small shear box, this force came from calibrated weights added to a lever arm; for the large shear box, weights were added directly to the load plate for normal forces < 1 kN, and via a pneumatic loading system for forces ≥ 1 kN. The equivalent normal stress, $\sigma$, was calculated from stress = force/area. The shear box consisted of an upper and
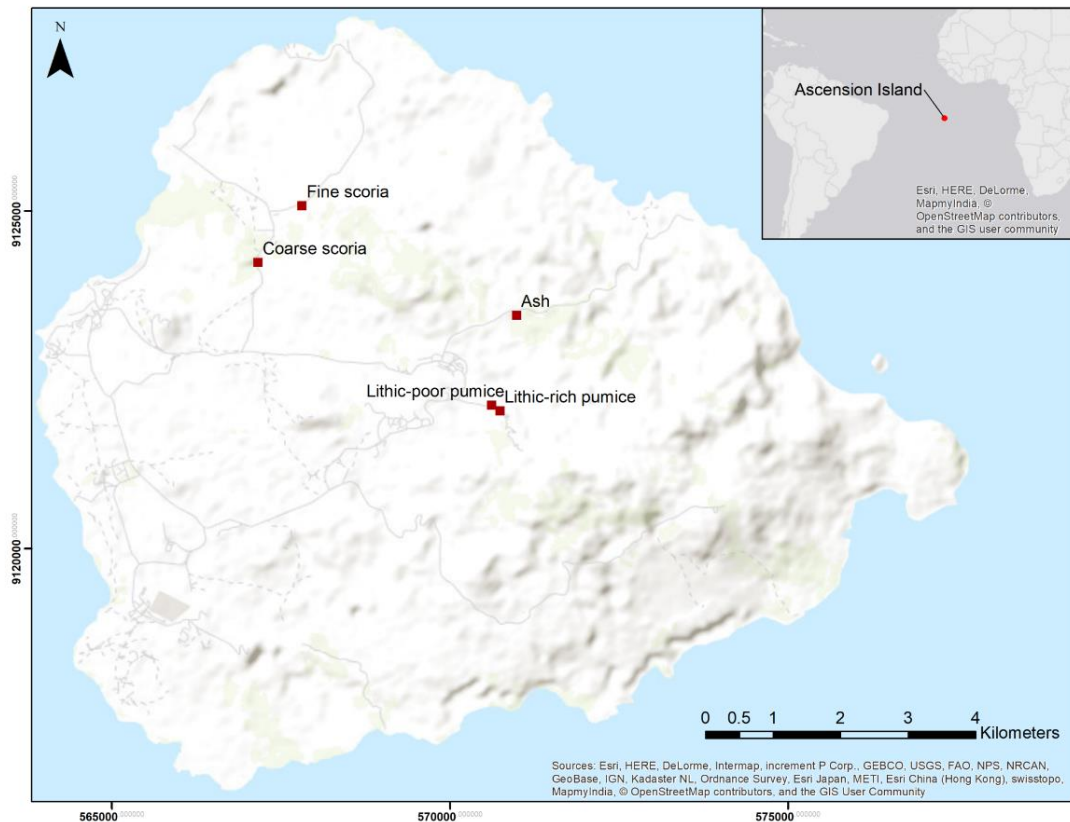
**Fig. 2-2** Map of Ascension Island showing the locations of tephra samples used in this study

lower section which were gradually moved relative to each other. The shear force required to move the sections was measured using a proving ring. Values were recorded throughout the test and used to calculate the equivalent shear stress, $\tau$. Horizontal and vertical displacement in the sample were also recorded using Linear Variable Differential Transformers (LVDT). The test finished when the shear force peaked or reached a plateau, as this represented the maximum shear stress in the sample before failure. Tests were carried out at different normal stresses ($\sigma$) and plotted against corresponding values of shear stress ($\tau$). The internal angle of friction of the sample ($\varphi_f$) is the gradient of the best fit line through the data points on a $\sigma$ vs $\tau$ plot (Eq. 2-1).

To minimise any scale effects, BS 1377-7 specified that the largest grain size in the sample must be $\leq$ one tenth of the specimen height in the shear box. We used small shear box tests (sample size 100 $\times$ 100 $\times$ 20 mm) for samples $\leq$ 2 mm in diameter and large shear box tests (sample size 300 $\times$ 300 $\times$ 160 mm) for samples $\leq$ 16 mm in diameter. We conducted tests at normal stresses of 3–35 kPa, representing deposit depths for our test samples of

33

~ 50–220 cm. These depths can lead to roof failure depending on the density of the deposit (Blong 1984; Jenkins et al. 2014).

To compare $\varphi_f$ values for the test tephra to natural samples, small shear box tests were also used to determine the internal friction angle for the Ascension ash ($\leq 2$ mm) samples. The sample volumes of pumice and scoria were too small to enable large shear box tests to be carried out on these materials.

## Results

### Near-source GSDs

Published proximal GSDs vary widely, even for eruptions with similar magma compositions Fig. 2-3a-c for mafic (basalt, $\leq 52$ % $SiO_2$), intermediate (basaltic andesite—andesite, 52–63 % $SiO_2$) and silicic (dacite—rhyolite, > 63 % $SiO_2$) eruptions detailed in Table 2-1). The Ascension deposits (Fig. 2-3d) also show coarse to fine GSDs. When all the GSDs are plotted together (Fig. 2-4) there is a large overlap and, for these proximal deposits, magma composition does not seem to control GSD. The coarse and fine GSDs of the test tephra (also shown on Fig. 2-4) were selected to be representative of both published data and the Ascension Island samples. The coarse test distribution is at the finer end of the published range of GSDs; however, a maximum grain size of 16 mm was chosen because of size constraints of the laboratory equipment, and because we are interested in the properties of the bulk deposit rather than properties of individual large clasts.

### Deposit densities

Deposit densities compiled from published data reveal a range of values from ~ 400 to 1500 kg m$^{-3}$ for all magma compositions. For individual eruptions, where proximal/medial and distal bulk densities are reported separately, distal values are usually higher, likely indicating higher grain density and/or more efficient packing of finer grains. For some eruptions e.g. Fuego 1973 (Rose et al. 2008) textural variation in the deposits results in both low and high proximal to medial bulk densities. There is more variability in the density for low to medium silica content materials and some high silica samples have lower bulk densities. However, when the dataset is taken as a whole, there are no clear trends relating to magma composition, eruption size or distance from source (Figs. 2-5 and 2-6). Densities of the (dry) test samples are within the range of values found in the published data, as shown in Table 2-2.
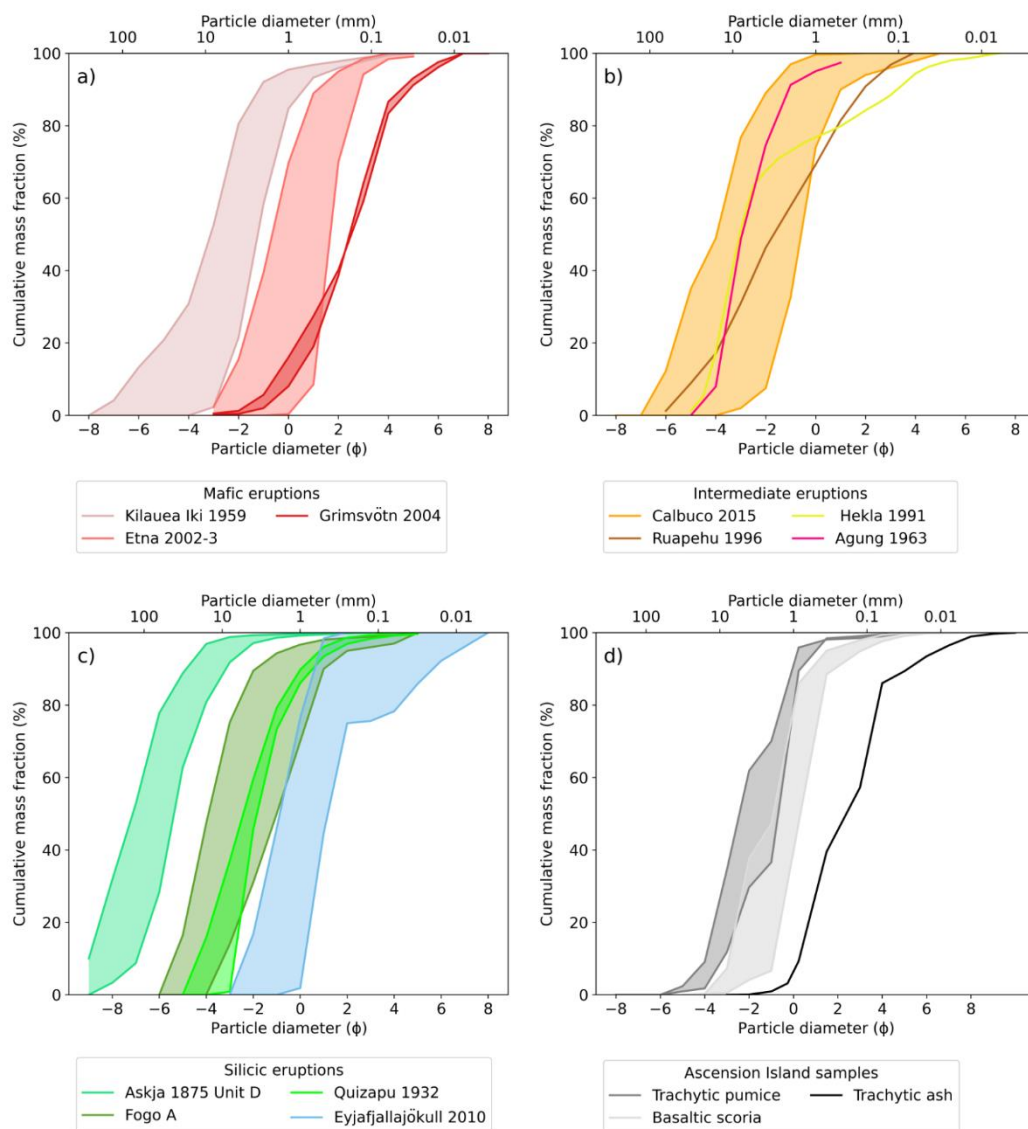
**Fig. 2-3** Grain size distributions for proximal ($\leq$ 10 km from source) samples from published data (Table 2-1) from a) mafic eruptions, b) intermediate eruptions and c) silicic eruptions. d) presents trachytic pumice and ash, and basaltic scoria samples from Ascension Island
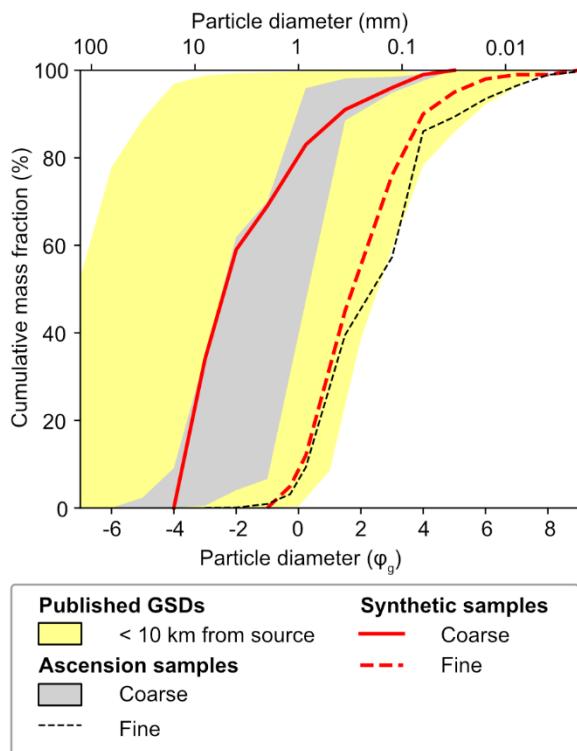
**Fig. 2-4** Summary of published grain size distributions (GSDs) for eruptions listed in Table 2-1 and presented in Fig. 2-3, plus GSDs for the Ascension samples and the test samples used in this study
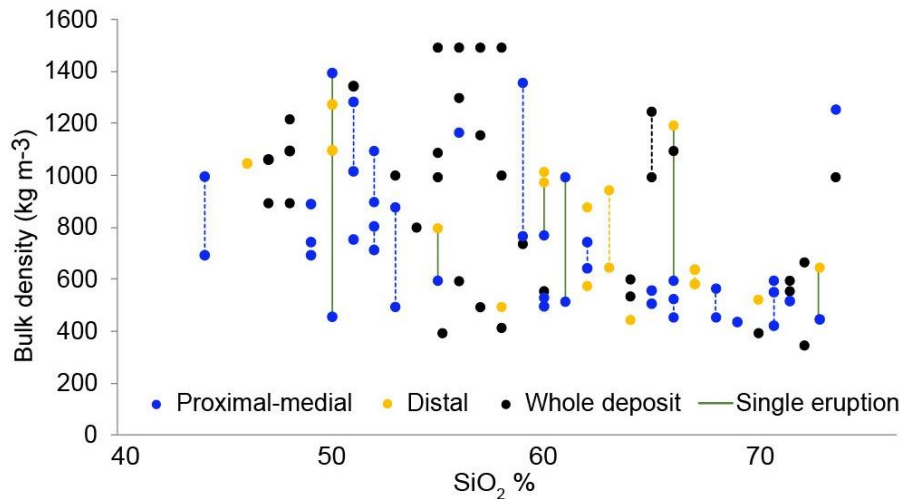


**Fig. 2-5** Variation of bulk density with magma composition. Values are for proximal-medial samples (< 50 km from source), distal samples ($\geq$ 50 km from source) or the whole deposit. Dotted lines indicate a range of values was reported. Proximal-medial and distal values from the same eruption are linked by a solid green line
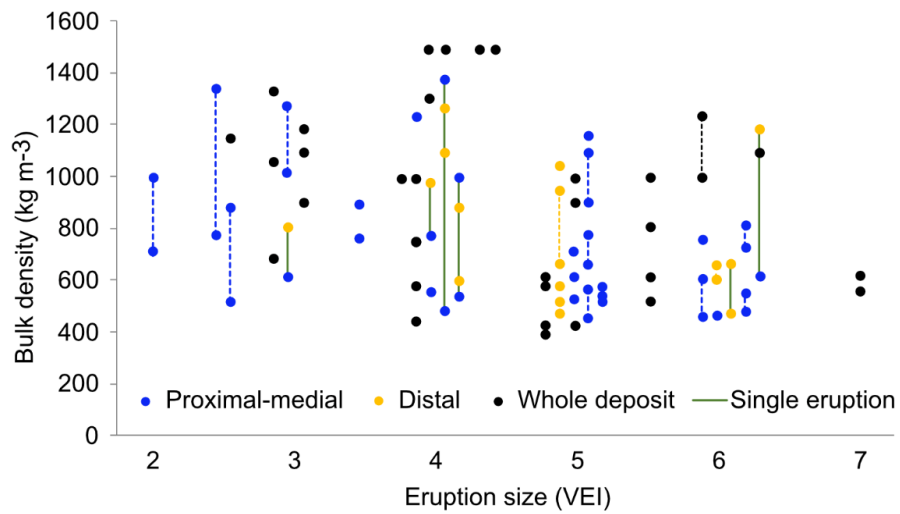
**Fig. 2-6** Variation of bulk density with eruption size (VEI). Values are for proximal-medial samples (< 50 km from source), distal samples (≥ 50 km from source) or the whole deposit. Dotted lines indicate a range of values was reported. Proximal-medial and distal values from the same eruption are linked by a solid green line.

**Table 2-2** Dry densities of test samples, and published data listed in the Appendix. Coarse and fine grain size distributions are shown in Fig. 2-4

| Sample | Grain size distribution | Mean density (kg m$^{-3}$) |
|---|---|---|
| Synthetic pumice | Fine | 602 |
| | Coarse | 412 |
| Synthetic scoria | Fine | 1532 |
| | Coarse | 1223 |
| Ascension ash | Fine | 1019 |
| Published data | All | 400 - 1500 |

## Peak stress and internal angle of friction

Results from the shear box tests (Figs. 2-7 and 2-8) reveal that after initial compaction the synthetic samples dilated and shear stress reached a peak value. In comparison, the Ascension ash samples compacted throughout the tests (negative vertical displacement) and shear stress reached a plateau rather than peaking. No breaking or crushing of the grains was observed, with changes in volume achieved by rearrangement of deposit packing.

On plots of normal stress vs peak shear stress, for both pumice and scoria the coarse and fine GSDs plot on the same line (Fig. 2-9). The friction angles ($\varphi_f$), calculated using Eq. (2-1), are very similar for the test samples and the Ascension ash, at between 35.8 and 36.5° (Table 2-3). These results suggest that the internal angle of friction is independent of both tephra composition and grain size at the low normal stresses of these tests.

**Table 2-3** Internal angle of friction from shear box tests for synthetic pumice and scoria and Ascension Island ash

|                   | Friction angle (°) |
| ----------------- | ------------------ |
| Synthetic pumice  | 36.5               |
| Synthetic scoria  | 35.8               |
| Ascension ash     | 36.4               |

# Discussion

## Near-source grain size distribution data

Typically, GSDs of deposits become finer with increasing distance from the vent, as larger particles fall out close to source and finer particles remain in the plume (Koyaguchi and Ohno 2001a). However, the GSD of a proximal deposit depends on many factors which influence the eruption, transport and sedimentation of tephra. The magma fragmentation process influences the total grainsize distribution of the erupted products (e.g. Kueppers et al. 2006; Cashman and Rust 2016), while sedimentation is affected by particle aggregation (e.g. Mueller et al. 2018; Rossi et al. 2021), plume dynamics (e.g. Scollo et al. 2017) and atmospheric conditions (e.g. Genareau et al. 2019; Poulidis et al. 2021). Our results reflect this complexity as eruptions of similar compositions show a wide range of near-source

GSDs, while there is a large overlap between samples with different compositions and from eruptions of different sizes. The Ascension samples are not fresh (with last known eruptions $\geq$ 500 y ago) and may have been reworked, however, the Ascension GSDs are consistent with the published data for proximal samples from 11 eruptions (Table 2-1).
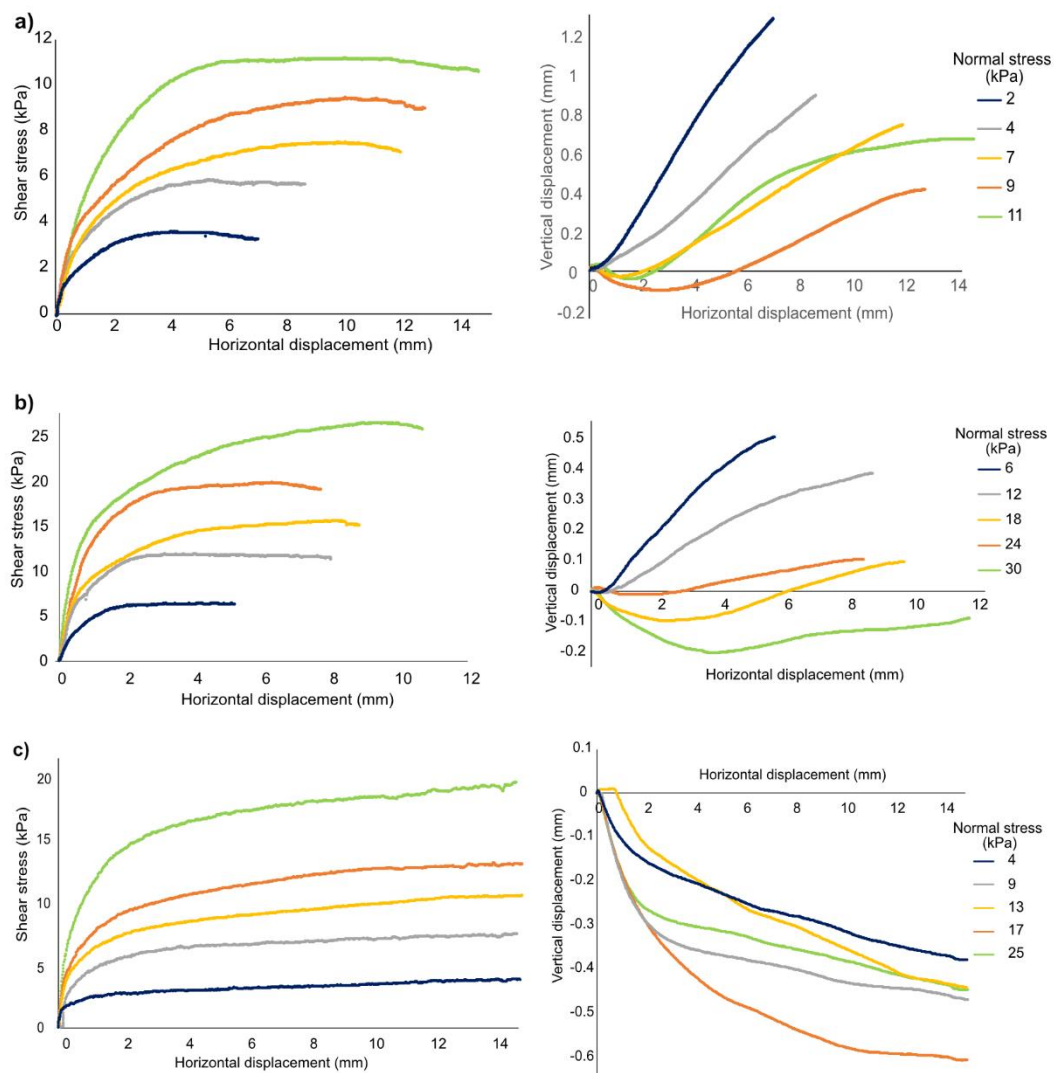


**Fig. 2-7** Results of small shear box tests for particles $\leq$ 2 mm, horizontal displacement vs shear stress (left column) and horizontal vs vertical displacement (right column). a) Synthetic pumice, b) Synthetic scoria, c) Ascension ash. The tests are limited by the maximum amount of travel available for the sample in the shear box. The rate of change of shear stress vs time has been examined and this shows the rate of change peaking early in the test and then subsiding to alternate between small positive and negative values oscillating around 0. Therefore, we are confident that the peak shear stress value measured is representative
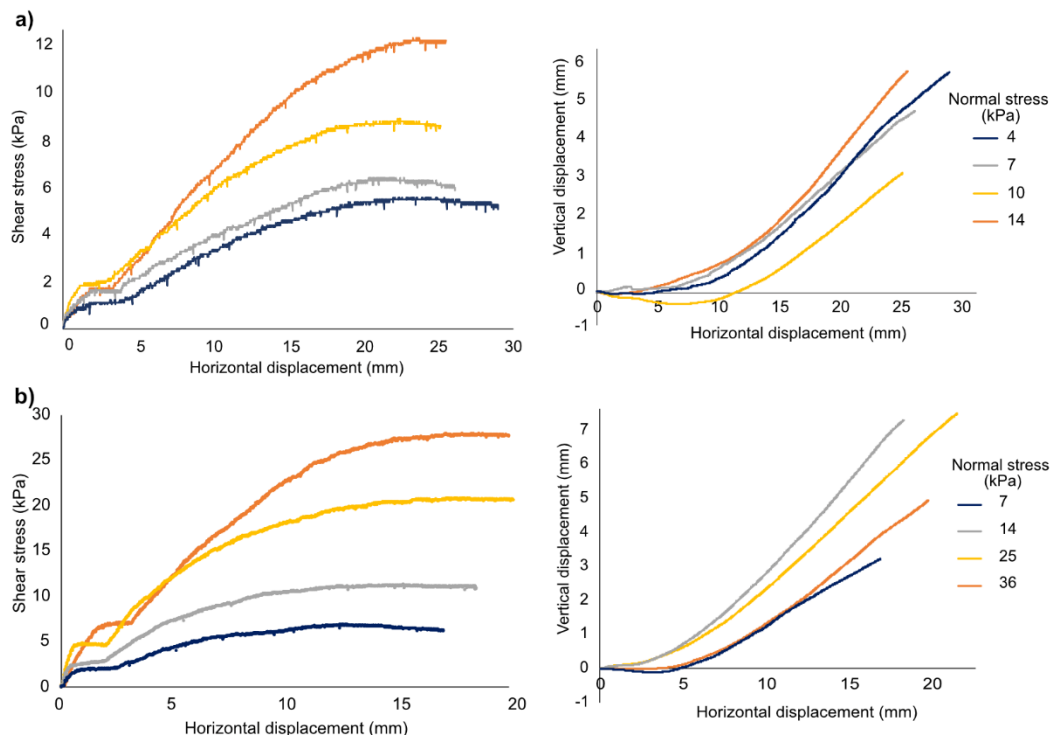
**Fig. 2-8** Results of large shear box tests for particles ≤ 16 mm, horizontal displacement vs shear stress (left column) and horizontal vs vertical displacement (right column). a) Synthetic pumice, b) Synthetic scoria
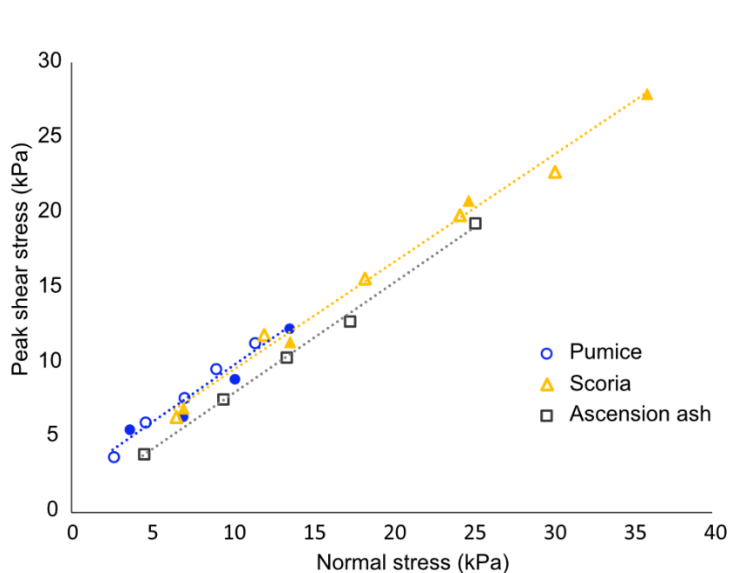


**Fig. 2-9** Peak shear stress vs normal stress for synthetic pumice and scoria and Ascension Island ash. Open markers indicate small shear box tests for particle diameters ≤ 2 mm, filled markers indicate large shear box tests for particle diameters ≤ 16 mm

## Deposit densities

Bulk density is influenced by both the density of individual grains, degree of saturation and the deposit packing. The latter depends on grain size distribution as this affects the extent to which voids between coarser grains can be filled by finer particles. A small number of eruptions have published data on both proximal/medial and distal bulk densities, with some having higher distal values (e.g. Thorarinsson and Sigvaldason 1972; Walker 1980; Todde et al. 2017), likely due to distal deposits having a higher crystal content or higher pumice density, as smaller particles have a relatively lower proportion of vesicles. However, this pattern is not followed for all eruptions (e.g. Thorarinsson 1954; Rose et al. 2008), particularly where the range of proximal densities is wide. Uncertainties with these data include the impact of changes over time, both short-term (compaction) and long-term (weathering), as well as the different methods used to measure deposit density. As noted in the introduction, tests in this study were only performed on dry samples, and the degree of saturation may add further uncertainly. The wide range of reported bulk densities and the lack of a clear trend relating to magma composition, eruption size or distance from source suggest these factors alone cannot reliably be used to estimate tephra loading.

## Properties of synthetic samples

The GSDs and internal angles of friction of our synthetic samples matched well with the natural samples from Ascension for the grain sizes we considered ($\geq -4$ $\phi_g$, $\leq 16$ mm) and the densities of the synthetic samples (412–1532 kg m$^{-3}$) lie within the range of published deposit densities. These important findings provide confidence that we can use synthetic samples to test the geomechanical behaviour of tephra deposits and so avoid the difficulties and costs associated with collecting and transporting natural samples.

## Internal angle of friction

In plots of peak shear stress vs normal stress, results for coarse and fine GSDs plotted on the same line for both synthetic pumice and scoria (Fig. 2-9). This suggests that the friction angle is independent of grain size at the low normal stresses likely to be experienced in roof loads, where field surveys indicate that collapse can occur at ~ 1–10 kPa (Jenkins et al. 2014). This contrasts with results at higher normal stresses (> 100 kPa) where the internal angle of friction has been shown to vary with grain size (e.g. Hamidi et al. 2009; Mostefa

Kara et al. 2013; Alias et al. 2014). At higher normal stresses the largest grains may provide a greater barrier to movement than found in our study.

Values of the internal angle of friction were very similar for pumice and scoria (36.5° and 35.8° respectively) suggesting that the friction angle is also independent of magma composition and deposit density. This implies that any internal sliding of the deposit will be consistent across a range of different compositions and grain sizes, at least for the compositions and GSDs tested here. This in turn is important, as tests at one GSD could provide information about the friction angle of other GSDs. However, these results should be confirmed by laboratory sliding tests.

The peak shear stresses for the volcanic ash from Ascension Island were lower than values for the synthetic samples at similar normal stresses. The ash also compacted throughout the tests, whereas the synthetic samples mainly showed dilatory behaviour after initial compaction. This is thought to be due to the natural sample having a higher proportion of very fine grains, which more easily reorganised and compacted into void spaces between the larger grains when stresses were applied. However, despite these differences in behaviour, the angle of friction of the Ascension ash (36.4°) was similar to the synthetic samples (36.5° and 35.8°) and consistent with values for a range of volcanic rocks at similar normal stresses (Heap and Violay 2021). This indicates that this friction angle is applicable across different tephra compositions and grain sizes, including the synthetic deposits.

The angle of repose and the internal angle of friction ($\varphi_f$) may not be the same, as the failure plane is constrained when $\varphi_f$ is determined using shear box tests. However, they are both related to the frictional properties of the grains. Tests on a range of granular materials (with maximum grain size ~ 6 mm) found that the angle of repose after consolidation closely matched the internal friction angle and was independent of grain size distribution (Metcalf 1966). This suggests that our results are relevant when considering the minimum roof pitch at which tephra will slide.

## Relevance to tephra loading on roofs

The load transferred to a roof depends on the depth and density of a tephra fall deposit. Our results show that bulk density varies widely, even within a single eruption, and cannot be reliably estimated from magma composition or eruption size. Hence when assessing building vulnerability or designing new buildings to withstand tephra fall it is important to understand the range of loads likely to be experienced. This study has considered mafic and

silicic deposits, with low to high bulk densities and coarse and fine GSDs and so our results are likely to be relevant when considering roof loading from future eruptions. However, our dataset should be supplemented where possible with relevant data from historic eruptions.

## Limitations

This work only considered dry tephra and the addition of water would change the properties of the deposit considerably. Deposit densities have been reported to increase by 45–100% following rain (Blong 1981; Macedonio and Costa 2012; Hayes et al. 2019; Williams et al. 2021) and further work is needed to consider how water affects bulk densities and friction angles. As our shear box tests were limited to grains $\geq -4\ \phi_g$ ($\leq 16$ mm), we did not consider how larger particles may affect the internal angle of friction within a deposit. Aspects other than simple gravitational sliding (e.g. drifting) may also change the distribution of material on a roof and these also need further investigation. In order to understand more about tephra sliding behaviour and how this impacts the load transferred to a roof, the effect of roof properties, for example, material and pitch, must also be considered. This should be the focus of future work that will allow development of standards to account for tephra loads in building design and risk analysis.

## Conclusions

We combined published data and experimental results to investigate key geomechanical properties of tephra: bulk density, grain size distribution and internal angle of friction. These properties influence roof loading and are therefore important when assessing the vulnerability of buildings to collapse.

Published tephra deposit densities and near-source grain size distributions (≤ 10 km) vary widely but there are no clear trends when considering eruptions of different compositions and sizes that can be used when assessing vulnerability.

Our laboratory experiments revealed that, at the low normal stresses likely to be experienced in roof loads (≤ 35 kPa), values of the internal angle of friction were very similar across all our tests (35.8°– 36.5°). As the friction angle influences deposit sliding behaviour, this suggests that any internal sliding of the deposit will be consistent across a range of different magma compositions, deposit densities and grain sizes.

We have shown that synthetic tephra samples, made from crushing and grading volcanic aggregates, can be used to represent natural tephra deposits in tests of geomechanical properties relevant to roof loading, regardless of eruption type or composition. This is of particular importance given the difficulty of sourcing the required volumes of natural tephra.

We considered deposits with a wide range of magma compositions, densities and grain size distributions and so we have provided an envelope of values for parameters relevant to roof loading (Tables 2-2 and 2-3), in which future eruptions are likely to sit.

## List of abbreviations

$\phi_g$: Grain size (Phi scale);

$\tau$: Shear stress at failure along a plane;

$\sigma$: Normal stress;

$\varphi_f$: Internal angle of friction;

$c$: Cohesion.

## Acknowledgements

Many thanks to Dr. Richard Brown of Durham University for collecting samples of pumice, scoria and ash on Ascension Island and to Kirk Handley at University of Leeds for assistance with the shear box tests.

## Declarations

### Authors' contributions

The project was devised by MT and JC and supervised by MT, JC and SC. SO undertook the data collection, laboratory work and analysis. SO wrote the manuscript with inputs from MT, JC and SC. All authors read and approved the final manuscript.

### Funding

**Availability of data and materials**

References to published sources are listed in Table 2-1 and the Appendix. Shear box test data are available on request.

**Competing interests**

The authors declare that they have no competing interests.

# References

Alfano F, Bonadonna C, Volentik ACM, Connor CB, Watt SFL, Pyle DM, Connor LJ (2011) Tephra stratigraphy and eruptive volume of the May, 2008, Chaiten eruption, Chile. Bull Volcanol 73:613‑630. https://doi.org/10.1007/s00445-010-0428-x

Alias R, Kasa A, Taha MR (2014) Particle size effect on shear strength of granular materials in direct shear test. World Acad Sci Eng Technol Open Sci Index 95, Int J Civ Environ Eng 8:1144‑1147

American Society of Civil Engineers and Structural Engineering Institute 2017. ASCE/SEI 7-16: minimum design loads and associated criteria for buildings and other structures

Andrews BJ (2014) Magmatic storage conditions, decompression rate, and incipient caldera collapse of the 1902 eruption of Santa Maria volcano, Guatemala. J Volcanol Geotherm Res 282:103‑114. https://doi.org/10.1016/J.JVOLGEORES.2014.06.009

Andronico D, Branca S, Calvari S, Burton M, Caltabiano T, Corsaro RA, Del Carlo P, Garf G, Lodato L, Miraglia L, Murè F, Neri M, Pecora E, Pompilio M, Salerno G, Spampinato L (2005) A multi-disciplinary study of the 2002–03 Etna eruption: insights into a complex plumbing system. Bull Volcanol 67:314–330. https://doi.org/10.1007/s00445-004-0372-8

Andronico D, Cioni R (2002) Contrasting styles of Mount Vesuvius activity in the period between the Avellino and Pompeii Plinian eruptions, and some implications for assessment of future hazards. Bull Volcanol 64:372–391. https://doi.org/10.1007/s00445-002-0215-4

Andronico D, Scollo S, Caruso S, Cristaldi A (2008) The 2002–03 Etna explosive activity: tephra dispersal and features of the deposits. J Geophys Res. https://doi.org/10.1029/2007JB005126

# Chapter 2: Geomechanical properties of tephra

Bernard A, Knittel U, Weber B, Weis D, Albrecht A, Hattori K, Klein J (1996) Petrology and geochemistry of the 1991 eruption products of mount Pinatubo. In: Newhall CG, Punongbayan R (eds) Fire and mud: eruptions and lahars of mount Pinatubo, Philippines. University of Washington Press, Seattle

Blong R (2003) Building damage in Rabaul, Papua New Guinea, 1994. Bull Volcanol 65:43–54. https://doi.org/10.1007/s00445-002-0238-x

Blong RJ (1981) Some effects of tephra falls on buildings. In: Self S, Sparks RSJ (eds) Tephra studies. Proc. NATO ASI "tephra studies as a tool in quaternary research", Iceland, 1980. Reidel; NATO advanced study institute studies, series C, vol 75, pp 405–420. https://doi.org/10.1007/978-94-009-8537-7_27

Blong RJ (1984) Volcanic hazards: a source book on the effects of eruptions. Academic Press, Sydney

Bonadonna C, Cioni R, Pistolesi M, Elissondo M, Baumann V (2015) Sedimentation of long-lasting wind-affected volcanic plumes: the example of the 2011 rhyolitic Cordon Caulle eruption, Chile. Bull Volcanol. https://doi.org/10.1007/s00445-015-0900-8

Bonadonna C, Costa A (2013) Plume height, volume, and classification of explosive volcanic eruptions based on the Weibull function. Bull Volcanol. https://doi.org/10.1007/s00445-013-0742-1

Bonadonna C, Genco R, Gouhier M, Pistolesi M, Cioni R, Alfano F, Hoskuldsson A, Ripepe M (2011) Tephra sedimentation during the 2010 Eyjafjallajökull eruption (Iceland) from deposit, radar, and satellite observations. J Geophys Res. https://doi.org/10.1029/2011JB008462

Bonadonna C, Phillips JC, Houghton BF (2005) Modeling tephra sedimentation from a Ruapehu weak plume eruption. J Geophys Res. https://doi.org/10.1029/2004JB003515

Boudon G, Komorowski JC, Villemant B, Semet MP (2008) A new scenario for the last magmatic eruption of La Soufriere of Guadeloupe (Lesser Antilles) in 1530 A.D.: evidence from stratigraphy radiocarbon dating and magmatic evolution of erupted products. J Volcanol Geotherm Res 178:474‑490. https://doi.org/10.1016/J.JVOLGEORES.2008.03.006

British Standards Institution (1990) BS 1377–7:1990. Methods of test for soils for civil engineering purposes. Shear strength tests (total stress). BSI, London

British Standards Institution (2006) BS ISO 13322-2: particle size analysis. Image analysis methods. Dynamic image analysis methods. BSI, London

British Standards Institution (2009) BS EN 1991-1-3: 2003 + A1:2015. Eurocode 1 – actions on structures. Part 1–3: general actions – snow loads. BSI, London

Carey RJ, Houghton BF, Thordarson T (2010) Tephra dispersal and eruption dynamics of wet and dry phases of the 1875 eruption of Askja volcano, Iceland. Bull Volcanol 72:259–278. https://doi.org/10.1007/s00445-009-0317-3

Cashman KV, Rust AC (2016) Volcanic ash: generation and spatial variations. In: Mackie S, Cashman KV, Ricketts H, Rust AC, Watson M (eds) Volcanic ash: Hazard observation. Elsevier, Amsterdam, pp 5‑22. https://doi.org/10.1016/B978-0-08-100405-0.00002-1

Cassidy M, Manga M, Cashman K, Bachmann O (2018) Controls on explosive-effusive volcanic eruption styles. Nat Commun. https://doi.org/10.1038/s41467-018-05293-3

Castruccio A, Clavero J, Segura A, Samaniego P, Roche O, Le Pennec JL, Droguett B (2016) Eruptive parameters and dynamics of the April 2015 sub-Plinian eruptions of Calbuco volcano (southern Chile). Bull Volcanol. https://doi.org/10.1007/s00445-016-1058-8

Cioni R, Longo A, Macedonio G, Santacroce R, Sbrana A, Sulpizio R, Andronico D (2003) Assessing pyroclastic fall hazard through field data and numerical simulations: example from Vesuvius. J Geophys Res Solid Earth. https://doi.org/10.1029/2001j b000642

Crosweller HS, Arora B, Brown SK, Cottrell E, Deligne NI, Guerrero NO, Hobbs L, Kiyosugi K, Loughlin SC, Lowndes J, Nayembil M, Siebert L, Sparks RSJ, Takarada S, Venzke E (2012) Global database on large magnitude explosive volcanic eruptions (LaMEVE). J Appl Volcanol. https://doi.org/10.1186/2191-5040-1-4

Di Roberto A, Bertagnini A, Del Carlo P, Meletlidis S, Pompilio M (2016) The 1909 Chinyero eruption on Tenerife (Canary Islands): insights from historical accounts, and tephro-stratigraphic and geochemical data. Bull Volcanol. https://doi.org/10.1007/s00445-016-1083-7

# Chapter 2: Geomechanical properties of tephra

Estrada N (2016) Effects of grain size distribution on the packing fraction and shear strength of frictionless disk packings. Phys Rev E. https://doi.org/10.1103/PhysRevE.94.062903

Eychenne J, Le Pennec JL, Ramón P, Yepes H (2013) Dynamics of explosive paroxysms at open-vent andesitic systems: high-resolution mass distribution analyses of the 2006 Tungurahua fall deposit (Ecuador). Earth Planet Sci Lett 361:343–355. https://doi.org/10.1016/j.epsl.2012.11.002

Geist D, Harpp K, Oswald P, Wallace P, Bindeman I, Christensen B (2021) Hekla revisited: fractionation of a magma body at historical timescales. J Petrol. https://doi.org/10.1093/petrology/egab001

Genareau K, Wallace KL, Gharghabi P, Gafford J (2019) Lightning effects on the grain size distribution of volcanic ash. Geophys Res Lett 46:3133‑3141. https://doi.org/10.1029/2018GL081298

Gudnason J, Thordarson T, Houghton BF, Larsen G (2017) The opening subplinian phase of the Hekla 1991 eruption: properties of the tephra fall deposit. Bull Volcanol. https://doi.org/10.1007/s00445-017-1118-8

Hamidi A, Yazdanjou V, Salimi N (2009) Shear strength characteristics of sand-gravel mixtures. Int J Geotech Eng 3:29‑38. https://doi.org/10.3328/IJGE.2009.03.01.29-38

Hampton SJ, Cole JW, Wilson G, Wilson TM, Broom S (2015) Volcanic ashfall accumulation and loading on gutters and pitched roofs from laboratory empirical experiments: implications for risk assessment. J Volcanol Geotherm Res 304:237–252. https://doi.org/10.1016/j.jvolgeores.2015.08.012

Hayes JL, Calderón R, Deligne NI, Jenkins SF, Leonard GS, Mcsporran AM, Williams GT, Wilson TM (2019) Timber-framed building damage from tephra fall and lahar: 2015 Calbuco eruption, Chile. J Volcanol Geotherm Res 374:142–159. https://doi.org/10.1016/j.jvolgeores.2019.02.017

Heap MJ, Violay MES (2021) The mechanical behaviour and failure modes of volcanic rocks: a review. Bull Volcanol. https://doi.org/10.1007/s00445-021-01447-2

Hildreth W, Drake RE (1992) Volcan Quizapu, Chilean Andes. Bull Volcanol 54:93–125. https://doi.org/10.1007/BF00278002

International Standards Organization (2013) ISO 4355:2013 - bases for design of structures — determination of snow loads on roofs. ISO, Geneva

Janebo MH, Houghton BF, Thordarson T, Bonadonna C, Carey RJ (2018) Total grain-size distribution of four Subplinian–Plinian tephras from Hekla volcano, Iceland: implications for sedimentation dynamics and eruption source parameters. J Volcanol Geotherm Res 357:25–38. https://doi.org/ 10.1016/j.jvolgeores.2018.04.001

Jenkins SF, Spence RJS, Fonseca JFBD, Solidum RU, Wilson TM (2014) Volcanic risk assessment: quantifying physical vulnerability in the built environment. J Volcanol Geotherm Res 276:105‑120. https://doi.org/10.1016/j.jvolgeores.2014.03.002

Jude-Eton, T.C., 2013. Eruption dynamics within an emergent subglacial setting: a case study of the 2004 eruption at Grimsvötn volcano, Iceland. Ph.D. Thesis. University of Edinburgh

Komorowski J-C, Legendre Y, Caron B, Boudon G (2008) Reconstruction and analysis of sub-plinian tephra dispersal during the 1530 A.D. Soufriere (Guadeloupe) eruption: implications for scenario definition and hazards assessment. J Volcanol Geotherm Res 178:491‑515. https://doi.org/10.1016/j.jvolgeores.2007.11.022

Koyaguchi T, Ohno M (2001a) Reconstruction of eruption column dynamics on the basis of grain size of tephra fall deposits: 1. Methods. J Geophys Res Solid Earth 106:6499‑6512. https://doi.org/10.1029/2000jb900426

Koyaguchi T, Ohno M (2001b) Reconstruction of eruption column dynamics on the basis of grain size of tephra fall deposits: 2. Application to the Pinatubo 1991 eruption. J Geophys Res Solid Earth 106:6513–6533. https://doi.org/10.1029/2000jb900427

Kratzmann DJ, Carey SN, Fero J, Scasso RA, Naranjo J-A (2009) Simulations of tephra dispersal from the 1991 explosive eruptions of Hudson volcano, Chile. J Volcanol Geotherm Res 190:337–352. https://doi.org/10.1016/j. jvolgeores.2009.11.021

Kueppers U, Scheu B, Spieler O, Dingwell DB (2006) Fragmentation efficiency of explosive volcanic eruptions: a study of experimentally generated pyroclasts. J Volcanol Geotherm Res 153:125–135. https://doi.org/10. 1016/j.jvolgeores.2005.08.006

# Chapter 2: Geomechanical properties of tephra

Kutterolf S, Freundt A, Burkert C (2011) Eruptive history and magmatic evolution of the 1.9 kyr Plinian dacitic Chiltepe tephra from Apoyeque volcano in west-central Nicaragua. Bull Volcanol 73:811–831. https://doi.org/10. 1007/s00445-011-0457-0

Kutterolf S, Freundt A, Pérez W, Wehrmann H, Schmincke HU (2007) Late Pleistocene to Holocene temporal succession and magnitudes of highly explosive volcanic eruptions in west-central Nicaragua. J Volcanol Geotherm Res 163:55–82. https://doi.org/10.1016/ j.jvolgeores.2007.02. 006

Landauer J, Kuhn M, Nasato DS, Foerst P, Briesen H (2020) Particle shape matters – using 3D printed particles to investigate fundamental particle and packing properties. Powder Technol 361:711–718. https://doi.org/10. 1016/j.powtec.2019.11.051

Larsson W (1936) Vulkanische Asche vom Ausbruch des chilenischen Vulkans Quizapú (1932) in Argentina gesammelt. Bull Geol Inst Univ Upsala 26:27–52

Macedonio G, Costa A (2012) Brief communication: rain effect on the load of tephra deposits. Nat Hazards Earth Syst Sci 12:1229–1233. https://doi.org/ 10.5194/nhess-12-1229-2012

Metcalf JR (1966) Angle of repose and internal friction. Int J Rock Mech Min Sci 3:155–161. https://doi.org/10.1016/0148-9062(66)90005-2

Mostefa Kara E, Meghachou M, Aboubekr N (2013) Contribution of particles size ranges to sand friction. Eng Technol Appl Sci Res 3:497–501. https:// doi.org/10.48084/etasr.361

Mueller SB, Houghton BF, Swanson DA, Poret M, Fagents SA (2019) Total grain size distribution of an intense Hawaiian fountaining event: case study of the 1959 Kīlauea Iki eruption. Bull Volcanol. https://doi.org/10.1007/s00445-019-1304-y

Mueller SB, Kueppers U, Huber MS, Hess K-U, Poesges G, Ruthensteiner B, Dingwell DB (2018) Aggregation in particle rich environments: a textural study of examples from volcanic eruptions, meteorite impacts, and fluidized bed processing. Bull Volcanol. https://doi.org/10.1007/s00445-018-1207-3

Oddsson, B., 2007. The Grimsvötn eruption in 2004: dispersal and total mass of tephra and comparison with plume transport models. M.Sc. thesis. University of Iceland

Pappalardo L, Mastrolorenzo G (2010) Short residence times for alkaline Vesuvius magmas in a multi-depth supply system: evidence from geochemical and textural studies. Earth Planet Sci Lett 296:133‑143. https://doi.org/10.1016/j.epsl.2010.05.010

Pensa A, Cas R, Giordano G, Porreca M, Wallenstein N (2015) Transition from steady to unsteady Plinian eruption column: the VEI 5, 4.6 ka Fogo A Plinian eruption, São Miguel, Azores. J Volcanol Geotherm Res. https://doi.org/10.1016/j.jvolgeores.2015. 09. 012

Petersen GN, Bjornsson H, Arason P (2012) The impact of the atmosphere on the Eyjafjallajökull 2010 eruption plume. J Geophys Res Atmos. https://doi.org/10.1029/ 2011J D016762

Pichavant M, Poussineau S, Lesne P, Solaro C, Bourdier J-L (2018) Experimental parametrization of magma mixing: application to the AD 1530 eruption of La Soufriere, Guadeloupe (Lesser Antilles). J Petrol 59:257‑282. https://doi.org/10.1093/petrology/ egy030

Poulidis AP, Biass S, Bagheri G, Takemi T, Iguchi M (2021) Atmospheric vertical velocity - a crucial component in understanding proximal deposition of volcanic ash. Earth Planet Sci Lett 566:116980. https://doi.org/10.1016/j.epsl.2021.116980

Poulidis AP, Phillips JC, Renfrew IA, Barclay J, Hogg A, Jenkins SF, Robertson R, Pyle DM (2018) Meteorological controls on local and regional volcanic ash dispersal. Sci Rep. https://doi.org/10.1038/s41598-018-24651-1

Preece K, Barclay J, Brown RJ, Chamberlain KJ, Mark DF (2021) Explosive felsic eruptions on ocean islands: a case study from Ascension Island (South Atlantic). J Volcanol Geotherm Res. https://doi.org/10.1016/j.jvolgeores.2021.107284

Rampey ML, Oppenheimer C, Pyle DM, Yirgu G (2014) Physical volcanology of the Gubisa formation, Kone volcanic complex, Ethiopia. J African Earth Sci 96:212–219. https://doi.org/10.1016/j.jafrearsci.2014.04.009

Romero JE, Morgavi D, Arzilli F, Daga R, Caselli A, Reckziegel F, Viramonte J, Díaz-Alvarado J, Polacci M, Burton M, Perugini D (2016) Eruption dynamics of the 22–23 April 2015 Calbuco volcano (southern Chile): analyses of tephra fall deposits. J Volcanol Geotherm Res 317:15–29. https://doi.org/ 10.1016/j.jvolgeores.2016.02.027

# Chapter 2: Geomechanical properties of tephra

Romero JE, Vera F, Polacci M, Morgavi D, Arzilli F, Alam MA, Bustillos JE, Guevara A, Johnson JB, Palma JL, Burton M, Cuenca E, Keller W (2018) Tephra from the 3 March 2015 sustained column related to explosive lava fountain activity at Volcán Villarrica (Chile). Front Earth Sci. https://doi.org/10.3389/ feart.2018.00098

Rose WI, Bonis S, Stoiber RE, Keller M, Bickford T (1973) Studies of volcanic ash from two recent central American eruptions. Bull Volcanol 37:338–364. https://doi.org/10.1007/ BF02597633

Rose WI, Self S, Murrow PJ, Bonadonna C, Durant AJ, Ernst GGJ (2008) Nature and significance of small volume fall deposits at composite volcanoes: insights from the October 14, 1974 Fuego eruption, Guatemala. Bull Volcanol 70:1043–1067. https://doi.org/10.1007/s00445-007-0187-5

Rossi E, Bagheri G, Beckett F, Bonadonna C (2021) The fate of volcanic ash: premature or delayed sedimentation? Nat Commun 12:1303. https://doi. org/10.1038/s41467-021-21568-8

Rowe MC, Carey RJ, White JDL, Kilgour G, Hughes E, Ellis B, Rosseel JB, Segovia A (2021) Tarawera 1886: an integrated review of volcanological and geochemical characteristics of a complex basaltic eruption. New Zeal J Geol Geophys 64:296–319. https://doi.org/10.1080/00288306.2021.1914118

Sarna-Wojcicki AM, Shipley S, Waitt RB, Dzurisin D, Wood SH (1981) Areal distribution, thickness, mass, volume and grain size of air-fall ash from the six major eruptions of 1980. In: Lipman PW, Mullineaux DR (eds) The 1980 eruptions of mount St. Helens. USGS, Washington DC, pp 577–600

Scasso RA, Corbella H, Tiberi P (1994) Sedimentological analysis of the tephra from the 12-15 August 1991 eruption of Hudson volcano. Bull Volcanol 56:121–132. https://doi.org/10.1007/BF00304107

Scollo S, Bonadonna C, Manzella I (2017) Settling-driven gravitational instabilities associated with volcanic clouds: new insights from experimental investigations. Bull Volcanol 79:39. https://doi.org/10.1007/ s00445-017-1124-x

Self S, King AJ (1996) Petrology and sulfur and chlorine emissions of the 1963 eruption of Gunung Agung, Bali, Indonesia. Bull Volcanol 58:263–285. https://doi.org/10.1007/ s004450050139

Self S, Rampino MR (2012) The 1963-1964 eruption of Agung volcano (Bali, Indonesia). Bull Volcanol 74:1521–1536. https://doi.org/10.1007/ s00445-012-0615-z

Seropian G, Schipper CI, Harmon LJ, Smithies SL, Kennedy BM, Castro JM, Alloway BV, Forte P (2021) A century of ongoing silicic volcanism at Cordón Caulle, Chile: new constraints on the magmatic system involved in the 1921–1922, 1960 and 2011–2012 eruptions. J Volcanol Geotherm Res. https://doi.org/10.1016/J.JVOLGEORES.2021.107406

Sparks RSJ, Wilson L, Sigurdsson H (1981) The pyroclastic deposits of the 1875 eruption of Askja, Iceland. Philos Trans R Soc A Math Phys Eng Sci 299:241–273. https://doi.org/ 10.1098/rsta.1981.0023

Sutton AN, Blake S, Wilson CJN (1995) An outline geochemistry of rhyolite eruptives from Taupo volcanic centre, New Zealand. J Volcanol Geotherm Res 68:153–175. https://doi.org/10.1016/0377-0273(95)00011-I

Suzuki YJJ, Costa A, Koyaguchi T (2016) On the relationship between eruption intensity and volcanic plume height: insights from three-dimensional numerical simulations. J Volcanol Geotherm Res 326:120–126. https://doi. org/10.1016/j.jvolgeores. 2016.04.016

Thorarinsson S (1954) The tephra-fall from Hekla on March 29th 1947. Erupt Hekla 1947-1948(2):1–68

Thorarinsson S (1958) The Oraefajökull eruption of 1362. Acta Naturalia Islandica 2(2):1–99

Thorarinsson S, Sigvaldason GE (1972) The Hekla eruption of 1970. Bull Volcanol 36:269–288. https://doi.org/10.1007/BF02596870

Todde A, Cioni R, Pistolesi M, Geshi N, Bonadonna C (2017) The 1914 Taisho eruption of Sakurajima volcano: stratigraphy and dynamics of the largest explosive event in Japan during the twentieth century. Bull Volcanol. https://doi.org/10.1007/s00445-017-1154-4

Varekamp JC, Luhr JF, Prestegaard KL (1984) The 1982 eruptions of El Chichon volcano (Chiapas, Mexico): character of the eruptions, ash-fall deposits, and gasphase. J Volcanol Geotherm Res 23:39–68. https://doi.org/10.1016/0377-0273(84)90056-8

Venzke E (2013) Global volcanism program: volcanoes of the world, v. 4.8.5. https://doi.org/10.5479/si.GVP.VOTW4-2013 Accessed 20 Jan 2021

# Chapter 2: Geomechanical properties of tephra

Vidal CM, Komorowski JC, Metrich N, Pratomo I, Kartadinata N, Prambada O, Michel A, Carazzo G, Lavigne F, Rodysill J, Fontijn K, Surono (2015) Dynamics of the major plinian eruption of Samalas in 1257 A.D. (Lombok, Indonesia). Bull Volcanol. https://doi.org/

Walker GPL (1980) The Taupo pumice: product of the most powerful known (ultraplinian) eruption? J Volcanol Geotherm Res 8:69–94. https://doi.org/ 10.1016/0377-0273(80)90008-6

Walker GPL, Croasdale R (1970) Two Plinian-type eruptions in the Azores. J Geol Soc Lond 127:17–55. https://doi.org/10.1144/gsjgs.127.1.0017

Walker GPL, Self S, Wilson L (1984) Tarawera 1886, New Zealand - a basaltic plinian fissure eruption. J Volcanol Geotherm Res 21:61–78. https://doi. org/10.1016/0377-0273(84)90016-7

Watt SFL, Pyle DM, Mather TA, Martin RS, Matthews NE (2009) Fallout and distribution of volcanic ash over Argentina following the May 2008 explosive eruption of Chaiten, Chile. J Geophys Res. https://doi.org/10.1029/2008JB006219

Widom E, Schmincke H-U, Gill JB (1992) Processes and timescales in the evolution of a chemically zoned trachyte: Fogo A, São Miguel, Azores. Contrib Mineral Petrol 111:311‑328. https://doi.org/10.1007/BF00311194

Williams GT, Jenkins SF, Lee DWJ, Wee SJ (2021) How rainfall influences tephra fall loading- an experimental approach. Bull Volcanol 83: 42. https://doi.org/10.1007/ s00445-021-01465-0

Williams SN, Self S (1983) The October 1902 plinian eruption of Santa Maria volcano, Guatemala. J Volcanol Geotherm Res 16:33–56. https://doi.org/ 10.1016/0377-0273(83)90083-5

Winstanley, R., 2020. A preliminary investigation into the growth of the sisters scoria cone complex, Ascension Island. M.Sc. thesis. University of Durham

Zawacki EE, Clarke AB, Arrowsmith JR, Bonadonna C, Lynch DJ (2019) Tecolote volcano, pinacate volcanic field (Sonora, Mexico): a case of highly explosive basaltic volcanism and shifting eruptive styles. J Volcanol Geotherm Res 379:23–44. https://doi.org/ 10.1016/j.jvolgeores.2019.04.011

# Chapter 3

# Laboratory tests to understand tephra sliding behaviour on roofs

Sara Osman[1], Mark Thomas[1], Julia Crummy[2], Anna Sharp[1] and Stephen Carver[3]

[1] University of Leeds, School of Earth and Environment, Woodhouse, Leeds LS2 9JT, UK

[2] British Geological Survey, The Lyell Centre, Research Avenue South, Edinburgh EH14 4AP, UK

[3] University of Leeds, School of Geography, Woodhouse, Leeds LS2 9JT, UK

Material published as Supplementary material for this paper is presented in Appendix B1.

Calculations on the volume of corrugations of the metal and fibre cement sheets (referenced in the Methods - Sliding tests section) are given in Appendix B2.

# Chapter 3: Tephra sliding tests

## Abstract

Following explosive eruptions, loading from tephra fall deposits can lead to roof collapse. However, the load may be reduced significantly by tephra sliding on pitched roofs. We present small-scale laboratory tests to investigate tephra sliding behaviour on metal, fibre cement sheet and tile roofing. We tested 10–30 cm thicknesses for dry and wet deposits of pumice, scoria and basaltic ash. We found that tephra did not slide on roof pitches ≤ 15° for coarse-grained deposits and ≤ 12° for dry ash. Thin deposits of wet ash were stable at pitches ≤ 30°. In addition, tephra was mainly shed on pitches ≥ 32° for metal roofs and ≥ 35° for fibre cement and tiles. Using these results, we have produced an initial set of sliding coefficients for tephra for simply pitched roofs that can be used to help prioritise roofs for clearing during an eruption and assist in designing roofs to withstand tephra fall.

## Introduction

Tephra is the most widespread volcanic hazard, impacting large numbers of people and causing disruption across many sectors including infrastructure, agriculture and transport (e.g. Wilson et al. 2014; Jenkins et al. 2015). Buildings and building support systems can be damaged by even small amounts of tephra fall (≤ 10 mm thick) if heating, ventilation and air-conditioning equipment is clogged by ash (Wilson et al. 2014) or leachates lead to corrosion of metal roofs over the longer term (Oze et al. 2014; Miller et al. 2022). Thicknesses of 10–100 mm may cause collapse of structures which are not built to regulated building design standards (non-engineered buildings) or which are in poor condition (Jenkins et al. 2014; Hayes et al. 2019a), as we observed on La Palma, Canary Islands during the 2021 eruption of Cumbre Vieja. Thicker deposits can lead to more widespread failure of roofs when the load exceeds the strength of the roof material or the supporting structure (Jenkins et al. 2014; Hampton et al. 2015).

Clean-up operations can mitigate the likelihood of roof failure (Hayes et al. 2015) and an understanding of loads on individual buildings can enable the most vulnerable structures to be prioritised. On flat roofs, the tephra load is likely to be similar to that of the deposit on the ground (unless the roof is particularly sheltered or windswept) but on pitched roofs some of the tephra can slide off, potentially reducing the load on the roof significantly; therefore, it is important to understand tephra sliding behaviour. Tephra loads also have the potential to increase if conditions are wet, with field and laboratory observations

showing load increases of 30 – 45 % when rain falls after deposition (Hayes et al. 2019a; Williams et al. 2021).

Surveys following eruptions indicate that roofs can collapse at tephra loads of ~ 1–10 kPa, equivalent to tephra thicknesses of ~ 10 cm – 1 m depending on deposit density. Key factors in determining the collapse load are the roof material, quality of construction and condition of the building (Blong 2003; Jenkins et al. 2014; Hayes et al. 2019a; Williams et al. 2020). However, despite almost 60 million people living within 10 km of a volcano that has the potential to erupt (Freire et al. 2019), global building standards do not routinely consider tephra loading. The loads imposed by heavy snowfall are however considered in some standards (e.g. British Standards Institution 2009; International Standards Organization 2013) and the approach they take on snow loading can help when considering how to assess tephra loading during building design. The Eurocodes are a harmonised set of documents that cover the technical aspects of structural and fire design of buildings and the civil engineering of structures. Document BS EN 1991-1-3 from within the Eurocodes deals with snow loads and a characteristic value of the load on the ground is selected using decades of historical data (Sanpaolesi et al. 1998; British Standards Institution 2009). This is then multiplied by a shape coefficient ($\mu$), which takes account of sliding, to produce the load on the roof. Snow sliding behaviour depends mainly on temperature and altitude, and $\mu$ values are defined by empirical equations based on roof load data (Sanpaolesi et al. 1999).

For consideration of tephra loads, this approach needs to be amended as large historical datasets for tephra fall do not exist. It is difficult to collect field data proximal to source, given the obvious hazard during the eruption and the speed at which tephra deposits may subsequently be compacted or modified by wind and rain (e.g. Varekamp et al. 1984; Hayes et al. 2019b; Del Bello et al. 2021). Characteristic tephra ground loads for different eruption scenarios can be estimated using probabilistic tephra dispersion models (e.g. Barker et al. 2019; Vázquez et al. 2019; Wild et al. 2019), while tephra sliding behaviour depends on the density and thickness of the deposit and the roof material (Fig. 3-1, amended from Osman et al. 2022). Bulk (i.e. whole deposit) density varies with tephra type i.e. pumice, scoria or ash (which impacts grain density), the grain size distribution (which impacts deposit packing) and the amount of water in the deposit. To quantify how tephra sliding reduces roof load, we have carried out a series of laboratory tests to identify the roof pitches at which tephra loads are reduced or completely removed by sliding and have investigated

how tephra type, grain size distribution, water content, deposit thickness and roof material influenced the angle of sliding (Fig. 3-1). From our results we have produced an indicative set of sliding coefficients for tephra loading as a first step to help assess the technical impact of tephra loading on simply pitched buildings in volcanic environments.
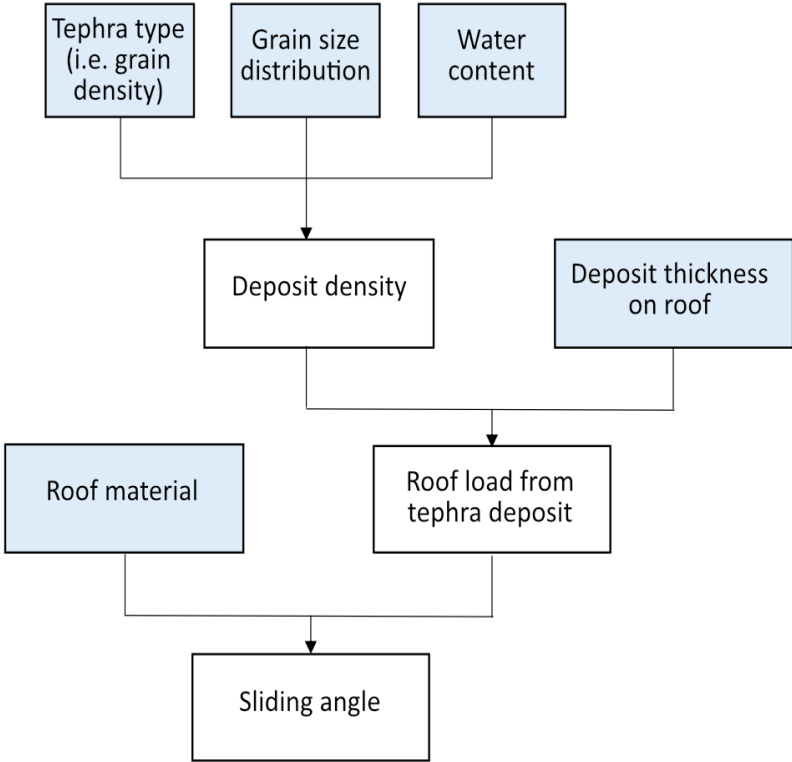


**Fig. 3-1** Key factors affecting sliding angle of tephra on roofs (amended from Osman et al. 2022). Shaded boxes represent the factors investigated in this study

## Methods

We carried out over 400 small-scale tilt table experiments to investigate sliding of pumice, scoria and basaltic ash in dry and wet conditions. We tested three roof materials: metal sheet (galvanized steel, 3" corrugated profile), fibre cement sheet (corrugated Eternit Profile 3 (Eternit 2021)) and clay tiles (Terreal Rustique plain tile (Terreal)). Tephra was loaded into Perspex cells with dimensions 22 x 22 x 10 cm (Fig. 3-2). The cells could move freely over each other, facilitated by the application of PTFE tape ('TEFSIL 3' from Techbelt Ltd, with coefficient of friction ≤ 0.10) between the cells to reduce friction. This ensured that sliding could occur both within the deposit and at the interface between the deposit and the roof material. We used one, two and three cells to observe sliding for tephra thicknesses of 10, 20 and 30 cm, respectively. Sliding tests were conducted with dry tephra

on a dry roof (dry-dry), dry tephra on a wet roof (dry-wet) and wet tephra on a wet roof (wet-wet). Consideration of the impact the cell had on sliding is presented in a later section.



**Fig. 3-2** Tilt table set-up**.** The roof material was placed on the horizontal tilt table, the cell was placed on it and filled with tephra. The inclination of the table was then increased in half degree increments until tephra sliding occurred

## Tephra samples

Large volumes of material were needed for the sliding tests, therefore synthetic tephra was used, created by crushing and grading commercially available volcanic aggregates of mafic and silicic composition. This material has been shown to be well matched to natural samples when considering the properties that are likely to affect sliding behaviour: bulk density, grain size distribution and internal angle of friction (Osman et al. 2022). To investigate the influence of grain size distribution and bulk density on sliding behaviour, we used three tephra samples (detailed in Fig. 3-3 and Table 3-1): low density, coarse-to-fine grain size distribution (GSD) (pumice); high density, coarse-to-fine GSD (scoria) and high density, fine GSD (ash). We wanted to consider sliding from uniformly applied loads and hence minimise any effect from individual large clasts and we therefore selected a maximum grain size of -4 ɸ (16 mm). This maximum grain size is also consistent with samples used to assess the geomechanical properties of tephra (Osman et al, 2022), where the size of the apparatus used to conduct the geomechanical tests limits the maximum size of individual particles relative to the total sample size.
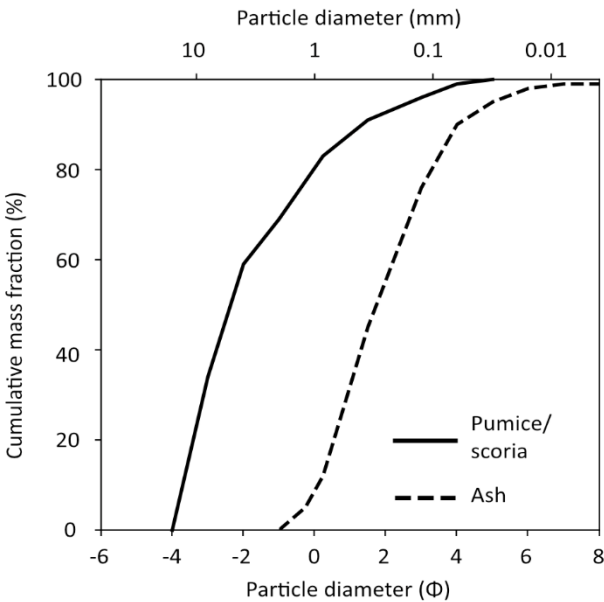
**Fig. 3-3** Grain size distribution for pumice, scoria and ash used in sliding tests

**Table 3-1** Grain size, deposit density and equivalent tephra loads for pumice, scoria and ash test samples

| Tephra type | Wet/ Dry | Median grain size | | Maximum grain size | | Mean deposit density | Equivalent distributed tephra load (kPa) for test deposit thickness | | |
|---|---|---|---|---|---|---|---|---|---|
| | | (φ) | (mm) | (φ) | (mm) | (kg m⁻³) | 10cm | 20cm | 30 cm |
| Pumice | Dry | -2.3 | 5 | -4 | 16 | 433 | 0.42 | 0.85 | 1.27 |
| Pumice | Wet | -2.3 | 5 | -4 | 16 | 556 | 0.55 | 1.09 | 1.64 |
| Scoria | Dry | -2.3 | 5 | -4 | 16 | 1235 | 1.21 | 2.42 | 3.63 |
| Scoria | Wet | -2.3 | 5 | -4 | 16 | 1152 | 1.13 | 2.26 | 3.39 |
| Ash | Dry | 1.7 | 0.3 | -1 | 2 | 1443 | 1.41 | 2.83 | 4.24 |
| Ash | Wet | 1.7 | 0.3 | -1 | 2 | 1574 | 1.54 | 3.09 | 4.63 |

We tested both wet and dry tephra. For the wet samples we aimed to simulate tephra that was naturally saturated by rainfall, adding the maximum amount of water to the sample and stopping as soon as any runoff from the sample occurred. The dry tephra sample was weighed and placed on a board inclined at 5°, to allow excess water to drain. Water was added gradually so that the finest grains were not washed out, and the sample was then

mixed thoroughly to ensure it was uniformly wet. When water was observed draining from the sample it was left to fully drain off any excess water and then reweighed. The water content was calculated by:

$$\text{Water content (weight \%)} = \frac{(\text{wet weight of tephra} - \text{dry weight of tephra}) * 100}{\text{dry weight of tephra}}$$

The recorded water contents for pumice, scoria and ash were 40 wt%, 15 wt% and 22 wt% respectively, which were then used in all "wet" sliding tests for these materials.

The mean bulk densities of the dry samples ranged from 433 to 1443 kg m$^{-3}$ (Table 3-1). These values are within published deposit density values of ~ 400 – 1500 kg m$^{-3}$, covering a wide range of eruption sizes and compositions (Osman et al. 2022). However, when loaded into the test cell, wet sample bulk deposit density did not increase as much as expected based on theoretical literature values (Macedonio and Costa 2012). In the dry deposits, any finer particles were free to move relative to the larger grains, filling void spaces. When wet, the fine particles aggregated around and adhered to larger grains, leading to less efficient deposit packing and more void space. This resulted in the bulk density of wet pumice increasing by 28 %, while the bulk density of wet scoria actually decreased by 7 % compared to the dry samples. For ash, the dry deposit flowed like a powder but when wet, it did not flow at all and density changes between – 6 % and + 10 %, with respect to the dry density, were possible. To better constrain the wet ash bulk density, we used a value consistent with field samples of basaltic ash and lapilli collected during the La Palma 2021 eruption. For these samples, collected within a few days of deposition and following rain, the natural deposit density was measured as ~ 10 % higher than the sample's dry density (after oven drying). We therefore aimed to replicate this for all our wet ash tests (Table 3-1).

For the coarser deposits, we investigated whether pouring tephra into the load cell from a greater height (forcing greater compaction) would increase the bulk density and whether this would impact the sliding angle. We poured tephra into the load cell directly and from a height of ~ 1.5 m when particles ≤ 1 mm diameter would reach terminal velocity (Bagheri and Bonadonna 2016). Deposit density increased for the samples poured from height (from ~ 500 to 600 kg m$^{-3}$ for pumice and from ~ 1000 to 1200 kg m$^{-3}$ for scoria) but the sliding angle did not change. We therefore ensured deposit density was within these ranges for all our sliding tests with wet pumice and scoria (Table 3-1).

# Chapter 3: Tephra sliding tests

## Initial sliding tests

We conducted a series of tests to ensure that sliding was controlled by the tephra and not the Perspex cell, including consideration of the weight of the cell and its placement over the ridges (rather than the troughs) of the corrugated sheets.

## Control of sliding

We conducted sliding tests with an empty cell to identify the minimum angle at which sliding would be controlled by the tephra. The edges of the empty cell were coated in PTFE tape ('TEFSIL 3' from Techbelt Ltd, with coefficient of friction ≤ 0.10) to reduce friction (Fig. 3-4a). The cell was placed on each roof material and the roof angle increased until sliding occurred (Fig. 3-4b). Sliding angles are shown in Table 3-2. For the tiles, the sliding angle was > 30° which is similar to the expected internal angle of friction for tephra deposits (Osman et al. 2022), and so the PTFE tape was also the applied to the tile directly beneath the cell.
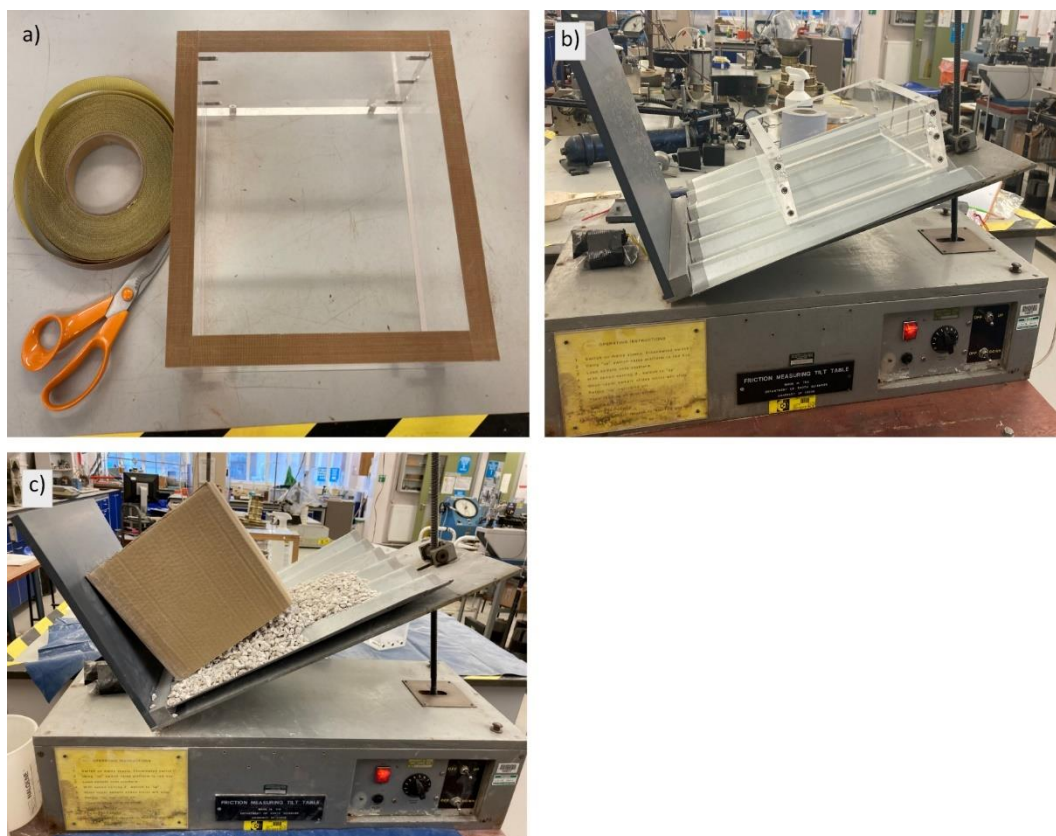


**Fig. 3-4** Initial test set-up, a) Perspex cell with edges coated in PTFE tape, b) testing the sliding angle for one empty Perspex cell on metal sheet, c) testing the sliding angle using a cardboard cell

**Effect of corrugations**

For the corrugated metal and fibre cement sheets, tests with 10 cm thickness of pumice were carried out with the cell edges over the troughs and the ridges of the roofing sheet to check whether the direct contact of the ridges along the entire down-slope length of the cell impacted the sliding angle. When the cell edges were over the ridges, little tephra leakage occurred. When the edges were over the troughs, the weight of tephra held the deposit in place with tephra only leaking as we started to fill the cell and when it slid along the roof material. No measurable difference was found in the sliding angle (Table 3-2) between these two tests and so for all the remaining tests the cell was placed over the ridges, as this minimised tephra loss when sliding occurred.

**Table 3-2** Sliding angles for the empty Perspex cell on all roof materials used in the sliding tests and for the Perspex cell with 10 cm thickness of pumice on the corrugated sheets. For corrugated sheets, angles were measured with the cell placed over the ridges and over the troughs. In each case, 3 tests were performed

| Roofing material | Cell over ridge or trough | Mean empty cell sliding angle (°) | Mean sliding angle (°) with 10 cm thickness of pumice |
|---|---|---|---|
| Fibre cement | Ridge | 24 | 32 |
| Fibre cement | Trough | 21 | 32 |
| Metal sheet | Ridge | 19 | 26 |
| Metal sheet | Trough | 13 | 27 |
| Tile (no PTFE tape) | N/A | 32 | |
| Tile (with PTFE tape) | N/A | 24 | |

**Effect of cell weight**

To investigate whether the presence of the Perspex cell or the area of the cell in contact with the roofing material affected the sliding angle, we carried out tests using a cardboard cell weighing < 50 g, with the cell walls being ~ 0.3 cm thick (Fig. 3-4c). We tested 10 and 20 cm of pumice on all roof materials using the cardboard cell. The only notable observed difference between the Perspex cell (of weight 2.35 kg for each 10 cm depth) and the cardboard cell was that on tiles with 20cm thickness of pumice, the tephra "leaked" from

beneath the sides of the cell before sliding occurred. No measurable difference was seen between the sliding angles for tests using the cardboard and Perspex cells (Fig. 3-5).

Despite the significant difference in material, weight and cell wall size, changing from one cell type to the other had no effect on the recorded sliding angles and as a result of these tests, we are confident that it is the tephra that is controlling the sliding rather than any of the test equipment. The tests and results discussed in this manuscript therefore assume that all sliding behaviour is controlled by the tephra.
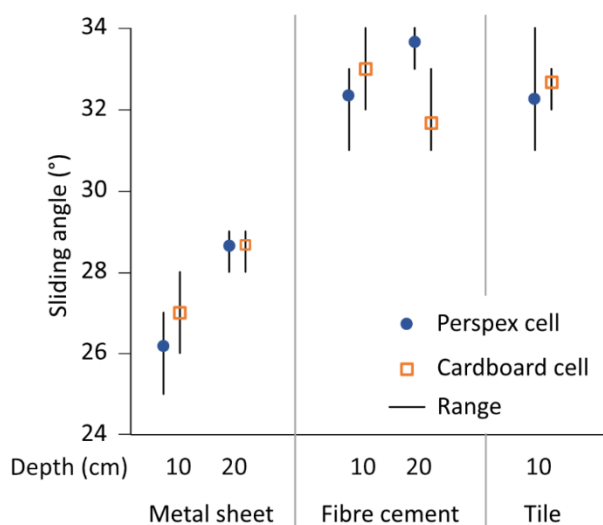
**Fig. 3-5** Comparison of sliding angles for cardboard and Perspex cells with 10 and 20 cm thickness of pumice on metal sheet, fibre cement and tiles

## Angle of repose and initial movement of tephra grains

The repose angle of the deposit and initial movement of the grains (rolling and sliding on the surface of the deposit) were investigated with the tilt table set horizontally, by gently pouring tephra to approximately half fill one side of the cell. The repose angle was measured, and the table was then raised in half degree increments until the grains on the surface of the deposit started to move. In some tests, individual grains rolled at low tilt angles, but the initial movement angle was measured when grains moved across a substantial part of the deposit surface. By investigating when the deposit starts to move with only one half of the cell filled, we are able to account for the fact that the deposit is

completely contained in the cell during the sliding tests and mitigate any possibility that the initial recorded onset of sliding would be inhibited by the cell.

## Sliding tests

With the tilt table set horizontally, the roof material and then the load cell were added (Fig. 3-2). The tephra sample was weighed, and tephra was carefully poured into the cell and distributed to ensure that the deposit was evenly dispersed into the corners of the cell. After the cell was filled, the remaining tephra was weighed and the mass of test tephra in the cell was calculated. This mass was kept constant throughout the series of tests. The volume of tephra was calculated from measurements of the dimensions of the cell (plus an estimate of the volume of the corrugations for the metal and fibre cement sheets) and from this the bulk density of the test deposit was calculated (Table 3-1). Tephra loads for the tests ranged from 0.42 kPa for 10 cm of dry pumice to 4.63 kPa for 30 cm of wet ash (Table 3-1).

To ensure the motion of the tilt table did not initiate sliding, slope angle was increased slowly in half degree increments until sliding occurred, when the angle of tilt was measured with a clinometer. Tests were replicated five times, apart from 10 cm of pumice on the corrugated roof sheets, where 6 tests were carried out (3 with the cell over the ridges and 3 over the troughs).

For the dry-wet and wet-wet tests, the tilt table was set to 5°, the empty load cell was added, and the roof was thoroughly wetted ensuring the whole area within the cell was wet. Any excess water was allowed to run off and tephra was then immediately poured onto the roofing before the surface dried.

The effect of roof condition was also investigated by testing 20 cm of both pumice and scoria on a very weathered (moss-covered) fibre cement sheet and a weathered metal sheet. Both sheets, supplied by Garage Revamps (http://www.revamps.co.uk), had been on garage roofs in the UK for > 10 years. The weathered fibre cement tests were only able to be carried out twice, as the surface in contact with the tephra was substantially changed after each test due to the sliding deposit scouring the moss and material that had built up on the surface of the roof.

## Results

### Angle of repose and initial movement of the grains

The mean angle of repose was the same for all dry deposits (35°), with a range of 33–36° for pumice and 34–37° for scoria and ash (Fig. 3-6). For the wet deposit, the mean repose angle increased to 48° for pumice, 43° for scoria and 42° for ash.

In dry samples, grains initially started rolling and sliding over each other at tilt angles of 10–14° for ash (mean: 12°) and 13–16° for the coarser-grained samples (mean: 14° for pumice and 15° for scoria). No change was seen when scoria was wetted, but wet pumice grains required a higher tilt before movement started (mean value 18°), as shown in Fig. 3-6. Wet ash behaved very differently to the dry sample, with apparent cohesion between the grains resulting in more stable deposits. The 10 cm deposit failed by sliding at the base at a tilt angle of 28° on metal sheet, and slumping at a tilt of 30° on fibre cement and tile. At 20 cm thickness, slumping occurred at tilts of 21°.
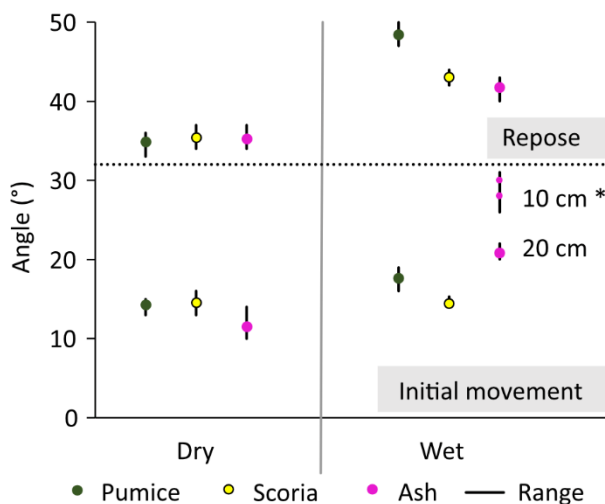


**Fig. 3-6** Repose angle and angle at which tephra grains started to move on the surface of the deposit for dry and wet pumice, scoria and ash. * Initial movement of wet ash varied with deposit thickness. 10 cm: sliding at the base (between tephra and roof) at 28° on metal sheet and slumping of deposit at 30° on fibre cement and tile; 20 cm: slumping at 21°

### Sliding tests

Mean sliding angles varied between 26° and 33° for pumice, 24° and 36° for scoria and 23° and 36° for ash (range for total dataset: 22–37°) (Fig. 3-7). Deposits slid at shallower angles
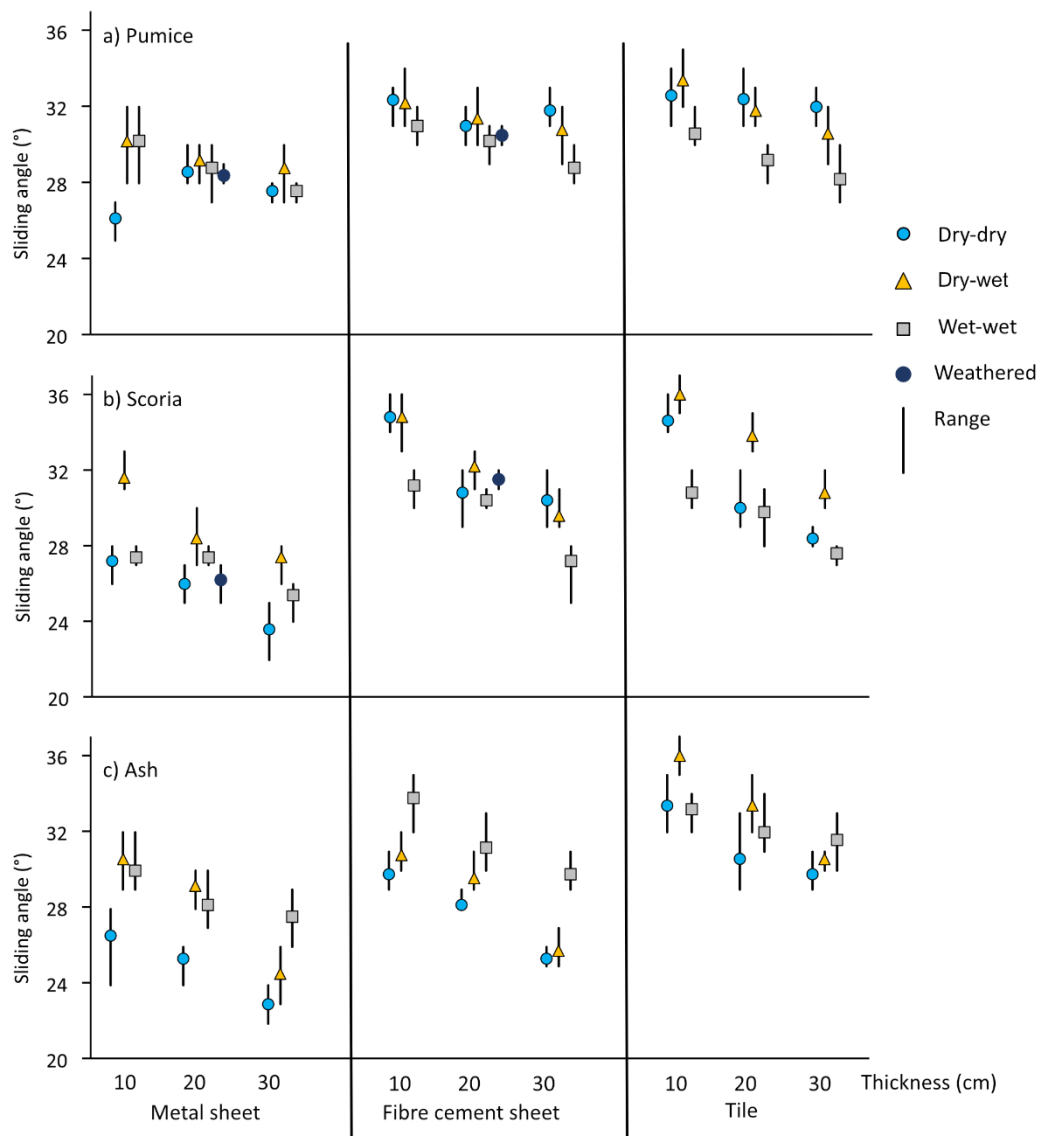
**Fig. 3-7** Mean sliding angles and range of values for tilt tests with 10–30 cm of pumice, scoria and ash on metal sheet, fibre cement and tile roofing. Dry deposits were tested on dry and wet roofs; wet deposits were tested on wet roofs. Dry deposits of 10 and 20 cm of pumice and scoria were also tested on dry weathered metal and fibre cement. In the key the hyphenated symbol descriptions refer to the state (dry or wet) of the deposit-roof. All results are available in Supplementary material

# Chapter 3: Tephra sliding tests

on metal sheet compared to fibre cement and tiles (Fig. 3-8), and at shallower angles on each roof material when the deposit was thicker (Fig. 3-8a). There were no clear trends when considering grain size (Fig. 3-8b) but on fibre cement and tile, the steepest sliding angles for pumice were lower than for scoria and ash (Fig. 3-8c).
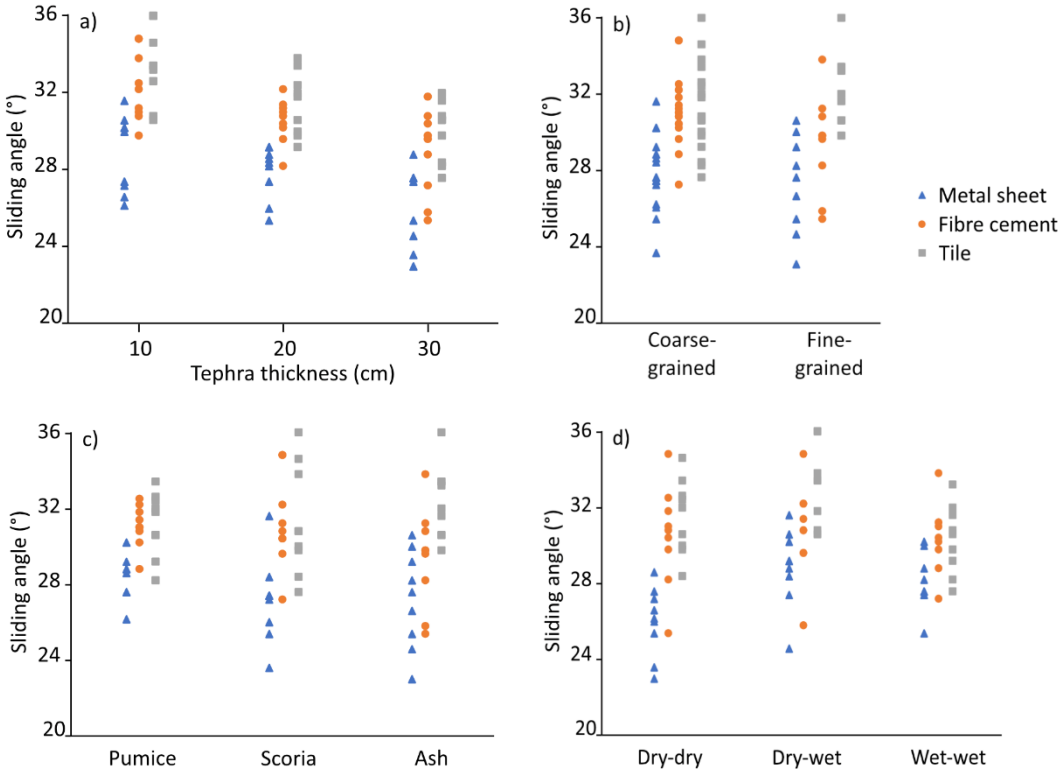


**Fig. 3-8** Impact of key factors (shown in Fig. 3-1) on mean sliding angles for tilt tests, a) deposit thickness: 10, 20, 30 cm, b) grain size: coarse-grained, fine-grained (defined in Fig. 3-3), c) tephra type: pumice, scoria, ash, d) presence of water: dry tephra on dry roof, dry tephra on wet roof, wet tephra on wet roof. Plots show results on three roof materials: metal sheet, fibre cement sheet and tiles

When considering the impact of water, for the low friction metal sheet the dry-dry tests resulted in the shallowest sliding angle for all tephra types and the dry-wet test typically gave the steepest sliding angle (Figs. 3-7 and 3-8d). When the roof was wet, the tephra in contact with the metal sheet formed a distinct layer that appeared to hold the deposit at steeper roof angles. On fibre cement and tiles, results varied with tephra type (Fig. 3-7). For

68

fibre cement, the steepest sliding angles were for the dry-dry and dry-wet tests for the coarse-grained deposits and the wet-wet tests for ash. On tiles, the dry-dry and dry-wet tests gave the steepest sliding angles for pumice, the dry-wet tests for scoria and the dry-wet and wet-wet tests for ash. Sliding angles on weathered metal and fibre cement sheet fell within the range found for new roofing sheets for both pumice and scoria deposits (Fig. 3-7).

For the dry, coarser-grained tephra, sliding always occurred at the base of the deposit, that is at the interface of the deposit and the roofing material, except for one test with 30 cm of pumice on fibre cement, where sliding occurred within the deposit. For dry ash, sliding always occurred at the base on the metal sheet and fibre cement. On tiles, approximately half of the dry-dry and dry-wet tests failed within the tephra at 20 cm thickness, and all failed within the tephra for the 30 cm thick deposit (Table 3-3). For wet tephra, 20 cm thick deposits always slid at the base, but at 30 cm thickness, sliding was observed both at the base and within the tephra (Table 3-3). Thicker deposits failed more often by overcoming the internal friction between the grains rather than the friction between the tephra and the roofing material. For ash this mechanism was more likely when the deposit was dry, while for the coarser-grained samples it mainly occurred in wet deposits.

**Table 3-3** Number of sliding tests (of 5 in total in each case) where failure occurred through sliding within the tephra rather than at the base of the deposit. For all other tests, sliding occurred between the tephra and the roofing material

| Test | Tephra thickness | |
|---|---|---|
| | 20 cm | 30 cm |
| Dry-dry | Ash: 2 on tile | Pumice: 1 on fibre cement |
| | | Ash: 5 on tile |
| Dry-wet | Ash: 3 on tile | Ash: 5 on tile |
| Wet-wet | | Pumice: 3 on fibre cement; 4 on tile |
| | | Scoria: 1 on fibre cement; 5 on tile |
| | | Ash: 2 on fibre cement; 1 on tile |

## Discussion

When assessing whether roofs are likely to collapse under tephra loading, we need to consider how much, if any, of a tephra deposit will slide off and so reduce the load. Our experiments considered low- and high-density tephra, coarse and fine grain size distributions, both dry and wet, at thicknesses up to 30 cm on metal, fibre cement and tile roofing. These results can therefore provide initial bounds on when sliding is likely to occur for a range of deposits and roof materials for simply pitched roofs.

### Angle of repose and initial movement of grains

Our mean repose angle of 35° for dry tephra is consistent with the internal angle of friction of 35.8–36.5° observed in shear box tests for dry samples with the same grain size distributions (Osman et al, 2022). Published experimental results of 35° for ash and 40–45° for coarse tephra (Hornby et al. 2020; Williams et al. 2021) seem to suggest that the finer grains in our sample are controlling the repose angle. Mean repose angles of 42–48° for wet deposits are consistent with findings for other granular materials that water increases the repose angle (e.g. Hornbaker et al. 1997; Beakawi Al-Hashemi and Baghabra Al-Amoudi 2018).

The angle at which grains initially move gives an indication of the shallowest roof pitch where sliding might occur. Our values of ~ 15° for the coarser-grained deposits and ~ 12° for dry ash are consistent with experiments simulating ash deposition on metal roofing, which found 26 % of the ash was shed from a 15° roof (Hampton et al. 2015). The behaviour of wet ash, where a 10 cm deposit could be stable to ~ 30° and a 20 cm deposit slumped at ~ 21°, requires further investigation on larger scale roofs and at greater tephra thickness than possible with our equipment. However, overall, our results suggest that low pitched roofs can be considered as flat when assessing how sliding may reduce tephra loading, consistent with our observations in La Palma, Canary Islands, following the 2021 Cumbre Vieja eruption (Fig. 3-9).

**Fig. 3-9** Low pitched roofs in a) Las Manchas and b) Tacande, La Palma following the Cumbre Vieja 2021 eruption, showing no evidence of the deposit sliding except at the deposit edges where the angle of repose has been formed

## Sliding

The angle at which the entire test deposit slid gives an indication of the shallowest roof pitch on which most of the deposit will be shed. For steeper angles than those recorded we expect the load to be entirely removed as we have assumed that the tephra is not inhibited from sliding off the roof by the presence of guttering or snow guards. Roof collapse occurs when the tephra load exceeds the roof failure load. Even without sliding, our maximum tested pumice test loads of < 2 kPa (Fig. 3-10a) are unlikely to lead to collapse unless roofs are of poor quality or badly maintained (Jenkins et al. 2014). However, test loads of 1–4 kPa and 1–5 kPa for scoria and ash respectively could lead to collapse in good quality buildings, hence sliding is an important factor to consider. As expected, our results show that sliding occurs at a shallower angle on the lower friction metal sheet compared to the rougher surfaces of fibre cement and tiles (Fig. 3-10b). When considering the other factors we investigated (shown in Fig. 3-1), namely deposit thickness, tephra type, grain size distribution and presence of water, there is a clear trend on each roof type for the sliding angle to be lower for higher loads (i.e. thicker deposits) (Fig. 3-10), but no clear trends related to the other factors (Fig. 3-10a, c). This suggests the increased weight of tephra is key in overcoming the frictional forces that resist sliding when compared to other factors.
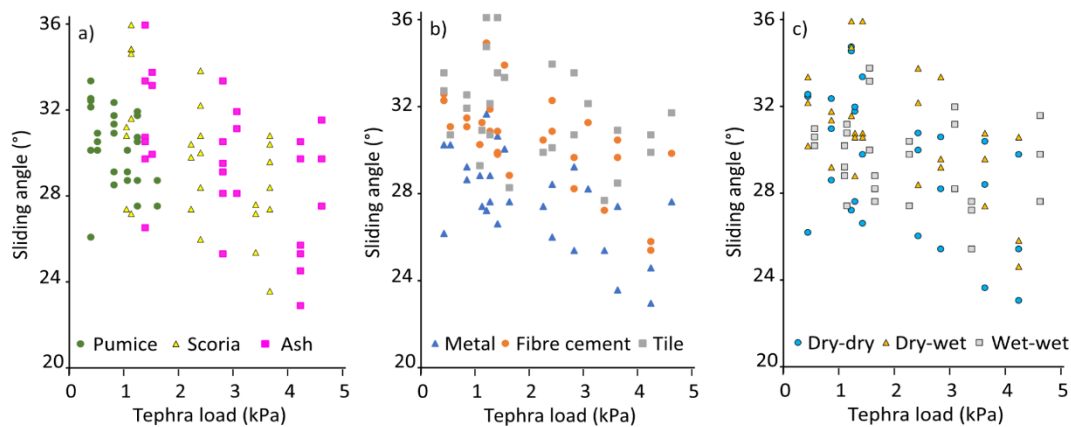
**Fig. 3-10** Summary plot showing variation of mean sliding angle with tephra load for all tests, highlighted by a) tephra type, b) roof material and c) presence of water

We found that metal roofs require a pitch ≥ 32° to ensure the deposit is substantially shed, consistent with larger scale tests using dry basaltic ash, where ~ 45 % of the deposit remained on a 30° metal sheet roof, reducing to < 10 % at 35° (Hampton et al. 2015). For fibre cement and tiles, a pitch of ≥ 35° is needed to significantly shed tephra, which is consistent with our observations of tile roofs in La Palma, where sliding had occurred on a pitch ~ 35° but tephra built up on a ~ 20° section (Fig. 3-11).

The impact of rainfall on deposit behaviour likely depends on whether it occurs before, during or after tephra deposition. Our "wet" tests aimed to simulate tephra falling during rain as the tephra was wet before deposition into the test cells. Our measured wet density increases of 28 % for pumice and 9 % for ash are consistent with observations following the eruption of Pinatubo in 1991 (Spence et al. 2005) and our findings on La Palma in 2021, respectively. However, for wet scoria, as our bulk density was 7 % lower than for the dry deposit, higher saturated loads may be possible if deposition from the plume leads to more efficient grain packing than achieved in our tests. For rain falling after deposition, grain size distribution and rainfall intensity affect the depth to which water can penetrate and hence its impact on sliding (Tarasenko et al. 2019; Williams et al. 2021). Our maximum sliding angle for wet tephra (36° for both scoria and ash) is substantially lower than previous results where wet ash remained stable at 45° pitch (Hampton et al. 2015). These higher values, taken with our observations that wet ash deposits demonstrated apparent cohesion, suggest that further work, including at large scale, is particularly needed to investigate the behaviour of fine-grained tephra when water is present.

**Fig. 3-11** Tephra deposit on a roof in Tacande, La Palma, December 2021 during the Cumbre Vieja eruption. Tephra has slid on the steeper part of the roof (~ 35° pitch) but accumulated on the lower, shallower part (~ 20°)

In our tests, sliding mainly occurred at the base of the tephra, between the deposit and the roof material. However, on the higher friction roofing material, and in particular for thicker deposits and when water was present, sliding also occurred within the deposit (Table 3-3). This suggests that for these roofs and for thicker, wetter tephra deposits, the failure mechanism depends on the internal angle of friction of the tephra rather than the type of roofing material and that the frictional strength at the deposit-roof interface in these situations is higher than the internal frictional strength of the tephra deposit.

## Implications for disaster risk management

Disaster risk considers the potential harms to people and infrastructure in a community resulting from their exposure to a hazard, mitigated by their capacity to deal with its impacts (United Nations Office for Disaster Risk Reduction 2016). Understanding when tephra fall loads might lead to building collapse and how deposit sliding may reduce vulnerability can help when assessing priorities for clean-up during and after an eruption and when planning for future eruptions.

For buildings proximal to the source, clearing roofs of tephra can significantly reduce vulnerability to building failure, but clean-up operations often pose significant logistical and health and safety challenges (Hayes et al. 2015; IVHHN 2021). Our results can help prioritise roofs for clearance by highlighting when the deposit is likely to be reduced by sliding. We found that pumice and scoria deposits are unlikely to slide on roofs with pitches ≤ ~ 15°

while for fine-grained tephra, roofs ≤ ~ 12° can be treated as flat. In addition, much of the load is likely to be shed on metal roofs with pitches ≥ 32° and fibre cement or tile roofs with pitches ≥ 35°.

We also found that weathering of the roof material did not significantly change tephra sliding behaviour, although when considering the physical load that a roof can withstand, it would be important to consider any deterioration in the material strength due to environmental exposure which might result in collapse at lower imposed loads. Of course, the roofing material may not be the weakest part of the roof and collapse may occur through failure of weak structural support, as was observed following the Cordón Caulle 2011 eruption (Elissondo et al. 2016) and most recently in La Palma after the 2021 eruptions (e.g. Dominguez Barragan et al. 2022). Surveys of roofs on both engineered and non-engineered buildings around Galeras volcano in Columbia estimated that collapse after tephra fall could occur under loads of 0.5–5 kPa, with the roof support structure and the type and quality of roofing material being key factors in determining failure load (Torres-Corredor et al. 2017). A range of failure points were also identified following the Pinatubo 1991, Rabaul 1994 and Kelud 2014 eruptions (roof covering, rafters and purlins), with longer span roofs and those with overhangs performing poorly (Blong 2003; Spence et al. 2005; Williams et al. 2020).

Over the longer term, vulnerability in areas susceptible to tephra fall could be reduced by planning buildings with pitches ≥ 35° to enhance the likelihood of tephra sliding. Existing buildings where tephra is unlikely to slide could also be identified and roof strengthening considered for particular key buildings (e.g. Zuccaro and Leone 2012).

## Implications for building design

Building design standards aim to ensure that buildings remain fit for purpose during their design life and take account of transient loads such as snow (e.g. British Standards Institution 2009; International Standards Organization 2013). Although tephra loads are not routinely considered, the snow load approach could be adapted for tephra loading. The Eurocode standard for snow loading (BS EN 1991-3) first defines a characteristic value for snow load on the ground, taken as the load with an expected 50-year return period (British Standards Institution 2009). This value is calculated using an empirical equation which was derived from statistical analyses of historical snow depth measurements and takes account of local climatic conditions (Sanpaolesi et al. 1998). The ground load is then multiplied by a

shape coefficient (ranging from 0 to 1) which accounts for the fraction of the load that slides off a roof depending on its shape. These shape coefficients were derived from measurements of ground and roof snow loads collected for 81 buildings over the 1998–99 winter season (Sanpaolesi et al. 1999).

For tephra loading, the characteristic value of the ground load could routinely be obtained from numerical modelling of different eruption scenarios (e.g. Barker et al. 2019; Vázquez et al. 2019; Wild et al. 2019). To build up a comprehensive set of sliding coefficients tephra sliding behaviour must be quantified on a wide range of roof shapes and materials. As a first step towards this, our results can inform values for simply pitched roofs. By making the following assumptions, we can summarise all our results to show how the fraction of ground load remaining on a roof varies with roof pitch for the different tephra types we considered (Fig. 3-12a-c):

- The angle at which grains initially move (Fig. 3-6) represents the lowest roof pitch at which any tephra load is likely to be removed by sliding.
- The deposit sliding angle (Fig. 3-7) represents the steepest pitch on which any ash will remain.
- Load reduces linearly for roofs with pitches between these values.
- Initial sliding occurs at the same angle in 20 and 30 cm deposits (as we were unable to measure this for 30 cm thickness with our equipment).
- Where tephra deposits slide internally rather than at the interface with the roofing material, this action results in the erosion of the underlying deposit so that there is little difference between deposits that fail at the base or internally.

We can then select characteristic curves for each tephra type (Fig. 3-12d). In building design, it is usual to present results with a 95 % confidence interval, but the number of tests needed for that is beyond the scope of this study due to the limited size of the test equipment and roofing materials available to test. We have however selected conservative values and, for this initial assessment, chosen changes of slope at 5° intervals (i.e. at 15, 20, 30 and 35°). Pumice and scoria can be represented by a single curve (Fig. 3-12a,b), while ash requires two curves (Fig. 3-12c): one for thin, wet deposits, which are stable at steep roof pitches, and one for all other ash.
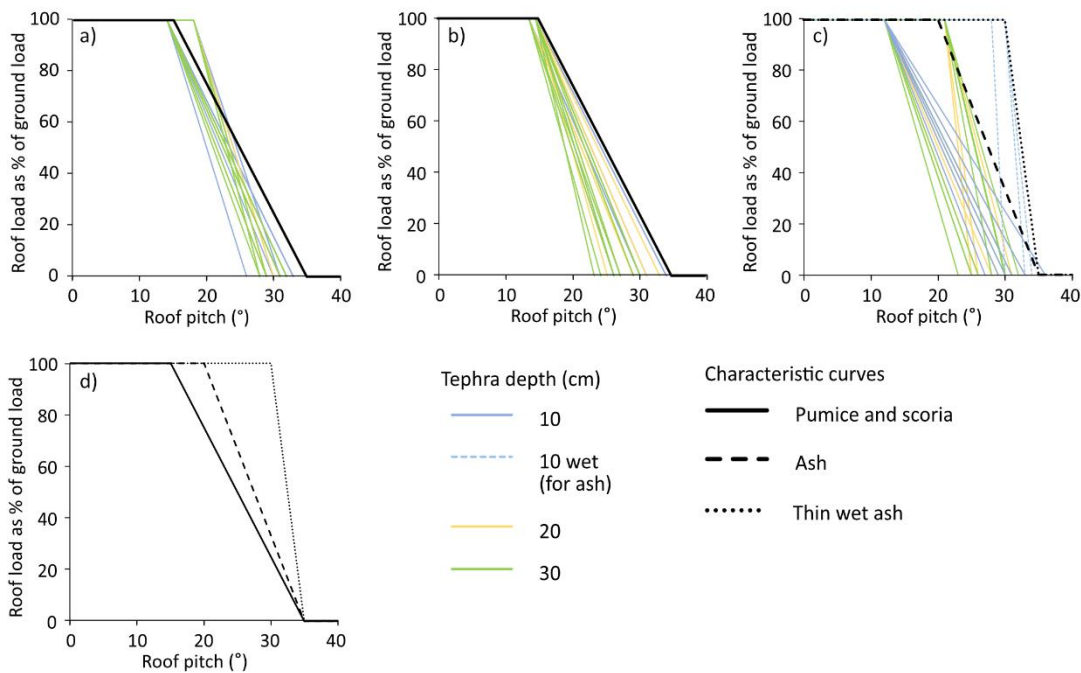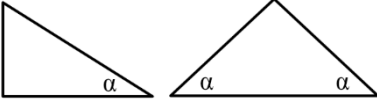
**Fig. 3-12** Summary of all tests showing percentage of ground tephra load expected to remain on a roof for deposits of a) pumice, b) scoria, c) ash. Characteristic values for each tephra type are shown in d). Load is assumed to reduce linearly for roof pitches between lab values for initial movement and total sliding

As a final step, we can present these results as indicative sliding coefficient equations for simply pitched roofs (Table 3-4), using the same format as the Eurocode snow loading coefficients. The sliding coefficient, $\mu$, varies with roof pitch and is a multiplier that converts tephra load on the ground to tephra load on a roof. The geological setting is important when considering likely deposit characteristics in any future eruption, and expert judgement of local hazard should be used to select the most appropriate Eqs. (3-1, 3-2 or 3-3) in any area.

## Limitations and future work

When considering building failure due to natural hazards, there will ultimately be the possibility of loss. For financial loss, insurance companies typically use vulnerability curves to link hazard intensity (in our case, tephra fall loads) to likely damage for different building types (Blong et al. 2017; Oramas-Dorta et al. 2021). Exposure is often considered at a regional scale, aligning with information held by insurers, as exposure data at the level of individual buildings are rarely available (Silva et al. 2018; Murnane et al. 2019). However,

**Table 3-4** Tephra sliding coefficients for monopitch and simply pitched roofs

| Roof type | Monopitch or simply pitched, with pitch = α | | | |
|---|---|---|---|---|



| Tephra type | Low pitch | Medium pitch | Steep pitch | Equation |
|---|---|---|---|---|
| Coarse-grained (Pumice or scoria) | $\alpha \leq 15°$ $\mu_{coarse} = 1$ | $15° < \alpha < 35°$ $\mu_{coarse} = (35 - \alpha)/20$ | $35° \leq \alpha$ $\mu_{coarse} = 0$ | (3-1) |
| Fine-grained (Ash) | $\alpha \leq 20°$ $\mu_{fine} = 1$ | $20° < \alpha < 35°$ $\mu_{fine} = (35 - \alpha)/15$ | $35° \leq \alpha$ $\mu_{fine} = 0$ | (3-2) |
| Wet ash < 20 cm thick[a] | $\alpha \leq 30°$ $\mu_{finewet} = 1$ | $30° < \alpha < 35°$ $\mu_{finewet} = (35 - \alpha)/5$ | $35° \leq \alpha$ $\mu_{finewet} = 0$ | (3-3) |

[a] When considering critical roof loads, this case will likely only lead to failure for dense deposits or low strength roofs.

where detailed asset information is obtained, we see the potential of using our results to shift the vulnerability curves depending on tephra type and roof shape, providing more accurate damage and loss estimates for tephra fall events. In the case of loss of life, the best approach to avoid this is to identify the hazard and reduce the risk. The hazard posed by tephra loading leading to roof collapse is obvious, but vulnerability (and hence also risk) is controlled by the quality of the structure and ability of the tephra load to be shed. The characteristic curves developed here demonstrate the process through which this risk can begin to be calculated.

To fully realise the potential benefits of this work more testing on different materials and at different scales is needed. The findings presented here relate to uniform loads on simply pitched roofs and assume that the tephra load is removed when the deposit slides, rather than being redistributed on the roof. Our experiments do not represent the process of deposition, where the deposit may be stratified by grain size (Eychenne and Engwell 2022) and tephra falls on an inclined surface, whereas in our tests we poured tephra onto a horizontal surface which was then inclined. The rate of deposition may also affect the ability of tephra to slide or be cleared, clogging of gutters may form barriers inhibiting

sliding (Hampton et al. 2015) and for multi-pitched roofs, sliding from one area may lead to increased loading elsewhere. We have not considered post-depositional changes, where rain can lead to deposit surfaces becoming cemented, which may affect the sliding behaviour (Tarasenko et al. 2019). Wind can also cause drifting on sheltered roofs, and this can significantly increase loading as has been seen from field observations and laboratory tests for snow loads (e.g. Bennett et al. 2014; Wang et al. 2020; Zhang et al. 2021).

We have focused on one of the hazards of tephra fall, namely increased roof loading. However, fire from hot tephra and impact from larger ballistics should also be considered (e.g. Hampton et al. 2015; Williams et al. 2019). In addition, if the deposit remains in place long term, corrosion may weaken metal roofs, as was reported in Montserrat (Sword-Daniels et al. 2014) and Rabaul, Papua New Guinea (Blong 2003), although laboratory tests indicate this is unlikely to occur over timescales less than one month (Oze et al. 2014). It would be useful to investigate how tephra fall may promote corrosion and lead to building failures beyond proximal areas, considering both the residue left after sliding (as we found in our dry-wet tests) and deposits thinner than 10 cm. We have also not considered any structural aspects of roofs, but these are important when assessing the collapse vulnerability for individual roofs (Torres-Corredor et al. 2017).

The largest limitation of our work is that our tests were small-scale and considered sliding on a simple slope for three roof materials. The volumes of tephra required for large-scale testing precluded statistically relevant testing on even just three roofing materials within the scope of this project, and the importance of testing the influence of different roofing materials was considered a priority. Larger scale experiments are however now needed to confirm our results and assess the impact of the roof structure on failure. Tests covering other roof materials and more complex roof geometries would also add to these findings and allow application to a wider range of roof types found in areas susceptible to tephra loading.

In contrast to our other tephra samples, wet ash did not flow and thin deposits were stable to high angles (30° on fibre cement and tiles) before failing by slumping or sliding along the roof. This means that our assumption that roof loads decrease linearly for roofs with pitches between the initial movement and final sliding angles (Fig. 3-12) may not be valid for this deposit. Again, larger scale tests should investigate how varying thicknesses of wet ash behave on different roof materials and slopes.

## Conclusions

Using small-scale laboratory tests to investigate tephra sliding behaviour on roofs, we have developed a set of preliminary sliding coefficients for monopitched or simply pitched roofs. These have been derived by adapting the European Eurocode standard procedure for snow loads on roofs. Our tests considered thicknesses of 10, 20 and 30 cm on corrugated metal, fibre cement sheets and tiles for dry and wet deposits of low-density pumice and high-density scoria with a coarse-to-fine grain size distribution (median grain size = -2.3 $\phi$ (5 mm)), as well as high density basaltic ash (median grain size = 1.7 $\phi$ (0.3 mm)).

Our results show that sliding of coarse-grained deposits is unlikely to occur on roofs with pitches ≤ ~ 15°, while for dry ash this value is ~ 12°. Wet ash behaved differently with thin deposits (10 cm thick) stable at pitches up to 30°; however, our results for wet ash are inconclusive and further work is needed to investigate the effects of water on ash deposits. In addition, the load is mainly shed on metal roofs with pitches ≥ 32° and fibre cement or tiles with pitches ≥ 35°, values that hold for both new and weathered roofing.

For monopitch and simply pitched roofs, we have produced characteristic curves and sliding coefficients enabling tephra loads on a roof to be estimated from the ground load. These results can assist in prioritising roofs to be cleared during and after an eruption. This is a first step towards developing building standards for tephra loading; however, there is further work to be done. Additional roof types need consideration to build up a comprehensive set of sliding coefficients that can be used in building design and large, structure-scale testing is required to validate the laboratory results.

## Supplementary information

The online version contains supplementary material available at https://doi.org/10. 1186/ s13617- 023- 00137-2.

## Acknowledgements

## Declarations

**Authors' contributions**

The project was devised by MT and JC and supervised by MT, JC and SC. SO undertook laboratory work and data analysis. AS contributed to laboratory work. SO wrote the manuscript with inputs from MT, JC, AS and SC.

**Funding**

**Availability of data and materials**

All sliding test results are available as Supplementary material.

**Ethics approval and consent to participate**

Not applicable

**Competing interests**

The authors declare that they have no competing interests.

## References

Bagheri G, Bonadonna C (2016) Aerodynamics of volcanic particles: characterization of size, shape, and settling velocity. In: Mackie S, Cashman K, Ricketts H, Rust A, and Watson M (eds). Volcanic ash: hazard observation. Elsevier, pp39–52. https://doi.org/10.1016/B978-0-08-100405-0.00005-7

Barker SJ, Van Eaton AR, Mastin LG, Wilson CJN, Thompson MA, Wilson TM, Davis C, et al. (2019) Modeling ash dispersal from future eruptions of Taupo Supervolcano. Geochem Geophys Geosys 20(7), 3375–3401. https://doi.org/10.1029/2018GC008152

Beakawi Al-Hashemi HM, Baghabra Al-Amoudi OS (2018) A review on the angle of repose of granular materials. Powder Technol 330, 397–417. https://doi.org/10.1016/j.powtec.2018.02.003

Bennett PJ, Peterka JA and Harris JR (2014) A case study in drifting snow behavior. In: Proceedings of the 2014 Structures Congress. American Society of Civil Engineers, pp34–45. https://doi.org/10.1061/9780784413357.004

Blong R (2003) Building damage in Rabaul, Papua New Guinea, 1994. Bull Volcanol 65(1), 43–54. https://doi.org/10.1007/s00445-002-0238-x

Blong RJ, Grasso P, Jenkins SF, Magill CR, Wilson TM, McMullan K, et al. (2017) Estimating building vulnerability to volcanic ash fall for insurance and other purposes. J Appl Volcanology 6, 2. https://doi.org/10.1186/s13617-017-0054-9

British Standards Institution (2009) BS EN 1991-1-3: 2003 + A1:2015. Eurocode 1 – actions on structures. Part 1-3: general actions – snow loads. London: BSI.

Del Bello E, Taddeucci J, Merrison JP, Rasmussen KR, Andronico D, Ricci T, et al. (2021) Field-based measurements of volcanic ash resuspension by wind. Earth Planet Sci Lett 554, 116684. https://doi.org/ 10.1016/j.epsl.2020.116684

Dominguez Barragan L, Di Maio L, Reyes Hardy M-P, Frischknecht C, Zuccaro G, Perez N, Bonadonna C (2022) Impact assessment of buildings exposed to the tephra fallout of the 2021 Cumbre Vieja eruption in La Palma, Spain. EGU General Assembly 2022, Vienna, Austria, 23–27 May 2022, EGU22-12678. https://doi.org/10.5194/egusphere-egu22-12678

Elissondo M, Baumann V, Bonadonna C, Pistolesi M, Cioni R, Bertagnini A, Biass S, et al. (2016) Chronology and impact of the 2011 Cordón Caulle eruption, Chile. Nat Hazards Earth Sys Sci 16(3), 675–704. https://doi.org/10.5194/nhess-16-675-2016

Eternit (2021) Profiled sheeting: description, properties and performance. Technical note Et-01/08/en/v1. https://www.eternit.co.uk/-/dam/eternit-material-information-data-sheet/pd17895/original/eternit-material-information-data-sheet.pdf Accessed: 28/01/2022

Eychenne J, Engwell SL (2022) The grainsize of volcanic fall deposits: spatial trends and physical controls. GSA Bull 135 (7-8), 1844–1858. https://doi.org/10.1130/B36275.1

Freire S, Florczyk AJ, Pesaresi M, and Sliuzas R (2019) An improved global analysis of population distribution in proximity to active volcanoes, 1975-2015. ISPRS Int J Geo-Information 8, 341. https://doi.org/10.3390/ijgi8080341

Hampton SJ, Cole JW, Wilson G, Wilson TM, Broom S (2015) Volcanic ashfall accumulation and loading on gutters and pitched roofs from laboratory empirical experiments: implications for risk assessment. J Volcanol Geotherm Res 304, 237–252. https://doi.org/10.1016/j.jvolgeores.2015.08.012

Hayes JL, Wilson TM, Magill C (2015) Tephra fall clean-up in urban environments. J Volcanol Geotherm Res 304, 359–377. https://doi.org/10.1016/j.jvolgeores.2015.09.014

Hayes JL, Calderón R, Deligne NI, Jenkins SF, Leonard GS, Mcsporran AM, Williams GT et al. (2019a) Timber-framed building damage from tephra fall and lahar: 2015 Calbuco eruption, Chile. J Volcanol Geotherm Res 374, 142–159. https://doi.org/10.1016/j.jvolgeores.2019.02.017

Hayes JL, Wilson TM, Stewart C, Villarosa G, Salgado P, Beigt D, et al. (2019b) Tephra clean-up after the 2015 eruption of Calbuco volcano, Chile: a quantitative geospatial assessment in four communities. J Appl Volcanology 8, 7. https://doi.org/10.1186/s13617-019-0087-3

Hornbaker DJ, Albert R, Albert I, Barabasi AL, Schiffer P (1997) What keeps sandcastles standing? Nature 387, 765. https://doi.org/10.1038/42831

Hornby AJ, Kueppers U, Maurer B, Poetsch C, Dingwell DB (2020) Experimental constraints on volcanic ash generation and clast morphometrics in pyroclastic density currents and granular flows. Volcanica 3(2), 263–283. https://doi.org/10.30909/VOL.03.02.263283

International Standards Organization. (2013) ISO 4355:2013. Bases for design of structures — determination of snow loads on roofs. ISO, Geneva

IVHHN (2021) Health and safety considerations for ashfall clean-up: briefing note. https://www.ivhhn.org/uploads/IVHHN_briefing_note_clean-up_health_safety.pdf Accessed: 28/03/2023

Jenkins SF, Spence RJS, Fonseca JFBD, Solidum RU, Wilson TM (2014) Volcanic risk assessment: quantifying physical vulnerability in the built environment. J Volcanol Geotherm Res 276, 105–120. https://doi.org/10.1016/j.jvolgeores.2014.03.002

Jenkins SF, Wilson T, Magill C, Miller V, Stewart C, Blong R, Marzocchi W et al. (2015) Volcanic ash fall hazard and risk. In: Global volcanic hazards and risk. Loughlin SC, Sparks RSJ, Brown SK, Jenkins SF, Vye-Brown C (eds). Cambridge University Press, 173–221. https://doi.org/10.1017/CBO9781316276273.005

Macedonio G, Costa A (2012) Brief communication: rain effect on the load of tephra deposits. Nat Hazards Earth Syst Sci, 12(4), 1229–1233. https://doi.org/10.5194/nhess-12-1229-2012

Miller VL, Joseph EP, Sapkota N, Szarzynski J (2022) Challenges and opportunities for risk management of volcanic hazards in small-island developing states. Mt Res Dev 42(2), D22–D31. https://doi.org/10.1659/MRD-JOURNAL-D-22-00001.1

Murnane RJ, Allegri G, Bushi A, Dabbeek J, de Moel H, Duncan M, et al. (2019) Data schemas for multiple hazards, exposure and vulnerability. Disaster Prev Manage 28(6), 752–763. https://doi.org/ 10.1108/DPM-09-2019-0293

Oramas-Dorta D, Tirabassi G, Franco G, Magill C (2021) Design of parametric risk transfer solutions for volcanic eruptions: an application to Japanese volcanoes. Nat Hazards Earth Syst Sci 21(1), 99–113. https://doi.org/10.5194/nhess-21-99-2021

Osman S, Thomas M, Crummy J, and Carver S (2022) Investigation of geomechanical properties of tephra relevant to roof loading for application in vulnerability analyses. J Appl Volcanology 11, 9. https://doi.org/10.1186/s13617-022-00121-2

Oze C, Cole J, Scott A, Wilson T, Wilson G, Gaw S, Hampton S et al. (2014) Corrosion of metal roof materials related to volcanic ash interactions. Nat Hazards 71(1) 785–802. https://doi.org/10.1007/s11069-013-0943-0

Sanpaolesi L, Brettle M, Currie D, Dillon P, Sims P, Delpech P, Dufresne M et al. (1999) Scientific support activity in the field of structural stability of civil engineering works: snow loads. Final Report Phase II. Commission of the European Communities DGIII/D-3, Brussels. www2.ing.unipi.it/dic/snowloads/Final Report II.pdf Accessed: 30/9/2022

Sanpaolesi L, Currie D, Sims P, Sacré C, Stieffel U, Lozza S, Eiselt B et al. (1998) Scientific support activity in the field of structural stability of civil engineering works: snow loads. Final Report Phase I. Commission of the European Communities DGIII/D-3, Brussels. www2.ing.unipi.it/dic/snowloads/Final Report I.pdf Accessed: 30/9/2022

Silva V, Yepes-Estrada C, Dabbeek J, Martins L, Brzev S (2018) GED4ALL – global exposure database for multi-hazard risk analysis – multi-hazard exposure taxonomy, GEM Technical Report 2018-01. Pavia, Italy: GEM Foundation. http://www.gfdrr.org/sites/default/files/publication/Exposure%20data%20schema_final%20report.pdf. Accessed: 30/09/2023

Spence RJS, Kelman I, Baxter PJ, Zuccaro G, Petrazzuoli S (2005) Residential building and occupant vulnerability to tephra fall. Nat Hazards Earth Syst Sci 5(5), 477–494. https://doi.org/10.5194/nhess-5-477-2005

Sword-Daniels V, Wilson TM, Sargeant S, Rossetto T, Twigg J, Johnston DM, Loughlin SC et al. (2014) Consequences of long-term volcanic activity for essential services in Montserrat: challenges, adaptations and resilience. In: The Eruption of Soufrière Hills Volcano, Montserrat from 2000 to 2010. Wadge G, Robertson REA, Voight, B (eds). Geological Society, London, 471-488. https://doi.org/10.1144/M39.26

Tarasenko I, Bielders CL, Guevara A, and Delmelle P (2019) Surface crusting of volcanic ash deposits under simulated rainfall. Bull Volcanol 81, 30. https://doi.org/10.1007/S00445-019-1289-6

Terreal. (n.d.) Roofing book. https://terreal.co.uk/fileadmin/UK/4_Downloads/TERREAL-RoofingBook.pdf Accessed: 31/01/2022

Torres-Corredor RA, Ponce-Villarreal P, Gómez-Martínez DM (2017) Vulnerabilidad física de cubiertas de edificaciones de uso de ocupación normal ante caídas de ceniza en la zona de influencia del Volcán Galeras. Boletín de Geología 39(2), 67–82. https://doi.org/10.18273/revbol.v39n2-2017005

United Nations Office for Disaster Risk Reduction (2016) Report of the open-ended Intergovernmental Expert Working Group on indicators and terminology relating to disaster risk reduction. New York: UNDRR. https://www.undrr.org/publication/report-open-ended-intergovernmental-expert-working-group-indicators-and-terminology. Accessed: 04/07/2023

Varekamp JC, Luhr JF, Prestegaard KL (1984) The 1982 eruptions of El Chichón Volcano (Chiapas, Mexico): character of the eruptions, ash-fall deposits, and gasphase. J Volcanol Geotherm Res 23(1–2), 39–68. https://doi.org/10.1016/0377-0273(84)90056-8

Vázquez R, Bonasia R, Folch A, Arce JL, Macías JL (2019) Tephra fallout hazard assessment at Tacaná volcano (Mexico). J S Am Earth Sci 91, 253–259. https://doi.org/10.1016/j.jsames.2019.02.013

Wang J, Liu H, Chen Z, Ma K. (2020) Wind tunnel test of wind-induced snowdrift on stepped flat roofs during snowfall. Nat Hazards 104, 731–752. https://doi.org/10.1007/s11069-020-04188-1

Wild AJ, Wilson TM, Bebbington MS, Cole JW, Craig HM (2019) Probabilistic volcanic impact assessment and cost-benefit analysis on network infrastructure for secondary evacuation of farm livestock: a case study from the dairy industry, Taranaki, New Zealand. J Volcanol Geotherm Res 387, 106670. https://doi.org/10.1016/j.jvolgeores.2019.106670

Williams GT, Jenkins SF, Biass S, Wibowo HE, Harijoko A (2020) Remotely assessing tephra fall building damage and vulnerability: Kelud Volcano, Indonesia. J Appl Volcanology 9, 10. https://doi.org/10.1186/s13617-020-00100-5

Williams GT, Jenkins SF, Lee, DWJ, Wee, SJ (2021) How rainfall influences tephra fall loading - an experimental approach. Bull Volcanol 83, 42. https://doi.org/10.1007/s00445-021-01465-0

Williams GT, Kennedy BM, Lallemant D, Wilson TM, Allen N, Scott A, and Jenkins SF (2019) Tephra cushioning of ballistic impacts: quantifying building vulnerability through pneumatic cannon experiments and multiple fragility curve fitting approaches. J Volcanol Geotherm Res 388, 106711. https://doi.org/10.1016/j.jvolgeores.2019.106711

Wilson G, Wilson TM, Deligne NI, Cole JW (2014) Volcanic hazard impacts to critical infrastructure: a review. J Volcanol Geotherm Res 286, 148–182. https://doi.org/10.1016/j.jvolgeores.2014.08.030

Zhang G, Zhang Q, Fan F, Shen S (2021) Field measurements of snowdrift characteristics on reduced scale building roofs based on the size effect study. Structures 32, 2020–2031. https://doi.org/10.1016/J.ISTRUC.2021.04.002

# Chapter 3: Tephra sliding tests

Zuccaro G, Leone MF (2012) Building technologies for the mitigation of volcanic risk: Vesuvius and Campi Flegrei. Nat Hazards Rev 13(3), 221–232. https://doi.org/10.1061/(ASCE)NH.1527-6996.0000071

# Chapter 4

# Probabilistic hazard analysis for a small island: quantifying tephra fall hazard and appraising the possible impact on Ascension Island

Sara Osman[1], Julia Crummy[2], Mark Thomas[1] and Stephen Carver[3]

[1] University of Leeds, School of Earth and Environment, Woodhouse, Leeds LS2 9JT, UK

[2] British Geological Survey, The Lyell Centre, Research Avenue South, Edinburgh EH14 4AP, UK

[3] University of Leeds, School of Geography, Woodhouse, Leeds LS2 9JT, UK

## Abstract

Proximal to source, tephra fall can cause severe disruption, and populations of small volcanically active islands can be particularly susceptible. Volcanic hazard assessments draw on data from past events generated from historic observations and the geological record. However, on small volcanic islands many eruptive deposits are under-represented or missing due to the bulk of tephra being deposited offshore and high erosion rates from weather and landslides. Ascension Island, is such an island, located in the South Atlantic, with geological evidence of mafic and felsic explosive volcanism. Limited tephra preservation makes it difficult to correlate explosive eruption deposits and constrain the frequency or magnitude of past eruptions. We therefore combined knowledge from the geological record together with eruptions from the analogous São Miguel island, Azores to probabilistically model a range of possible future explosive eruption scenarios. We simulated felsic events from a single vent in the east of the island and, as mafic volcanism has largely occurred from monogenetic vents, we accounted for uncertainty in future vent location by using a grid of equally probable source locations within the areas of most recent eruptive activity. We investigated the hazards and some potential impacts of short-lived explosive events where tephra fall deposits could cause significant damage and our results provide probabilities of tephra fall loads from modelled events exceeding threshold values for potential damage. For basaltic events with 6–10 km plume heights, we found a 50 % probability that tephra fallout across the west side of the island would impact roads and the airport during a single explosive event and, if roofs cannot be cleared, three modelled explosive phases produced tephra loads that may be sufficient to cause roof collapse ($\geq$ 100 kg m$^{-2}$). For trachytic events our results show a 50 % probability of loads of 2–12 kg m$^{-2}$ for a plume height of 6 km increasing to 898–3167 kg m$^{-2}$ for a plume height of 19 km. Our results can assist in raising awareness of the potential impacts of tephra fall from short-lived explosive events on small islands.

## Introduction

Tephra is produced in all explosive volcanic eruptions, with a range of observed impacts depending on the size and duration of the eruption and proximity to the source. For communities in volcanically active areas, airborne or remobilised tephra can lead to health issues (IVHHN 2021; Stewart et al. 2022; Eychenne et al. 2022) while deposits can cause significant disruption depending on their thickness and the loading placed on structures

(Table 4-1). Accumulations of < 1 mm (~ 1 kg m$^{-2}$ depending on deposit density) can affect roads and airports, with markings covered and skid resistance reduced (Blake et al. 2017). Tephra loads of 1–10 kg m$^{-2}$ (thickness ~ 1–10 mm) can damage power, water and communications networks and severely disrupt road and rail travel (Jenkins et al. 2015; Blake et al. 2017; Hayes et al. 2022). At these loads, crops can suffer discolouration or loss of leaves and abrasion or rotting of fruit, but the severity depends on the stage of the crop development cycle (Jenkins et al. 2015; Wilson et al. 2017; Ligot et al. 2022). Tephra loads ~ 100 kg m$^{-2}$ have been observed to cause extensive infrastructure damage and result in collapse of the weakest roofs, while loads above ~ 150 kg m$^{-2}$ have potential to cause significant roof damage or collapse regardless of condition (Jenkins et al. 2014; Wilson et al. 2014; Hayes et al. 2022).

**Table 4-1** Summary of likely impacts at different tephra fall loads (amended from Jenkins et al. 2014)

| Tephra load (kg m$^{-2}$) | Likely impact |
| --- | --- |
| 1 | Skid resistance reduced and markings covered at airports and on roads |
| 10 | Damage to power, water and communications networks<br>Severe impact to roads and closure of airports<br>Impact on crops, depending on stage in growth cycle |
| 100 | Collapse of weakest roofs |
| 150 | Collapse of long span roofs |
| 300 | Collapse of good quality metal roofs |
| 400 | Collapse of good quality tile roofs |
| 700 | Collapse of good quality concrete roofs |

Populations of small volcanically active islands can be especially susceptible to the impacts of tephra fall because of their proximity to the vent. It is therefore crucial to understand this potential hazard to aid in planning for possible future explosive events. However, there

# Chapter 4: Probabilistic hazard analysis for Ascension

are large uncertainties associated with the lack of geological data, as small ocean islands often have significant gaps in our knowledge of their eruptive history. This is due to a substantial proportion of tephra being deposited offshore, high erosion rates from rainfall and wind, and the susceptibility of volcanic islands to landslides. To address these knowledge gaps, we can use data from well-studied analogue volcanoes to model possible future events (e.g. Hone et al. 2007; Cashman and Biggs 2014; Tierz et al. 2019; Burgos et al. 2023).

To gain a better understanding of tephra fall hazard and impact on a remote island, we have carried out an exploratory probabilistic tephra fall analysis for Ascension Island in the South Atlantic (referred to as Ascension hereafter) for a range of discrete, short-lived explosive events from selected vent locations across the island. Ascension is a strategically important UK Overseas Territory, located ~ 90 km west of the mid-Atlantic ridge in the South Atlantic Ocean, with an area of ~ 98 km² and ~ 780 residents (Fig. 4-1). Key infrastructure includes the airport, Royal Air Force (Travellers Hill) and US Air Force (USAF) bases, the South Atlantic Relay communications station, a power plant and the small settlements of Georgetown and Two Boats (Fig. 4-1). Ascension has been volcanically active for ~ 6 Ma and recent research has given insights into its magmatic history, with deposits providing evidence for past effusive and explosive eruptions of both mafic and felsic composition (e.g. Chamberlain et al. 2016, 2019, 2020; Winstanley 2020; Davies et al. 2021; Preece et al. 2021). The most recent known effusive eruptive activity has been dated to just 500 years ago (Preece et al. 2018); however, poor tephra preservation (with deposits missing from the record and units being untraceable across the island) means that past explosive eruptions are not well constrained (Preece et al. 2021). We have therefore used eruption source parameters from analogue eruptions together with published geological data to model a range of possible future explosive events and discuss potential impacts on infrastructure.

Tephra fall is, of course, just one of the potential volcanic hazards that are considered in comprehensive hazard and impact assessments, which often use event trees to quantify the likelihood of each hazard (including lava flows, pyroclastic density currents and lahars, as well as tephra fall) (e.g. Newhall and Hoblitt 2002; Marzocchi et al. 2012; Alatorre-Ibargüengoitia et al. 2021; Tadini et al. 2021). Such assessments are beyond the scope of this work, in which we consider only the largest explosive events, where the additional loading on roofs due to tephra fall deposits may lead to collapse. Because of the knowledge

gaps in the Ascension's eruptive history (Preece et al. 2021), we have no indication of the frequency of these large explosive events. Our results therefore provide conditional probabilities of tephra fall loads exceeding threshold values ie. probabilities given that an explosive event has occurred. If future research provides more detailed data on the eruptive history of Ascension, our results could be combined with the probabilities of such events occurring to produce unconditional probabilities (Connor et al. 2015).

## Geological background

The volcanic edifice of Ascension is built on oceanic crust from ~ 7 Ma, with borehole evidence suggesting subaerial eruptions began ~ 2.5 Ma and the oldest surface deposits dated to ~ 1Ma (Minshull et al. 2010; Jicha et al. 2013). Eruptive products cover the full compositional range from basalt to rhyolite, with alkaline felsic magmas produced by fractional crystallisation in a closed system (Chamberlain et al. 2016). Felsic eruptive vents are concentrated in the centre and east of the island while mafic vents occur in the north, south and west. Spatial separation of mafic and felsic volcanism indicates a crustal control on composition and has been interpreted to result from low magma flux, a pattern also seen at other ocean islands e.g. São Miguel, Azores (Chamberlain et al. 2019). At least 80 explosive felsic eruptions have occurred over the past 1 Ma, with the most recent occurring ~ 60 ka in the Eastern Felsic Complex (Preece et al. 2021). Deposits provide evidence of a range of styles from Strombolian to Plinian (Davies et al. 2021). Mafic eruptions occur from monogenetic vents and $^{40}$Ar/$^{39}$Ar dating of the youngest lava flows gave ages of ~ 500 years and suggested the three more recent eruptive areas are around Comfortless Cove, Sister's Peak and to the east of the airport (Airport East), shown in Fig. 4-1 (Jicha et al. 2013; Preece et al. 2018).

## Methods

Our simulations considered discrete explosive events (our model scenarios) with eruptive plumes ranging from 6–27 km above sea level (a.s.l.) and durations of 1–12 hours. While the reasoning for the location of the events is discussed further below, this work simply assumes that an event will occur at the chosen locations without further supporting evidence indicating active volcanic unrest in the areas. For each model scenario we assessed the probability of tephra fall loads exceeding failure thresholds for different roof types.
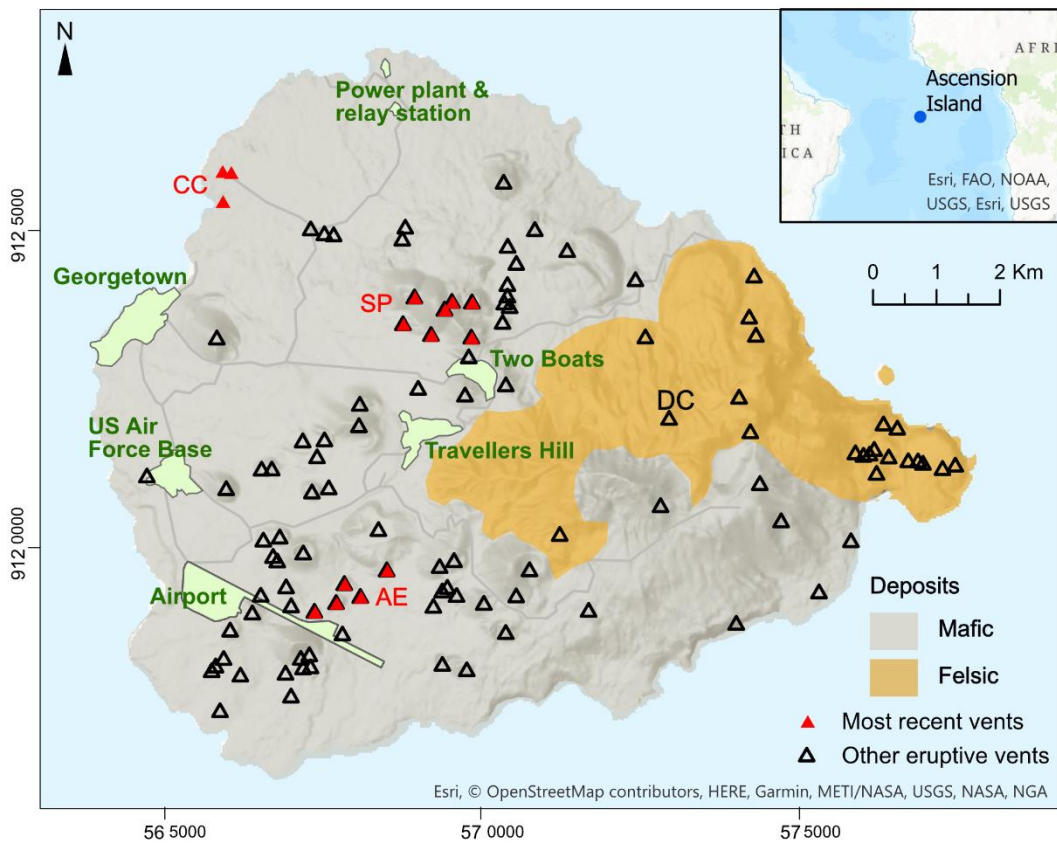
**Fig. 4-1** Map of Ascension Island showing main settlements and infrastructure, eruptive vents and approximate areas of felsic and mafic volcanism. Eruptive vent: DC = Devil's Cauldron vent. Most recent vents: CC = Comfortless Cove, SP = Sister's Peak, A = Airport East. Mafic and felsic deposits amended from Chamberlain et al. 2020, vent locations from Vye-Brown et al. 2019

Despite the geological data on Ascension in the published literature, there are large uncertainties around the eruption source parameters, plume heights, erupted volumes and grain size distributions. We therefore make assumptions and rely on analogues to derive the input parameters for our model scenarios (detailed further below).

## Selection of analogues

Based on geological setting, geochemistry of eruptive products and deposit characteristics, the oceanic island of São Miguel in the Azores has been used as an analogue for Ascension. São Miguel exhibits a wide compositional range of erupted products, formed by fractional crystallisation in a low magma flux environment with spatial separation of felsic and mafic

eruptions (Guest et al. 1999; Chamberlain et al. 2019). The eruptive history for the past 5 ka is well constrained, with trachytic eruptions from Sete Cidades, Fogo (Agua de Pau) and Furnas volcanoes and basaltic activity in the Picos and Congro Fissural Volcanic Systems (Guest et al. 1999). The well-studied peralkaline, trachytic deposits of the Fogo A (4.6 ka, plume height 21–30 km) and Fogo 1563 (plume height ~ 19 km) eruptions (Carey and Sigurdsson 1989; Guest et al. 1999; Pensa et al. 2015) enable estimates of eruption source parameters to be made for future large, felsic eruptions. These provide good analogues for the thick pyroclastic deposits of alkaline trachyte on Ascension (Chamberlain et al. 2019; Preece et al. 2021). Thirty-six basaltic eruptions have occurred over the past 5 ka in the Picos Fissural Volcanic System (Gaspar et al. 2015). The Serra Gorda eruption (3–5 ka), estimated at VEI 3, produced the largest scoria cone in this system with deposits 50 cm thick at distances up to 4 km from source (Booth et al. 1978; Newhall and Self 1982; Ferreira et al. 2015). Although there are many examples of smaller eruptions of this type, including on Ascension (Winstanley 2020),  we consider this eruption a good analogue for the scale of monogenetic volcanism on Ascension that might produce tephra fall deposits sufficient to cause roof collapse (hence of interest to this study), without commenting on the likelihood of an event of this size.

## Selection of model scenarios

Our simulations build on initial tephra fall modelling for Ascension carried out by the British Geological Survey (BGS) (Vye-Brown et al. 2019) and specific to this study, aim to quantify tephra fall hazard from a range of possible explosive events where deposit loads may lead to significant roof damage. Both the felsic and mafic explosive events were modelled using eruption source parameters from our selected analogue eruptions on São Miguel.

### Felsic events

We simulated explosive, trachytic events from the Devil's Cauldron vent (Fig. 4-1) in the Eastern Felsic Complex, with plume heights of 6–27 km a.s.l. This was the assumed vent for an eruption ~ 65 ka, (Preece et al. 2021). To investigate potential impacts from specifically large events we ran simulations with 19 and 27 km plume heights, based on the Fogo 1563 and Fogo A eruptions on São Miguel (Walker and Croasdale 1970; Carey and Sigurdsson 1989; Gaspar et al. 2015; Pensa et al. 2015). We also simulated smaller volume events (Davies et al. 2021) with 6, 12 and 15 km plume heights.

**Mafic events**

To investigate an explosive basaltic event with tephra fall deposits that may cause significant roof damage, we ran simulations based on the São Miguel Serra Gorda eruption (Booth et al. 1978). Our model scenarios used vent locations in each of the three most recent eruptive areas, namely Comfortless Cove, Sister's Peak and Airport East and modelled a single event with plume heights sampled in the range 6 – 10 km. We also explored the tephra fall footprint and potential impacts from multiple explosive pulses during an eruption, as observed during the 2021 eruptions at Soufrière St Vincent (Miller et al. 2022), and Cumbre Vieja, La Palma (Bonadonna et al. 2022; Martí et al. 2022) by simulating three separate events, each with 6–10 km plume heights. It can be difficult to clear tephra deposits from roofs proximal to the source because of the possibility of further volcanic activity and the need to ensure safe working conditions and avoid injuries due to falls from roofs or ladders (Wardman, et al. 2012; Magill et al. 2013). We therefore summed the loads from each pulse, simulating a worst-case scenario where roofs were not cleared and there was no erosion of the fall deposit between explosive phases.

## Accounting for uncertainty in vent location

Many mafic eruptions on Ascension have occurred from monogenetic vents, but assessing the hazard from monogenetic volcanic fields is difficult due to uncertainty with respect to the location of future vents (Valentine and Connor 2015). This is a particular issue on small ocean islands, including Ascension, where gaps in the eruptive record can make it difficult to assess the age relationships between vents, precluding the use of statistical methods to define vent opening probabilities (e.g. le Corvec et al. 2013; Connor et al. 2019; Gallant et al. 2021). However, selection of a single vent location for simulations can underestimate the area over which tephra loadings may exceed given thresholds compared to modelling a spread of possible vent locations. We therefore used a novel approach to model multiple vent locations within a specified area in order to consider a wider spread of tephra impacts, given the uncertainty of vent location. We defined an area in which we assumed a new vent would occur by creating a buffer around the most recent vents. For the youngest vents in both the Sister's Peak and Airport East areas, the average spacing between the vents has been estimated at ~ 400 m (Vye-Brown et al. 2019). We therefore assumed that the source of a future eruption would be within 400 m of these historic vents. Within this buffer area we created a grid of vents with equal probability of eruption and selected a grid spacing of 200 m, to ensure meaningful differences in model outputs, balanced with computational

resource to run multiple simulations (Fig. 4-2). For Comfortless Cove, on the west of the island, the prevailing winds from the south-east would result in most tephra being deposited over the sea with vent location having little impact on tephra loads on land, therefore, for this location our scenarios were based on a single vent.
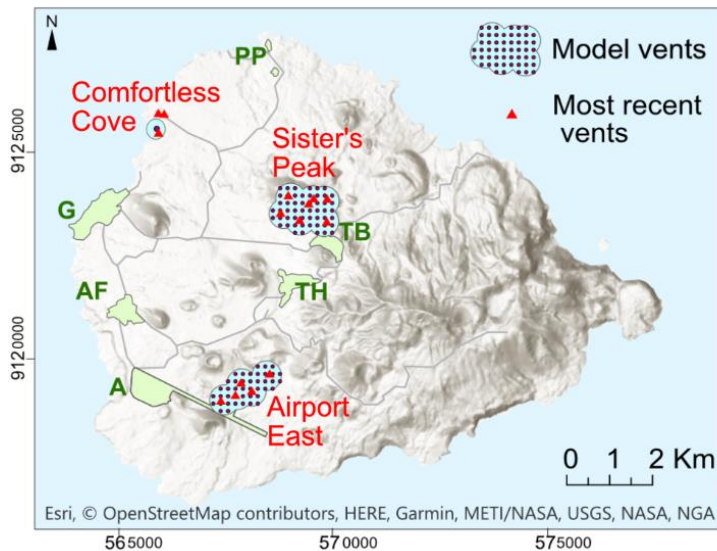


**Fig. 4-2** Areas of most recent volcanism on Ascension and grid of model vents used for mafic eruptive scenarios. Key locations: A: airport, G: Georgetown, PP: power plant and South Atlantic Relay station, TB: Two Boats, TH: Travellers Hill, AF: US Air Force Base.

## Wind data

Wind velocity influences the direction of spread of the volcanic plume as well as the sedimentation of tephra, which controls the extent of the tephra footprint on the ground. We took account of variations in the wind field by stochastically sampling wind velocity from a ten-year ERA5 dataset for Ascension. The ERA5 reanalysis data covered the period 2010–2019 and comprised six-hourly wind data at 37 pressure levels within the atmosphere with horizontal resolution of ~ 30 km (Hersbach et al. 2018, 2020). To investigate seasonal variability, we analysed wind speed and direction by month using TephraProb (Biass et al. 2016). Wind roses for 3-monthly intervals at heights up to ~ 30 km above sea level (covering the heights of our simulated plumes) did not show significant seasonal trends (Fig. C-1 in Appendix C1) and therefore we sampled winds from the whole 10-year dataset for each of our simulations (14608 wind profiles in total) (Fig. 4-3).
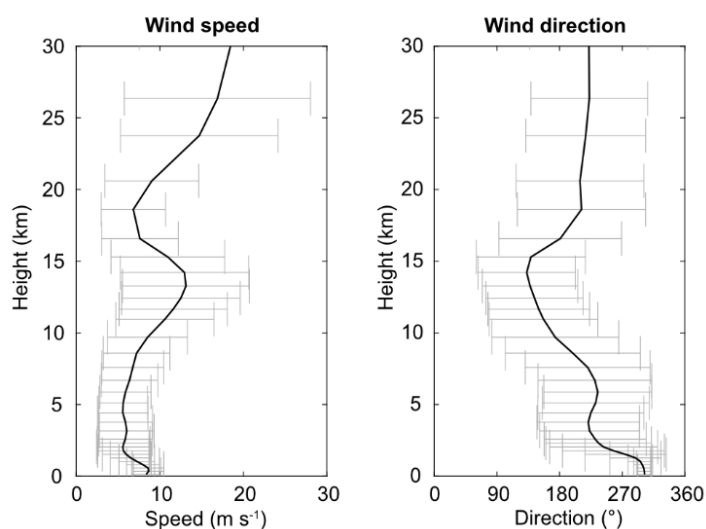
**Fig. 4-3** Summary of wind conditions on Ascension Island (mean speed and mean direction that the wind is blowing towards) from the ERA5 2010–2019 reanalysis dataset (Hersbach et al. 2018) stochastically sampled for all simulations

## Tephra modelling

We used Tephra2 with the TephraProb Matlab package for our probabilistic hazard modelling (Bonadonna et al. 2005; Connor and Connor 2006; Biass et al. 2016). Tephra2 takes inputs defining eruptive conditions (plume height, eruption duration, total mass erupted, grain size distribution, particle density) and solves the advection-diffusion equation in two dimensions to calculate tephra accumulation on the ground. The model uses a wind field that is assumed to be vertically stratified but horizontally constant, an assumption that is likely to be valid over the small area of Ascension. TephraProb enables multiple runs of Tephra2, with input parameters sampled within user-defined ranges, to be combined into a probabilistic output. Both Tephra2 and TephraProb have been widely used and the outputs are now routinely accepted in scenario-based tephra fall hazard assessments of possible future events (e.g. Wild et al. 2019; Warwick et al. 2022; Aravena et al. 2023) and inversion modelling to recreate past events (e.g. Crummy et al. 2019; Jenkins et al. 2020; Tennant et al. 2021). We used analogue eruptions on São Miguel to calibrate the model and select best-fit values for model variables (including diffusion coefficient, fall time threshold and the plume model, detailed in Tables 4-2 and 4-3) which describe the release, transport and deposition of particles.

**Table 4-2** Input parameters used for felsic simulations

| Parameter | Value | | | Rationale |
|---|---|---|---|---|
| Plume height (km asl) | 27 | 19 | | Selected to best match Fogo 1563 and Fogo A eruptions (Walker and Croasdale 1970; Carey and Sigurdsson 1989; Gaspar et al. 2015; Pensa et al. 2015). |
| Mass erupted (kg) | $10^{11}$–$5 \times 10^{12}$ | $10^{10}$–$10^{12}$ | | |
| Duration (h) | 3–12 | 2–6 | | |
| Plume height (km asl) | 15 | 12 | 6 | Selected to model smaller volume eruptions (e.g. Davies et al. 2021). |
| Mass erupted (kg) | $10^{10}$–$5 \times 10^{11}$ | $10^{9}$–$10^{11}$ | $10^{7}$–$10^{10}$ | |
| Duration (h) | 1–4 | 1–3 | 1–3 | |
| **Grain size distribution** | | | | |
| $\Phi$ range (Md$_\Phi$) | -5 – 6 (0.5) | | | Based on published grain size distributions for Fogo 1563 and Fogo A eruptions (Walker and Croasdale 1970). |
| $\sigma_\Phi$ | 2 | | | |
| Aggregation | No | | | |
| **Particle densities** | | | | |
| $\rho$ lithic (kg m$^{-3}$) | 2400 | | | Scollo (2008) found particle density has negligible effect on modelled tephra loads and so we used typical values for trachytic tephra deposits on São Miguel (Kueppers et al. 2019). |
| $\rho$ pumice (kg m$^{-3}$) | 800 | | | |
| **Model parameters** | | | | |
| Diffusion coefficient (m s$^{-2}$) | 5000 | | | Selected so that tephra loads best matched observed Fogo A deposit (with tephra depths converted to loads using published deposit density of 500 kg m$^{-3}$) (Walker and Croasdale 1970). β distributions reflect the vertical distribution of mass in the plume. We tested: |
| Fall time threshold (s) | 6000 | | | α = 1, β = 1 (mass evenly distributed) |
| Plume model β distribution (α, β) | 1,1 | | | α = 2, β = 2 (mass concentrated at centre of the plume) α = 3, β = 2 (mass concentrated towards plume top) α = 2, β = 3 (mass concentrated towards plume bottom) |
| Column integration steps | 50 | | | Produced stable load contours while optimising run time |

**Table 4-3** Input parameters used for mafic simulations

| Parameter | Value | Rationale |
|---|---|---|
| Plume height (km asl) | 6–10 | Selected to simulate relatively small eruption, but one that could lead to tephra deposits likely to cause roof collapse. 6 km was minimum plume height where deposit loads reached roof collapse values beyond the vent area. |
| Mass erupted (kg) | $10^9$–$10^{10}$ | |
| Duration (h) | 1–6 | |
| **Grain size distribution** | | |
| $\Phi$ range (Md$_\Phi$) | -5 – 5 (-1) | Based on maximum and median grain size data from Serra Gorda eruption (Booth et al. 1978). |
| $\sigma_\Phi$ | 2 | |
| Aggregation | No | |
| **Particle densities** | | |
| $\rho$ lithic (kg m$^{-3}$) | 2900 | Scollo (2008) found particle density has negligible effect on modelled tephra loads and so we used typical values (https://volcanoes.usgs.gov/volcanic_ash/ density_hardness.html) |
| $\rho$ pumice (kg m$^{-3}$) | 1000 | |
| **Model parameters** | | |
| Diffusion coefficient (m s$^{-2}$) | 4000 | Selected to best match observed Serra Gorda deposit (Booth et al. 1978), (with tephra depths converted to loads using estimated deposit density of 1000 kg m$^{-3}$). β distributions reflect the vertical distribution of mass in the plume. We tested: |
| Fall time threshold (s) | 5000 | |
| | | $\alpha = 1, \beta = 1$ (mass evenly distributed). |
| Plume model β distribution (α, β) | 2, 2 | $\alpha = 2, \beta = 2$ (mass concentrated at centre of the plume). $\alpha = 3, \beta = 2$ (mass concentrated towards plume top). $\alpha = 2, \beta = 3$ (mass concentrated towards plume bottom). |
| Column integration steps | 50 | Produced stable load contours while optimising run time |

We ran 1000 simulations for each model scenario and accounted for uncertainty in meteorological conditions by randomly selecting a wind profile from the ERA5 2010–2019 dataset for each simulation. Tephra fall loads were mapped onto a 500 m grid, selected to produce a stable output while optimising run time. For each felsic simulation, plume height was fixed, and event duration was sampled from a range (Table 4-2). Values were constrained so that combinations of duration and mass eruption rate (calculated within TephraProb from plume height and wind data using Degruyter and Bonadonna (2012)) were only selected for the simulations when the resulting total erupted mass fell within the ranges defined based on our analogue eruptions (Biass et al. 2016). All input parameters for the felsic model scenarios and the rationale for their selection are shown in Table 4-2.

For each mafic scenario, we ran 1000 simulations from each model vent (Fig. 4-2 and Table C-1). Plume height was sampled within the range 6–10 km, using a logarithmic distribution to account for small eruptions occurring more frequently than large ones, with combinations of plume height, duration and total mass erupted constrained as for the felsic simulations. All input parameters for the mafic model scenarios and the rationale for their selection are shown in Table 4-3.

Output from TephraProb can be expressed as the probability of tephra load on the ground exceeding a threshold or ground tephra loads given a threshold probability. Our focus is on investigating the probabilities of key reported load thresholds (Table 4-1) being exceeded and therefore we report our results as ground tephra loads with probabilities of exceedance of 10, 50 and 90 %.  This enables us to explore both more probable and rare-but-possible outcomes. It is important to note that the probabilistic results are explicitly linked to the modelled event(s) and are calculated on the basis that the modelled events we defined have happened. While we have selected events with a possibility of occurring on Ascension, we offer no appraisal of the likelihood of such events, or their location, simply the potential impacts of tephra loading if such an event were to occur.

For a simulation of an eruption, using one vent location and consisting of a total of $N$ runs, each model run, $i$, gives a tephra load, $l_{ix}$, at grid cell, $x$. The probability, $P,$ of the modelled load in grid cell x ($l_x$) exceeding a mass threshold, $T,$ is shown in Eq. 4-1 (Biass et al. 2016).

$$P(l_x \geq T | 1 \text{ eruption from vent } v) = \sum_{i=1}^{N} \frac{n_i}{N}$$

$$\text{where} \quad v = \text{known vent and } n_i = \begin{cases} 1 \text{ if } l_{ix} \geq T \\ 0 \text{ otherwise} \end{cases} \tag{4-1}$$

When the vent location is uncertain, we can run simulations from a vent $V$, selected from a set of $m$ possible vent locations ($v_1, v_2, .... v_m$), which we assume are all equally likely to be the source. The output combines the results from all simulations to give the probability of the modelled load exceeding $T$ in grid cell $x$ for an eruption from any one of $m$ vents. In this case, Eq. 4-1 is modified to Eq. 4-2.

$$P(l_x \geq T | 1 \text{ eruption from vent } V) = \sum_{j=1}^{m} \sum_{i=1}^{N} \frac{n_{ij}}{Nm}$$

$$\text{where } V \in (v_1 ..... v_m) \text{ and } n_{ij} = \begin{cases} 1 \text{ if } l_{ix} \geq T \\ 0 \text{ otherwise} \end{cases} \tag{4-2}$$

The grid spacing described in the Accounting for uncertainty in vent location section gives values of $m = 42$ and $m = 53$ for Airport East and Sister's Peak areas respectively.

When considering multiple events, we assumed the load is not cleared between eruptions (a worst-case scenario) and hence the tephra load from each event is summed in each grid cell. For $K$ eruptions, during model run, $i$, the total load in grid cell $x$ ($L_{ix}$) is given by Eq. 4-3:

$$L_{ix} = \sum_{k=1}^{K} l_{ixk} \tag{4-3}$$

In this case, Eqs. 4-1 and 4-2 are modified to Eqs. 4-4 and 4-5 respectively:

$$P(L_x \geq T | K \text{ eruptions from vent } v) = \sum_{i=1}^{N} \frac{n_i}{N}$$

$$\text{Where } v = \text{known vent and } n_i = \begin{cases} 1 \text{ if } L_{ix} \geq T \\ 0 \text{ otherwise} \end{cases} \tag{4-4}$$

$$P(L_x \geq T | K \text{ eruptions from vent } V) = \sum_{j=1}^{m} \sum_{i=1}^{N} \frac{n_{ij}}{Nm}$$

$$\text{Where } V \in (v_1 ..... v_m) \text{ and } n_{ij} = \begin{cases} 1 \text{ if } L_{ix} \geq T \\ 0 \text{ otherwise} \end{cases} \tag{4-5}$$

## Results

### Felsic events

For all our selected model simulations from Devil's Cauldron tephra fall covered the whole island with a 50 % probability of loads ≥ 2 kg m$^{-2}$ for a 6 km plume height and a 90 % probability of loads ≥ 1250 kg m$^{-2}$ for a plume reaching 27 km a.s.l. (Table 4-4). For our scenario with a plume height of 6 km lasting 1–3 hours, there was a 50 % probability of tephra loads ≥ 1 kg m$^{-2}$ over most of the island, with loads at key locations reaching threshold values ranging from 2 kg m$^{-2}$ at Georgetown, the airport and the USAF Base to 12 kg m$^{-2}$ at Two Boats (Fig. 4-4a and Table 4-4). Loads with a 10 % probability of exceedance ranged from 4 kg m$^{-2}$ at the airport to 23 kg m$^{-2}$ at Two Boats (Fig. 4-5a and Table 4-4) and there was a 90 % probability of loads of 2–6 kg m$^{-2}$ at Two Boats, Travellers Hill, the power plant and South Atlantic Relay station with loads at other key locations < 1 kg m$^{-2}$ (Fig. 4-5b and Table 4-4).
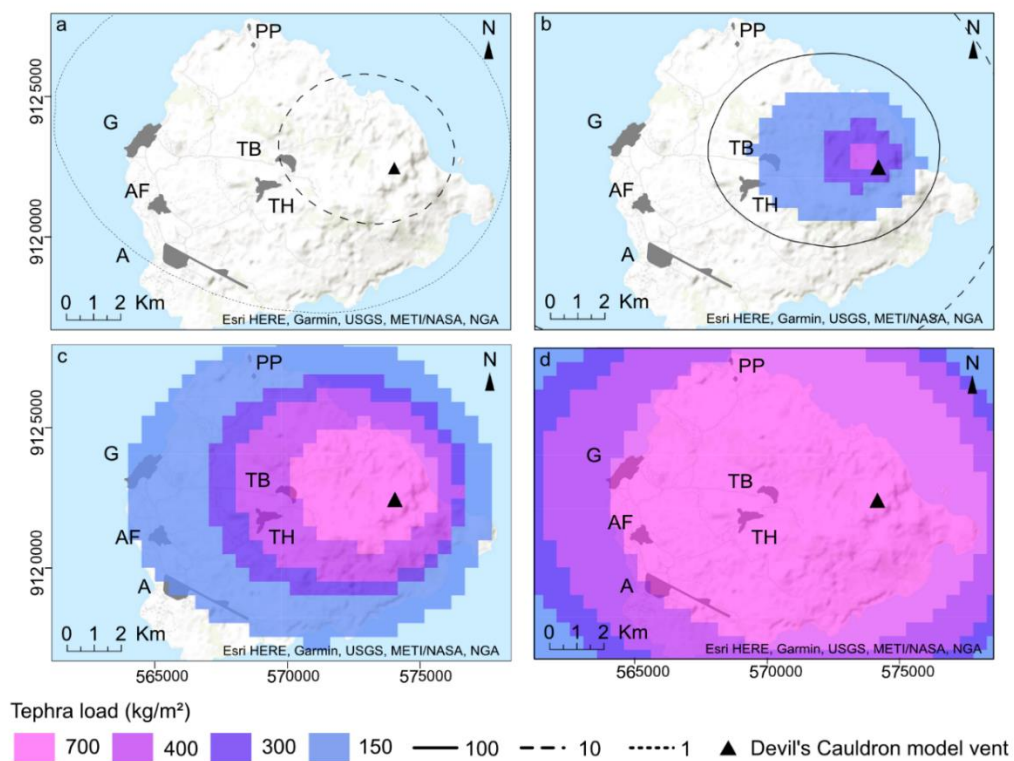


**Fig. 4-4** Tephra ground loads with 50 % probability of exceedance for trachytic event from Devil's Cauldron with plume height a) 6 km, b) 12 km, c) 15 km, d) 19 km. Key locations: A: airport, G: Georgetown, PP: power plant and South Atlantic Relay station, TB: Two Boats, TH: Travellers Hill, AF: US Air Force Base.

**Table 4-4** Highest modelled tephra ground loads at key locations for trachytic model scenarios from Devil's Cauldron (Fig. 4-1), with 10, 50 and 90 % probability of exceedance

| Plume height (km) | Probability (%) | Tephra ground load (kg m$^{-2}$) | | | | | |
|---|---|---|---|---|---|---|---|
| | | Georgetown | Two Boats | Travellers Hill | Airport | USAF Base | Power plant/ South Atlantic Relay station |
| 6 | 10 | 5 | 23 | 17 | 4 | 5 | 8 |
| | 50 | 2 | 12 | 8 | 2 | 2 | 4 |
| | 90 | <1 | 6 | 4 | <1 | <1 | 2 |
| 12 | 10 | 120 | 364 | 290 | 100 | 111 | 143 |
| | 50 | 53 | 194 | 154 | 44 | 50 | 66 |
| | 90 | 14 | 93 | 69 | 14 | 14 | 24 |
| 15 | 10 | 482 | 1413 | 1184 | 472 | 488 | 522 |
| | 50 | 198 | 724 | 577 | 193 | 198 | 242 |
| | 90 | 55 | 329 | 241 | 61 | 55 | 92 |
| 19 | 10 | 1952 | 5238 | 4337 | 1880 | 1943 | 2216 |
| | 50 | 898 | 3167 | 2583 | 926 | 918 | 1067 |
| | 90 | 221 | 1548 | 1192 | 308 | 253 | 350 |
| 27 | 90 | 1250 | 8744 | 6821 | 1890 | 1453 | 2048 |
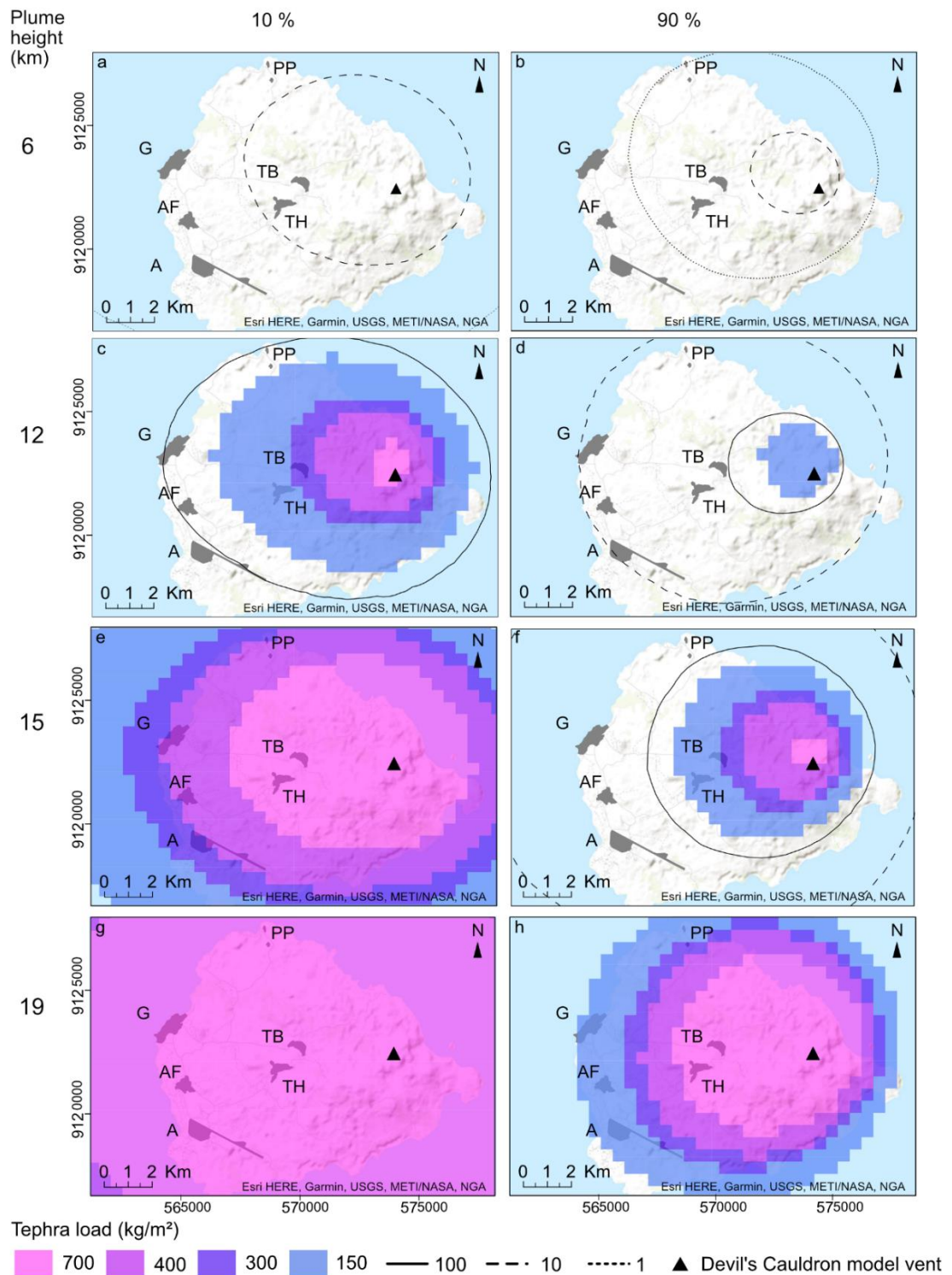
**Fig. 4-5** Tephra ground loads with 10 and 90 % probability of exceedance respectively for trachytic event from Devil's Cauldron with plume height a) and b) 6 km, c) and d) 12 km, e) and f) 15 km, g) and h) 19 km. Key locations: A: airport, G: Georgetown, PP: power plant and South Atlantic Relay station, TB: Two Boats, TH: Travellers Hill, AF: US Air Force Base.

# Chapter 4: Probabilistic hazard analysis for Ascension

For our scenario with a 12 km plume height, results revealed a 50 % probability of tephra loads ≥ 50 kg m$^{-2}$ over the whole island with loads of 154 and 194 kg m$^{-2}$ at Travellers Hill and Two Boats respectively (Fig. 4-4b and Table 4-4). There was a 10 % probability of loads between 100 kg m$^{-2}$ (at the airport) and 364 kg m$^{-2}$ (at Two Boats). For a 90 % probability of exceedance, loads ranged from 14 kg m$^{-2}$ at the airport, Georgetown and the USAF Base to 93 kg m$^{-2}$ at Two Boats (Fig. 4-5c, d and Table 4-4).

Our scenario of a 1–4 hour event with a 15 km plume height produced a 50 % probability of tephra loads ≥ 150 kg m$^{-2}$ in all key locations, with the highest loads at Travellers Hill and Two Boats (724 and 577 kg m$^{-2}$ respectively) (Fig. 4-4c and Table 4-4). There was a 10 % probability of loads ≥ 450 kg m$^{-2}$ across the whole island, with a maximum load at Two Boats of 1413 kg m$^{-2}$ (Fig. 4-5e and Table 4-4). When considering a 90 % probability of exceedance, loads ranged from 55 kg m$^{-2}$ at Georgetown and the USAF Base to 329 kg m$^{-2}$ at Two Boats (Fig. 4-5f and Table 4-4).

For a plume height of 19 km lasting 3–6 hours, we found a 50 % probability of loads ≥ ~ 900 kg m$^{-2}$ and a 10 % probability of loads ≥ 1800 kg m$^{-2}$ at all key locations (Figs. 4-4d, 4-5g and Table 4-4). There was a probability of 90 % of loads ≥ 1100 kg m$^{-2}$ at Two Boats and Travellers Hill, with loads of 200–350 kg m$^{-2}$ elsewhere (Fig. 4-5h and Table 4-4). An event similar to Fogo A (with a plume of 27 km lasting up to 12 hours) resulted in a 90 % probability of loads ≥ 1250 kg m$^{-2}$ across the entire island (Table 4-4).

## Mafic events

### Single phase

For our basaltic scenario with a plume height of 6–10 km lasting 1–6 hours, our scenarios from Sister's Peak resulted in a 50 % probability of the north and west of the island receiving a tephra load ≥ 1 kg m$^{-2}$, with values in key locations ranging from 5 kg m$^{-2}$ at the airport to 87 kg m$^{-2}$ at Two Boats (Fig. 4-6a and Table 4-5). Loads with a 10 % probability of being exceeded ranged from 18 kg m$^{-2}$ at the airport to 231 kg m$^{-2}$ at Two Boats and there was a 90 % probability of loads of 1–24 kg m$^{-2}$ at the key locations (Table 4-5 and Figs. C-2a and C-3a).

When the vent was in the Airport East area, we found a 50 % probability of loads ≤ 1 kg m$^{-2}$ at the power plant and South Atlantic Relay station, with loads at other key locations ranging from 7 kg m$^{-2}$ (at Two Boats) to 203 kg m$^{-2}$ (at the airport) (Fig. 4-6b and Table 4-5). For a 10 % probability of exceedance, we found loads between 3 kg m$^{-2}$ (at the power plant
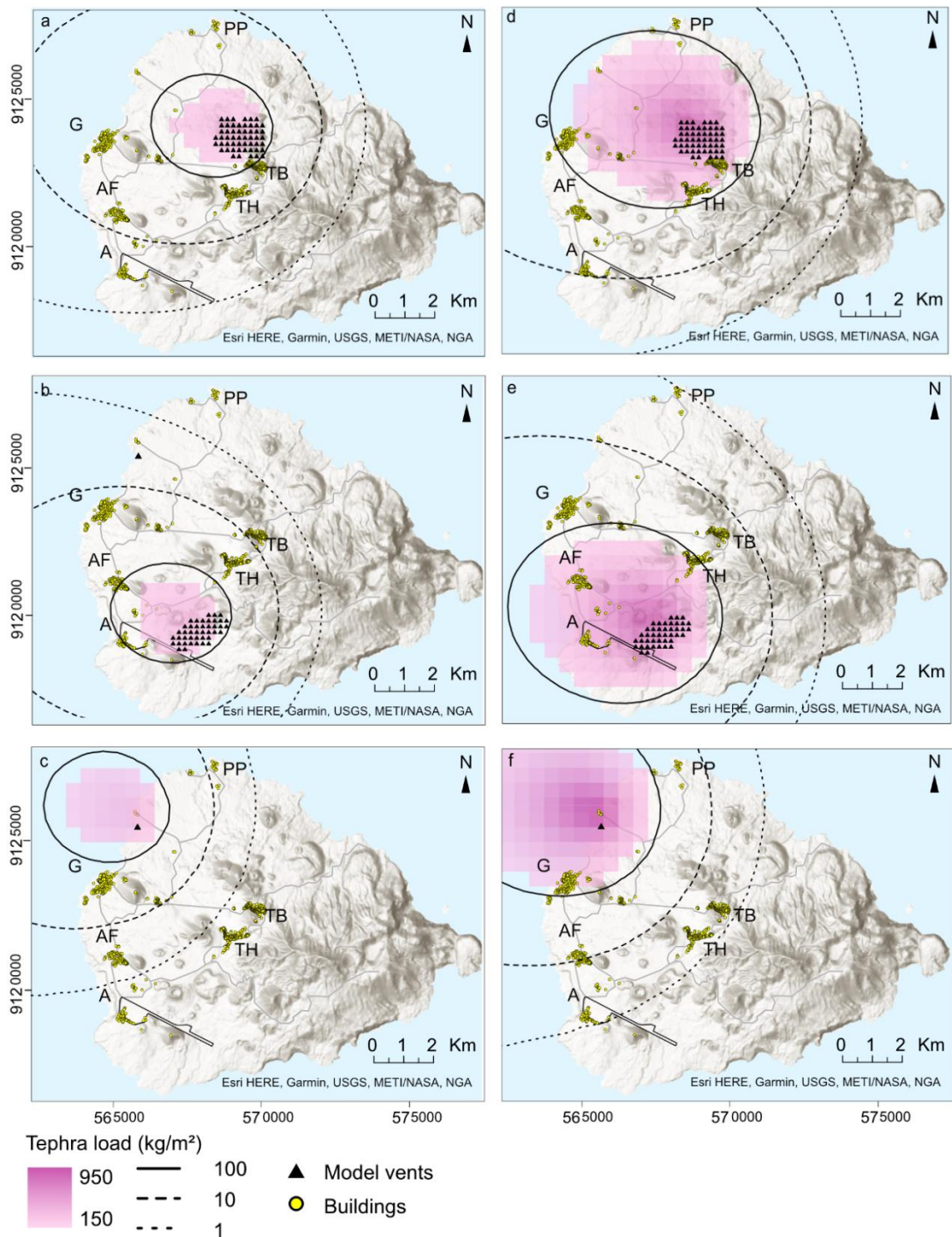
**Fig. 4-6** Tephra ground loads with 50 % probability of exceedance for basaltic events. a), b) and c) show results for one event with 6–10 km plume height, d), e) and f) show results for three events, each with 6–10 km plume height, from Sister's Peak, Airport East and Comfortless Cove respectively. For multiple events, we assume the tephra is not cleared or eroded between each pulse. Key locations: A: airport, G: Georgetown, PP: power plant and South Atlantic Relay station, TB: Two Boats, TH: Travellers Hill, AF: US Air Force Base.

**Table 4-5** Highest modelled tephra ground loads at key locations (Fig. 4-1) for basaltic model scenarios from Sister's Peak, Airport East and Comfortless Cove (Fig. 4-2) with 10, 50 and 90 % probability of exceedance

| Source location | No. of eruptions | Probability (%) | Tephra ground load (kg m$^{-2}$) | | | | | |
|---|---|---|---|---|---|---|---|---|
| | | | Georgetown | Two Boats | Travellers Hill | Airport | USAF Base | Power plant/ South Atlantic Relay station |
| Sister's Peak | 1 | 10 | 119 | 231 | 183 | 18 | 57 | 114 |
| | | 50 | 49 | 87 | 76 | 5 | 21 | 47 |
| | | 90 | 15 | 23 | 24 | 1 | 6 | 15 |
| | 3 | 10 | 298 | 615 | 473 | 46 | 143 | 303 |
| | | 50 | 163 | 290 | 257 | 20 | 74 | 149 |
| | | 90 | 73 | 107 | 107 | 7 | 30 | 73 |
| Airport East | 1 | 10 | 65 | 35 | 206 | 387 | 248 | 3 |
| | | 50 | 27 | 7 | 71 | 203 | 131 | <1 |
| | | 90 | 9 | <1 | 16 | 82 | 51 | <1 |
| | 3 | 10 | 159 | 89 | 546 | 1025 | 634 | 7 |
| | | 50 | 92 | 30 | 240 | 631 | 412 | 2 |
| | | 90 | 46 | 7 | 79 | 354 | 237 | <1 |

**Table 4-5** continued

| Source location | No. of eruptions | Probability (%) | Tephra ground load (kg m$^{-2}$) | | | | | | |
|---|---|---|---|---|---|---|---|---|---|
| | | | Georgetown | Two Boats | Travellers Hill | Airport | USAF Base | Power plant/ South Atlantic Relay station | |
| Comfortless Cove | 1 | 10 | 121 | 6 | 7 | 4 | 19 | 49 | |
| | | 50 | 55 | <1 | <1 | <1 | 5 | 9 | |
| | | 90 | 20 | <1 | <1 | <1 | 1 | 2 | |
| | 3 | 10 | 278 | 19 | 18 | 9 | 47 | 92 | |
| | | 50 | 176 | 2 | 4 | 3 | 21 | 47 | |
| | | 90 | 104 | <1 | <1 | <1 | 9 | 18 | |

and South Atlantic Relay station) and 387 kg m$^{-2}$ (at the airport) (Table 4-5 and Fig. C-2b). There was a 90 % probability of loads of 82 kg m$^{-2}$ at the airport and ≤ 51 kg m$^{-2}$ across the rest of the island (Table 4-5 and Fig. C-3b).

For our scenario of an event from Comfortless Cove, there was a 50 % probability of loads < 1 kg m$^{-2}$ at Travellers Hill, Two Boats and the airport, with Georgetown having the highest load of 55 kg m$^{-2}$ (Fig. 4-6c and Table 4-5). Loads with a 10 % probability of being exceeded ranged from 6 kg m$^{-2}$ at Two Boats to 121 kg m$^{-2}$ at Georgetown (Table 4-5 and Fig. C-2c). For a 90 % probability, Georgetown received a load of 20 kg m$^{-2}$ and loads at the other key locations were ≤ 2 kg m$^{-2}$ (Table 4-5 and Fig. C-3c).

**Multiple phases**

Simulations of three explosive pulses of similar plume height and duration, with no erosion or clearing of the deposit between pulses, showed a 50 % probability of all key locations receiving a tephra load ≥ 20 kg m$^{-2}$ for an event from Sister's Peak, with the highest tephra load of 290 kg m$^{-2}$ at Two Boats (Fig. 4-6d and Table 4-5). There was a 10 % probability of loads of 46–615 kg m$^{-2}$, with all key locations except the airport receiving loads > 100 kg m$^{-2}$ (Table 4-5 and Fig. C-2d). There was a 90 % probability of loads of 7–107 kg m$^{-2}$ with the highest loads at Two Boats and Travellers Hill (Table 4-5 and Fig. C-3d).

For a multi-phase event from Airport East, tephra loads with a 50 % probability of exceedance ranged from 2 kg m$^{-2}$ at the power plant and South Atlantic Relay station to 631 kg m$^{-2}$ at the airport (Fig. 4-6e and Table 4-5). There was a 10 % probability of loads between 7 and 1025 kg m$^{-2}$, with loads > 500 kg m$^{-2}$ at Travellers Hill, the airport and the USAF Base, and a 90 % probability of loads of 354 kg m$^{-2}$ at the airport, 237 kg m$^{-2}$ at the USAF Base and < 80 kg m$^{-2}$ at the other key locations (Table 4-5 and Figs. C-2e and C-3e).

Our multi-phase scenario from Comfortless Cove revealed a 50 % probability of all settlements and infrastructure receiving loads ≥ 2 kg m$^{-2}$. At Georgetown there was a 50 % probability of loads reaching 176 kg m$^{-2}$ (with 10 % and 90 % probabilities of loads of 278 kg m$^{-2}$ and 104 kg m$^{-2}$ respectively) (Table 4-5 and Figs. 4-6f, C-2f and C-3f).

## Discussion

We have modelled a set of defined discrete explosive events of various plume heights from vent locations across Ascension to explore the range of tephra fall hazard footprints and impacts from such short-lived events. These events have been selected based on analogue

eruptions from other small islands together with published geological data to represent a range of possible future explosive events. The results of these models are explicitly linked to the models themselves, and while they are within the range of possible events on Ascension, we make no comment of the likelihood of such events, only commenting on the outputs of the models, assuming such events have occurred. A probabilistic approach to these events allows us to investigate the intrinsically variable nature of volcanic processes and atmospheric conditions which affect tephra dispersal and deposition.

## Modelling assumptions and uncertainties

When considering possible future explosive events on Ascension, we must take account of uncertainties related to our knowledge of past eruptions and make assumptions when selecting input parameters for our model runs, as well as being aware of uncertainties in the model itself.

Gaps in our knowledge of the island's eruptive history and limited preservation of tephra fall deposits meant that it was necessary to use well-studied analogue eruptions to provide input parameters for our modelling. Our approach builds on the outcomes of an expert elicitation and initial modelling work conducted by BGS (Vye-Brown et al. 2019). As detailed in the Methods section, we selected eruptions on São Miguel, Azores which matched the characteristics of Ascension tephra fall deposits. We used these analogue eruptions to calibrate the model, including selecting optimal model parameters covering dispersal and deposition of particles, and to select eruption source parameters (plume height, mass erupted, grain size distribution) for our simulations. We assume that these are representative of explosive events that could occur in future on Ascension.

As discussed in previous sections both Tephra2 and TephraProb have been widely used, and the outputs are now routinely accepted in scenario-based tephra fall hazard assessments. However, as with all models they necessarily simplify physical processes to enable outputs to be obtained within reasonable timescales. Tephra2 solves a two-dimensional version of the advection-diffusion equation and assumes a vertically stratified and horizontally constant wind field. It therefore does not account for small scale atmospheric features such as eddies or temporal changes within the timescale of each wind profile (in our case 6 hours). Tephra2 also assumes that the specified input parameters are representative of average conditions during peak eruptive activity (Connor and Connor, 2006). Hence, events modelled here do not fully reflect the waxing and waning of an ongoing eruption with

multiple explosive phases, as observed at the 2021 eruptions at Soufrière St Vincent (Cole et al. 2024) and Cumbre Vieja, La Palma (Martí et al. 2022), but rather treat each event as a discrete explosion.

## Potential impact of explosive events on Ascension

### Felsic events

Our results revealed that short-lived explosive events on Ascension could result in widespread tephra fall, potentially impacting the island's residents and key power, transport and communications infrastructure. Even a small felsic eruption from Devil's Cauldron, with a 6 km plume height, would impact the airport and many roads with 50 % probability of loads ≥ 1 kg m$^{-2}$ (~ 1 mm depth, depending on deposit density) across the island (Fig. 4-4a and Table 4-1). A 12 km plume could additionally affect power and communications with our results showing a 90 % probability of loads ≥ 10 kg m$^{-2}$ across the majority of the island (Fig. 4-5d) and a 50 % probability of loads ≥ 150 kg m$^{-2}$ at Two Boats and Travellers Hill (Fig. 4-4b and Table 4-4). Previous studies have shown that, if roofs are not cleared of tephra, these loads can be sufficient to cause collapse in weak or long span structures (Table 4-1 and Jenkins et al. 2014). Larger volume events could cause widespread disruption and even collapse of good quality roofs. For a 15 km plume, we found a 50 % probability of loads ≥ 150 kg m$^{-2}$ at all key locations. The highest loads were at Two Boats and Travellers Hill, with a 90 % probability of loads ≥ 150 kg m$^{-2}$, a 50 % probability of loads sufficient to cause collapse of good quality metal and tile roofs (≥ 400 kg m$^{-2}$) and a 10 % probability of loads that have the potential to collapse even the strongest roofs (≥ 700 kg m$^{-2}$) (Table 4-1, Figs4- 4c, 4-5e,f). When considering a 19 km plume height, these impacts could be far greater and more widespread, with a 50 % probability of loads ≥ 700 kg m$^{-2}$ (Figs. 4-4d, 4-5h), necessitating extensive clean-up operations (Hayes et al. 2015).

### Mafic events

Some of the recent deposits on Ascension came from monogenetic basaltic eruptions (Fig. 4-1) and probabilistic spatial density distributions using mapped vent locations have identified areas where future vents are most likely to occur (Vye-Brown et al. 2019). However it is not possible to assess the temporal relationship between these vents because of limited deposit preservation on the island and hence we are unable to assess vent opening probability. This is a common issue on small volcanic Islands, our simulations therefore took account of the uncertainty in the source location of a future eruption by

using a grid of equally probable vent locations within the most recently active areas (Fig. 4-2). This approach reduces the likelihood of overestimating loads proximal to the source as the results produced a smaller area where there is 90 % probability of tephra fall loading sufficient to cause roof collapse ($\geq$ 100 kg m$^{-2}$). It also better highlights the full extent of the area that could be impacted, with a larger area having a 10 % probability of tephra fall loading $\geq$ 100 kg m$^{-2}$. For one basaltic event with a 6–10 km plume height, we found a 50 % probability of tephra loads > 1 kg m$^{-2}$ across the west side of the island, a deposit that could impact roads. In two of the three scenarios the airport also received similar tephra loads (Fig. 4-6 a-c). There was a 10 % probability of loads that may cause roof collapse ($\geq$ 100 kg m$^{-2}$) with Georgetown, Two Boats, Travellers Hill, the power plant and South Atlantic Relay station impacted by an event from Sister's Peak, and Travellers Hill, the USAF Base and the airport impacted by an event from Airport East. Georgetown was also impacted by an event from Comfortless Cove (Fig. C-2 a-c).

The 2021 eruption of Soufrière St Vincent showed that build-up of tephra from multiple small events can create substantial hazard, particularly near to source if clean-up is not possible between eruptive events (Miller et al. 2022). Multiple pulses over a timescale of weeks were also seen during the eruption of Cumbre Vieja, La Palma in 2021 (Bonadonna et al. 2022; Martí et al. 2022), showing the importance of considering this type of scenario. For our multi-phase events, we assumed that tephra was not cleared from roofs between pulses, a worst-case scenario. For three pulses from Sister's Peak, we found a 50 % probability of tephra loads that could lead to collapse of poor quality and long span roofs ($\geq$ 150 kg m$^{-2}$) in Georgetown, Travellers Hill and Two Boats (Fig. 4-7a). Three pulses from Airport East could lead to collapse of these types of roof in Travellers Hill, as well as collapse of metal and tile roofs around the airport and at the USAF Base (loads $\geq$ 400 kg m$^{-2}$) (Fig. 4-7b). For events from Comfortless Cove, deposition was mainly over the sea, although there was a 50 % probability that poor quality and long span roofs may be vulnerable in Georgetown, if tephra was not cleared (Fig. 4-7c). For three events from Sister's Peak or Airport East, there was a 10 % probability of loads that could collapse good quality metal and tile roofs ($\geq$ 400 kg m$^{-2}$) and for three events from any of our source areas, we found a 90 % probability of loads that could cause collapse of poor-quality roofs ($\geq$ 100 kg m$^{-2}$) (Figs. C-4 and C-5 Table 4-1).

In this work, we have only considered the impacts of tephra fall but within a few hundred metres of a vent, ballistics can also cause serious injury and damage to infrastructure

(Fitzgerald et al. 2020; Massaro et al. 2022). This should be investigated, given the proximity of the airport, Two Boats and Travellers Hill to the most recent eruptive areas. Airborne ash could also lead to health issues (e.g. IVHHN 2021; Eychenne et al. 2022; Stewart et al. 2022) and the plume could have a substantial impact on airspace, particularly for larger eruptions (e.g. Witham et al. 2012; Hirtl et al. 2020; Mastin et al. 2021).
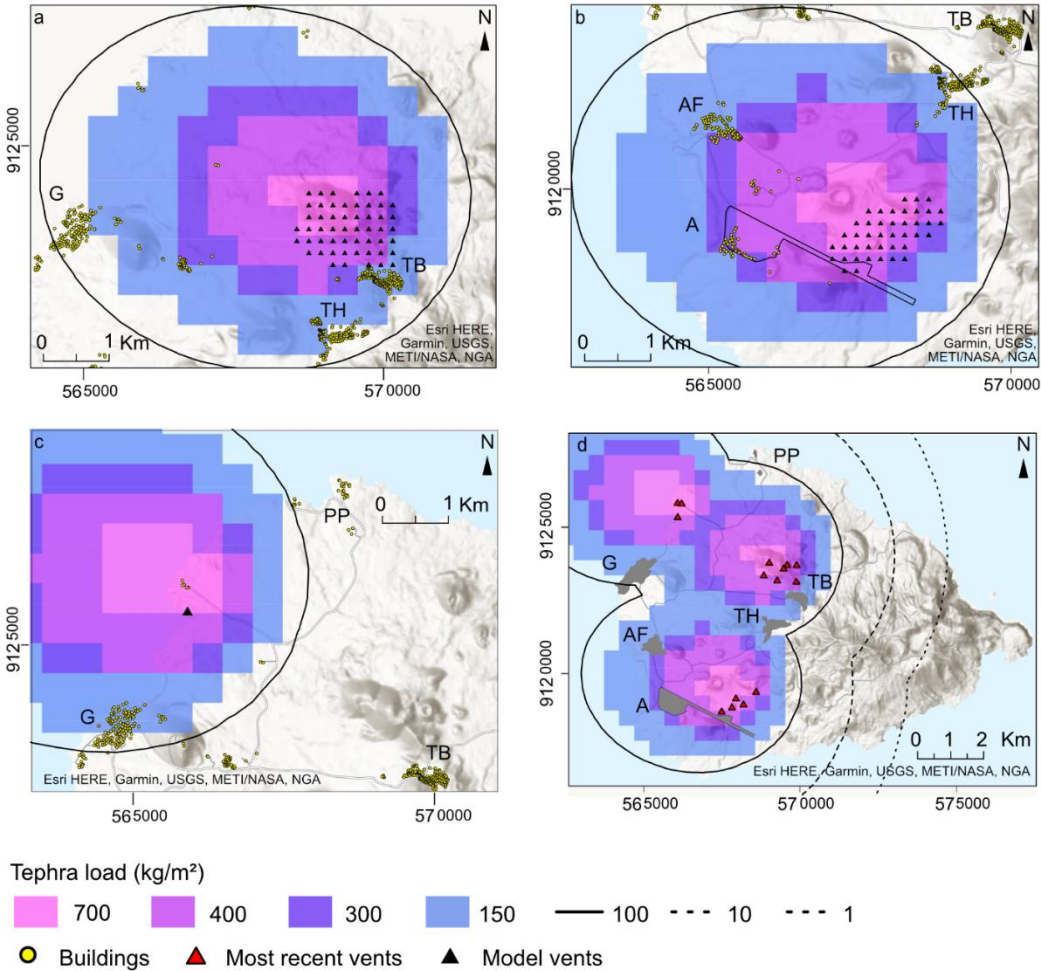


**Fig. 4-7** Tephra ground loads likely to cause roof collapse (> 150 kg m$^{-2}$) with 50 % probability of exceedance for three basaltic eruptions, each with 6–10 km plume from a) Sister's Peak, b) Airport East and c) Comfortless Cove, d) one of Sister's Peak, Airport East and Comfortless Cove. Contours show likely collapse loads for different roof types (Table 4-1). We assume the tephra is not cleared or eroded between each pulse. Key locations: A: airport, G: Georgetown, PP: power plant and South Atlantic Relay station, TB: Two Boats, TH: Travellers Hill, AF: US Air Force Base.

## Conclusion

Small volcanic islands can be particularly susceptible to the impacts of tephra fall, given their size and potential proximity to the vent. Using Ascension as a case study, we carried out a probabilistic hazard analysis to quantify tephra fall hazard and discuss potential impacts on infrastructure from a suite of defined eruptive events. As eruptive deposits are poorly preserved on the island, we combined existing geological data from Ascension with analogue eruptions from São Miguel, Azores to model a wide range of possible future short-lived explosive events of both felsic and mafic composition.

Perhaps unsurprisingly, our felsic model scenarios revealed there could be significant impacts on the island, ranging from a few millimetres of tephra fall potentially causing disruption to transport and infrastructure (for a 6 km plume), to widespread impacts including damage to key infrastructure and buildings, including potential collapse of roofs (from a 15–19 km plume).

There are numerous mafic monogenetic vents across the north, west and south of the island, but insufficient data to carry out probabilistic vent susceptibility modelling. We have therefore taken account of vent uncertainty by modelling basaltic eruptions from the monogenetic volcanic field using a grid of possible vent locations within the most recently active areas. Results reveal that for an explosive event with a 6–10 km plume, there was a 50 % probability that tephra fallout from a single pulse would disrupt the airport and impact roads across the west side of the island. For our scenarios comprising three distinct explosive phases, there was a 50 % probability of loads that could lead to roof collapse in settlements close to the vent, assuming that roofs are not cleared between phases. In nearly all of our mafic scenarios, the airport was impacted while the eastern side of the island was least likely to be disrupted, given prevailing wind to the west.

Our results are not predictive as we have no data pertaining to the likelihood of an eruption, its location, type or size, but they clearly show, given the modelling of events which may be possible on Ascension, that consideration should be given to the impact from tephra fall hazard on key infrastructure. Our approach is relevant to other low-data volcanic islands where it can assist in planning for possible future eruptions, by identifying areas most susceptible to tephra loading.

## Declarations

### Conflicts of interest/Competing interests

The authors declare they have no conflicts of interest or competing interests.

### Availability of data and material

Relevant data are available in the tables or Supplementary information.

## References

Alatorre-Ibargüengoitia MA, Hernández-Urbina K, Ramos-Hernández SG (2021) Long- and short-term volcanic hazard assessment of El Chichón Volcano (Mexico) through Bayesian inference. Nat Hazards 106:1011–1035. https://doi.org/10.1007/s11069-021-04506-1

Aravena A, Bevilacqua A, Neri A, et al (2023) Scenario-based probabilistic hazard assessment for explosive events at the San Salvador volcanic complex, El Salvador. J Volcanol Geoth Res 438:107809. https://doi.org/10.1016/j.jvolgeores.2023.107809

Biass S, Bonadonna C, Connor LJ, Connor CB (2016) TephraProb: a Matlab package for probabilistic hazard assessments of tephra fallout. J Appl Volcanology 5:10. https://doi.org/10.1186/s13617-016-0050-5

Blake DM, Deligne NI, Wilson TM, et al (2017) Investigating the consequences of urban volcanism using a scenario approach II: Insights into transportation network damage and functionality. J Volcanol Geotherm Res 340:92–116. https://doi.org/10.1016/j.jvolgeores.2017.04.010

Bonadonna C, Connor CB, Houghton BF, et al (2005) Probabilistic modeling of tephra dispersal: Hazard assessment of a multiphase rhyolitic eruption at Tarawera, New Zealand. J Geophys Res Solid Earth 110:B03203. https://doi.org/10.1029/2003JB002896

Bonadonna C, Pistolesi M, Biass S, et al (2022) Physical characterization of long-lasting hybrid eruptions: the 2021 Tajogaite eruption of Cumbre Vieja (La Palma, Canary Islands). J Geophys Res Solid Earth 127:e2022JB025302. https://doi.org/10.1029/2022JB025302

Booth B, Croasdale R, Walker GPL (1978) A quantitative study of five thousand years of volcanism on Sao Miguel, Azores. Philos. Trans. Royal Soc. A 288:271–319. https://doi.org/10.1098/rsta.1978.0018

Burgos V, Jenkins SF, Bono Troncoso L, et al (2023) Identifying analogues for data-limited volcanoes using hierarchical clustering and expert knowledge: a case study of Melimoyu (Chile). Front Earth Sci 11:1144386. https://doi.org/10.3389/feart.2023.1144386

Carey S, Sigurdsson H (1989) The intensity of plinian eruptions. Bull Volcanol 51:28–40. https://doi.org/10.1007/BF01086759

Cashman K, Biggs J (2014) Common processes at unique volcanoes - a volcanological conundrum. Front Earth Sci 2:28. https://doi.org/10.3389/feart.2014.00028

Chamberlain K, Barclay J, Preece K, et al (2016) Origin and evolution of silicic magmas at ocean islands: perspectives from a zoned fall deposit on Ascension Island, South Atlantic. J Volcanol Geotherm Res 327:349–360. https://doi.org/10.1016/j.jvolgeores.2016.08.014

Chamberlain K, Barclay J, Preece K, et al (2020) Deep and disturbed: conditions for formation and eruption of a mingled rhyolite at Ascension Island, south Atlantic. Volcanica 3:139–153. https://doi.org/10.30909/vol.03.01.139153

# Chapter 4: Probabilistic hazard analysis for Ascension

Chamberlain K, Barclay J, Preece K, et al (2019) Lower crustal heterogeneity and fractional crystallization control evolution of small-volume magma batches at ocean island volcanoes (Ascension Island, South Atlantic). J Petrol 60:1489–1522. https://doi.org/10.1093/petrology/egz037

Connor C, Bebbington M, Marzocchi W (2015) Probabilistic volcanic hazard assessment. In: Sigurdsson H, Houghton B, McNutt S, Rymer H (eds) The Encyclopedia of Volcanoes, 2nd edn. Elsevier, Oxford, pp 897–910

Connor LJ, Connor CB (2006) Inversion is the key to dispersion: understanding eruption dynamics by inverting tephra fallout. In: Mader H, Coles; SG, Connor; CB, Connor LJ (eds) Statistics in Volcanology. Geological Society, London, pp 231–242. https://doi.org/10.1144/IAVCEI001.18

Connor CB, Connor L, Germa A, et al (2019) How to use kernel density estimation as a diagnostic and forecasting tool for distributed volcanic vents. Statistics in Volcanology 4:1–25. https://doi.org/10.5038/2163-338X.4.3

Crummy JM, Savov IP, Loughlin SC, et al (2019) Challenges of determining frequency and magnitudes of explosive eruptions even with an unprecedented stratigraphy. J Appl Volcanology 8:3. https://doi.org/10.1186/s13617-019-0083-7

Davies BV, Brown RJ, Barclay J, et al (2021) Rapid eruptive transitions from low to high intensity explosions and effusive activity: insights from textural analysis of a small-volume trachytic eruption, Ascension Island, South Atlantic. Bull Volcanol 83:58. https://doi.org/10.1007/S00445-021-01480-1

Degruyter W, Bonadonna C (2012) Improving on mass flow rate estimates of volcanic eruptions. Geophys Res Lett 39: L16308. https://doi.org/10.1029/2012GL052566

Eychenne J, Gurioli L, Damby D, et al (2022) Spatial distribution and physicochemical properties of respirable volcanic ash from the 16–17 August 2006 Tungurahua eruption (Ecuador), and alveolar epithelium response in-vitro. Geohealth 6:e2022GH000680. https://doi.org/10.1029/2022GH000680

Ferreira T, Gomes A, Gaspar JL, Guest J (2015) Distribution and significance of basaltic eruptive centres: São Miguel, Azores. In: Gaspar JL, Guest JE, Duncan AM, et al. (eds) Volcanic geology of Sao Miguel Island (Azores Archipelago). Geol Soc Lond Mem 44, pp 135–146. https://doi.org/10.1144/M44.10

Fitzgerald RH, Kennedy BM, Gomez C, et al (2020) Volcanic ballistic projectile deposition from a continuously erupting volcano: Yasur Volcano, Vanuatu. Volcanica 3:183–204. https://doi.org/10.30909/vol.03.02.183204

Gallant E, Cole L, Connor C, et al (2021) Modelling eruptive event sources in distributed volcanic fields. Volcanica 4:325–343. https://doi.org/10.30909/vol.04.02.325343

Gaspar JL, Guest JE, Queiroz G, et al (2015) Eruptive frequency and volcanic hazards zonation in São Miguel Island, Azores. In: Gaspar JL, Guest JE, Duncan AM, et al. (eds) Volcanic geology of Sao Miguel Island (Azores Archipelago). Geol Soc Lond Mem 44, pp 155–166. https://doi.org/10.1144/M44.12

Guest JE, Gaspar JL, Cole PD, et al (1999) Volcanic geology of Furnas Volcano, São Miguel, Azores. J Volcanol Geotherm Res 92:1–29. https://doi.org/10.1016/S0377-0273(99)00064-5

Hayes JL, Biass S, Jenkins SF, et al (2022) Integrating criticality concepts into road network disruption assessments for volcanic eruptions. J Appl Volcanology 11:8. https://doi.org/10.1186/S13617-022-00118-X

Hersbach H, Bell B, Berrisford P, et al (2018) ERA5 hourly data on pressure levels from 1979 to present. Copernicus Climate Change Service (C3S) Climate Data Store (CDS). https://doi.org/10.24381/cds.bd0915c6

Hersbach H, Bell B, Berrisford P, et al (2020) The ERA5 global reanalysis. Q J R Meteorol Soc 146:1999–2049. https://doi.org/10.1002/qj.3803

Hirtl M, Arnold D, Baro R, et al (2020) A volcanic-hazard demonstration exercise to assess and mitigate the impacts of volcanic ash clouds on civil and military aviation. Nat Hazards Earth Syst Sci 20:1719–1739. https://doi.org/10.5194/NHESS-20-1719-2020

Hone DWE, Mahony SH, Sparks RSJ, Martin KT (2007) Cladistic analysis applied to the classification of volcanoes. Bull Volcanol 70:203–220. https://doi.org/10.1007/s00445-007-0132-7

IVHHN (2021) The health hazards of volcanic ash: a guide for the public. http://ivhhn.org/images/pamphlets/Health_Guidelines_English_WEB.pdf. Accessed 2 May 2023

Jenkins SF, Spence RJS, Fonseca JFBD, et al (2014) Volcanic risk assessment: quantifying physical vulnerability in the built environment. J Volcanol Geotherm Res 276:105–120. https://doi.org/10.1016/j.jvolgeores.2014.03.002

Jenkins SF, Wilson T, Magill C, et al (2015) Volcanic ash fall hazard and risk. In: Loughlin SC, Sparks RSJ, Brown SK, et al. (eds) Global volcanic hazards and risk. Cambridge University Press, Cambridge, pp 173–221

Jenkins SF, Phua M, Warren JF, et al (2020) Reconstructing eruptions from historical accounts: Makaturing c. 1765, Philippines. J Volcanol Geotherm Res 404:107022. https://doi.org/10.1016/j.jvolgeores.2020.107022

Jicha BR, Singer BS, Valentine MJ (2013) $^{40}Ar/^{39}Ar$ geochronology of subaerial Ascension Island and a re-evaluation of the temporal progression of basaltic to rhyolitic volcanism. J Petrol 54:2581–2596. https://doi.org/10.1093/petrology/egt058

Kueppers U, Pimentel A, Ellis B, et al (2019) Biased volcanic hazard assessment due to incomplete eruption records on ocean islands: an example of Sete Cidades Volcano, Azores. Front Earth Sci, 7, 122. https://doi.org/10.3929/ETHZ-B-000346887

Le Corvec N, Bebbington MS, Lindsay JM, McGee LE (2013) Age, distance, and geochemical evolution within a monogenetic volcanic field: analyzing patterns in the Auckland Volcanic Field eruption sequence. Geochem, Geophys, Geosys 14:3648–3665. https://doi.org/10.1002/ggge.20223

Ligot N, Guevara A, Delmelle P (2022) Drivers of crop impacts from tephra fallout: insights from interviews with farming communities around Tungurahua volcano, Ecuador. Volcanica 5:163–181. https://doi.org/10.30909/vol.05.01.163181

Magill C, Wilson T, Okada T (2013) Observations of tephra fall impacts from the 2011 Shinmoedake eruption, Japan. Earth Planets Space 65:677–698. https://doi.org/10.5047/eps.2013.05.010

Martí J, Becerril L, Rodríguez A (2022) How long-term hazard assessment may help to anticipate volcanic eruptions: the case of La Palma eruption 2021 (Canary Islands). J Volcanol Geotherm Res 431:107699. https://doi.org/10.1016/j.jvolgeores.2022.107669

Massaro S, Rossi E, Sandri L, et al (2022) Assessing hazard and potential impact associated with volcanic ballistic projectiles: the example of La Soufrière de Guadeloupe volcano (Lesser Antilles). J Volcanol Geotherm Res 423:107453. https://doi.org/10.1016/j.jvolgeores .2021.107453

Mastin L, Pavolonis M, Engwell S, et al (2021) Progress in protecting air travel from volcanic ash clouds. Bull Volcanol 84:9. https://doi.org/10.1007/S00445-021-01511-X

Marzocchi W, Newhall C, Woo G (2012) The scientific management of volcanic crises. J Volcanol Geotherm Res 247–248:181–189. https://doi.org/10.1016/j.jvolgeores.2012.08.016

Miller VL, Joseph EP, Sapkota N, Szarzynski J (2022) Challenges and opportunities for risk management of volcanic hazards in small-island developing states. Mt Res Dev 42:D22–D31. https://doi.org/10.1659/MRD-JOURNAL-D-22-00001.1

Minshull TA, Ishizuka O, Garcia-Castellanos D (2010) Long-term growth and subsidence of Ascension Island: constraints on the rheology of young oceanic lithosphere. Geophys Res Lett 37:L23306. https://doi.org/10.1029/2010GL045112

Newhall C, Hoblitt R (2002) Constructing event trees for volcanic crises. Bull Volcanol 64:3–20. https://doi.org/10.1007/s004450100173

Newhall CG, Self S (1982) The volcanic explosivity index (VEI) an estimate of explosive magnitude for historical volcanism. J Geophys Res 87:1231. https://doi.org/10.1029/JC087iC02p01231

Pensa A, Cas R, Giordano G, et al (2015) Transition from steady to unsteady Plinian eruption column: the VEI 5, 4.6 ka Fogo A Plinian eruption, São Miguel, Azores. J Volcanol Geotherm Res 305:1–18. https://doi.org/10.1016/j.jvolgeores.2015.09.012

Preece K, Barclay J, Brown RJ, et al (2021) Explosive felsic eruptions on ocean islands: a case study from Ascension Island (South Atlantic). J Volcanol Geotherm Res 416:107284. https://doi.org/10.1016/j.jvolgeores.2021.107284

Preece K, Mark DF, Barclay J, et al (2018) Bridging the gap: [40]Ar/[39]Ar dating of volcanic eruptions from the "Age of Discovery." Geology 46:1035–1038. https://doi.org/10.1130/G45415.1

Scollo S, Tarantola S, Bonadonna C, Coltelli M, Saltelli A (2008) Sensitivity analysis and uncertainty estimation for tephra dispersal models. J Geophys Res, 113, B06202. https://doi.org/10.1029/2006JB004864

Stewart C, Damby DE, Horwell CJ, et al (2022) Volcanic air pollution and human health: recent advances and future directions. Bull Volcanol 84:11. https://doi.org/10.1007/s00445-021-01513-9

Tadini A, Roche O, Samaniego P, et al (2021) Eruption type probability and eruption source parameters at Cotopaxi and Guagua Pichincha volcanoes (Ecuador) with uncertainty quantification. Bull Volcanol 83: 35. https://doi.org/10.1007/s00445-021-01458-z

Tennant E, Jenkins SF, Winson A, et al (2021) Reconstructing eruptions at a data limited volcano: a case study at Gede (West Java). J Volcanol Geotherm Res 418:107325. https://doi.org/10.1016/.jvolgeores.2021.107325

Tierz P, Loughlin SC, Calder ES (2019) VOLCANS: an objective, structured and reproducible method for identifying sets of analogue volcanoes. Bull Volcanol 81:76. https://doi.org/10.1007/s00445-019-1336-3

Vye-Brown, C., Brown, R., Crummy, J., Engwell, S., & Loughlin, S. (2019). Volcanic history and future hazards affecting Ascension Island. Open File Report OFR/19/026. British Geological Survey, Edinburgh

Walker GPL, Croasdale R (1970) Two Plinian-type eruptions in the Azores. J Geol Soc London 127:17–55. https://doi.org/10.1144/gsjgs.127.1.0017

Wardman, J, Sword-Daniels V, Stewart C, Wilson T (2012) Impact assessment of the May 2010 eruption of Pacaya volcano, Guatemala. GNS Science Report 2012/09. https://ir.canterbury.ac.nz/handle/10092/10563. Accessed 5 July 2023

Warwick R, Williams-Jones G, Kelman M, Witter J (2022) A scenario-based volcanic hazard assessment for the Mount Meager Volcanic Complex, British Columbia. J Appl Volcanology 11:5. https://doi.org/10.1186/s13617-022-00114-1

Wild AJ, Wilson TM, Bebbington MS, et al (2019) Probabilistic volcanic impact assessment and cost-benefit analysis on network infrastructure for secondary evacuation of farm livestock: a case study from the dairy industry, Taranaki, New Zealand. J Volcanol Geotherm Res 387:106670. https://doi.org/10.1016/j.jvolgeores.2019.106670

Wilson G, Wilson TM, Deligne NI, et al (2017) Framework for developing volcanic fragility and vulnerability functions for critical infrastructure. J Appl Volcanology 6:14. https://doi.org/10.1186/s13617-017-0065-6

Wilson G, Wilson TM, Deligne NI, Cole JW (2014) Volcanic hazard impacts to critical infrastructure: a review. J Volcanol Geotherm Res 286:148–182. https://doi.org/10.1016/j.jvolgeores.2014.08.030

Winstanley R (2020) A preliminary investigation into the growth of the Sisters scoria cone complex, Ascension Island. M.Sc. Thesis, University of Durham

Witham C, Webster H, Hort M, et al (2012) Modelling concentrations of volcanic ash encountered by aircraft in past eruptions. Atmos Environ 48:219–229. https://doi.org/10.1016/j.atmosenv.2011.06.073

# Chapter 5

# From probabilistic tephra load modelling to vulnerability assessment: a GIS tool to identify buildings susceptible to roof collapse

Sara Osman[1], Julia Crummy[2], Stephen Carver[3] and Mark Thomas[1]

[1] University of Leeds, School of Earth and Environment, Woodhouse, Leeds LS2 9JT, UK

[2] British Geological Survey, The Lyell Centre, Research Avenue South, Edinburgh EH14 4AP, UK

[3] University of Leeds, School of Geography, Woodhouse, Leeds LS2 9JT, UK

The Appendix for this paper is presented as Appendix D.

## Abstract

Following large explosive eruptions, tephra fall can severely impact buildings proximal to the source and roof collapse may occur when the tephra load exceeds a building's failure load. However, the hazard may be reduced when tephra slides off pitched roofs. By understanding which buildings are vulnerable to failure, mitigation measures can be prioritised. We have developed a GIS tool for ArcGIS Pro and QGIS that estimates vulnerability to roof collapse under tephra fall loads at an individual building scale. The tool combines modelled tephra fall loads on the ground with building characteristics (location, roof material and pitch, building condition and long or short span construction) and uses published data on tephra sliding and typical collapse loads from post-eruption surveys to estimate a Fail fraction, $F$. This is the ratio of tephra fall load to roof failure load, where for values of $F \geq 1$ the roof is potentially vulnerable to collapse. The tool can easily be run multiple times with different modelled tephra loadings to assess the impact of a range of eruption scenarios.

## Introduction

Tephra fall is a key hazard to consider when assessing the impact of explosive volcanic eruptions on communities and infrastructure. Buildings proximal to the source can be impacted by deposits a few centimetres thick, which can clog heating and ventilation equipment, dislodge gutters and damage other non-structural elements (Wilson et al. 2012; Hampton et al. 2015). When the deposit is thicker, structural damage may occur including buckling or collapse of roof materials and supports (Hayes et al. 2019; Blong, 2003; Spence et al. 1996; Jenkins et al. 2014).

Roof or building collapse because of tephra fall is estimated to have resulted in > 2400 deaths in the past 500 years, including > 300 fatalities following the eruption of Pinatubo, Philippines in 1991 and 100 deaths during the 1982 eruption of El Chichón, Mexico (Brown et al. 2017). Exposure of communities is increasing as the global population grows and in 2015 it was estimated that 59 million people lived within 10 km of a Holocene volcano (one that has erupted in the last ~ 11 ka), double the number compared to forty years previously (Freire et al. 2019). In order to assess impacts, we must understand both the additional load resulting from tephra fall and whether a roof's failure load will be exceeded.

Tephra fall load on a building depends on the interplay of many factors including distance from the source, size and intensity of the eruption and weather conditions, as wind velocity and precipitation influence tephra transport and deposition. Post deposition, deposit sliding on pitched roofs may reduce the load, assuming tephra is removed from the roof rather than being redistributed (Osman et al. 2023). The deposit will cause structural damage if it exceeds the failure load for the roof and this varies with the type of construction and the condition of the building (Spence et al. 2005; Torres-Corredor et al. 2017; Thouret et al. 2022). If we can identify buildings that may be susceptible to collapse under tephra loading, they can be prioritised for mitigation measures. These might include roof clearing during and after an eruption (Hayes et al. 2015; Magill et al. 2013) and longer-term interventions such as strengthening roof supports or increasing roof pitches to enable deposit sliding (Zuccaro and Leone 2012).

To address this issue, we have developed a tool for GIS users which enables susceptibility to roof collapse under tephra fall loading to be assessed for individual buildings and different eruption scenarios. Building data (location, roof material and pitch, building condition and long or short span construction) are used to estimate vulnerability to collapse at a building scale. The tool uses tephra load on the ground as a starting point and this is typically the output from a tephra dispersion model (sometimes presented as tephra thickness by assuming a constant deposit density) (e.g. Biass et al. 2016b; Barker et al. 2019). The tool takes this output in raster file format (i.e. gridded cells with the value of each cell representing tephra load on the ground) and interpolates tephra load on the ground at a building's location for the eruption scenario under consideration. It then calculates the fraction of that load expected to remain on the roof, taking account of tephra sliding on pitched roofs. It assesses the collapse load for the roof, by adjusting a typical failure load for that roof type (taken from published post-eruption field surveys) to reflect individual building characteristics. Finally, it calculates a Fail fraction, $F$, as the ratio of tephra fall load to roof failure load, where for values of $F \geq 1$ the roof is potentially vulnerable to collapse. The tool can be run multiple times to assess impacts for a range of eruption scenarios.

To show how the tool can be used, we present a theoretical case study of Ascension Island, a volcanically active UK Overseas Territory in the South Atlantic. As is typical for small islands, buildings across Ascension could be impacted by tephra fall loads during an explosive eruption and our tool can assist in planning for potential future events. Our case study (described in more detail in a later section) takes a scenario where tephra fall loads

may be high enough to cause building failure and uses synthetic building characteristic data (roof material, pitch, condition, long- or short-span). This enables us to showcase key aspects of the tool. We utilise typical roof failure loads derived from mean values for good quality roofs based on post-eruption field surveys (Jenkins et al. 2014). However, the tool is flexible and alternative values can be used depending on local circumstances.

## The tool

### Overview

The GIS tool and full instructions can be downloaded from https://doi.org/10.5518/1458. It is available as an ArcGIS Pro toolbox and two QGIS models. A layer file is also provided to symbolise the map output. GIS requirements and details of the processing steps are given in Appendix D. The steps in the tool are also summarised in Fig. 5-1. The user must first select which version of the tool to use for the eruption scenario being considered: coarse- or fine-grained tephra (described further in the Input data section). The decision should be based on knowledge of the eruptive history of the volcano of interest.
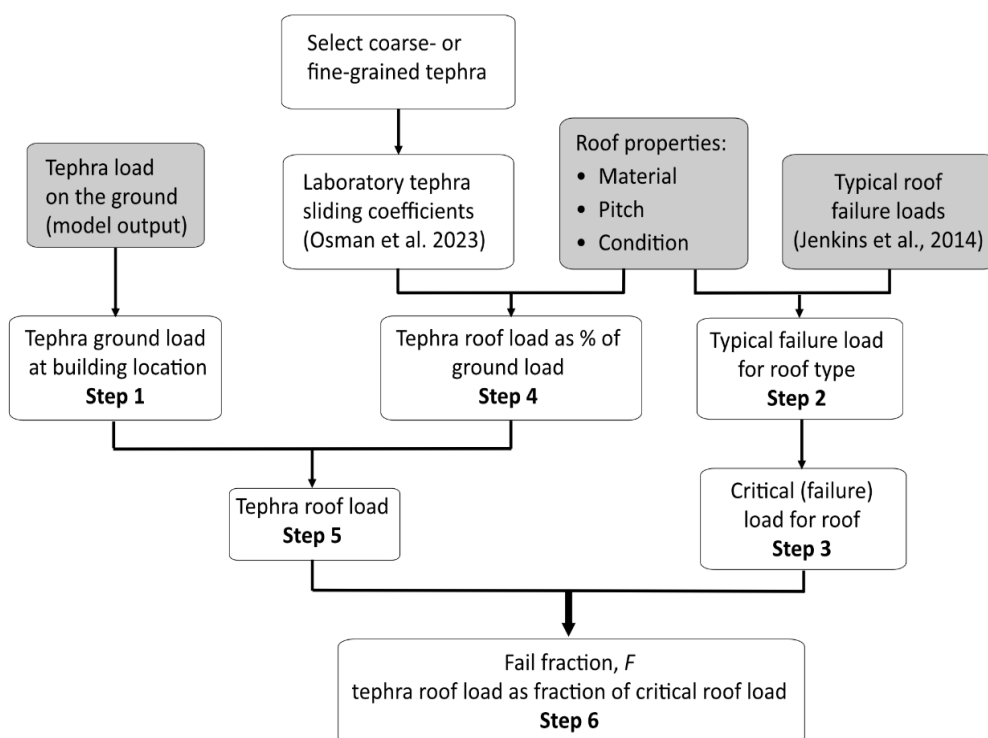


**Fig. 5-1** Overview of the GIS tool steps to calculate Fail fraction for a roof under tephra fall loading. Tool inputs are shaded

As inputs the tool takes:

- A raster file of tephra loads on the ground ('tephra raster').
- A vector file of building point data including roof characteristics ('building data').
- A table of typical failure loads by roof material ('typical loads').

The key processing steps are:

1. Estimate the tephra load on the ground at each building location.
2. Identify the typical collapse load for each building based on its roof material.
3. Calculate the expected failure load for each building based on its construction (short or long span) and condition.
4. Calculate what fraction of tephra load on the ground is expected to remain on the roof.
5. Calculate the expected tephra load on the roof.
6. Calculate the Fail fraction, $F$ (tephra load on the roof as a fraction of the roof failure load).

The output is a map of the building points, symbolised by the layer file to show the Fail fraction value for each building.

## Input data

### Tephra loads

The tool requires a raster file of tephra load on the ground, which is typically the output from a tephra transport and dispersion model (e.g. Barsotti et al. 2008; Biass et al. 2016b). Probabilistic hazard analyses (PHA), which combine results from many simulations, take account of uncertainties in source and atmospheric conditions and output probabilistic estimates of tephra loads. PHA results can be presented as exceedance probability maps i.e. tephra loads on the ground for a given probability of exceedance (e.g. Biass et al. 2016a; Massaro et al. 2023) and we require this type of model output as an input for the GIS tool.

### Deposit grain size distribution

Tephra load on a roof is likely to be the same as the load on the ground for flat roofs, but on pitched roofs sliding of the deposit can reduce the load. Laboratory sliding tests have shown the tephra roof load depends on the grain size distribution (GSD) of the deposit and the roof pitch, with fine-grained deposits being stable on steeper roofs compared to coarse-grained ones (Osman et al. 2023). The two versions of the tool, for coarse and fine

tephra are based on the GSDs used in the Osman et al. (2023) study (Fig. 5-2). The user must select the most appropriate version of the tool, based on expert judgement of the likely grain-size distribution of the deposit for the eruption under investigation. The fine-grained tephra tool provides a more conservative estimate of roof loads, and this should be used if the likely grain-size distribution for the scenario being considered is unknown.
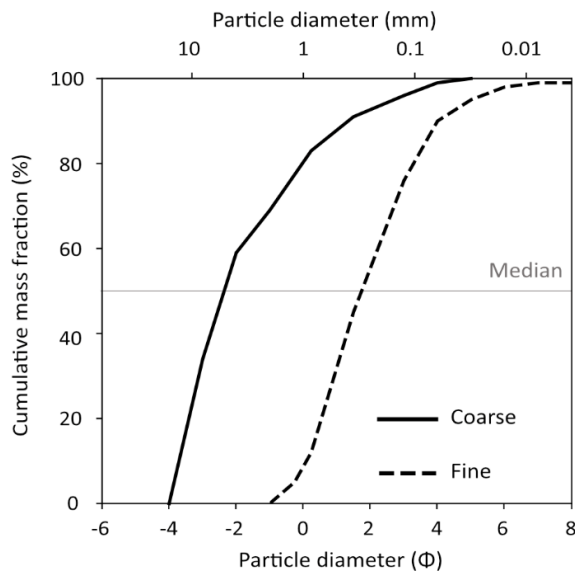


**Fig. 5-2** Grain size distributions of coarse and fine tephra used in GIS tool (amended from Osman et al. 2023). Maximum/median grain sizes: 16/5 mm (- 4/- 2.3 φ) for coarse tephra; 2/ 0.3 mm (- 1/1.7 φ) for fine tephra

**Building data**

Buildings are represented by point data and the characteristics required for each building are: location, roof material, roof pitch, roof condition (good or poor) and long span (yes or no). These parameters have been shown to affect roof collapse load (Jenkins et al. 2014) and are used in the Fail fraction calculations (detailed in the Processing steps section).

**Typical collapse loads**

This input table details typical collapse loads for different roof materials in good quality buildings (reduced failure loads for poor quality buildings are calculated during the tool run). We have used mean collapse loads from published data from post-eruption surveys (Jenkins et al. 2014), but values in the typical loads table can be amended to reflect local circumstances.

## Sliding equations

Tephra sliding behaviour in the tool is based on laboratory tests that quantified sliding on simply pitched roofs, following the approach of the Eurocode standard for snow loading (Osman et al. 2023; British Standards Institution 2009). The research investigated sliding of low- and high-density coarse-grained tephra (pumice and scoria) and high-density ash on metal sheet, fibre cement sheet and clay tile roofing. The results were used to produce characteristic sliding curves and roof shape factor (RSF) equations (Fig. 5-3 and Table 5-1). The tool uses the RSF multiplier to convert tephra loads on the ground to loads on the roof.
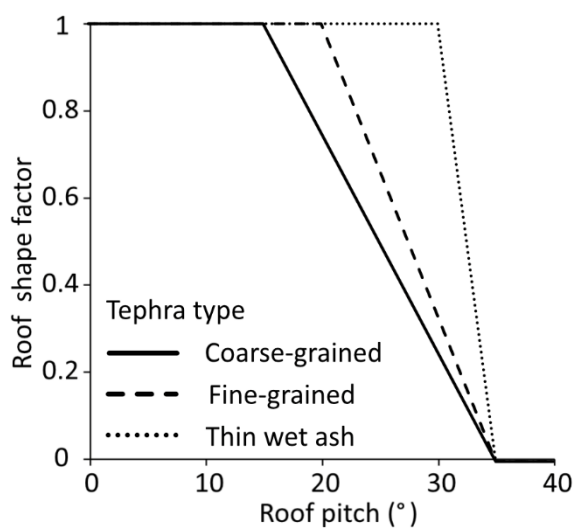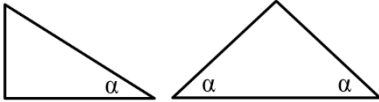


**Fig. 5-3** Variation of roof shape factor (RSF) with roof pitch for coarse- and fine- grained tephra. RSF is the fraction of the tephra load on the ground expected to remain on a roof (amended from Osman et al. 2023). Coarse and fine grain size distributions are detailed in Fig. 5-2. The curve for thin wet ash is not used in the GIS tool

Sliding depended on the grain-size of the deposit and the pitch of the roof, with fine-grained deposits stable on higher roof pitches compared to coarse-grained deposits. No sliding was observed on roof pitches ≤ 15 ° for coarse-grained deposits and ≤ 20 ° for fine-grained deposits i.e. tephra load on the roof is expected to be the same as on the ground. In all cases the whole deposit was removed for roof pitches ≥ 35 °. It was assumed that tephra load decreased linearly with increasing roof pitch between these values.

**Table 5-1** Roof shape factors (RSF) for monopitch and simply pitched roofs (amended from Osman et al. 2023). RSF is a multiplier which allows tephra load on a roof to be calculated from load on the ground. Coarse and fine grain size distributions are detailed in Fig. 5-2

| Roof type | Monopitch or simply pitched, with pitch = $\alpha$ | | | |
|---|---|---|---|---|



| Tephra type | Low pitch | Medium pitch | Steep pitch | Equation |
|---|---|---|---|---|
| Coarse-grained | $\alpha \leq 15°$ | $15° < \alpha < 35°$ | $35° \leq \alpha$ | (5-1) |
| | $RSF_{coarse} = 1$ | $RSF_{coarse} = (35 - \alpha)/20$ | $RSF_{coarse} = 0$ | |
| Fine-grained | $\alpha \leq 20°$ | $20° < \alpha < 35°$ | $35° \leq \alpha$ | (5-2) |
| | $RSF_{fine} = 1$ | $RSF_{fine} = (35 - \alpha)/15$ | $RSF_{fine} = 0$ | |

A note on thin wet ash: The sliding tests also showed that thin (10 cm) deposits of wet ash were stable to high roof pitches (30 °) (Fig. 5-3) and in this case the deposit often failed by slumping rather than sliding. These conditions are not considered in our GIS tool, as we are focusing on tephra sliding behaviour and hence the tool in the presented format is not appropriate for this type of deposit. Loading from 10 cm of wet ash is likely to be 0.6–2.2 kPa (assuming dry bulk deposit densities of 400–1500 kg m$^{-3}$ and water increasing load by ~ 50 % (Hayes et al. 2019; Osman et al. 2022)), which may lead to failure for low strength roofs (Jenkins et al. 2014) but expert judgement is needed to assess the likelihood of building failure under these conditions.

## Processing steps

Tephra deposits typically thin with distance from source (Pyle 1989) and so the first step is to estimate tephra load at each building point (Step 1, Table 5-2). A typical collapse load is then identified for each building based on the roof material (Step 2) and this is adjusted to account for lower expected failure loads for long span or poor-quality buildings (Step 3, based on Jenkins et al. 2014). RSF is then calculated to take account of tephra sliding (Step 4, based on Osman et al. 2023) and this is used to calculate the expected tephra load on

**Table 5-2** Tool calculation steps

| Step | Task | Calculation |
|------|------|-------------|
| 1 | Estimate tephra load on the ground at each building location | Interpolate values in the Tephra raster to each building point (using bilinear interpolation) |
| 2 | Identify typical failure load for each roof (in good condition) based on roof material | Take values from Typical loads table |
| 3 | Calculate the expected fail load for each roof | Value from Step 2 is adjusted for buildings that are not short span and in good condition:<br>Long span:  failure = 200 kg m$^{-2}$<br>Poor quality: value is divided by 2 |
| 4 | Calculate the Roof Shape Factor (RSF) i.e. the fraction of the ground tephra load expected to remain on the roof | Calculate RSF using appropriate equation from Table 5-1 for coarse and fine tephra |
| 5 | Calculate the expected tephra load on the roof | Tephra load on the ground multiplied by RSF. (Step 1 multiplied by Step 4) |
| 6 | Calculate the Fail fraction, *F* | Tephra load on the roof divided by roof failure load. (Step 5 divided by Step 3). If F > 10, F is set to 10 to enable the map output to be symbolised consistently |

each roof (Step 5). Finally, the Fail fraction, *F,* is calculated as the ratio of tephra load to roof failure load (Step 6). Values of $F > 1$ indicate that the failure load has been exceeded and roof collapse is possible.

Full details of the calculations are given in Appendix D.

The output from the tool is a map with building points categorised by *F* values where vulnerability to collapse is low ($F < 0.7$), medium ($F = 0.7–1$) and high ($F > 1$). This highlights buildings that should be prioritised for mitigation measures.

## Limits of the tool

The calculations of tephra load removed by sliding were based on small-scale laboratory tests on simply pitched roofs of three materials: metal and fibre cement sheets and tiles (Osman et al. 2023) and it should therefore only be used for these roof types. However, as data on other roof materials become available the tool will be expanded. We also assumed that sliding completely removed the deposit and it was not retained in gutters or redistributed to another part of the roof.

In addition, we assumed uniform loading from tephra fall and did not consider drifting of the deposit or how ballistics may alter loading and sliding behaviour (Williams et al. 2019). We also assumed that roof collapse occurs because the roof material fails, but in some cases structural supports may fail at loads that the roof material can withstand (e.g. Blong 2003; Spence et al. 2005; Williams et al. 2020).

As detailed in the Sliding equations section, thin (10 cm) wet ash often failed by slumping rather than sliding and so this type of deposit was not considered in this tool.

The typical failure loads for each roof material are taken from post-eruption field surveys (Jenkins et al. 2014), but these cover a limited range of buildings and roof types and therefore this dataset will need to be expanded for widespread use of the tool.

## Theoretical case study for Ascension Island

To demonstrate the usability of the tool, we have applied it to Ascension Island using probabilistic hazard analysis results (detailed in Chapter 4 (Osman et al. *Bull Volc* in review)) combined with synthetic field data. In order to highlight key features of our GIS tool, we selected an event where tephra loads may be sufficient to cause roof collapse, but we make no comment on the likelihood of such an event occurring. The case study used tephra

ground loads with a 50 % probability of exceedance from three explosive basaltic events from Sister's Peak, each with 6–10 km plume height and lasting 1–6 hours (shown in Fig. 5-4). Eruptions from Sister's Peak have produced deposits with median grain size ranging from 0.3 – - 3.2 φ (0.8–9.0 mm) (Winstanley 2020) and so we selected the coarse-grained version of the tool.
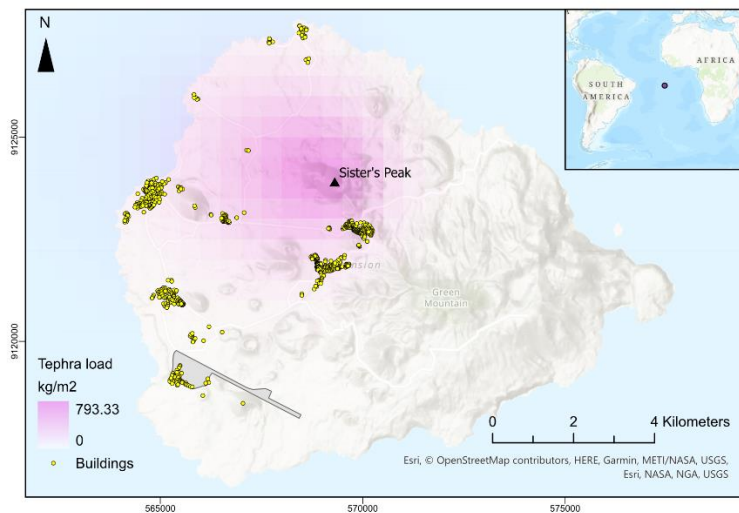


**Fig. 5-4** Tephra ground loads with 50 % probability of exceedance for three basaltic events, each with 6–10 km plume height, from Sister's Peak, Ascension Island. We assume the tephra is not cleared or eroded between each pulse (amended from Fig. 4-5a)

The building data we used are synthetic (Fig. 5-5a) with the exception of building location. We do not present any data relating to building characteristics on Ascension and this case study simply uses building locations on the island, with randomised roof data, for model testing purposes only. These data are not intended to represent the characteristics (roof material, pitch, condition) of any buildings on Ascension and are used solely to show features of our GIS tool. For our typical collapse loads table (Fig. 5-5b), we selected mean values from published data for post-eruption surveys (Jenkins et al. 2014).

The output map and associated building attribute table are shown in Fig. 5-6. The output data are synthetic, but they show how buildings located close to each other could have very different Fail fraction values. This is because tephra load is influenced by roof pitch (which controls tephra sliding) and failure load depends on the building construction (roof

material, short- or long-span) and its condition. These results can be used to prioritise buildings for mitigation measures in a more appropriate way than assuming hazard and risk are based solely on the distance from an eruption centre. Few population centres consist of buildings constructed in an identical way, at an identical time, with an identical usage history and this tool addresses the resulting variations in susceptibility of structures to tephra loading.

**a)**

| ID | RoofType | RoofPitch | RoofCondit | Longspan |
|----|----------|-----------|------------|----------|
| 0 | 1 | 12 | 1 | 0 |
| 1 | 3 | 19 | 1 | 0 |
| 2 | 2 | 17 | 1 | 0 |
| 3 | 3 | 5 | 1 | 0 |
| 4 | 1 | 18 | 1 | 0 |
| 5 | 1 | 3 | 1 | 0 |
| 6 | 2 | 8 | 0 | 0 |
| 7 | 1 | 23 | 0 | 0 |
| 8 | 2 | 0 | 0 | 1 |
| 9 | 3 | 24 | 1 | 0 |
| 10 | 3 | 0 | 1 | 0 |

**b)**

| Roof_type | Typical_load | Roof_material |
|-----------|--------------|---------------|
| 1 | 300 | Fibre cement sheet |
| 2 | 400 | Metal sheet |
| 3 | 300 | Tile |

**Fig. 5-5** Ascension Island case study input data a) Synthetic building point data, b) Typical collapse load table (from Jenkins 2014). Building point data are for model testing purposes only and do not represent characteristics of buildings on Ascension

## Concluding remarks

Tephra fall can lead to roof failure in buildings proximal to source, but the impact on individual buildings depends on many factors. Roof collapse can occur when the tephra fall load is greater than the roof failure load and this depends on the building construction and its condition. In addition, tephra may slide off pitched roofs and so the load on the roof may differ from the load on the ground.

To assist in building-scale assessments of susceptibility to roof collapse under tephra fall loading, we have developed a GIS tool for ArcGIS Pro and QGIS. This uses tephra fall loads from numerical simulations (Chapter 4), sliding data from laboratory tests (Osman et al. 2023), typical collapse loads for different roofs materials from post-eruption surveys

(Jenkins et al. 2014) and characteristics of individual buildings. The output is a Fail fraction value for each building which estimates tephra load on the roof as a fraction of the roof failure load. The tool can be used to assess the impact of different eruption scenarios and the output enables the most vulnerable buildings to be identified so that appropriate mitigation measures can be considered.



| ID | Roof_mat | Pitch | Condition | Longspan | RSF | FailLoad | TephraLoad | Fail_Frac |
|---|---|---|---|---|---|---|---|---|
| 0 | Fibre cement sheet | 12 | 1 | 0 | 1 | 300 | 201.136 | 0.67 |
| 1 | Tile | 19 | 1 | 0 | 0.8 | 300 | 161.455 | 0.54 |
| 2 | Metal sheet | 17 | 1 | 0 | 0.9 | 400 | 163.767 | 0.41 |
| 3 | Tile | 5 | 1 | 0 | 1 | 300 | 183.608 | 0.61 |
| 4 | Fibre cement sheet | 18 | 1 | 0 | 0.85 | 300 | 159.639 | 0.53 |
| 5 | Fibre cement sheet | 3 | 1 | 0 | 1 | 300 | 190.147 | 0.62 |
| 6 | Metal sheet | 8 | 0 | 0 | 1 | 200 | 192.09 | 0.96 |
| 7 | Fibre cement sheet | 23 | 0 | 0 | 0.6 | 150 | 112.814 | 0.75 |
| 8 | Metal sheet | 0 | 0 | 1 | 1 | 100 | 172.791 | 1.72 |
| 9 | Tile | 24 | 1 | 0 | 0.55 | 300 | 94.522 | 0.32 |
| 10 | Tile | 0 | 1 | 0 | 1 | 300 | 165.111 | 0.55 |

**Fig. 5-6** Ascension Island case study model output. a) Map b) Attribute table. Building data are for model testing purposes only and do not represent characteristics of buildings on Ascension

## Declarations

### Conflicts of interest/Competing interests

The authors declare they have no conflicts of interest or competing interests.

### Availability of data and material

The tools and full instructions for their use are available at: https://doi.org/10.5518/1458

## References

Barker SJ, Van Eaton, AR, Mastin LG, Wilson CJN, Thompson MA, Wilson TM, Davis C, Renwick JA (2019) Modeling ash dispersal from future eruptions of Taupo Supervolcano. Geochem Geophys Geosys 20: 3375–3401. https://doi.org/10.1029/2018GC008152

Barsotti S, Neri A, Scire JS (2008) The VOL-CALPUFF model for atmospheric ash dispersal: 1. Approach and physical formulation. J Geophys Res 113:B03208. https://doi.org/10.1029/2006JB004623

Biass S, Bonadonna C, Connor LJ, Connor CB (2016a) TephraProb: a Matlab package for probabilistic hazard assessments of tephra fallout. J Appl Volcanology 5:10. https://doi.org/10.1186/s13617-016-0050-5

Biass S, Bonadonna C, di Traglia F, Pistolesi M, Rosi M, Lestuzzi P (2016b) Probabilistic evaluation of the physical impact of future tephra fallout events for the Island of Vulcano, Italy. Bull Volcanol 78:37. https://doi.org/10.1007/s00445-016-1028-1

Blong R (2003) Building damage in Rabaul, Papua New Guinea, 1994. Bull Volcanol 65:43–
54. https://doi.org/10.1007/s00445-002-0238-x

British Standards Institution (2009) BS EN 1991-1-3: 2003 + A1:2015. Eurocode 1 – actions
on structures. Part 1-3: general actions – snow loads. BSI, London

Brown SK, Jenkins SF, Sparks RSJ, Odbert H, and Auker MR (2017) Volcanic fatalities
database: analysis of volcanic threat with distance and victim classification. J Appl
Volcanology 6:15. https://doi.org/10.1186/s13617-017-0067-4

Freire S, Florczyk AJ, Pesaresi M, Sliuzas R (2019) An improved global analysis of population
distribution in proximity to active volcanoes, 1975-2015. ISPRS Int J Geoinf 8:341.
https://doi.org/10.3390/ijgi8080341

Hampton SJ, Cole JW, Wilson G, Wilson T, Broom S (2015) Volcanic ashfall accumulation
and loading on gutters and pitched roofs from laboratory empirical experiments:
implications for risk assessment. J Volcanol Geotherm Res 304:237–252.
https://doi.org/10.1016/j.jvolgeores.2015.08.012

Hayes JL, Calderón R, Deligne NI, Jenkins SF, Leonard GS, Mcsporran AM, Williams GT,
Wilson TM (2019) Timber-framed building damage from tephra fall and lahar: 2015
Calbuco eruption, Chile. J Volcanol Geotherm Res 374:142–159.
https://doi.org/10.1016/j.jvolgeores.2019.02.017

Hayes JL, Wilson TM, Magill C (2015) Tephra fall clean-up in urban environments. J Volcanol
Geotherm Res 304:359–377. https://doi.org/10.1016/j.jvolgeores.2015.09.014

Jenkins SF, Spence RJS, Fonseca JFBD, Solidum RU, Wilson TM (2014) Volcanic risk
assessment: quantifying physical vulnerability in the built environment. J Volcanol
Geotherm Res 276:105–120. https://doi.org/10.1016/j.jvolgeores.2014.03.002

Magill C, Wilson T, Okada T (2013) Observations of tephra fall impacts from the 2011
Shinmoedake eruption, Japan. Earth Planets Space 65:677–698. https://doi.org/
10.5047/eps.2013.05.010

# Chapter 5: GIS tool

Massaro S, Stocchi M, Martínez Montesinos B, Sandri L, Selva J, Sulpizio R, Giaccio B, Moscatelli M, Peronace E, Nocentini M, Isaia R, Titos Luzón M, Dellino P, Naso G, Costa A (2023) Assessing long-term tephra fallout hazard in southern Italy from Neapolitan volcanoes. Nat Hazards Earth Syst Sci 23:2289–2311. https://doi.org/10.5194/nhess-23-2289-2023

Osman S, Thomas M, Crummy J, Sharp A, Carver S (2023) Laboratory tests to understand tephra sliding behaviour on roofs. J Appl Volcanology 12:11. https://doi.org/10.1186/s13617-023-00137-2

Osman S, Thomas M, Crummy J, Carver S (2022) Investigation of geomechanical properties of tephra relevant to roof loading for application in vulnerability analyses. J Appl Volcanology 11:9. https://doi.org/10.1186/s13617-022-00121-2

Pyle DM (1989) The thickness, volume and grainsize of tephra fall deposits. Bull Volcanol 51:1–15. https://doi.org/10.1007/BF01086757

Spence RJS, Kelman I, Baxter PJ, Zuccaro G, Petrazzuoli S (2005) Residential building and occupant vulnerability to tephra fall. Nat Hazards Earth Syst Sci 5:477–494. https://doi.org/10.5194/nhess-5-477-2005

Spence RJS, Pomonis A, Baxter PJ, Coburn AW, White M, Dayrit M, Field Epidemiology Training Program Team (1996) Building damage caused by the Mount Pinatubo eruption of June 15, 1991. In: Newhall CG, Punongbayan RS (eds) Fire and mud: eruptions and lahars of Mount Pinatubo, Philippines. University of Washington Press, Seattle, pp 1055–1061

Thouret J-C, Arapa E, Charbonnier S, Guerrero A, Kelfoun K, Cordoba G, Rodriguez D, Santoni O (2022) Modeling tephra fall and sediment-water flows to assess their impacts on a vulnerable building stock in the city of Arequipa, Peru. Front Earth Sci 10:865989. https://doi.org/10.3389/feart.2022.865989

Torres-Corredor RA, Ponce-Villarreal P, Gómez-Martínez DM (2017) Vulnerabilidad física de cubiertas de edificaciones de uso de ocupación normal ante caídas de ceniza en la zona de influencia del Volcán Galeras. Boletín de Geología 39:67–82. https://doi.org/10.18273/revbol.v39n2-2017005

Williams GT, Jenkins SF, Biass S, Wibowo HE, Harijoko A (2020) Remotely assessing tephra fall building damage and vulnerability: Kelud Volcano, Indonesia. J Appl Volcanology 9:10. https://doi.org/10.1186/s13617-020-00100-5

Williams GT, Kennedy BM, Lallemant D, Wilson TM, Allen N, Scott A, Jenkins SF (2019) Tephra cushioning of ballistic impacts: quantifying building vulnerability through pneumatic cannon experiments and multiple fragility curve fitting approaches. J Volcanol Geotherm Res 388:106711. https://doi.org/10.1016/j.jvolgeores.2019.106711

Wilson TM, Stewart C, Sword-Daniels V, Leonard GS, Johnston DM, Cole JW, Wardman J, Wilson G, Barnard ST (2012) Volcanic ash impacts on critical infrastructure. Phys Chem Earth 45–46:5–23. https://doi.org/10.1016/j.pce.2011.06.006

Winstanley R (2020) A preliminary investigation into the growth of the Sisters scoria cone complex, Ascension Island. M.Sc. thesis. MSc. Thesis, University of Durham

Zuccaro G, Leone MF (2012) Building technologies for the mitigation of volcanic risk: Vesuvius and Campi Flegrei. Nat Hazards Rev 13:221–232. https://doi.org/10.1061/(ASCE)NH.1527-6996.0000071

# Chapter 6

# Discussion and conclusions

In this chapter I summarise the main findings of my work and discuss how each strand of the project can be combined to improve our understanding of roof vulnerability under tephra fall loading.

When assessing whether tephra fall will lead to roof collapse there are many factors to be considered. These include eruption parameters, atmospheric conditions and building characteristics. When undertaking roof vulnerability assessments, it will likely never be possible to consider all of these elements for every potentially affected structure, so it is important to identify which have the most impact on roof loading and failure.

I have used a combination of published data, laboratory tests, field observation and numerical modelling to show how tephra sliding may reduce the load on a roof, and how buildings might be prioritised for mitigation measures. I have used small scale experiments on a limited number of roof types, but my results show the process through which a wider range of buildings could be assessed. There is, however, more work to be done and I expand on this in the Further work section.

# Chapter 6: Discussion and conclusions

## Comparison of natural and synthetic tephra

The first objective of the project was to confirm that synthetic samples match well to natural samples when considering the geomechanical properties relevant to tephra loading on roofs. I created synthetic samples with coarse and fine grain size distributions (GSD) matching those of natural tephra (samples from Ascension Island and published data), and deposit densities within the range of published values. At the low normal stresses typical of roof loads ($\leq$ 35 kPa), the internal angle of friction of the synthetic tephra (~ 36 °) was the same as for natural samples (Table 2-3). This important finding confirmed that synthetic samples can be reliably used for laboratory testing of tephra loading and sliding, reducing the cost and difficulty associated with acquiring and transporting large quantities of tephra from proximal locations following an eruption. However, further testing of a wider range of natural tephra samples from different eruptions would make this conclusion more robust.

One outstanding question from my shear tests was when a peak value of shear stress is reached for natural tephra, as the limited horizontal displacement of the small shear box meant I did not see clear peak and residual shear stress values for my Ascension Island ash (Fig. 2-7c). I was however able to show that there was no clear indication that the shear stress was still increasing in these tests (Appendix A2), so I was confident in reporting this as a peak shear stress. I have recently participated in tests for another project, using an Imperial ring shear (Bishop et al. 1971), and these have provided additional data for samples of ash from Taupo, New Zealand and Brown Tuff from Lipari, Italy. In contrast to the small shear box, maximum horizontal travel is not constrained in the ring shear, and tests on dry tephra recorded peak values of shear stress after horizontal displacements of ≤ 160 cm and clear, lower residual values. Data from these tests have been plotted in Fig. 6-1 (amended from Fig. 2-9) showing these new peak shear stress values fit well with my earlier results for Ascension Island ash, with an estimated angle of friction for all these natural samples of 35.7 °. This provides further validation for using synthetic tephra in roof loading tests, as proposed in Chapter 2.

## Tephra loading and eruption parameters

I investigated trends in GSD by compiling published data from a wide range of eruptions and found that proximal deposit density and GSD cannot be inferred from magma composition or eruption size (Figs. 2-3, 2-5, 2-6). The range of bulk densities within a single deposit and between deposits from similar eruptions was at least as large as any trends

related to composition or size. There are of course uncertainties in the data used for these compilations because it can be impossible to quantify how much post-depositional change has occurred. Compaction can increase deposit density by up to 50 % in just two years (Engwell et al. 2013) and the extent of any reworking varies with climate, ground slope and the presence of vegetation (Dugmore et al. 2020; Morison and Streeter 2022). In addition, dry and windy conditions can favour remobilisation which may winnow out the finest grains (Del Bello et al. 2021; Fries et al. 2021; Cutler et al. 2021).

However, these results confirm that assessments of roof vulnerability should not use a default bulk density value based on eruption size or composition. When estimating proximal tephra loading, we need to take a more nuanced approach, for example by modelling tephra dispersion as demonstrated in Chapter 4.
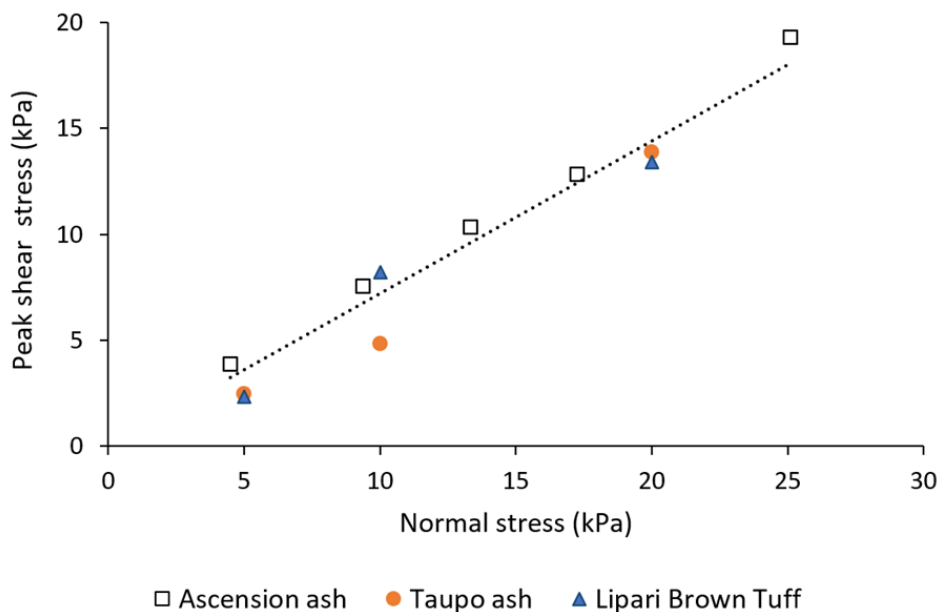


**Fig. 6-1** Peak shear stress vs normal stress for Ascension Island ash (small shear box tests, **Fig.** 2-9), Taupo ash and Lipari Brown Tuff (Imperial ring shear tests)

## Post depositional tephra sliding

Tephra load on roofs that are not flat may be reduced if the roof slope is steep enough for the tephra to slide, i.e. if the weight of the tephra acting downslope can overcome the frictional forces within the deposit or between the tephra and the roof material. However, the load is only reduced if tephra is completely removed. If the deposit is simply redistributed, for example by clogging gutters, locally higher loads may lead to deformation

or detachment of guttering and damage to the roof material or structure (Hampton et al. 2015).

Here, I assumed that sliding completely removed the load and my laboratory tests focused on one roof shape and three materials that are typically used in engineered buildings (i.e. those built to regulated design standards): a simply pitched roof of metal sheet, fibre cement and tiles. For this roof shape, my experiments tested a range of tephra deposits: wet and dry; low and high density; coarse and fine GSDs.

With the limited size of the laboratory equipment, I used separate tests to identify:

- The roof pitch at which grains began to move (simulating shedding from the front edge of the deposit)
- The pitch at which the whole deposit slid (simulating complete removal of the load).

When considering all of the tests, I found that coarser grained deposits started to move at shallower roof pitches (~ 15 °) compared to finer deposits (~ 20 °). Thin, wet ash was stable up to ~ 30 °, but this needs further investigation at larger scale to confirm my findings. Sliding of the whole deposit was controlled by roof material and pitch, with the load mainly shed on roofs with pitches ≥ 32 ° for metal sheet and ≥ 35 ° for fibre cement and tiles. In all the tests the roof pitch at which sliding occurred reduced as the tephra load increased (Fig. 3-8) suggesting that my results, with tephra thicknesses of 10–30 cm, can be taken as conservative values for tephra sliding. When considering both shedding of the load at the free surface and sliding of the entire deposit, I found that, as expected, roof pitch is a key factor, but grain size must also be taken into account as finer-grained deposits are stable on steeper roof pitches.

## Field observations in La Palma

Although laboratory tests enable a wide range of conditions to be explored, field observations are necessary to validate experimental and numerical modelling results. During the 2021 Tajogaite eruption of Cumbre Vieja on La Palma, Canary Islands, I was invited to join the monitoring team from the Instituto Geológico y Minero de España (IGME) from 1–3 December. The 85-day eruption (19 September to 13 December) consisted of alternating (and sometimes simultaneous) lava flows and tephra plumes (Bonadonna et al. 2022) and IGME staff were sampling at several proximal locations. This enabled me to

undertake a visual survey of 47 buildings in the exclusion zone (within ~ 5 km of the source) which had all been affected by tephra fall. The survey covered building type, roof material and pitch, building condition and damage. Details of survey locations and results are given in Appendix E1 and Appendix E2 details key findings which I shared with IGME.

The visit enabled me to validate my laboratory findings, to witness the impact of an eruption on local communities and to better understand the work of emergency responders and researchers during a crisis. House roofs were being cleared of tephra by emergency crews and they mainly appeared to be undamaged. I observed collapse of weaker structures (outbuildings, porches etc) because of failures in roof material, roof supports and building structure, highlighting the importance of considering all these elements when assessing potential failure mechanisms. An earlier survey (in October 2021) had also only found failure of secondary structures (Dominguez Barragan et al. 2022) and confirms that fire crews clearing house roofs play a key role in reducing collapses, particularly for long lasting eruptions. The long span metal sheet roof of the wrestling arena in Las Manchas (~ 3 km from the vent) had partially collapsed (Fig. 6-2), while nearby houses appeared undamaged, a finding consistent with observations following other eruptions that long span buildings (with > 5 m between supports) may have failure loads only ~ 50 % of those of short span buildings (Wardman, et al. 2012; Magill et al. 2013; Jenkins et al. 2014). This could be important if buildings such as sports halls are identified as possible emergency evacuation centres, as they may be susceptible to collapse under relatively low tephra loads.



**Fig. 6-2** Partial roof collapse at the wrestling arena in Las Manchas

# Chapter 6: Discussion and conclusions

I was able to validate results from my sliding tests as I observed tephra had slid on steeper (35°) sections of roofs, but not on shallower sections (20°) and that there was no sliding on roofs with pitches ≤ 15°. From tephra samples I collected, I estimated the in-situ bulk density as 1460–1680 kg m$^{-3}$ and dry density as 1335–1535 kg m$^{-3}$ and I used these values to constrain ash densities in my sliding tests (Chapter 3).

I also estimated the collapse load of thin metal sheet roofing as the roof of one outbuilding had buckled under 26 cm depth of undisturbed tephra but had not completely failed. This indicated it was very close to its failure load (Appendix E3). Using the estimated bulk density above suggests a collapse load of 3.7–4.3 kPa, consistent with published data from surveys following previous eruptions which found an interdecile range of collapse loads for metal sheet roofs of 1.3–7.6 kPa (Jenkins et al. 2014).

While this research has focused on roof materials of engineered buildings, my field visit highlighted the importance of also considering impacts on non-engineered structures. Bananas are a key crop in La Palma and while some greenhouses (covered in plastic sheet) failed under the tephra load, more extensive damage was caused by rain washing tephra inside the greenhouses through seams in the sheeting. This resulted in failure of the banana crop which may take years to recover. Crop damage in greenhouses was also reported after the 2011 Shinmoedake eruption, Japan. However, in that case the vinyl coverings were undamaged, but crops were lost because tephra deposits lowered light levels inside the greenhouses and blocked vents leading to higher humidity (Magill et al. 2013).

## Using laboratory results to assess tephra load on a roof

The Eurocode approach to designing for snow loading uses field observations of deposit sliding to produce empirical equations that calculate snow load on a roof from the load on the ground (British Standards Institution 2009). For tephra loads, my laboratory results showed that the load on the roof is expected to be the same as the load on the ground for roof pitches shallower than ~ 15 ° if the deposit is coarse-grained and ~ 20 ° if it is fine-grained.  I found the load was substantially shed for roof pitches ≥ 35 ° (Fig. 3-12) and I assumed that once significant movement was observed in the test, the deposit would completely slide off the roof. I also made the assumption that the load reduces linearly as increasing amounts of the deposit slide with increasing roof pitch. This is shown in cartoon form in Fig. 6-3, which includes supporting observations from La Palma.

The sliding coefficient equations I produced (Eqns. 3-1 – 3-3) demonstrate how laboratory tests could inform tephra load assessments where field observations are difficult to obtain. This approach could be used to investigate sliding on the other roof shapes included in the Eurocode standards to produce equivalent sliding equations for multi-span and cylindrical roofs (British Standards Institution 2009). Large-scale testing is required to validate the laboratory results (discussed in the Further work section), but these equations could then be used when assessing loads during the building design process. This could reduce vulnerability to roof collapse for buildings in volcanic areas, where wind, snow and seismic loads are already assessed (British Standards Institution 2009, 2010, 2013).
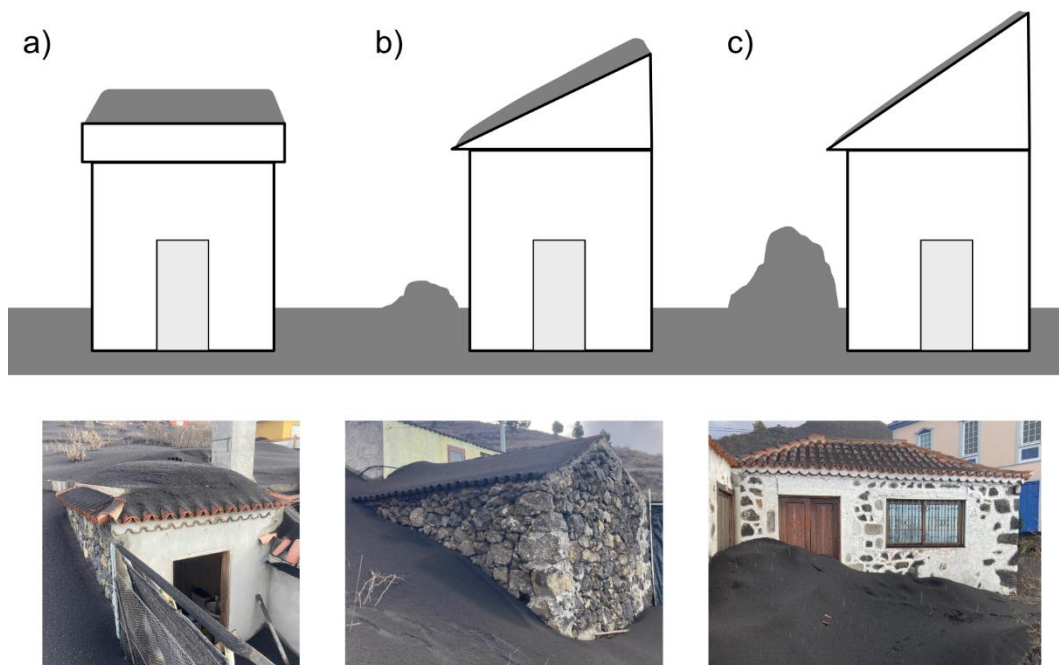


**Fig. 6-3** Cartoon showing expected tephra sliding on roofs that are a) flat or low pitched, b) medium pitched, c) steep, including examples of these roof types from La Palma during the 2021 eruption of Cumbre Vieja

## Tephra fall hazard in disaster risk management

As well as the need for design standards that ensure buildings can withstand tephra fall loading, it is important to have procedures in place to check the standards are followed. Lack of building code enforcement can lead to buildings being more susceptible to collapse from a range of natural hazards including hurricanes and earthquakes, as seen in the

# Chapter 6: Discussion and conclusions

Caribbean in 2017 and 2018, and in south-east Turkey in February 2023 (Clarke 2021; Kajastie 2023). However, in some areas the cost of using materials and methods that comply with standards may be prohibitive, especially for family dwellings (Giordano et al. 2023).

We must also consider non-engineered buildings and the use of traditional roof materials such as thatch, which are likely to inhibit tephra sliding. Tephra fall from the eruption of Manaro Voui on Ambae, Vanuatu in 2018 damaged many traditional buildings but mitigations implemented within communities included placing tarpaulins over the roofs to increase tephra sliding and installation of temporary internal props to strengthen roof supports (McSporran 2019). These low-cost solutions provided a quick and cost-effective method of reducing building damage from tephra fall and may be the most appropriate mitigation in some areas.

## Accounting for knowledge gaps when modelling tephra fall hazard

Understanding how tephra slides is important in assessing roof loading from tephra fall, but when planning for future eruptions, we must also understand the range of loads that a roof may have to withstand. Probabilistic hazard analysis allows the possible tephra fall load on the ground to be quantified for different eruption scenarios. I used Ascension Island as a case study to investigate the potential impact on roofs from a suite of short-lived eruptive events. Because tephra is poorly preserved on Ascension, in common with many small volcanic islands, I could not assess the frequency of these large explosive events and my impact assessments are conditional on the event having occurred. Analogue eruptions from São Miguel, Azores allowed me to model a wider range of scenarios than would have been possible using only deposit data from Ascension. For mafic events from the monogenetic field, I also had to account for uncertainty in vent location, but with insufficient data to estimate temporal vent opening probability. By using a grid of equally probable locations within the area of the most recent vents, I was able to provide a more realistic estimate of tephra loads (lower maximum values but a larger area over which tephra loadings may exceed given thresholds) than by selecting one vent location. This is a method that can be used in other data-poor environments, including small volcanic islands, where it is not possible to statistically assess vent opening probabilities.

### Future uncertainties

Wind velocity is a key factor controlling tephra dispersal and for my model runs I used ERA5 reanalysis data randomly sampled from the past decade. However, this assumes that weather patterns and plume dynamics are not changing, and with a warming atmosphere these assumptions may no longer be valid (Aubry et al. 2016, 2022). In addition, climate change increases the likelihood of other natural hazards including wildfires and landslides (Fink and Ajibade 2022) making it important for future studies to assess the impact of multiple hazards that may occur at the same time.

## Understanding impacts at a building scale

The final step in understanding the impact of tephra fall on a roof is converting tephra load on the ground to load on the roof (using the modelled tephra ground loads and sliding coefficients) and comparing that with the roof failure load. The GIS tool I have developed uses typical failure loads for different roof materials which are then reduced for more vulnerable buildings (long span or in poor condition). For the Ascension Island case study (Chapter 5) I took published values from post-eruption surveys (Jenkins et al. 2014), but depending on the local context these typical values may come from building design standards or local surveys. For example, as part of a tephra fall hazard assessment for Heimaey, Iceland, a detailed building survey of > 2000 buildings calculated mean roof failure loads of 561–807 kg m$^{-2}$ (Pfeffer et al. 2020). This tool can be used by building managers and disaster risk professionals to assess the vulnerability of building stock to roof collapse under tephra fall loading.

## Further work

My laboratory tests have all been small-scale and now building-scale tests are needed to confirm these results. I have also only considered failure of the roof material, but tests should also include the roof support structures as the weakest point is not always the roof material, as observed on La Palma.

In line with the Eurocode standards, more complex roof geometries should also be assessed including multi-span roofs where sliding from one area may increase loading in other areas. The impact of wind, where tephra drifting could lead to non-uniform loading, should also be investigated. Fig. 6-4 shows an example of the Eurocode 1 roof shape coefficients (multipliers to convert ground loads to roof loads) for a multispan roof under drifted snow,

where sheltered roof sections may be under loading that is considerably higher than the snow load on the ground (British Standards Institution 2009). The conditions required to remobilise tephra are likely to differ from those needed for snow drifting, with grain size distribution, particle shape and vesicularity important parameters as well as wind speed and humidity (Del Bello et al. 2021). However, observations of fresh deposits in Iceland show that significant reworking by wind is possible, particularly when tephra is dry and fine-grained (Arnalds et al. 2013) and therefore drifting should be considered when assessing tephra loads on roofs.
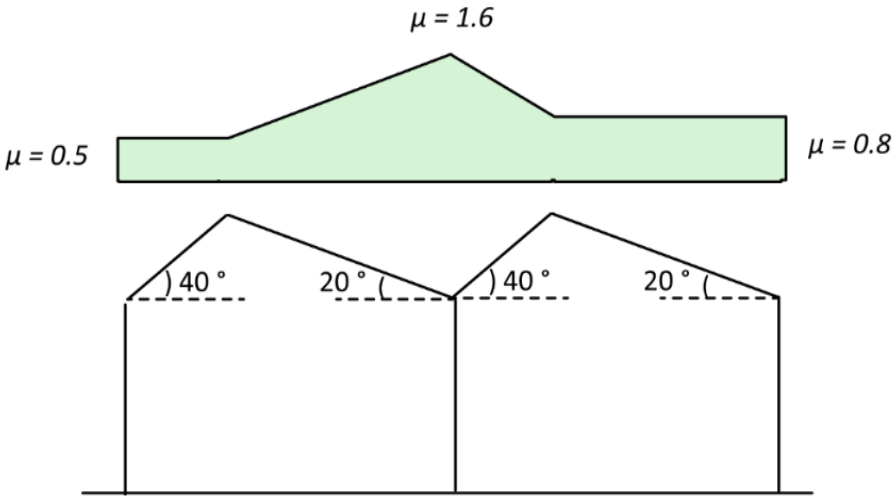


**Fig. 6-4** Roof shape coefficients ($\mu$) used in snow load calculations for a multispan roof with drifting snow (based on British Standards Institution 2009)**.**

I have focused on the impact of tephra fall but explosive eruptions often produce multiple, and sometimes cascading, hazards. Multi-hazard analysis should consider how roof vulnerability may also be impacted by pyroclastic density currents, ballistics and fire from hot tephra.

My tests considered materials used in engineered buildings but in many areas of high volcanic hazard non-engineered buildings are by far the most common. Further work is needed to understand the specific vulnerabilities of these buildings and identify possible mitigation strategies.

## Summary and key findings

The overall aim of this research was to better understand the factors influencing roof vulnerability to collapse under tephra fall loading. I have explored different strands within that aim before combining my results into a GIS tool that can assist in identifying roofs that are susceptible to roof collapse.

Key findings of this project are:

1.  The geomechanical properties of synthetic tephra that are relevant to deposit sliding behaviour i.e. bulk density, grain size distribution and internal angle of friction, match well to those of natural samples. This means that synthetic tephra (of unknown chemical composition) can be used to investigate tephra sliding, avoiding the hazards of proximal sampling and the costs of transporting large volumes of material.

2.  Published data on tephra deposit densities and proximal grain size distributions (≤ 10 km from source) show large variations within single eruptions and between eruptions of similar size or composition. However, there are no clear trends relating to magma composition or eruption size and therefore a more nuanced approach is needed when assessing roof vulnerability to tephra loads.

3.  Laboratory tests show that tephra sliding behaviour on roofs depends, as expected, on roof material and pitch, with the load mainly shed on metal roofs with pitches ≥ 32° and fibre cement or tiles with pitches ≥ 35°. Grain size is also a key factor when considering initial movement of the deposit. Coarse-grained deposits are unlikely to slide on roofs with pitches ≤ ~ 15°, while for dry ash this value is ~ 12°. Results for wet ash are inconclusive with initial movement on roof pitches of 21–30 °, although larger scale tests are needed to confirm this result.

4.  An initial set of tephra sliding coefficients for simply pitched roofs have been compiled, using an approach based on the Eurocode building standard for snow loads (Eqns. 3-1 – 3-3). These use roof pitch to calculate the fraction of tephra ground load expected to remain on a roof, with equations for coarse- and fine-grained tephra.

5.  A probabilistic tephra fall hazard analysis for Ascension Island assessed impacts to buildings from potential future eruptions that were large enough to cause roof

collapse. To account for gaps in our understanding of Ascension's eruptive history I selected eruption parameters from analogue eruptions on São Miguel, Azores and used a grid of equally possible vent locations to account for vent uncertainty in the monogenetic field. For mafic events with 6–10 km plumes, there was a 50 % probability that three pulses could produce loads sufficient to cause roof collapse in settlements close to the vent, if roofs were not cleared between phases. Larger felsic eruptions could also lead to widespread disruption across the island.

6. I created a GIS tool (for ArcGIS and QGIS) that combines tephra fall loads from numerical simulations, my sliding coefficients, published roof collapse loads and data on individual buildings. The output highlights the buildings most susceptible to failure under tephra fall loading, which can then be prioritised for mitigation measures.

## Conclusion

With an ever-increasing number of people living close to a Holocene volcano (59 million within 10 km in 2015 (Freire et al. 2019)), it is critical to understand the factors influencing roof vulnerability to collapse under tephra fall loading, so that impacts on affected communities can be reduced. My research has combined laboratory tests, field work, numerical modelling and GIS to better understand the impact of tephra fall on a limited number of roof types, and created the blueprint for a tool that could help emergency planning managers to identify buildings most vulnerable to roof collapse. The processes I developed have the potential to be extended to investigate impacts for a wider range of roofs, building types and eruptive products, enabling mitigation measures to be planned and implemented more effectively.

## References

Arnalds O, Thorarinsdottir EF, Thorsson J, Waldhauserova PD, Agustsdottir AM (2013) An extreme wind erosion event of the fresh Eyjafjallajökull 2010 volcanic ash. Sci Rep, 3(1), 1257. https://doi.org/10.1038/srep01257

Aubry TJ, Farquharson JI, Rowell CR, et al (2022) Impact of climate change on volcanic processes: current understanding and future challenges. Bull Volcanol 84:58. https://doi.org/10.1007/s00445-022-01562-8

Aubry TJ, Jellinek AM, Degruyter W, et al (2016) Impact of global warming on the rise of
volcanic plumes and implications for future volcanic aerosol forcing. J Geophys Res
Atmos 121:326–351. https://doi.org/10.1002/2016JD025405

Birnbaum, J, Lev, E, Hernandez, PA, et al (2023) Temporal variability of explosive activity at
Tajogaite volcano, Cumbre Vieja (Canary Islands), 2021 eruption from ground-based
infrared photography and videography. Front Earth Sci, 11, 1193436.
https://doi.org/10.3389/feart.2023.1193436

Bishop AW, Green GE, Garga VK, Andresen A, Brown J D (1971) A new ring shear apparatus
and Its application to the measurement of residual strength. Géotechnique, 21:273–
328. https://doi.org/10.1680/geot.1971.21.4.273

Bolós, X, Macias, JL, Ocampo-Díaz, YZE, Tinoco, C (2021) Implications of reworking
processes on tephra distribution during volcanic eruptions: the case of Parícutin (1943–
1952, western Mexico). Earth Surf Process and Landf, 46(15), 3143–3157.
https://doi.org/10.1002/esp.5222

Bonadonna C, Pistolesi M, Biass S, et al (2022) Physical characterization of long-lasting
hybrid eruptions: the 2021 Tajogaite eruption of Cumbre Vieja (La Palma, Canary
Islands). J Geophys Res Solid Earth 127:e2022JB025302. https://doi.org/10.1029/
2022JB025302

British Standards Institution (2009) BS EN 1991-1-3: 2003 + A1:2015. Eurocode 1 – actions
on structures. Part 1-3: general actions – snow loads. BSI, London

British Standards Institution (2010) BS EN 1991-1-4: 2005 + A1:2010. Eurocode 1 – actions
on structures. Part 1-4: general actions – wind actions. BSI, London

British Standards Institution (2013) BS EN 1998-1: 2004 + A1:2013. Eurocode 8 — design of
structures for earthquake resistance. Part 1: General rules, seismic actions and rules for
buildings. BSI, London

Clarke RP (2021) Performance of buildings in two Caribbean Territories: Dominica under
Hurricane Maria in 2017 and Trinidad under the 2018 earthquake. Nat Hazards
109:1141–1165. https://doi.org/10.1007/s11069-021-04872-w

# Chapter 6: Discussion and conclusions

Cutler NA, Streeter RT, Dugmore AJ, Sear ER (2021) How do the grain size characteristics of a tephra deposit change over time? Bull Volcanol 83:45. https://doi.org/10.1007/s00445-021-01469-w

Del Bello E, Taddeucci J, Merrison JP, et al (2021) Field-based measurements of volcanic ash resuspension by wind. Earth Planet Sci Lett 554:116684. https://doi.org/10.1016/j.epsl.2020.116684

Dominguez Barragan L, Di Maio L, Reyes Hardy M-P, et al (2022) Impact assessment of buildings exposed to the tephra fallout of the 2021 Cumbre Vieja eruption in La Palma, Spain . EGU General Assembly 2022, Vienna, Austria, 23–27 May 2022 EGU22-12678. https://doi.org/10.5194/egusphere-egu22-12678

Dugmore AJ, Thompson PIJ, Streeter RT, et al (2020) The interpretative value of transformed tephra sequences. J Quat Sci 35:23–38. https://doi.org/10.1002/jqs.3174

Engwell SL, Sparks RSJ, Aspinall WP (2013) Quantifying uncertainties in the measurement of tephra fall thickness. J Appl Volcanology 2:5. https://doi.org/10.1186/2191-5040-2-5

Fink J, Ajibade I (2022) Future impacts of climate-induced compound disasters on volcano hazard assessment. Bull Volcanol 84:42. https://doi.org/10.1007/s00445-022-01542-y

Freire S, Florczyk AJ, Pesaresi M, Sliuzas R (2019) An improved global analysis of population distribution in proximity to active volcanoes, 1975-2015. ISPRS Int J Geoinf 8:341. https://doi.org/10.3390/ijgi8080341

Fries A, Lemus J, Jarvis PA, et al (2021) The influence of particle concentration on the formation of settling-driven gravitational instabilities at the base of volcanic clouds. Front Earth Sci 9:640090. https://doi.org/10.3389/feart.2021.640090

Giordano N, De Risi R, Macdonald J, et al (2023) Implications of building code enforcement and urban expansion on future earthquake loss in East Africa: case study—Blantyre, Malawi. Nat Hazards 117:1083–1104. https://doi.org/10.1007/s11069-023-05895-1

Hampton SJ, Cole JW, Wilson G, et al (2015) Volcanic ashfall accumulation and loading on gutters and pitched roofs from laboratory empirical experiments: implications for risk assessment. J Volcanol Geotherm Res 304:237–252. https://doi.org/10.1016/j.jvolgeores.2015.08.012

Jenkins SF, Spence RJS, Fonseca JFBD, et al (2014) Volcanic risk assessment: quantifying physical vulnerability in the built environment. J Volcanol Geotherm Res 276:105–120. https://doi.org/10.1016/j.jvolgeores.2014.03.002

Kajastie N (2023) Turkey-Syria earthquakes: Turkish building code updated four years ago. Ground Eng 10 February

Magill C, Wilson T, Okada T (2013) Observations of tephra fall impacts from the 2011 Shinmoedake eruption, Japan. Earth Planets Space 65:677–698. https://doi.org/10.5047/eps.2013.05.010

McSporran AM (2019) Impacts of tephra fall on buildings from the 2017-2018 eruption of Manaro Voui volcano, Ambae Island, Vanuatu. MSc thesis, University of Canterbury, NZ

Morison CAG, Streeter RT (2022) The influence of vegetation cover on the grain-size distributions and thicknesses of two Icelandic tephra layers. Volcanica 5:227–248. https://doi.org/10.30909/VOL.05.02.227248

Pfeffer MA, Barsotti S, Jensen EH, et al (2020) An initial volcanic hazard assessment of the Vestmannaeyjar Volcanic System: impacts of lava flow and tephra deposit on Heimaey. VI 2020-011. https://icelandicvolcanoes.is/data/Gosva/VI_2020_011_en.pdf. Accessed 3 Oct 2023

Wardman, J, Sword-Daniels V, Stewart C, Wilson T (2012) Impact assessment of the May 2010 eruption of Pacaya volcano, Guatemala. GNS Science report 2012/09. https://ir.canterbury.ac.nz/handle/10092/10563. Accessed 5 Jul 2023

# Appendix A

## Appendix to Chapter 2

The bulk tephra density data in Appendix A1 were included as the Appendix to:

Osman S, Thomas M, Crummy J, and Carver S (2022) Investigation of geomechanical properties of tephra relevant to roof loading for application in vulnerability analyses. *Journal of Applied Volcanology* 11, 9. https://doi.org/10.1186/s13617-022-00121-2

Appendix A2 shows the rate of change of shear stress with time for small shear box tests with Ascension ash referred to in Fig. 2-7

# Appendix A: Appendix to Chapter 2

## A1 Bulk density of tephra

Data used in Figs. 2-5 and 2-6. VEI and eruption magnitude, from (Crosweller et al. 2012; Venzke 2013). References are detailed in the reference list of Chapter 2.

| Eruption | VEI | Magnitude | Composition | SiO$_2$ % | Bulk density (kg m$^{-3}$) | Reference |
|---|---|---|---|---|---|---|
| Agua de Pau, Fogo A 4945 BP | 5 | 5.6 | Trachyte | 59-62 | 500 (proximal–medial) | (Walker and Croasdale 1970; Widom et al. 1992) |
| Agung, Bali 1963-4 | 5 | 5 | Basaltic andesite | 56 | 1170 (proximal) | (Self and King 1996; Self and Rampino 2012) |
| Apoyeque, Chiltepe 1.9 ka BP | 6 | 6.3 | Dacite | 64-68 | 460–530 (proximal-medial) | (Kutterolf et al. 2011) |
| Apoyeque, Mateare Tephra 3–6 ka BP | 5 | 5 | Andesite–dacite | 57-65 | 650–750 (proximal-medial) | (Kutterolf et al. 2007) |
| Apoyeque, Xiloa Tephra 6105 BP | 5 | 5.3 | Dacite | 64-65 | 560 (proximal-medial) | (Kutterolf et al. 2007) |
| Apoyeque, Los Cedros Tephra 2–4 ka BP | 5 | 5 | Dacite | 65-66 | 510 (proximal-medial) | (Kutterolf et al. 2007) |
| Apoyeque, Upper Apoyeque Pumice ~ 12.4 ka BP | 5 | 5.6 | Rhyodacite | 71 | 430–550 (proximal-medial) | (Kutterolf et al. 2007) |
| Apoyeque, Lower Apoyeque Pumice ~ 17 ka BP | 5 | 5.6 | Rhyodacite | 71 | 520 (proximal-medial) | (Kutterolf et al. 2007) |
| Apoyo, Lower Apoyo Tephra ~ 29 ka BP | 6 | 6.9 | Dacite | 68-69 | 440 (proximal-medial) | (Kutterolf et al. 2007) |
| Apoyo, Upper Apoyo Tephra ~ 29 ka BP | 6 | 5.8 | Dacite | 67-68 | 460–570 (proximal-medial) | (Kutterolf et al. 2007) |
| Askja 1875 | 5? 3? | | Rhyolite | 73 | 365 (mean value – unit D) 671 (mean value – unit B) | (Sparks et al. 1981; Carey et al. 2010) |
| Calbuco 1929 | 3 | | Andesite | 59 | 1016 (distal, freshly fallen) | (Larsson 1936) |
| Calbuco 2015 | 4 | | Basaltic andesite | 55 | 997, 1115 (mean values) | (Romero et al. 2016; Hayes et al. 2019) |
| Cerro Negro 1971 | 3 | | Basalt | 50-53 | 1350 (mean value) | (Rose et al. 1973) |

| Eruption | VEI | Magnitude | Composition | SiO$_2$ % | Bulk density (kg m$^{-3}$) | Reference |
|---|---|---|---|---|---|---|
| Chaitén 2008 | 4 | 4.9 | Rhyolite | 75 | 997 (distal, collected after rain) | (Watt et al. 2009) |
| | 4 | 4.5 | | 74-76 | 1250 (prox-medial lithic-rich Layer β) | (Alfano et al. 2011) |
| El Chichón 1982 | 5 | 5.1 | Trachyandesite | 58 | 500 (uncompacted); all medial-distal | (Varekamp et al. 1984) |
| El Chinyero 1909 (Tenerife) | 2 | | Basanite | 44 | 700–1000 (proximal) | (Di Roberto et al. 2016) |
| Cordón Caulle 2011 | 5 | 5 | Rhyolite | 71 | 560, 600 (different units, prox-distal) | (Bonadonna et al. 2015; Seropian et al. 2021) |
| Etna 2002–3 | 3 | | Basalt | 47 | 1067 (mean value) | ( Andronico et al. 2005; Andronico et al. 2008) |
| Fuego 1973 | 4 | 4.4 | Basalt | 47-53 | 460–1400 (proximal–medial) 1100–1280 (distal, mean 1140) | (Rose et al. 2008) |
| Grímsvötn 2004 | 3 | | Basalt | 50-51 | 1020–1290 (proximal) | (Oddsson 2007; Jude-Eton 2013) |
| Gubisa Formation, Kone caldera Ethiopia | 5 | 5.3 | Rhyolite | 69-72 | 600 (proximal) | (Rampey et al. 2014) |
| Hekla 1104 | 5 | 5.1 | Dacite | 69-70 | 400 (mean proximal–distal) | (Janebo et al. 2018; Geist et al. 2021) |
| Hekla 1300-D | 4 | 4 | Andesite | 59-60 | 740 (mean proximal–distal) | (Janebo et al. 2018; Geist et al. 2021) |
| Hekla 1693 | 4 | 4.3 | Andesite | 59-60 | 560 (mean proximal–distal) | (Janebo et al. 2018; Geist et al. 2021) |
| Hekla 1766 | 4 | 4.3 | Andesite | 56-60 | 420 (mean proximal–distal) | (Janebo et al. 2018; Geist et al. 2021) |
| Hekla 1947 | 4 | 4.1 | Andesite-dacite | 60-63 | 520–1000 (proximal-medial, mean 640); 580–880 (distal, mean 800) | (Thorarinsson 1954) |

| Eruption | VEI | Magnitude | Composition | SiO$_2$ % | Bulk density (kg m$^{-3}$) | Reference |
|---|---|---|---|---|---|---|
| Hekla 1970 | 3 | | Basaltic andesite | 55-56 | 600 (proximal)–800 (distal) | (Thorarinsson and Sigvaldason 1972) |
| Hudson 1991 | 5 | 5.8 | Trachyandesite | 60-65 | 650–950 distal | (Scasso et al. 1994; Kratzmann et al. 2009) |
| Katla 1755 | 5? | 5 | Basalt | 47 | 1050 (distal) *from laboratory tests* | (Thorarinsson 1958) |
| Masaya San Antonio Tephra ~ 6 ka BP | 6 | 6.3 | Basalt | 50-52 | 750 (proximal-medial) | (Kutterolf et al. 2007) |
| Masaya Fontana Tephra ~ 60 ka BP | 6 | 6 | Basaltic andesite | 52 | 720–810 (proximal-medial) | (Kutterolf et al. 2007) |
| Masaya Masaya Triple Layer ~ 2120 BP | 5 | 5.7 | Basalt | 50 | 700 (proximal-medial) | (Kutterolf et al. 2007) |
| Mount St Helens 1980 | 5 | 4.8 | Dacite | 63-64 | 450 (mean distal, 50-600 km) | (Sarna-Wojcicki et al. 1981) |
| Öraefajökull 1362 | 5 | 5.4 | Rhyolite | 69-70 | 560 (distal) 900 when compacted *from laboratory tests* | (Thorarinsson 1958) |
| Pinatubo 1991 | 6 | 6.1 | Dacite | 65 | 1000; 1250 (different units - no change with distance from vent) | (Bernard et al. 1996; Koyaguchi and Ohno 2001b) |
| Quizapu 1932 freshly fallen | > 5 | 6 | Dacite | 64-70 | 588–644 (distal uncompacted) | (Larsson 1936) |
| Sakurajima 1914 Taisho eruption | 4 | 4.7 | Andesite | 59-62 | 535, 765, 980 (prox., medial, distal) | (Todde et al. 2017) |
| Samalas 1257 (Lombok) | 7 | | Trachyte | 64 | 539, 603 mean medial–distal of different units. | (Vidal et al. 2015) |

| Eruption | VEI | Magnitude | Composition | SiO$_2$ % | Bulk density (kg m$^{-3}$) | Reference |
|---|---|---|---|---|---|---|
| Santa María, Guatemala 1902 | 6 | 6.3 | Dacite | 66 | 600 (proximal) – 1200 (distal) (average 1100) | (Williams and Self 1983; Andrews 2014) |
| Soufrière de Guadeloupe 1530 | 2–3 | | Andesite | 55-59 | 1160 (mean compacted value) | (Boudon et al. 2008; Komorowski et al. 2008; Pichavant et al. 2018) |
| Tarawera 1886 | 5 | 5.3 | Basalt | 52 | 900 (proximal) – 1100 (medial) | (Walker et al. 1984; Rowe et al. 2021) |
| Taupo 232 CE | 6 | 6.7 | Rhyolite | 74 | 450 (proximal) – 650 (distal) | (Walker 1980; Sutton et al. 1995) |
| Tecolote, Mexico 27 ka BP | 3–4 | | Basalt | 49 | 757; 894 (proximal–medial, 2 units) | (Zawacki et al. 2019) |
| Tungurahua 2006 | 2–3 | | Andesite | 58-59 | 770–1360 (proximal-medial) | (Eychenne et al. 2013) |
| Vesuvius 1944 | 3 | | Tephrite/phono-tephrite | 45-50 | 1200 (mean value) | (Cioni et al. 2003; Pappalardo and Mastrolorenzo 2010) |
| Vesuvius 1906 | 3 | | Tephrite/phono-tephrite | 45-50 | 1100 (mean value) | (Cioni et al. 2003; Pappalardo and Mastrolorenzo 2010) |
| Vesuvius 1631 | 5 | | Phono-tephrite/tephri-phonolite | 52 | 1000 (mean value) | (Cioni et al. 2003; Pappalardo and Mastrolorenzo 2010) |
| Vesuvius PM1-6 (6 eruptions 512 – 1570) | 3 | | Tephrite/phono-tephrite | 45-50 | 900 (mean value) | (Cioni et al. 2003; Pappalardo and Mastrolorenzo 2010) |
| Vesuvius Pollena 472 | 5 | | Phono-tephrite/tephri-phonolite | 46-49 | 900 (mean value) | (Cioni et al. 2003; Pappalardo and Mastrolorenzo 2010) |
| Vesuvius Pompeii White pumice 79 | 5–6 | | Phonolite | 57 | 500 (proximal and distal) | (Cioni et al. 2003; Pappalardo and Mastrolorenzo 2010) |
| Vesuvius Pompeii Grey pumice 79 | 5–6 | | Tephri-phonolite | 58 | 1000 (proximal and distal) | (Cioni et al. 2003; Pappalardo and Mastrolorenzo 2010) |
| Vesuvius AP5 | 4 | | Tephri-phonolite | 55-60 | 1500 (mean value) | (Andronico and Cioni 2002; Cioni et al. 2003) |

| Eruption | VEI | Magnitude | Composition | SiO$_2$ % | Bulk density (kg m$^{-3}$) | Reference |
|---|---|---|---|---|---|---|
| Vesuvius AP4 | 4 | | Tephri-phonolite / phonolite | 52-60 | 1300 (mean value) | (Andronico and Cioni 2002; Cioni et al. 2003) |
| Vesuvius AP3 ~ 2.7 ka BP | 4 | | Tephri-phonolite / phonolite | 52-60 | 1500 (mean value) | (Andronico and Cioni 2002; Cioni et al. 2003) |
| Vesuvius AP2 ~ 3 ka BP | 4-5 | | Tephri-phonolite / phonolite | 52-60 | 1500 (mean value) | (Andronico and Cioni 2002; Cioni et al. 2003) |
| Vesuvius AP1 ~ 3.2 ka BP | 4-5 | | Tephri-phonolite / phonolite | 52-60 | 1500 (mean value) | (Andronico and Cioni 2002; Cioni et al. 2003) |
| Vesuvius Avellino White pumice ~ 3.8 ka BP | 5 | | Phonolite | 55 | 400 (mean value) | (Cioni et al. 2003; Pappalardo and Mastrolorenzo 2010) |
| Vesuvius Avellino Grey pumice ~ 3.8 ka BP | 5-6 | | Tephri-phonolite | 54 | 800 (proximal and distal) | (Cioni et al. 2003; Pappalardo and Mastrolorenzo 2010) |
| Vesuvius Mercato ~ 8 ka BP | 5-6 | | Phonolite | 52-60 | 600 (proximal and distal) | (Cioni et al. 2003; Pappalardo and Mastrolorenzo 2010) |
| Villarrica 2015 | 2-3 | | Basaltic andesite | 53-55 | 500–880 (proximal-medial) | (Romero et al. 2018) |

## A2 Rate of change of shear stress vs time for small shear box tests with Ascension ash

Referred to in Fig. 2-7.
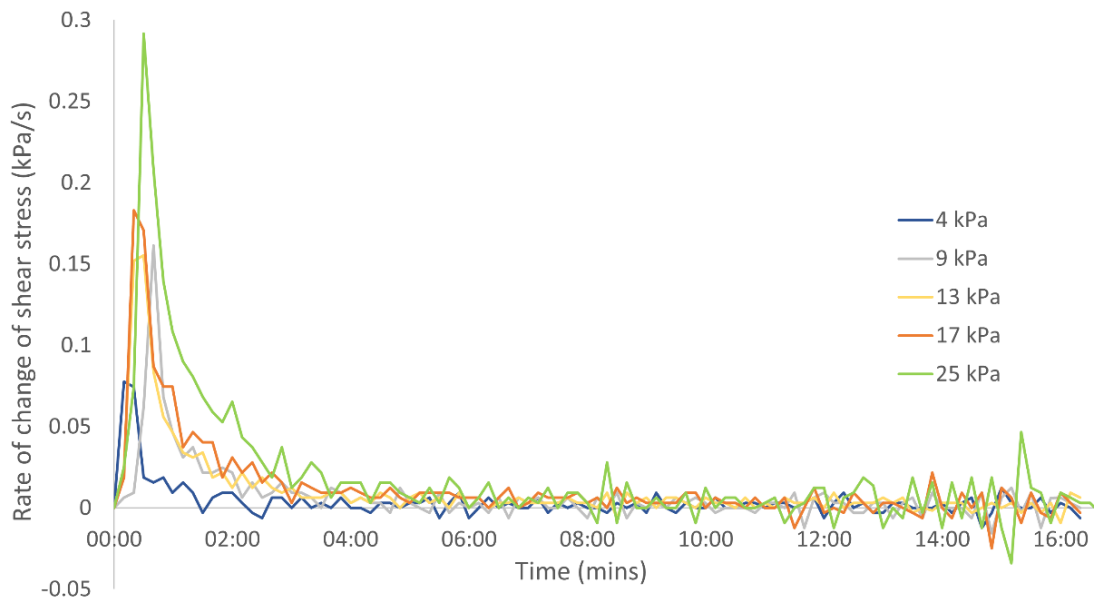
# Appendix B

## Supplementary material for Chapter 3

The sliding test results in Appendix B1 were included as Supplementary material for:

Osman S, Thomas M, Crummy J, Sharp, A and Carver S (2023) Laboratory tests to understand tephra sliding on roofs. *Journal of Applied Volcanology* 12, 11. https://doi.org/10.1186/s13617-023-00137-2

Appendix B2 contains calculations on the volume of corrugations of the metal and fibre cement sheets used for the sliding tests (referenced in the Methods - Sliding tests section).

# Appendix B: Supplementary material for Chapter 3

## B1 Sliding test results

**Initial sliding data** (further described in Initial sliding tests and Angle of repose sections)

| | |
|---|---|
| Tephra | Type of synthetic tephra used for test: pumice; scoria; ash |
| Roofing | Type of roofing: metal sheet; fibre cement sheet; tile |
| Ridge/Trough | For sheet materials, whether Perspex cell was placed over ridge or trough of corrugations. NA = not applicable for tiles |
| Wet/Dry | Dry (dry tephra on dry roof); wet (wet tephra on wet roof) |
| Depth | Depth of tephra deposit (cm) |
| Type | Type of test: Cell sliding (with empty cell); Initial movement (of grains at leading edge); Repose (angle of repose); Cardboard sliding (test with cardboard rather than Perspex cell) |
| Angle | Angle of repose, angle of initial movement or angle at which sliding occurred, depending on type of test (in degrees) |

**Sliding test data** (further described in Sliding tests section)

| | |
|---|---|
| Tephra | Type of synthetic tephra used for test: pumice; scoria; ash |
| Roofing | Type of roofing: metal sheet; fibre cement sheet; tile |
| Ridge/Trough | For sheet materials, whether Perspex cell was placed over ridge or trough of corrugations. NA = not applicable for tiles |
| Wet/Dry | Dry-dry (dry tephra on dry roof); dry-wet (dry tephra on a wet roof); wet-wet (wet tephra on wet roof) |
| Depth | Depth of tephra deposit (cm) |
| Sliding angle | Angle at which sliding occurred (in degrees) |
| Where sliding? | Where sliding occurs: base (between tephra and roofing material); tephra (within the deposit) |

## Initial sliding

| Tephra | Roofing | Ridge/Trough | Wet/Dry | Depth | Type | Angle |
|--------|---------|--------------|---------|-------|------|-------|
| NA | Metal sheet | Trough | Dry | 0 | Cell sliding | 13 |
| NA | Metal sheet | Ridge | Dry | 0 | Cell sliding | 19 |
| NA | Fibre cement | Trough | Dry | 0 | Cell sliding | 21 |
| NA | Fibre cement | Ridge | Dry | 0 | Cell sliding | 24 |
| NA | Tile no tape | NA | Dry | 0 | Cell sliding | 32 |
| NA | Tile with PTFE tape | NA | Dry | 0 | Cell sliding | 24 |
| Pumice | Metal sheet | Ridge | Dry | 10 | Cardboard cell sliding | 28 |
| Pumice | Metal sheet | Ridge | Dry | 10 | Cardboard cell sliding | 26 |
| Pumice | Metal sheet | Ridge | Dry | 10 | Cardboard cell sliding | 27 |
| Pumice | Fibre cement | Ridge | Dry | 10 | Cardboard cell sliding | 34 |
| Pumice | Fibre cement | Ridge | Dry | 10 | Cardboard cell sliding | 33 |
| Pumice | Fibre cement | Ridge | Dry | 10 | Cardboard cell sliding | 34 |
| Pumice | Tile | NA | Dry | 10 | Cardboard cell sliding | 32 |
| Pumice | Tile | NA | Dry | 10 | Cardboard cell sliding | 33 |
| Pumice | Tile | NA | Dry | 10 | Cardboard cell sliding | 33 |
| Pumice | Metal sheet | Ridge | Dry | 20 | Cardboard cell sliding | 29 |
| Pumice | Metal sheet | Ridge | Dry | 20 | Cardboard cell sliding | 29 |
| Pumice | Metal sheet | Ridge | Dry | 20 | Cardboard cell sliding | 28 |
| Pumice | Fibre cement | Ridge | Dry | 20 | Cardboard cell sliding | 31 |
| Pumice | Fibre cement | Ridge | Dry | 20 | Cardboard cell sliding | 33 |
| Pumice | Fibre cement | Ridge | Dry | 20 | Cardboard cell sliding | 31 |
| Pumice | Metal sheet | Ridge | Dry | 10 | Repose | 34 |
| Pumice | Metal sheet | Ridge | Dry | 10 | Repose | 33 |
| Pumice | Metal sheet | Ridge | Dry | 10 | Repose | 33 |
| Pumice | Metal sheet | Ridge | Dry | 20 | Repose | 34 |
| Pumice | Metal sheet | Ridge | Dry | 20 | Repose | 36 |
| Pumice | Metal sheet | Ridge | Dry | 20 | Repose | 36 |
| Pumice | Fibre cement | Ridge | Dry | 10 | Repose | 34 |
| Pumice | Fibre cement | Ridge | Dry | 10 | Repose | 35 |
| Pumice | Fibre cement | Ridge | Dry | 10 | Repose | 36 |
| Pumice | Fibre cement | Ridge | Dry | 20 | Repose | 36 |
| Pumice | Fibre cement | Ridge | Dry | 20 | Repose | 35 |
| Pumice | Fibre cement | Ridge | Dry | 20 | Repose | 36 |
| Pumice | Tile | NA | Dry | 10 | Repose | 35 |
| Pumice | Tile | NA | Dry | 10 | Repose | 34 |
| Pumice | Tile | NA | Dry | 10 | Repose | 36 |
| Pumice | Tile | NA | Dry | 20 | Repose | 34 |
| Pumice | Tile | NA | Dry | 20 | Repose | 35 |
| Pumice | Tile | NA | Dry | 20 | Repose | 35 |
| Pumice | Metal sheet | Ridge | Dry | 10 | Initial movement | 14 |
| Pumice | Metal sheet | Ridge | Dry | 10 | Initial movement | 15 |
| Pumice | Metal sheet | Ridge | Dry | 10 | Initial movement | 14 |
| Pumice | Metal sheet | Ridge | Dry | 20 | Initial movement | 14 |
| Pumice | Metal sheet | Ridge | Dry | 20 | Initial movement | 15 |
| Pumice | Metal sheet | Ridge | Dry | 20 | Initial movement | 15 |
| Pumice | Fibre cement | Ridge | Dry | 10 | Initial movement | 15 |
| Pumice | Fibre cement | Ridge | Dry | 10 | Initial movement | 13 |
| Pumice | Fibre cement | Ridge | Dry | 10 | Initial movement | 15 |
| Pumice | Fibre cement | Ridge | Dry | 20 | Initial movement | 14 |
| Pumice | Fibre cement | Ridge | Dry | 20 | Initial movement | 14 |
| Pumice | Fibre cement | Ridge | Dry | 20 | Initial movement | 14 |
| Pumice | Tile | NA | Dry | 10 | Initial movement | 14 |
| Pumice | Tile | NA | Dry | 10 | Initial movement | 13 |
| Pumice | Tile | NA | Dry | 10 | Initial movement | 14 |
| Pumice | Tile | NA | Dry | 20 | Initial movement | 14 |

# Appendix B: Supplementary material for Chapter 3

| Tephra | Roofing | Ridge/Trough | Wet/Dry | Depth | Type | Angle |
|--------|---------|--------------|---------|-------|------|-------|
| Pumice | Tile | NA | Dry | 20 | Initial movement | 14 |
| Pumice | Tile | NA | Dry | 20 | Initial movement | 15 |
| Pumice | Tile | NA | Wet | 10 | Repose | 50 |
| Pumice | Tile | NA | Wet | 10 | Repose | 48 |
| Pumice | Tile | NA | Wet | 10 | Repose | 47 |
| Pumice | Tile | NA | Wet | 10 | Repose | 50 |
| Pumice | Tile | NA | Wet | 10 | Repose | 47 |
| Pumice | Tile | NA | Wet | 10 | Initial movement | 19 |
| Pumice | Tile | NA | Wet | 10 | Initial movement | 16 |
| Pumice | Tile | NA | Wet | 10 | Initial movement | 18 |
| Pumice | Tile | NA | Wet | 10 | Initial movement | 16 |
| Pumice | Tile | NA | Wet | 10 | Initial movement | 19 |
| Scoria | Metal sheet | Ridge | Dry | 10 | Repose | 36 |
| Scoria | Metal sheet | Ridge | Dry | 10 | Repose | 36 |
| Scoria | Metal sheet | Ridge | Dry | 10 | Repose | 37 |
| Scoria | Metal sheet | Ridge | Dry | 20 | Repose | 34 |
| Scoria | Metal sheet | Ridge | Dry | 20 | Repose | 36 |
| Scoria | Metal sheet | Ridge | Dry | 20 | Repose | 34 |
| Scoria | Fibre cement | Ridge | Dry | 10 | Repose | 37 |
| Scoria | Fibre cement | Ridge | Dry | 10 | Repose | 35 |
| Scoria | Fibre cement | Ridge | Dry | 10 | Repose | 35 |
| Scoria | Fibre cement | Ridge | Dry | 20 | Repose | 35 |
| Scoria | Fibre cement | Ridge | Dry | 20 | Repose | 35 |
| Scoria | Fibre cement | Ridge | Dry | 20 | Repose | 36 |
| Scoria | Tile | NA | Dry | 10 | Repose | 35 |
| Scoria | Tile | NA | Dry | 10 | Repose | 34 |
| Scoria | Tile | NA | Dry | 10 | Repose | 36 |
| Scoria | Tile | NA | Dry | 20 | Repose | 36 |
| Scoria | Tile | NA | Dry | 20 | Repose | 35 |
| Scoria | Tile | NA | Dry | 20 | Repose | 35 |
| Scoria | Metal sheet | Ridge | Dry | 10 | Initial movement | 13 |
| Scoria | Metal sheet | Ridge | Dry | 10 | Initial movement | 16 |
| Scoria | Metal sheet | Ridge | Dry | 10 | Initial movement | 13 |
| Scoria | Metal sheet | Ridge | Dry | 20 | Initial movement | 14 |
| Scoria | Metal sheet | Ridge | Dry | 20 | Initial movement | 14 |
| Scoria | Metal sheet | Ridge | Dry | 20 | Initial movement | 15 |
| Scoria | Fibre cement | Ridge | Dry | 10 | Initial movement | 14 |
| Scoria | Fibre cement | Ridge | Dry | 10 | Initial movement | 15 |
| Scoria | Fibre cement | Ridge | Dry | 10 | Initial movement | 14 |
| Scoria | Fibre cement | Ridge | Dry | 20 | Initial movement | 15 |
| Scoria | Fibre cement | Ridge | Dry | 20 | Initial movement | 14 |
| Scoria | Fibre cement | Ridge | Dry | 20 | Initial movement | 16 |
| Scoria | Tile | NA | Dry | 10 | Initial movement | 15 |
| Scoria | Tile | NA | Dry | 10 | Initial movement | 15 |
| Scoria | Tile | NA | Dry | 10 | Initial movement | 16 |
| Scoria | Tile | NA | Dry | 20 | Initial movement | 13 |
| Scoria | Tile | NA | Dry | 20 | Initial movement | 14 |
| Scoria | Tile | NA | Dry | 20 | Initial movement | 15 |
| Scoria | Metal sheet | Ridge | Wet | 10 | Repose | 44 |
| Scoria | Metal sheet | Ridge | Wet | 10 | Repose | 43 |
| Scoria | Metal sheet | Ridge | Wet | 10 | Repose | 43 |
| Scoria | Metal sheet | Ridge | Wet | 10 | Repose | 42 |
| Scoria | Metal sheet | Ridge | Wet | 10 | Repose | 43 |
| Scoria | Metal sheet | Ridge | Wet | 10 | Initial movement | 14 |
| Scoria | Metal sheet | Ridge | Wet | 10 | Initial movement | 15 |
| Scoria | Metal sheet | Ridge | Wet | 10 | Initial movement | 14 |
| Scoria | Metal sheet | Ridge | Wet | 10 | Initial movement | 15 |
| Scoria | Metal sheet | Ridge | Wet | 10 | Initial movement | 14 |

| Tephra | Roofing | Ridge/Trough | Wet/Dry | Depth | Type | Angle |
|--------|---------|--------------|---------|-------|------|-------|
| Ash | Tile | NA | Dry | 10 | Repose | 35 |
| Ash | Ash | NA | Dry | 10 | Repose | 37 |
| Ash | Ash | NA | Dry | 10 | Repose | 35 |
| Ash | Ash | NA | Dry | 10 | Repose | 35 |
| Ash | Ash | NA | Dry | 10 | Repose | 34 |
| Ash | Ash | Ridge | Dry | 20 | Repose | 35 |
| Ash | Ash | Ridge | Dry | 20 | Repose | 36 |
| Ash | Ash | Ridge | Dry | 20 | Repose | 35 |
| Ash | Ash | Ridge | Dry | 20 | Repose | 36 |
| Ash | Ash | Ridge | Dry | 20 | Repose | 34 |
| Ash | Ash | NA | Dry | 10 | Initial movement | 14 |
| Ash | Ash | NA | Dry | 10 | Initial movement | 11 |
| Ash | Ash | NA | Dry | 10 | Initial movement | 12 |
| Ash | Ash | NA | Dry | 10 | Initial movement | 11 |
| Ash | Ash | NA | Dry | 10 | Initial movement | 11 |
| Ash | Ash | Ridge | Dry | 20 | Initial movement | 11 |
| Ash | Ash | Ridge | Dry | 20 | Initial movement | 10 |
| Ash | Ash | Ridge | Dry | 20 | Initial movement | 13 |
| Ash | Ash | Ridge | Dry | 20 | Initial movement | 12 |
| Ash | Ash | Ridge | Dry | 20 | Initial movement | 10 |
| Ash | Ash | Ridge | Wet | 10 | Repose | 42 |
| Ash | Ash | Ridge | Wet | 10 | Repose | 43 |
| Ash | Ash | Ridge | Wet | 10 | Repose | 40 |
| Ash | Ash | Ridge | Wet | 10 | Repose | 41 |
| Ash | Ash | Ridge | Wet | 10 | Repose | 43 |
| Ash | Ash | Ridge | Wet | 20 | Repose | 42 |
| Ash | Ash | Ridge | Wet | 20 | Repose | 41 |
| Ash | Ash | NA | Wet | 20 | Repose | 43 |
| Ash | Ash | NA | Wet | 20 | Repose | 40 |
| Ash | Ash | NA | Wet | 20 | Repose | 42 |
| Ash | Ash | Ridge | Wet | 10 | Initial movement | 28 |
| Ash | Ash | Ridge | Wet | 10 | Initial movement | 26 |
| Ash | Ash | Ridge | Wet | 10 | Initial movement | 28 |
| Ash | Ash | Ridge | Wet | 10 | Initial movement | 29 |
| Ash | Ash | Ridge | Wet | 10 | Initial movement | 28 |
| Ash | Ash | Ridge | Wet | 10 | Initial movement | 30 |
| Ash | Ash | Ridge | Wet | 10 | Initial movement | 29 |
| Ash | Ash | NA | Wet | 10 | Initial movement | 31 |
| Ash | Ash | NA | Wet | 10 | Initial movement | 30 |
| Ash | Ash | NA | Wet | 10 | Initial movement | 30 |
| Ash | Ash | Ridge | Wet | 20 | Initial movement | 20 |
| Ash | Ash | Ridge | Wet | 20 | Initial movement | 21 |
| Ash | Ash | NA | Wet | 20 | Initial movement | 22 |
| Ash | Ash | NA | Wet | 20 | Initial movement | 20 |
| Ash | Ash | NA | Wet | 20 | Initial movement | 21 |

## Sliding tests

| Tephra | Roofing | Ridge/ Trough | Wet/Dry | Depth | Sliding angle | Where sliding? |
|--------|---------|---------------|---------|-------|---------------|----------------|
| Pumice | Fibre cement | Ridge | Dry-Dry | 10 | 33 | Base |
| Pumice | Fibre cement | Ridge | Dry-Dry | 10 | 33 | Base |
| Pumice | Fibre cement | Ridge | Dry-Dry | 10 | 31 | Base |
| Pumice | Fibre cement | Trough | Dry-Dry | 10 | 33 | Base |
| Pumice | Fibre cement | Trough | Dry-Dry | 10 | 32 | Base |
| Pumice | Fibre cement | Trough | Dry-Dry | 10 | 32 | Base |
| Pumice | Fibre cement | Ridge | Dry-Dry | 20 | 32 | Base |
| Pumice | Fibre cement | Ridge | Dry-Dry | 20 | 31 | Base |

# Appendix B: Supplementary material for Chapter 3

| Tephra | Roofing | Ridge/ Trough | Wet/Dry | Depth | Sliding angle | Where sliding? |
|---|---|---|---|---|---|---|
| Pumice | Fibre cement | Ridge | Dry-Dry | 20 | 31 | Base |
| Pumice | Fibre cement | Ridge | Dry-Dry | 20 | 30 | Base |
| Pumice | Fibre cement | Ridge | Dry-Dry | 20 | 31 | Base |
| Pumice | Fibre cement - weathered | Ridge | Dry-Dry | 20 | 30 | Base |
| Pumice | Fibre cement - weathered | Ridge | Dry-Dry | 20 | 31 | Base |
| Pumice | Fibre cement | Ridge | Dry-Dry | 30 | 33 | Base |
| Pumice | Fibre cement | Ridge | Dry-Dry | 30 | 32 | Base |
| Pumice | Fibre cement | Ridge | Dry-Dry | 30 | 32 | Base |
| Pumice | Fibre cement | Ridge | Dry-Dry | 30 | 31 | Base |
| Pumice | Fibre cement | Ridge | Dry-Dry | 30 | 31 | Tephra |
| Pumice | Metal sheet | Ridge | Dry-Dry | 10 | 25 | Base |
| Pumice | Metal sheet | Ridge | Dry-Dry | 10 | 26 | Base |
| Pumice | Metal sheet | Ridge | Dry-Dry | 10 | 26 | Base |
| Pumice | Metal sheet | Trough | Dry-Dry | 10 | 26 | Base |
| Pumice | Metal sheet | Trough | Dry-Dry | 10 | 27 | Base |
| Pumice | Metal sheet | Trough | Dry-Dry | 10 | 27 | Base |
| Pumice | Metal sheet | Ridge | Dry-Dry | 20 | 30 | Base |
| Pumice | Metal sheet | Ridge | Dry-Dry | 20 | 28 | Base |
| Pumice | Metal sheet | Ridge | Dry-Dry | 20 | 29 | Base |
| Pumice | Metal sheet | Ridge | Dry-Dry | 20 | 28 | Base |
| Pumice | Metal sheet | Ridge | Dry-Dry | 20 | 28 | Base |
| Pumice | Metal sheet - weathered | Ridge | Dry-Dry | 20 | 29 | Base |
| Pumice | Metal sheet - weathered | Ridge | Dry-Dry | 20 | 28 | Base |
| Pumice | Metal sheet - weathered | Ridge | Dry-Dry | 20 | 28 | Base |
| Pumice | Metal sheet - weathered | Ridge | Dry-Dry | 20 | 28 | Base |
| Pumice | Metal sheet - weathered | Ridge | Dry-Dry | 20 | 29 | Base |
| Pumice | Metal sheet | Ridge | Dry-Dry | 30 | 28 | Base |
| Pumice | Metal sheet | Ridge | Dry-Dry | 30 | 28 | Base |
| Pumice | Metal sheet | Ridge | Dry-Dry | 30 | 27 | Base |
| Pumice | Metal sheet | Ridge | Dry-Dry | 30 | 28 | Base |
| Pumice | Metal sheet | Ridge | Dry-Dry | 30 | 27 | Base |
| Pumice | Tile | NA | Dry-Dry | 10 | 31 | Base |
| Pumice | Tile | NA | Dry-Dry | 10 | 33 | Base |
| Pumice | Tile | NA | Dry-Dry | 10 | 31 | Base |
| Pumice | Tile | NA | Dry-Dry | 10 | 34 | Base |
| Pumice | Tile | NA | Dry-Dry | 10 | 34 | Base |
| Pumice | Tile | NA | Dry-Dry | 20 | 34 | Base |
| Pumice | Tile | NA | Dry-Dry | 20 | 32 | Base |
| Pumice | Tile | NA | Dry-Dry | 20 | 32 | Base |
| Pumice | Tile | NA | Dry-Dry | 20 | 33 | Base |
| Pumice | Tile | NA | Dry-Dry | 20 | 31 | Base |
| Pumice | Tile | NA | Dry-Dry | 30 | 32 | Base |
| Pumice | Tile | NA | Dry-Dry | 30 | 33 | Base |
| Pumice | Tile | NA | Dry-Dry | 30 | 32 | Base |
| Pumice | Tile | NA | Dry-Dry | 30 | 32 | Base |
| Pumice | Tile | NA | Dry-Dry | 30 | 31 | Base |
| Pumice | Fibre cement | Ridge | Dry-Wet | 10 | 31 | Base |
| Pumice | Fibre cement | Ridge | Dry-Wet | 10 | 34 | Base |
| Pumice | Fibre cement | Ridge | Dry-Wet | 10 | 32 | Base |
| Pumice | Fibre cement | Ridge | Dry-Wet | 10 | 32 | Base |
| Pumice | Fibre cement | Ridge | Dry-Wet | 10 | 32 | Base |
| Pumice | Fibre cement | Ridge | Dry-Wet | 20 | 30 | Base |
| Pumice | Fibre cement | Ridge | Dry-Wet | 20 | 31 | Base |
| Pumice | Fibre cement | Ridge | Dry-Wet | 20 | 32 | Base |
| Pumice | Fibre cement | Ridge | Dry-Wet | 20 | 31 | Base |
| Pumice | Fibre cement | Ridge | Dry-Wet | 20 | 33 | Base |
| Pumice | Fibre cement | Ridge | Dry-Wet | 30 | 31 | Base |

| Tephra | Roofing | Ridge/ Trough | Wet/Dry | Depth | Sliding angle | Where sliding? |
|--------|---------|---------------|---------|-------|---------------|----------------|
| Pumice | Fibre cement | Ridge | Dry-Wet | 30 | 32 | Base |
| Pumice | Fibre cement | Ridge | Dry-Wet | 30 | 32 | Base |
| Pumice | Fibre cement | Ridge | Dry-Wet | 30 | 29 | Base |
| Pumice | Fibre cement | Ridge | Dry-Wet | 30 | 30 | Base |
| Pumice | Metal sheet | Ridge | Dry-Wet | 10 | 28 | Base |
| Pumice | Metal sheet | Ridge | Dry-Wet | 10 | 30 | Base |
| Pumice | Metal sheet | Ridge | Dry-Wet | 10 | 32 | Base |
| Pumice | Metal sheet | Ridge | Dry-Wet | 10 | 31 | Base |
| Pumice | Metal sheet | Ridge | Dry-Wet | 10 | 30 | Base |
| Pumice | Metal sheet | Ridge | Dry-Wet | 20 | 28 | Base |
| Pumice | Metal sheet | Ridge | Dry-Wet | 20 | 29 | Base |
| Pumice | Metal sheet | Ridge | Dry-Wet | 20 | 29 | Base |
| Pumice | Metal sheet | Ridge | Dry-Wet | 20 | 30 | Base |
| Pumice | Metal sheet | Ridge | Dry-Wet | 20 | 30 | Base |
| Pumice | Metal sheet | Ridge | Dry-Wet | 30 | 30 | Base |
| Pumice | Metal sheet | Ridge | Dry-Wet | 30 | 29 | Base |
| Pumice | Metal sheet | Ridge | Dry-Wet | 30 | 27 | Base |
| Pumice | Metal sheet | Ridge | Dry-Wet | 30 | 30 | Base |
| Pumice | Metal sheet | Ridge | Dry-Wet | 30 | 28 | Base |
| Pumice | Tile | NA | Dry-Wet | 10 | 32 | Base |
| Pumice | Tile | NA | Dry-Wet | 10 | 35 | Base |
| Pumice | Tile | NA | Dry-Wet | 10 | 33 | Base |
| Pumice | Tile | NA | Dry-Wet | 10 | 33 | Base |
| Pumice | Tile | NA | Dry-Wet | 10 | 34 | Base |
| Pumice | Tile | NA | Dry-Wet | 20 | 33 | Base |
| Pumice | Tile | NA | Dry-Wet | 20 | 31 | Base |
| Pumice | Tile | NA | Dry-Wet | 20 | 31 | Base |
| Pumice | Tile | NA | Dry-Wet | 20 | 32 | Base |
| Pumice | Tile | NA | Dry-Wet | 20 | 32 | Base |
| Pumice | Tile | NA | Dry-Wet | 30 | 29 | Base |
| Pumice | Tile | NA | Dry-Wet | 30 | 31 | Base |
| Pumice | Tile | NA | Dry-Wet | 30 | 31 | Base |
| Pumice | Tile | NA | Dry-Wet | 30 | 32 | Base |
| Pumice | Tile | NA | Dry-Wet | 30 | 30 | Base |
| Pumice | Fibre cement | Ridge | Wet-Wet | 10 | 32 | Base |
| Pumice | Fibre cement | Ridge | Wet-Wet | 10 | 31 | Base |
| Pumice | Fibre cement | Ridge | Wet-Wet | 10 | 30 | Base |
| Pumice | Fibre cement | Ridge | Wet-Wet | 10 | 32 | Base |
| Pumice | Fibre cement | Ridge | Wet-Wet | 10 | 30 | Base |
| Pumice | Fibre cement | Ridge | Wet-Wet | 20 | 30 | Base |
| Pumice | Fibre cement | Ridge | Wet-Wet | 20 | 31 | Base |
| Pumice | Fibre cement | Ridge | Wet-Wet | 20 | 29 | Base |
| Pumice | Fibre cement | Ridge | Wet-Wet | 20 | 31 | Base |
| Pumice | Fibre cement | Ridge | Wet-Wet | 20 | 30 | Base |
| Pumice | Fibre cement | Ridge | Wet-Wet | 30 | 29 | Base |
| Pumice | Fibre cement | Ridge | Wet-Wet | 30 | 28 | Base |
| Pumice | Fibre cement | Ridge | Wet-Wet | 30 | 30 | Tephra |
| Pumice | Fibre cement | Ridge | Wet-Wet | 30 | 29 | Tephra |
| Pumice | Fibre cement | Ridge | Wet-Wet | 30 | 28 | Tephra |
| Pumice | Metal sheet | Ridge | Wet-Wet | 10 | 30 | Base |
| Pumice | Metal sheet | Ridge | Wet-Wet | 10 | 30 | Base |
| Pumice | Metal sheet | Ridge | Wet-Wet | 10 | 28 | Base |
| Pumice | Metal sheet | Ridge | Wet-Wet | 10 | 31 | Base |
| Pumice | Metal sheet | Ridge | Wet-Wet | 10 | 32 | Base |
| Pumice | Metal sheet | Ridge | Wet-Wet | 20 | 27 | Base |
| Pumice | Metal sheet | Ridge | Wet-Wet | 20 | 28 | Base |
| Pumice | Metal sheet | Ridge | Wet-Wet | 20 | 29 | Base |

# Appendix B: Supplementary material for Chapter 3

| Tephra | Roofing | Ridge/ Trough | Wet/Dry | Depth | Sliding angle | Where sliding? |
|---|---|---|---|---|---|---|
| Pumice | Metal sheet | Ridge | Wet-Wet | 20 | 30 | Base |
| Pumice | Metal sheet | Ridge | Wet-Wet | 20 | 30 | Base |
| Pumice | Metal sheet | Ridge | Wet-Wet | 30 | 28 | Base |
| Pumice | Metal sheet | Ridge | Wet-Wet | 30 | 28 | Base |
| Pumice | Metal sheet | Ridge | Wet-Wet | 30 | 27 | Base |
| Pumice | Metal sheet | Ridge | Wet-Wet | 30 | 28 | Base |
| Pumice | Metal sheet | Ridge | Wet-Wet | 30 | 27 | Base |
| Pumice | Tile | NA | Wet-Wet | 10 | 30 | Base |
| Pumice | Tile | NA | Wet-Wet | 10 | 30 | Base |
| Pumice | Tile | NA | Wet-Wet | 10 | 30 | Base |
| Pumice | Tile | NA | Wet-Wet | 10 | 31 | Base |
| Pumice | Tile | NA | Wet-Wet | 10 | 32 | Base |
| Pumice | Tile | NA | Wet-Wet | 20 | 30 | Base |
| Pumice | Tile | NA | Wet-Wet | 20 | 28 | Base |
| Pumice | Tile | NA | Wet-Wet | 20 | 29 | Base |
| Pumice | Tile | NA | Wet-Wet | 20 | 30 | Base |
| Pumice | Tile | NA | Wet-Wet | 20 | 29 | Base |
| Pumice | Tile | NA | Wet-Wet | 30 | 27 | Base |
| Pumice | Tile | NA | Wet-Wet | 30 | 28 | Tephra |
| Pumice | Tile | NA | Wet-Wet | 30 | 29 | Tephra |
| Pumice | Tile | NA | Wet-Wet | 30 | 27 | Tephra |
| Pumice | Tile | NA | Wet-Wet | 30 | 30 | Tephra |
| Scoria | Fibre cement | Ridge | Dry-Dry | 10 | 35 | Base |
| Scoria | Fibre cement | Ridge | Dry-Dry | 10 | 35 | Base |
| Scoria | Fibre cement | Ridge | Dry-Dry | 10 | 34 | Base |
| Scoria | Fibre cement | Ridge | Dry-Dry | 10 | 36 | Base |
| Scoria | Fibre cement | Ridge | Dry-Dry | 10 | 34 | Base |
| Scoria | Fibre cement | Ridge | Dry-Dry | 20 | 31 | Base |
| Scoria | Fibre cement | Ridge | Dry-Dry | 20 | 32 | Base |
| Scoria | Fibre cement | Ridge | Dry-Dry | 20 | 31 | Base |
| Scoria | Fibre cement | Ridge | Dry-Dry | 20 | 29 | Base |
| Scoria | Fibre cement | Ridge | Dry-Dry | 20 | 31 | Base |
| Scoria | Fibre cement - weathered | Ridge | Dry-Dry | 20 | 31 | Base |
| Scoria | Fibre cement - weathered | Ridge | Dry-Dry | 20 | 32 | Base |
| Scoria | Fibre cement | Ridge | Dry-Dry | 30 | 29 | Base |
| Scoria | Fibre cement | Ridge | Dry-Dry | 30 | 30 | Base |
| Scoria | Fibre cement | Ridge | Dry-Dry | 30 | 31 | Base |
| Scoria | Fibre cement | Ridge | Dry-Dry | 30 | 32 | Base |
| Scoria | Fibre cement | Ridge | Dry-Dry | 30 | 30 | Base |
| Scoria | Metal sheet | Ridge | Dry-Dry | 10 | 27 | Base |
| Scoria | Metal sheet | Ridge | Dry-Dry | 10 | 27 | Base |
| Scoria | Metal sheet | Ridge | Dry-Dry | 10 | 28 | Base |
| Scoria | Metal sheet | Ridge | Dry-Dry | 10 | 28 | Base |
| Scoria | Metal sheet | Ridge | Dry-Dry | 10 | 26 | Base |
| Scoria | Metal sheet | Ridge | Dry-Dry | 20 | 26 | Base |
| Scoria | Metal sheet | Ridge | Dry-Dry | 20 | 26 | Base |
| Scoria | Metal sheet | Ridge | Dry-Dry | 20 | 26 | Base |
| Scoria | Metal sheet | Ridge | Dry-Dry | 20 | 25 | Base |
| Scoria | Metal sheet | Ridge | Dry-Dry | 20 | 27 | Base |
| Scoria | Metal sheet - weathered | Ridge | Dry-Dry | 20 | 25 | Base |
| Scoria | Metal sheet - weathered | Ridge | Dry-Dry | 20 | 26 | Base |
| Scoria | Metal sheet - weathered | Ridge | Dry-Dry | 20 | 27 | Base |
| Scoria | Metal sheet - weathered | Ridge | Dry-Dry | 20 | 26 | Base |
| Scoria | Metal sheet - weathered | Ridge | Dry-Dry | 20 | 27 | Base |
| Scoria | Metal sheet | Ridge | Dry-Dry | 30 | 24 | Base |
| Scoria | Metal sheet | Ridge | Dry-Dry | 30 | 22 | Base |
| Scoria | Metal sheet | Ridge | Dry-Dry | 30 | 24 | Base |

| Tephra | Roofing | Ridge/Trough | Wet/Dry | Depth | Sliding angle | Where sliding? |
|---|---|---|---|---|---|---|
| Scoria | Metal sheet | Ridge | Dry-Dry | 30 | 23 | Base |
| Scoria | Metal sheet | Ridge | Dry-Dry | 30 | 25 | Base |
| Scoria | Tile | NA | Dry-Dry | 10 | 34 | Base |
| Scoria | Tile | NA | Dry-Dry | 10 | 36 | Base |
| Scoria | Tile | NA | Dry-Dry | 10 | 34 | Base |
| Scoria | Tile | NA | Dry-Dry | 10 | 35 | Base |
| Scoria | Tile | NA | Dry-Dry | 10 | 34 | Base |
| Scoria | Tile | NA | Dry-Dry | 20 | 29 | Base |
| Scoria | Tile | NA | Dry-Dry | 20 | 31 | Base |
| Scoria | Tile | NA | Dry-Dry | 20 | 32 | Base |
| Scoria | Tile | NA | Dry-Dry | 20 | 29 | Base |
| Scoria | Tile | NA | Dry-Dry | 20 | 29 | Base |
| Scoria | Tile | NA | Dry-Dry | 30 | 28 | Base |
| Scoria | Tile | NA | Dry-Dry | 30 | 29 | Base |
| Scoria | Tile | NA | Dry-Dry | 30 | 29 | Base |
| Scoria | Tile | NA | Dry-Dry | 30 | 28 | Base |
| Scoria | Tile | NA | Dry-Dry | 30 | 28 | Base |
| Scoria | Fibre cement | Ridge | Dry-Wet | 10 | 33 | Base |
| Scoria | Fibre cement | Ridge | Dry-Wet | 10 | 35 | Base |
| Scoria | Fibre cement | Ridge | Dry-Wet | 10 | 36 | Base |
| Scoria | Fibre cement | Ridge | Dry-Wet | 10 | 34 | Base |
| Scoria | Fibre cement | Ridge | Dry-Wet | 10 | 36 | Base |
| Scoria | Fibre cement | Ridge | Dry-Wet | 20 | 31 | Base |
| Scoria | Fibre cement | Ridge | Dry-Wet | 20 | 32 | Base |
| Scoria | Fibre cement | Ridge | Dry-Wet | 20 | 33 | Base |
| Scoria | Fibre cement | Ridge | Dry-Wet | 20 | 32 | Base |
| Scoria | Fibre cement | Ridge | Dry-Wet | 20 | 33 | Base |
| Scoria | Fibre cement | Ridge | Dry-Wet | 30 | 30 | Base |
| Scoria | Fibre cement | Ridge | Dry-Wet | 30 | 31 | Base |
| Scoria | Fibre cement | Ridge | Dry-Wet | 30 | 29 | Base |
| Scoria | Fibre cement | Ridge | Dry-Wet | 30 | 29 | Base |
| Scoria | Fibre cement | Ridge | Dry-Wet | 30 | 29 | Base |
| Scoria | Metal sheet | Ridge | Dry-Wet | 10 | 32 | Base |
| Scoria | Metal sheet | Ridge | Dry-Wet | 10 | 31 | Base |
| Scoria | Metal sheet | Ridge | Dry-Wet | 10 | 31 | Base |
| Scoria | Metal sheet | Ridge | Dry-Wet | 10 | 31 | Base |
| Scoria | Metal sheet | Ridge | Dry-Wet | 10 | 33 | Base |
| Scoria | Metal sheet | Ridge | Dry-Wet | 20 | 28 | Base |
| Scoria | Metal sheet | Ridge | Dry-Wet | 20 | 28 | Base |
| Scoria | Metal sheet | Ridge | Dry-Wet | 20 | 27 | Base |
| Scoria | Metal sheet | Ridge | Dry-Wet | 20 | 29 | Base |
| Scoria | Metal sheet | Ridge | Dry-Wet | 20 | 30 | Base |
| Scoria | Metal sheet | Ridge | Dry-Wet | 30 | 28 | Base |
| Scoria | Metal sheet | Ridge | Dry-Wet | 30 | 27 | Base |
| Scoria | Metal sheet | Ridge | Dry-Wet | 30 | 26 | Base |
| Scoria | Metal sheet | Ridge | Dry-Wet | 30 | 28 | Base |
| Scoria | Metal sheet | Ridge | Dry-Wet | 30 | 28 | Base |
| Scoria | Tile | NA | Dry-Wet | 10 | 37 | Base |
| Scoria | Tile | NA | Dry-Wet | 10 | 36 | Base |
| Scoria | Tile | NA | Dry-Wet | 10 | 36 | Base |
| Scoria | Tile | NA | Dry-Wet | 10 | 35 | Base |
| Scoria | Tile | NA | Dry-Wet | 10 | 36 | Base |
| Scoria | Tile | NA | Dry-Wet | 20 | 33 | Base |
| Scoria | Tile | NA | Dry-Wet | 20 | 34 | Base |
| Scoria | Tile | NA | Dry-Wet | 20 | 33 | Base |
| Scoria | Tile | NA | Dry-Wet | 20 | 35 | Base |
| Scoria | Tile | NA | Dry-Wet | 20 | 34 | Base |

# Appendix B: Supplementary material for Chapter 3

| Tephra | Roofing | Ridge/ Trough | Wet/Dry | Depth | Sliding angle | Where sliding? |
|--------|---------|---------------|---------|-------|---------------|----------------|
| Scoria | Tile | NA | Dry-Wet | 30 | 31 | Base |
| Scoria | Tile | NA | Dry-Wet | 30 | 31 | Base |
| Scoria | Tile | NA | Dry-Wet | 30 | 30 | Base |
| Scoria | Tile | NA | Dry-Wet | 30 | 30 | Base |
| Scoria | Tile | NA | Dry-Wet | 30 | 32 | Base |
| Scoria | Fibre cement | Ridge | Wet-Wet | 10 | 32 | Base |
| Scoria | Fibre cement | Ridge | Wet-Wet | 10 | 31 | Base |
| Scoria | Fibre cement | Ridge | Wet-Wet | 10 | 31 | Base |
| Scoria | Fibre cement | Ridge | Wet-Wet | 10 | 30 | Base |
| Scoria | Fibre cement | Ridge | Wet-Wet | 10 | 32 | Base |
| Scoria | Fibre cement | Ridge | Wet-Wet | 20 | 30 | Base |
| Scoria | Fibre cement | Ridge | Wet-Wet | 20 | 30 | Base |
| Scoria | Fibre cement | Ridge | Wet-Wet | 20 | 31 | Base |
| Scoria | Fibre cement | Ridge | Wet-Wet | 20 | 30 | Base |
| Scoria | Fibre cement | Ridge | Wet-Wet | 20 | 31 | Base |
| Scoria | Fibre cement | Ridge | Wet-Wet | 30 | 25 | Base |
| Scoria | Fibre cement | Ridge | Wet-Wet | 30 | 28 | Base |
| Scoria | Fibre cement | Ridge | Wet-Wet | 30 | 28 | Base |
| Scoria | Fibre cement | Ridge | Wet-Wet | 30 | 28 | Base |
| Scoria | Fibre cement | Ridge | Wet-Wet | 30 | 27 | Tephra |
| Scoria | Metal sheet | Ridge | Wet-Wet | 10 | 27 | Base |
| Scoria | Metal sheet | Ridge | Wet-Wet | 10 | 27 | Base |
| Scoria | Metal sheet | Ridge | Wet-Wet | 10 | 28 | Base |
| Scoria | Metal sheet | Ridge | Wet-Wet | 10 | 28 | Base |
| Scoria | Metal sheet | Ridge | Wet-Wet | 10 | 27 | Base |
| Scoria | Metal sheet | Ridge | Wet-Wet | 20 | 27 | Base |
| Scoria | Metal sheet | Ridge | Wet-Wet | 20 | 28 | Base |
| Scoria | Metal sheet | Ridge | Wet-Wet | 20 | 27 | Base |
| Scoria | Metal sheet | Ridge | Wet-Wet | 20 | 28 | Base |
| Scoria | Metal sheet | Ridge | Wet-Wet | 20 | 27 | Base |
| Scoria | Metal sheet | Ridge | Wet-Wet | 30 | 24 | Base |
| Scoria | Metal sheet | Ridge | Wet-Wet | 30 | 26 | Base |
| Scoria | Metal sheet | Ridge | Wet-Wet | 30 | 26 | Base |
| Scoria | Metal sheet | Ridge | Wet-Wet | 30 | 25 | Base |
| Scoria | Metal sheet | Ridge | Wet-Wet | 30 | 26 | Tephra |
| Scoria | Tile | NA | Wet-Wet | 10 | 32 | Base |
| Scoria | Tile | NA | Wet-Wet | 10 | 31 | Base |
| Scoria | Tile | NA | Wet-Wet | 10 | 30 | Base |
| Scoria | Tile | NA | Wet-Wet | 10 | 31 | Base |
| Scoria | Tile | NA | Wet-Wet | 10 | 30 | Base |
| Scoria | Tile | NA | Wet-Wet | 20 | 30 | Base |
| Scoria | Tile | NA | Wet-Wet | 20 | 30 | Base |
| Scoria | Tile | NA | Wet-Wet | 20 | 28 | Base |
| Scoria | Tile | NA | Wet-Wet | 20 | 31 | Base |
| Scoria | Tile | NA | Wet-Wet | 20 | 30 | Base |
| Scoria | Tile | NA | Wet-Wet | 30 | 27 | Tephra |
| Scoria | Tile | NA | Wet-Wet | 30 | 27 | Tephra |
| Scoria | Tile | NA | Wet-Wet | 30 | 28 | Tephra |
| Scoria | Tile | NA | Wet-Wet | 30 | 28 | Tephra |
| Scoria | Tile | NA | Wet-Wet | 30 | 28 | Tephra |
| Ash | Fibre cement | Ridge | Dry-Dry | 10 | 30 | Base |
| Ash | Fibre cement | Ridge | Dry-Dry | 10 | 30 | Base |
| Ash | Fibre cement | Ridge | Dry-Dry | 10 | 29 | Base |
| Ash | Fibre cement | Ridge | Dry-Dry | 10 | 31 | Base |
| Ash | Fibre cement | Ridge | Dry-Dry | 10 | 29 | Base |
| Ash | Fibre cement | Ridge | Dry-Dry | 20 | 28 | Base |
| Ash | Fibre cement | Ridge | Dry-Dry | 20 | 28 | Base |

| Tephra | Roofing | Ridge/ Trough | Wet/Dry | Depth | Sliding angle | Where sliding? |
|--------|---------|---------------|---------|-------|---------------|----------------|
| Ash | Fibre cement | Ridge | Dry-Dry | 20 | 28 | Base |
| Ash | Fibre cement | Ridge | Dry-Dry | 20 | 29 | Base |
| Ash | Fibre cement | Ridge | Dry-Dry | 20 | 28 | Base |
| Ash | Fibre cement | Ridge | Dry-Dry | 30 | 25 | Base |
| Ash | Fibre cement | Ridge | Dry-Dry | 30 | 25 | Base |
| Ash | Fibre cement | Ridge | Dry-Dry | 30 | 26 | Base |
| Ash | Fibre cement | Ridge | Dry-Dry | 30 | 25 | Base |
| Ash | Fibre cement | Ridge | Dry-Dry | 30 | 26 | Base |
| Ash | Metal sheet | Ridge | Dry-Dry | 10 | 24 | Base |
| Ash | Metal sheet | Ridge | Dry-Dry | 10 | 26 | Base |
| Ash | Metal sheet | Ridge | Dry-Dry | 10 | 27 | Base |
| Ash | Metal sheet | Ridge | Dry-Dry | 10 | 28 | Base |
| Ash | Metal sheet | Ridge | Dry-Dry | 10 | 28 | Base |
| Ash | Metal sheet | Ridge | Dry-Dry | 20 | 24 | Base |
| Ash | Metal sheet | Ridge | Dry-Dry | 20 | 26 | Base |
| Ash | Metal sheet | Ridge | Dry-Dry | 20 | 26 | Base |
| Ash | Metal sheet | Ridge | Dry-Dry | 20 | 25 | Base |
| Ash | Metal sheet | Ridge | Dry-Dry | 20 | 26 | Base |
| Ash | Metal sheet | Ridge | Dry-Dry | 30 | 24 | Base |
| Ash | Metal sheet | Ridge | Dry-Dry | 30 | 23 | Base |
| Ash | Metal sheet | Ridge | Dry-Dry | 30 | 22 | Base |
| Ash | Metal sheet | Ridge | Dry-Dry | 30 | 23 | Base |
| Ash | Metal sheet | Ridge | Dry-Dry | 30 | 23 | Base |
| Ash | Tile | NA | Dry-Dry | 10 | 33 | Base |
| Ash | Tile | NA | Dry-Dry | 10 | 32 | Base |
| Ash | Tile | NA | Dry-Dry | 10 | 35 | Base |
| Ash | Tile | NA | Dry-Dry | 10 | 33 | Base |
| Ash | Tile | NA | Dry-Dry | 10 | 34 | Base |
| Ash | Tile | NA | Dry-Dry | 20 | 30 | Base |
| Ash | Tile | NA | Dry-Dry | 20 | 33 | Tephra |
| Ash | Tile | NA | Dry-Dry | 20 | 31 | Base |
| Ash | Tile | NA | Dry-Dry | 20 | 30 | Tephra |
| Ash | Tile | NA | Dry-Dry | 20 | 29 | Base |
| Ash | Tile | NA | Dry-Dry | 30 | 30 | Tephra |
| Ash | Tile | NA | Dry-Dry | 30 | 30 | Tephra |
| Ash | Tile | NA | Dry-Dry | 30 | 29 | Tephra |
| Ash | Tile | NA | Dry-Dry | 30 | 29 | Tephra |
| Ash | Tile | NA | Dry-Dry | 30 | 31 | Tephra |
| Ash | Fibre cement | Ridge | Dry-Wet | 10 | 30 | Base |
| Ash | Fibre cement | Ridge | Dry-Wet | 10 | 30 | Base |
| Ash | Fibre cement | Ridge | Dry-Wet | 10 | 32 | Base |
| Ash | Fibre cement | Ridge | Dry-Wet | 10 | 31 | Base |
| Ash | Fibre cement | Ridge | Dry-Wet | 10 | 31 | Base |
| Ash | Fibre cement | Ridge | Dry-Wet | 20 | 29 | Base |
| Ash | Fibre cement | Ridge | Dry-Wet | 20 | 30 | Base |
| Ash | Fibre cement | Ridge | Dry-Wet | 20 | 29 | Base |
| Ash | Fibre cement | Ridge | Dry-Wet | 20 | 29 | Base |
| Ash | Fibre cement | Ridge | Dry-Wet | 20 | 31 | Base |
| Ash | Fibre cement | Ridge | Dry-Wet | 30 | 26 | Base |
| Ash | Fibre cement | Ridge | Dry-Wet | 30 | 26 | Base |
| Ash | Fibre cement | Ridge | Dry-Wet | 30 | 25 | Base |
| Ash | Fibre cement | Ridge | Dry-Wet | 30 | 27 | Base |
| Ash | Fibre cement | Ridge | Dry-Wet | 30 | 25 | Base |
| Ash | Metal sheet | Ridge | Dry-Wet | 10 | 30 | Base |
| Ash | Metal sheet | Ridge | Dry-Wet | 10 | 31 | Base |
| Ash | Metal sheet | Ridge | Dry-Wet | 10 | 29 | Base |
| Ash | Metal sheet | Ridge | Dry-Wet | 10 | 31 | Base |

# Appendix B: Supplementary material for Chapter 3

| Tephra | Roofing | Ridge/ Trough | Wet/Dry | Depth | Sliding angle | Where sliding? |
|---|---|---|---|---|---|---|
| Ash | Metal sheet | Ridge | Dry-Wet | 10 | 32 | Base |
| Ash | Metal sheet | Ridge | Dry-Wet | 20 | 28 | Base |
| Ash | Metal sheet | Ridge | Dry-Wet | 20 | 30 | Base |
| Ash | Metal sheet | Ridge | Dry-Wet | 20 | 29 | Base |
| Ash | Metal sheet | Ridge | Dry-Wet | 20 | 29 | Base |
| Ash | Metal sheet | Ridge | Dry-Wet | 20 | 30 | Base |
| Ash | Metal sheet | Ridge | Dry-Wet | 30 | 24 | Base |
| Ash | Metal sheet | Ridge | Dry-Wet | 30 | 25 | Base |
| Ash | Metal sheet | Ridge | Dry-Wet | 30 | 25 | Base |
| Ash | Metal sheet | Ridge | Dry-Wet | 30 | 26 | Base |
| Ash | Metal sheet | Ridge | Dry-Wet | 30 | 23 | Base |
| Ash | Tile | NA | Dry-Wet | 10 | 37 | Base |
| Ash | Tile | NA | Dry-Wet | 10 | 36 | Base |
| Ash | Tile | NA | Dry-Wet | 10 | 35 | Base |
| Ash | Tile | NA | Dry-Wet | 10 | 36 | Base |
| Ash | Tile | NA | Dry-Wet | 10 | 36 | Base |
| Ash | Tile | NA | Dry-Wet | 20 | 33 | Base |
| Ash | Tile | NA | Dry-Wet | 20 | 35 | Tephra |
| Ash | Tile | NA | Dry-Wet | 20 | 34 | Tephra |
| Ash | Tile | NA | Dry-Wet | 20 | 32 | Tephra |
| Ash | Tile | NA | Dry-Wet | 20 | 33 | Base |
| Ash | Tile | NA | Dry-Wet | 30 | 30 | Tephra |
| Ash | Tile | NA | Dry-Wet | 30 | 31 | Tephra |
| Ash | Tile | NA | Dry-Wet | 30 | 30 | Tephra |
| Ash | Tile | NA | Dry-Wet | 30 | 31 | Tephra |
| Ash | Tile | NA | Dry-Wet | 30 | 31 | Tephra |
| Ash | Fibre cement | Ridge | Wet-Wet | 10 | 35 | Base |
| Ash | Fibre cement | Ridge | Wet-Wet | 10 | 33 | Base |
| Ash | Fibre cement | Ridge | Wet-Wet | 10 | 34 | Base |
| Ash | Fibre cement | Ridge | Wet-Wet | 10 | 32 | Base |
| Ash | Fibre cement | Ridge | Wet-Wet | 10 | 35 | Base |
| Ash | Fibre cement | Ridge | Wet-Wet | 20 | 30 | Base |
| Ash | Fibre cement | Ridge | Wet-Wet | 20 | 32 | Base |
| Ash | Fibre cement | Ridge | Wet-Wet | 20 | 33 | Base |
| Ash | Fibre cement | Ridge | Wet-Wet | 20 | 31 | Base |
| Ash | Fibre cement | Ridge | Wet-Wet | 20 | 30 | Base |
| Ash | Fibre cement | Ridge | Wet-Wet | 30 | 29 | Base |
| Ash | Fibre cement | Ridge | Wet-Wet | 30 | 30 | Tephra |
| Ash | Fibre cement | Ridge | Wet-Wet | 30 | 29 | Base |
| Ash | Fibre cement | Ridge | Wet-Wet | 30 | 30 | Tephra |
| Ash | Fibre cement | Ridge | Wet-Wet | 30 | 31 | Base |
| Ash | Metal sheet | Ridge | Wet-Wet | 10 | 29 | Base |
| Ash | Metal sheet | Ridge | Wet-Wet | 10 | 29 | Base |
| Ash | Metal sheet | Ridge | Wet-Wet | 10 | 31 | Base |
| Ash | Metal sheet | Ridge | Wet-Wet | 10 | 29 | Base |
| Ash | Metal sheet | Ridge | Wet-Wet | 10 | 32 | Base |
| Ash | Metal sheet | Ridge | Wet-Wet | 20 | 27 | Base |
| Ash | Metal sheet | Ridge | Wet-Wet | 20 | 29 | Base |
| Ash | Metal sheet | Ridge | Wet-Wet | 20 | 28 | Base |
| Ash | Metal sheet | Ridge | Wet-Wet | 20 | 27 | Base |
| Ash | Metal sheet | Ridge | Wet-Wet | 20 | 30 | Base |
| Ash | Metal sheet | Ridge | Wet-Wet | 30 | 26 | Base |
| Ash | Metal sheet | Ridge | Wet-Wet | 30 | 27 | Base |
| Ash | Metal sheet | Ridge | Wet-Wet | 30 | 28 | Base |
| Ash | Metal sheet | Ridge | Wet-Wet | 30 | 28 | Base |
| Ash | Metal sheet | Ridge | Wet-Wet | 30 | 29 | Base |
| Ash | Tile | NA | Wet-Wet | 10 | 34 | Base |

| Tephra | Roofing | Ridge/ Trough | Wet/Dry | Depth | Sliding angle | Where sliding? |
|---|---|---|---|---|---|---|
| Ash | Tile | NA | Wet-Wet | 10 | 32 | Base |
| Ash | Tile | NA | Wet-Wet | 10 | 34 | Base |
| Ash | Tile | NA | Wet-Wet | 10 | 33 | Base |
| Ash | Tile | NA | Wet-Wet | 10 | 33 | Base |
| Ash | Tile | NA | Wet-Wet | 20 | 31 | Base |
| Ash | Tile | NA | Wet-Wet | 20 | 31 | Base |
| Ash | Tile | NA | Wet-Wet | 20 | 31 | Base |
| Ash | Tile | NA | Wet-Wet | 20 | 33 | Base |
| Ash | Tile | NA | Wet-Wet | 20 | 34 | Base |
| Ash | Tile | NA | Wet-Wet | 30 | 33 | Tephra |
| Ash | Tile | NA | Wet-Wet | 30 | 30 | Base |
| Ash | Tile | NA | Wet-Wet | 30 | 33 | Base |
| Ash | Tile | NA | Wet-Wet | 30 | 32 | Base |
| Ash | Tile | NA | Wet-Wet | 30 | 30 | Base |

## B2 Volume of corrugated sheet troughs

Fibre cement profile



19 mm

72 mm

Metal profile



15 mm

76 mm
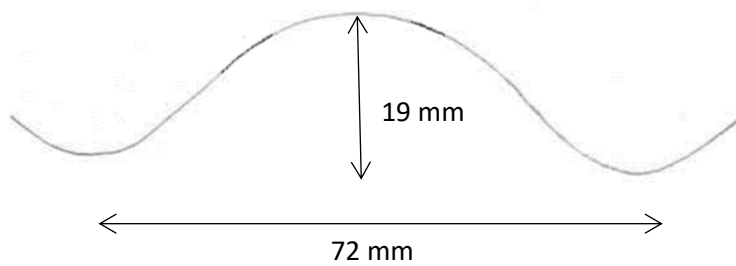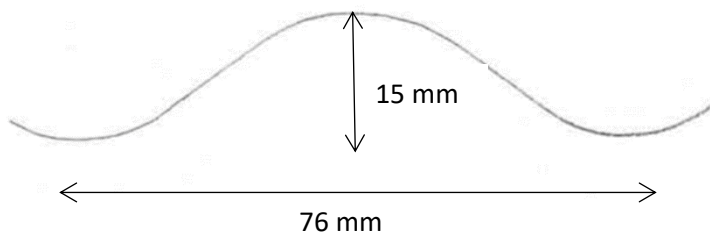
Both profiles are idealised as a half cylinder of radius 20 mm and length 220 mm.
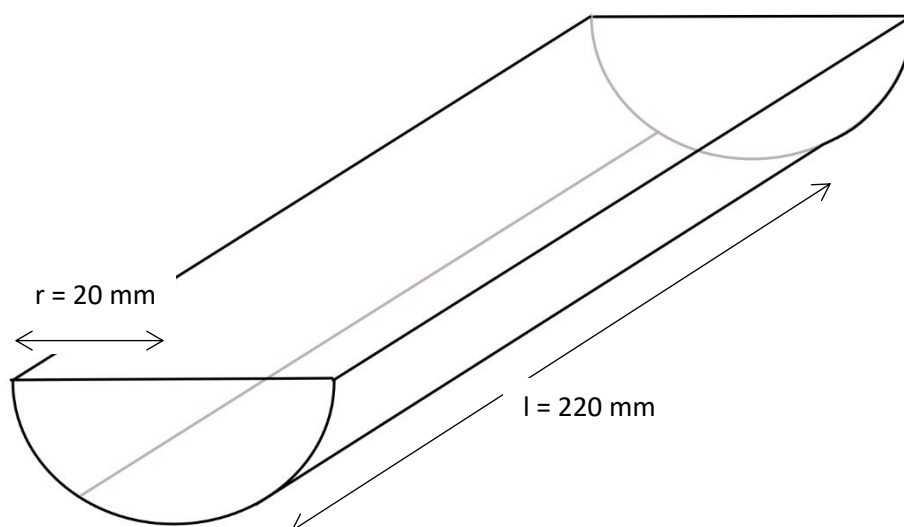
Trough area = ½ area of cylinder = ½ $\pi$ $r^2$ l = 138 cm$^3$

Each sheet has 3 troughs, so total trough area = 414 cm$^3$ = 0.000414 m$^3$

Volume of each Perspex cell = 22 x 22 x 10 = 4840 cm$^3$, so this is ~ 8.5 % of that volume.

# Appendix C

# Supplementary material for Chapter 4

The supplementary figures in Appendix C1 were included as Supplementary material for:

Osman S, Crummy J, Thomas M and Carver S Probabilistic hazard analysis for a small island: quantifying tephra fall hazard and appraising the possible impact on Ascension Island. Submitted to *Bulletin of Volcanology*

Appendix C1 includes the following:

Fig. C-1: ERA5 reanalysis data 2010-2019: 3-monthly wind roses up to ~ 30 km above sea level

Table C-1: Model vent locations for TephraProb simulations (UTM 28S)

Figs. C-2-C-5: Tephra ground loads with 10 and 90 % probability of exceedance

The material in Appendix C2 contains additional data on tephra dispersal model calibration, referred to in the Tephra modelling section.

## C1 Supplementary figures



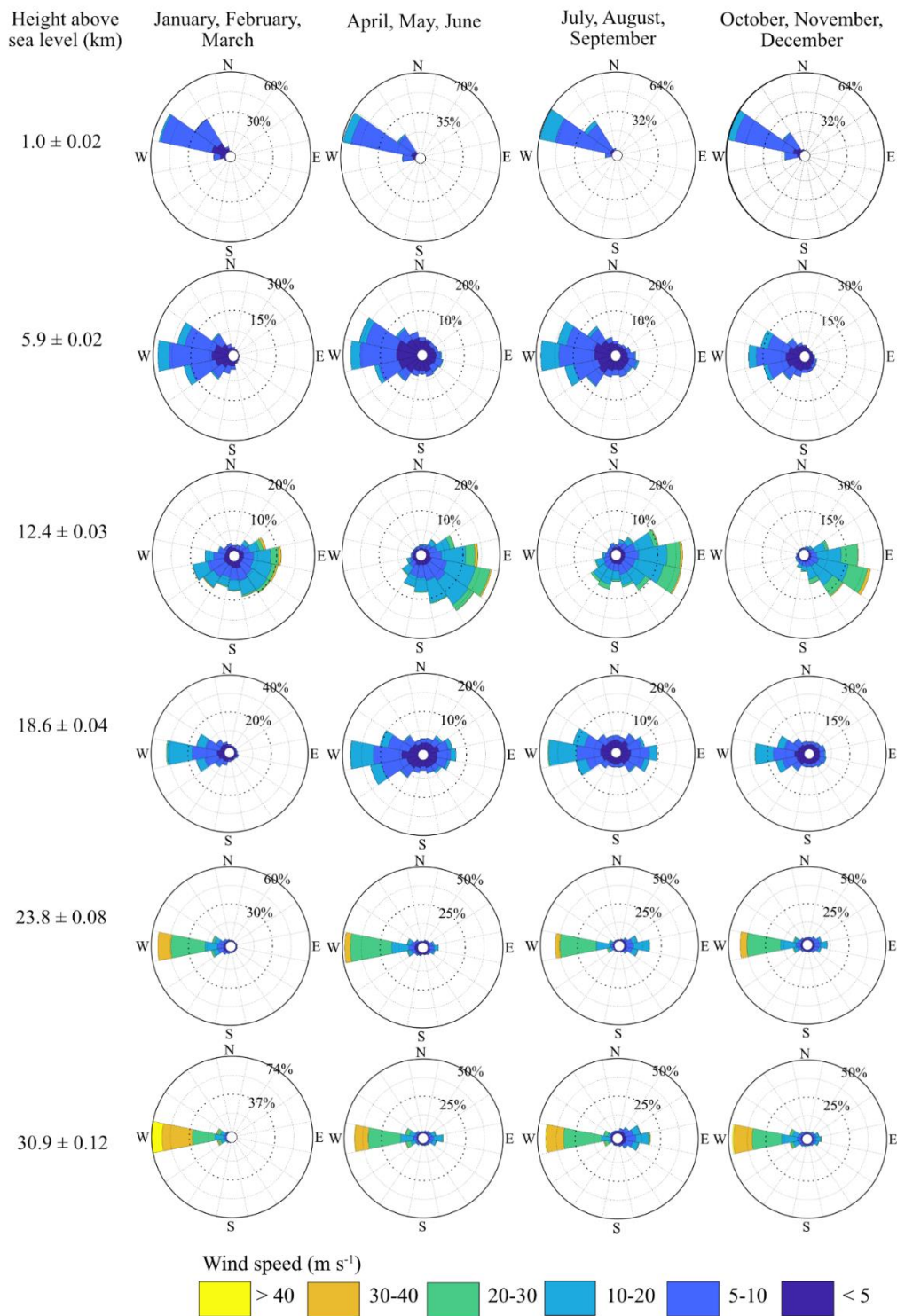**Fig. C-1** ERA5 reanalysis data 2010-2019 for Ascension Island: 3-monthly wind roses up to ~ 30 km above sea level

**Table C-1** Model vent locations for TephraProb simulations (UTM 28S)

| Simulations | Easting | Northing | Elevation (m) |
|---|---|---|---|
| Devil's Cauldron | 574119 | 9122490 | 520 |
| Comfortless Cove | 565917 | 9125544 | 30 |
| Airport_grid | 567292 | 9118700 | 89 |
| Airport_grid | 567492 | 9118700 | 79 |
| Airport_grid | 567092 | 9118900 | 73 |
| Airport_grid | 567292 | 9118900 | 72 |
| Airport_grid | 567492 | 9118900 | 78 |
| Airport_grid | 567692 | 9118900 | 71 |
| Airport_grid | 567892 | 9118900 | 74 |
| Airport_grid | 568092 | 9118900 | 88 |
| Airport_grid | 568292 | 9118900 | 88 |
| Airport_grid | 567092 | 9119100 | 80 |
| Airport_grid | 567292 | 9119100 | 75 |
| Airport_grid | 567492 | 9119100 | 83 |
| Airport_grid | 567692 | 9119100 | 93 |
| Airport_grid | 567892 | 9119100 | 84 |
| Airport_grid | 568092 | 9119100 | 84 |
| Airport_grid | 568292 | 9119100 | 93 |
| Airport_grid | 567292 | 9119300 | 80 |
| Airport_grid | 567492 | 9119300 | 84 |
| Airport_grid | 567692 | 9119300 | 83 |
| Airport_grid | 567892 | 9119300 | 87 |
| Airport_grid | 568092 | 9119300 | 89 |
| Airport_grid | 568292 | 9119300 | 107 |
| Airport_grid | 568492 | 9119300 | 115 |
| Airport_grid | 568692 | 9119300 | 135 |
| Airport_grid | 567492 | 9119500 | 93 |
| Airport_grid | 567692 | 9119500 | 91 |
| Airport_grid | 567892 | 9119500 | 112 |
| Airport_grid | 568092 | 9119500 | 101 |
| Airport_grid | 568292 | 9119500 | 107 |
| Airport_grid | 568492 | 9119500 | 133 |
| Airport_grid | 568692 | 9119500 | 136 |
| Airport_grid | 568892 | 9119500 | 146 |
| Airport_grid | 567692 | 9119700 | 109 |
| Airport_grid | 567892 | 9119700 | 101 |
| Airport_grid | 568092 | 9119700 | 108 |
| Airport_grid | 568292 | 9119700 | 129 |
| Airport_grid | 568492 | 9119700 | 168 |
| Airport_grid | 568692 | 9119700 | 143 |
| Airport_grid | 568892 | 9119700 | 143 |
| Airport_grid | 568292 | 9119900 | 198 |
| Airport_grid | 568492 | 9119900 | 188 |
| Airport_grid | 568692 | 9119900 | 162 |
| Sisters_grid | 569086 | 9123019 | 197 |
| Sisters_grid | 569286 | 9123019 | 193 |
| Sisters_grid | 569686 | 9123019 | 226 |
| Sisters_grid | 569886 | 9123019 | 161 |
| Sisters_grid | 570086 | 9123019 | 161 |
| Sisters_grid | 568686 | 9123219 | 178 |
| Sisters_grid | 568886 | 9123219 | 206 |
| Sisters_grid | 569086 | 9123219 | 179 |

# Appendix C: Supplementary material for Chapter 4

| Simulations | Easting | Northing | Elevation (m) |
|---|---|---|---|
| Sisters_grid | 569286 | 9123219 | 187 |
| Sisters_grid | 569486 | 9123219 | 166 |
| Sisters_grid | 569686 | 9123219 | 198 |
| Sisters_grid | 569886 | 9123219 | 92 |
| Sisters_grid | 570086 | 9123219 | 145 |
| Sisters_grid | 568486 | 9123419 | 182 |
| Sisters_grid | 568686 | 9123419 | 171 |
| Sisters_grid | 568886 | 9123419 | 145 |
| Sisters_grid | 569086 | 9123419 | 157 |
| Sisters_grid | 569286 | 9123419 | 98 |
| Sisters_grid | 569486 | 9123419 | 164 |
| Sisters_grid | 569686 | 9123419 | 152 |
| Sisters_grid | 569886 | 9123419 | 156 |
| Sisters_grid | 570086 | 9123419 | 73 |
| Sisters_grid | 568486 | 9123619 | 197 |
| Sisters_grid | 568686 | 9123619 | 192 |
| Sisters_grid | 568886 | 9123619 | 220 |
| Sisters_grid | 569086 | 9123619 | 178 |
| Sisters_grid | 569286 | 9123619 | 119 |
| Sisters_grid | 569486 | 9123619 | 91 |
| Sisters_grid | 569686 | 9123619 | 150 |
| Sisters_grid | 569886 | 9123619 | 168 |
| Sisters_grid | 570086 | 9123619 | 156 |
| Sisters_grid | 568686 | 9123819 | 168 |
| Sisters_grid | 568886 | 9123819 | 141 |
| Sisters_grid | 569086 | 9123819 | 231 |
| Sisters_grid | 569286 | 9123819 | 145 |
| Sisters_grid | 569486 | 9123819 | 205 |
| Sisters_grid | 569686 | 9123819 | 92 |
| Sisters_grid | 569886 | 9123819 | 187 |
| Sisters_grid | 570086 | 9123819 | 125 |
| Sisters_grid | 568686 | 9124019 | 158 |
| Sisters_grid | 568886 | 9124019 | 176 |
| Sisters_grid | 569086 | 9124019 | 243 |
| Sisters_grid | 569286 | 9124019 | 217 |
| Sisters_grid | 569486 | 9124019 | 172 |
| Sisters_grid | 569686 | 9124019 | 185 |
| Sisters_grid | 569886 | 9124019 | 174 |
| Sisters_grid | 570086 | 9124019 | 154 |
| Sisters_grid | 568686 | 9124219 | 228 |
| Sisters_grid | 568886 | 9124219 | 182 |
| Sisters_grid | 569086 | 9124219 | 217 |
| Sisters_grid | 569486 | 9124219 | 237 |
| Sisters_grid | 569686 | 9124219 | 205 |
| Sisters_grid | 569886 | 9124219 | 172 |

**Fig. C-2** Tephra ground loads with 10 % probability of exceedance for basaltic events. a), b) and c) show results for one event with 6–10 km plume height, d), e) and f) show results for three events, each with 6–10 km plume height from Sister's Peak, Airport East and Comfortless Cove respectively. For multiple events, we assume the tephra is not cleared or eroded between each pulse. Key locations: A: airport, G: Georgetown, PP: power plant and South Atlantic Relay station, TB: Two Boats, TH: Travellers Hill, AF: US Air Force Base
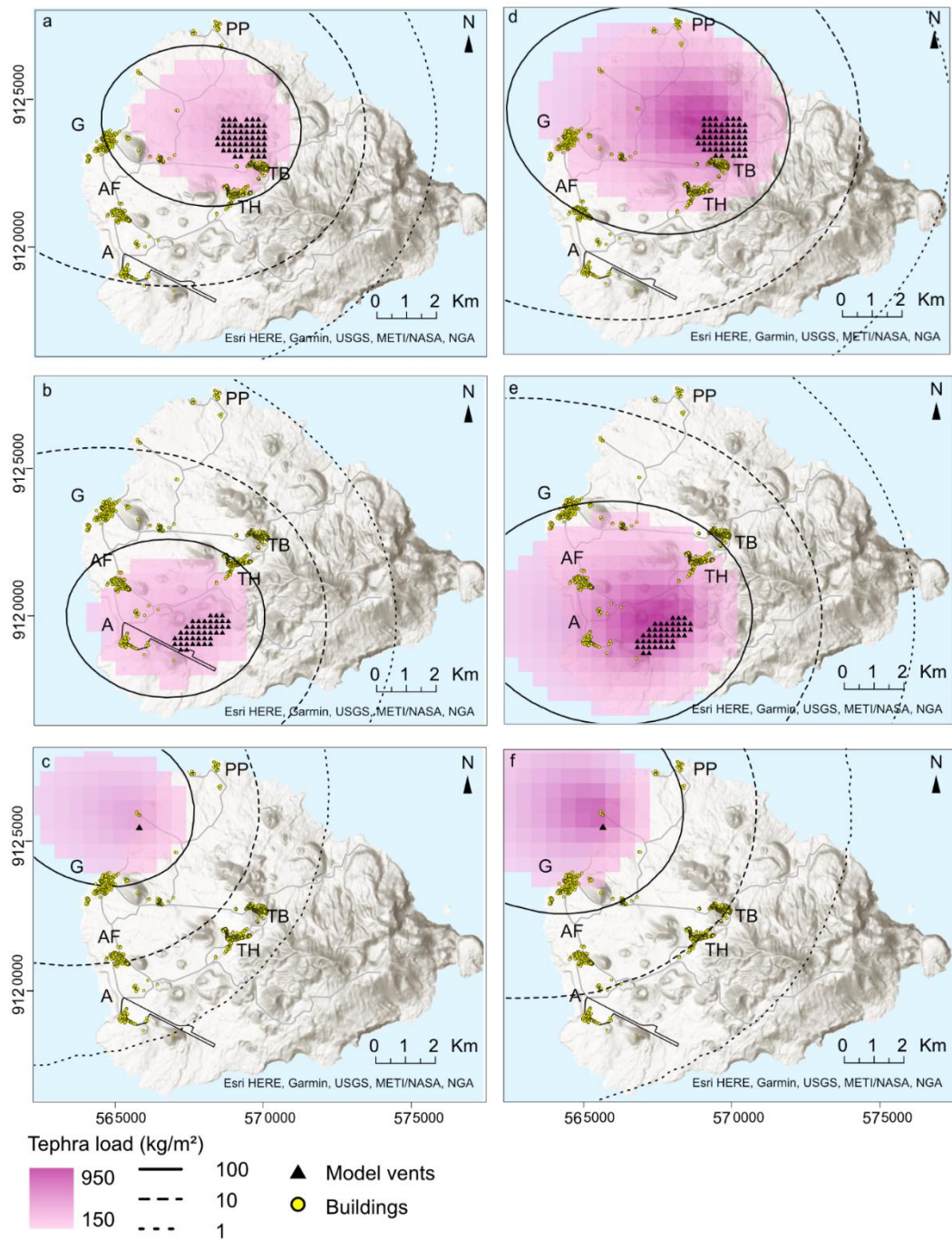
**Fig. C-3** Tephra ground loads with 90 % probability of exceedance for basaltic events. a), b) and c) show results for one event with 6–10 km plume height, d), e) and f) show results for three events, each with 6–10 km plume height from Sister's Peak, Airport East and Comfortless Cove respectively. For multiple events, we assume the tephra is not cleared or eroded between each pulse. Key locations: A: airport, G: Georgetown, PP: power plant and South Atlantic Relay station, TB: Two Boats, TH: Travellers Hill, AF: US Air Force Base
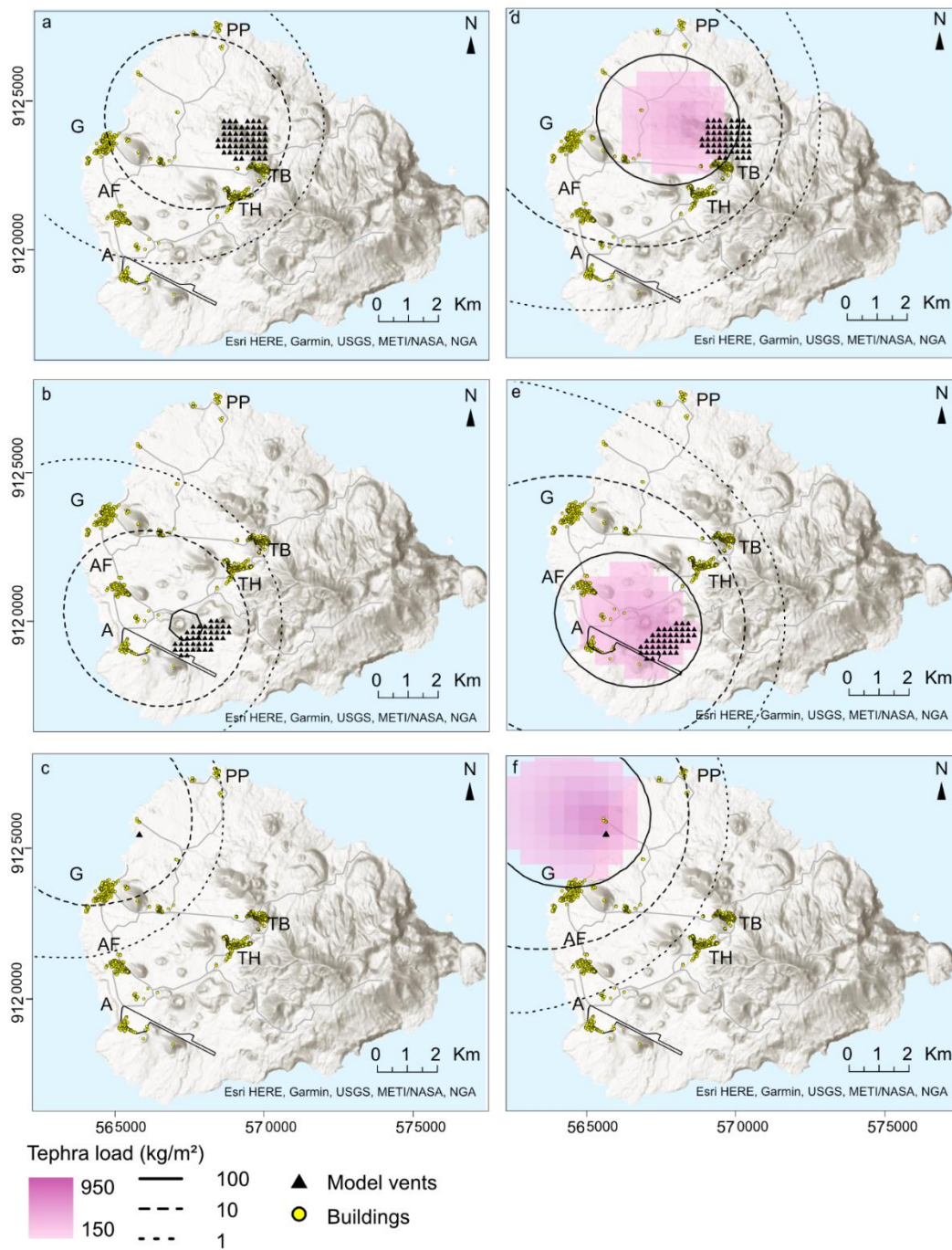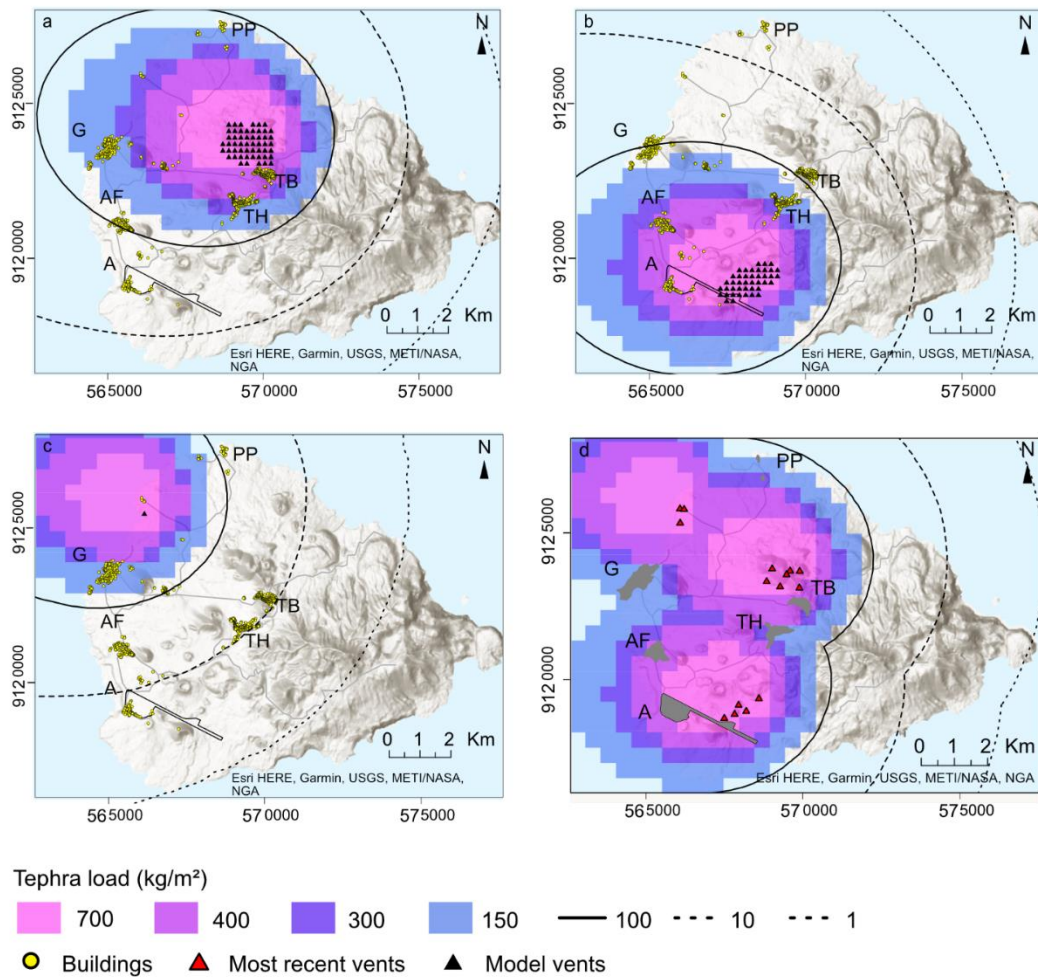
**Fig. C-4** Tephra ground loads likely to cause roof collapse (> 150 kg m$^{-2}$) with 10 % probability of exceedance for three basaltic eruptions, each with 6–10 km plume from a) Sister's Peak, b) Airport East and c) Comfortless Cove, d) one of Sister's Peak, Airport East and Comfortless Cove. Contours show likely collapse loads for different roof types (Table 1). We assume the tephra is not cleared or eroded between each pulse. Key locations: A: airport, G: Georgetown, PP: power plant and South Atlantic Relay station, TB: Two Boats, TH: Travellers Hill, AF: US Air Force Base
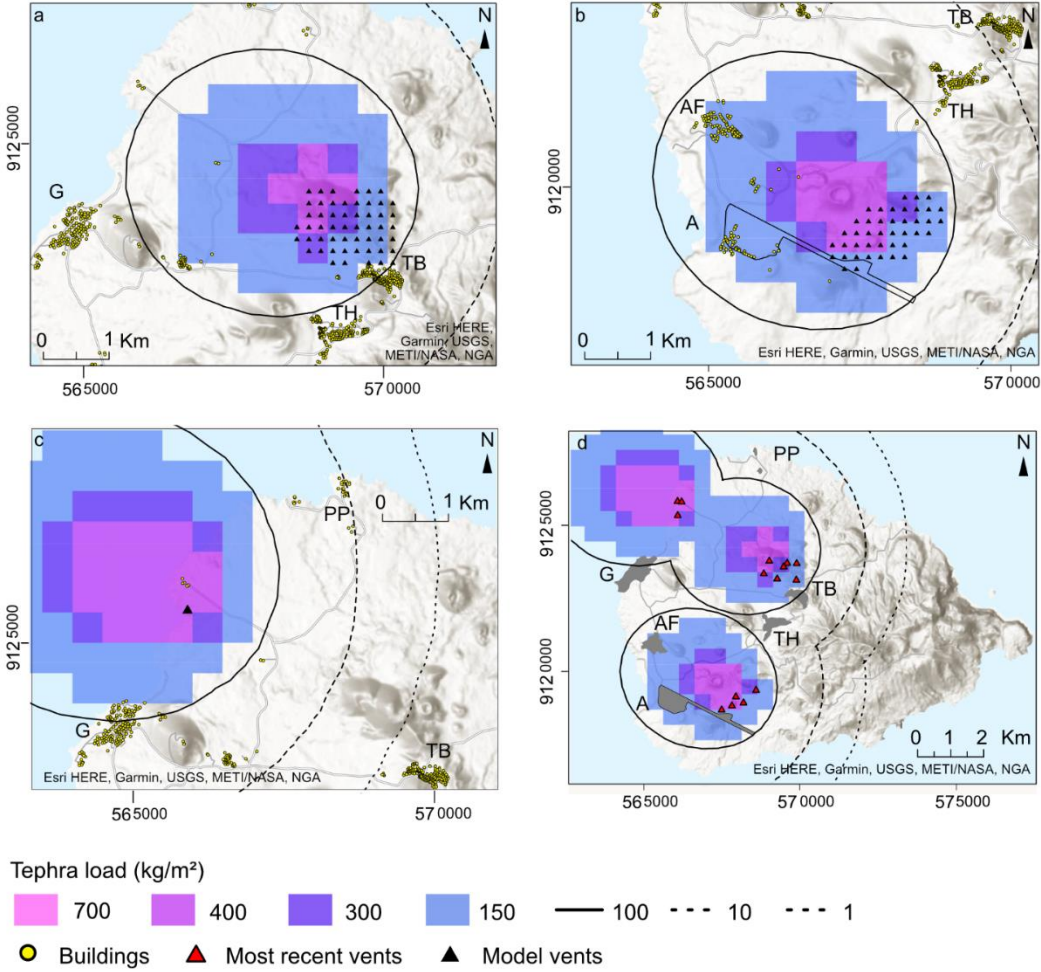
**Fig. C-5** Tephra ground loads likely to cause roof collapse (> 150 kg m$^{-2}$) with 90 % probability of exceedance for three basaltic eruptions, each with 6–10 km plume from a) Sister's Peak, b) Airport East and c) Comfortless Cove, d) one of Sister's Peak, Airport East and Comfortless Cove. Contours show likely collapse loads for different roof types (Table 1). We assume the tephra is not cleared or eroded between each pulse. Key locations: A: airport, G: Georgetown, PP: power plant and South Atlantic Relay station, TB: Two Boats, TH: Travellers Hill, AF: US Air Force Base

## C2 Tephra dispersal model calibration

The model was calibrated with published data from field observations on São Miguel, Azores: the trachytic Fogo A eruption for felsic simulations (Walker and Croasdale 1970; Carey and Sigurdsson 1989; Gaspar et al. 2015; Pensa et al. 2015) and the basaltic Serra Gorda eruption for mafic simulations (Booth et al. 1978). Tephra depths were converted to loads using published deposit density of 500 kg m$^{-3}$ for Fogo A (Walker and Croasdale 1970) and estimated deposit density of 1000 kg m$^{-3}$ for Serra Gorda. Input parameters are summarised in Table C-2.

**Table C-2** Input parameters used to calibrate model

| Parameter | Fogo A | Serra Gorda |
|---|:---:|:---:|
| Plume height (km asl) | 21 – 30 | 12 |
| Mass erupted (kg) | 2 – 4 x 10$^{12}$ | 10$^{10}$ – 10$^{11}$ |
| Duration (h) | 5 - 12 | 1 – 5 |
| $\Phi$ range (Md $\Phi$) | -5 – 6 (0.5) | -5 – 5 (-1) |
| $\sigma \Phi$ | 2 | 2 |
| $\rho$ lithic (kg m$^{-3}$) | 2400 | 2900 |
| $\rho$ pumice (kg m$^{-3}$) | 800 | 1000 |
| Aggregation | No | No |
| **Model parameters tested** | | |
| Diffusion coefficient (m s$^{-2}$) | 1500 - 5000 | 3000 - 5000 |
| Fall time threshold (s) | 2000 - 10000 | 3000 - 7000 |
| β distribution: α and β values | 1, 1    2, 2    3, 2    2, 3 | |
| Column integration steps | 50-100 | |

I selected wind profiles from a 10-year dataset of ERA5 6-hourly wind reanalysis dataset (Hersbach et al. 2018). For Fogo A I only used data from September (1200 wind profiles in total), chosen as the month with light, south-westerly winds most likely to create deposits that matched observations (Fig. C-6).  For Serra Gorda I selected south easterly/ southerly/ south-westerly winds (provenance 110 – 260 °) as most likely to create deposits that

matched observations. However, it was difficult to match the deposition upwind of the vent suggesting very light winds.
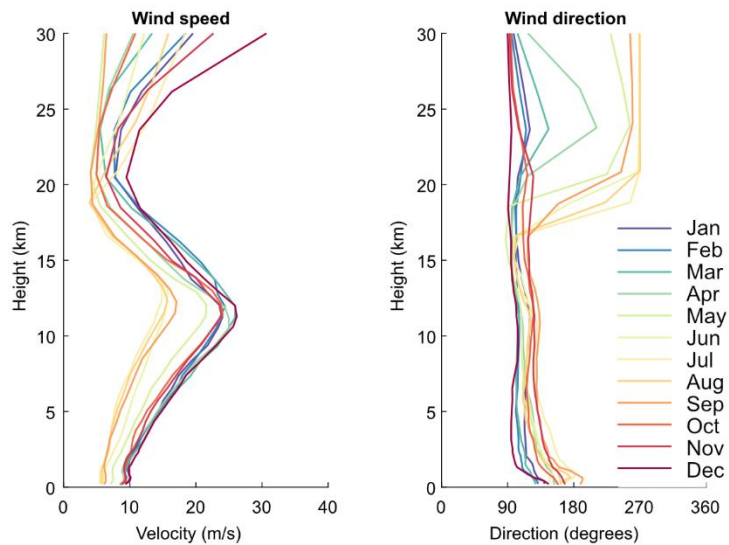


**Fig. C-6** Wind conditions (mean speed and direction the wind is blowing towards) by month for São Miguel, Azores from ERA5 2010-2019 reanalysis dataset (Hersbach et al. 2018)

The diffusion coefficient (DC) and fall-time threshold (FTT) are empirical model parameters. DC accounts for atmospheric advection and diffusion and FTT represents the fall time at which diffusion changes from a linear function (for large particles) to power law (for small particles). Mass distribution in the modelled plume is controlled by a β distribution, with α and β values used to specify where most mass is released (Fig. C-7). Optimised model results are shown in Fig. C-8.

The best fit values I chose for the Ascension Island simulations were:

- Felsic eruptions: DC 5000 m s$^{-1}$, FTT 6000 s, α=1, β=1.
- Mafic eruptions: DC 4000 m s$^{-1}$, FTT 5000 s, α=2, β=2.

When assessing the number of integration steps needed through the plume I found no difference between 50 and 100 steps for my model plume heights (mainly ≤ 15 km ) and so chose 50 steps for all model runs.

Grid spacing of 1000 m produced angular contours, spacing of 500 m produced smooth contours except very close to the vent and the only difference with a 250 m grid was

smoother contours very close to the vent. I also found that 1000 runs were needed to produce stable load contours, with no change in contours between 1000 and 2000 runs.

To optimise run time I therefore selected a grid of 500 m and 1000 runs for the individual scenarios and each element of the multiple vent scenario.
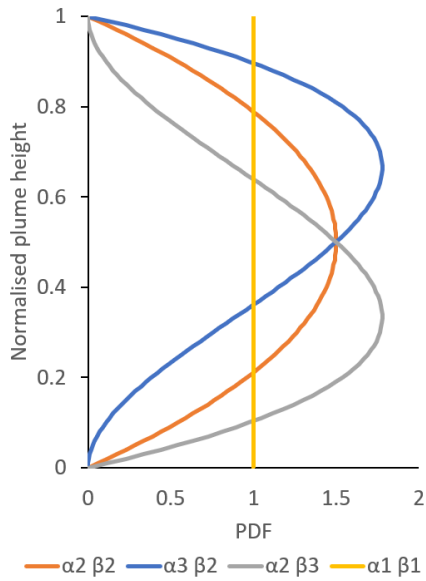


**Fig. C-7** Modelled distribution of mass within the plume for different α and β values of the β distribution
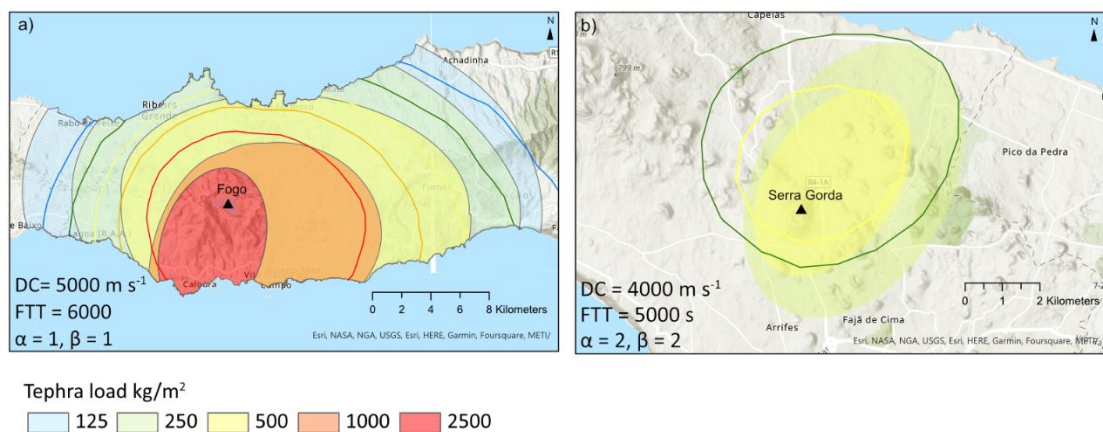


**Fig. C-8** Optimised model calibration results using a) Fogo A eruption (Walker and Croasdale 1980) and b) Serra Gorda eruption (Booth et al. 1978). Shading shows tephra load contours estimated from published data and lines show model results.

# Appendix C: Supplementary material for Chapter 4

## References for Appendix C2

Booth, B., Croasdale, R., & Walker, G. P. L. (1978). A quantitative study of five thousand years of volcanism on Sao Miguel, Azores. Philos. Trans. Royal Soc. A, 288(1352), 271–319. https://doi.org/10.1098/rsta.1978.0018

Carey, S., & Sigurdsson, H. (1989). The intensity of plinian eruptions. Bull Volcanol, 51(1), 28–40. https://doi.org/10.1007/BF01086759

Gaspar, J. L., Guest, J. E., Queiroz, G. et al (2015). Eruptive frequency and volcanic hazards zonation in São Miguel Island, Azores. In: Gaspar JL, Guest JE, Duncan AM, et al. (eds) Volcanic geology of Sao Miguel Island (Azores Archipelago). Geol Soc Lond Mem 44, pp 155–166. https://doi.org/10.1144/M44.12

Hersbach, H., Bell, B., Berrisford P, et al (2018) ERA5 hourly data on pressure levels from 1979 to present. Copernicus Climate Change Service (C3S) Climate Data Store (CDS). https://doi.org/10.24381/cds.bd0915c6https://doi.org/10.24381/cds.bd0915c6

Pensa, A., Cas, R., Giordano, G., Porreca, M., & Wallenstein, N. (2015). Transition from steady to unsteady Plinian eruption column: the VEI 5, 4.6 ka Fogo A Plinian eruption, São Miguel, Azores. J Volcanol Geotherm Res, 305, 1–18. https://doi.org/10.1016/j.jvolgeores.2015.09.012

Walker, G. P. L., & Croasdale, R. (1970). Two Plinian-type eruptions in the Azores. J Geol Soc London, 127(1), 17–55. https://doi.org/10.1144/gsjgs.127.1.0017

# Appendix D

## Appendix to Chapter 5

### GIS requirements

QGIS: the tool was developed in Version 3.28.12. It requires the Saga Next Gen plug in.

ArcGIS Pro: the tool was developed in Version 3.1.0. It requires Python to be activated.

### Using the Fail fraction tool

ArcGIS Pro and QGIS versions of the tool and full instructions, including details on formatting of input data, are available to download from: https://doi.org/10.5518/1458

# Appendix D: Appendix to Chapter 5

## Tool summary

// This code calculates Fail Fraction which is tephra load on a roof as a fraction of that roof's failure load. The output is a map showing which buildings are vulnerable to roof failure under the tephra loading scenario being considered. There are 2 options for the sliding calculations, for coarse and fine tephra and the user must select the most appropriate based on knowledge of the volcano of interest.

// Inputs are: a raster file of tephra fall loading on the ground, a point file of building data and a table of typical roof failure loads. The tool uses tephra sliding data (Osman et al. 2023) to estimate tephra load on each roof (the fraction of tephra load on the ground that is not removed by sliding) and combines typical roof failure loads with building data to estimate roof failure loads for each building. It calculates FailFraction (tephra roof load as a fraction of building failure load) and display values symbolised to highlight vulnerable buildings.

// Details of sliding equations in: Osman et al. (2023) Laboratory tests to understand tephra sliding behaviour on roofs. Journal of Applied Volcanology https://doi.org/10.1186/s13617-023-00137-2

SELECT appropriate tool for Coarse tephra or Fine tephra
INPUT  TephraLoadRaster, BuildingPointFile, RoofPropertiesTable, SymbologyFile

// Fields required in RoofPropertiesTable are:
Roof_type: numerical field with number allocated to each roof material
Typical_load: numerical field with typical collapse loads (in kg m$^{-2}$) for each roof material
Roof_material: text field of roof material

// Fields required in BuildingPointFile are:
RoofType: numerical field matching Roof_type in RoofPropertiesTable
RoofPitch: numerical field for angle of pitch (in degrees)
RoofCondit: 1 for good condition and 0 for poor condition
Longspan: 1 for long span roofs (over 5 m between supports) and 0 for short span roofs

// TephraLoadRaster requires tephra loads in kg m$^{-2}$

// Symbology file categorises vulnerability to roof failure as low, medium or high, with FailFraction values of less than 0.7, between 0.7 and 1 and between 1 and 10

EXTRACT value from TephraLoadRaster into new RasterValue field in BuildingPointFile interpolating between raster values to account for thinning of tephra deposit.
JOIN RoofPropertiesTable to BuildingPointFile using Rooftype as the key

```
FUNCTION FailLoad
// Calculates building-specific failure loads
    Pass In: Longspan, TypicalLoad, Condition
    IF Condition = 0 THEN multiplier = 0.5
    ELSE multiplier = 1
    ENDIF

    IF Longspan = 0 THEN calculate FailLoad as TypicalLoad times multiplier
    ELSE calculate FailLoad as 200 times multiplier
    ENDIF

    Pass Out: FailLoad
ENDFUNCTION

FUNCTION RSF
// Calculates RoofShapeFactor to take account of sliding based on Osman et al. 2023
    Pass In: TephraType, Pitch

    CASE TephraType of
       Coarse:
          IF Pitch is less than 16 THEN RoofShapeFactor is 1
          ELSEIF Pitch is greater than 35 THEN RoofShapeFactor is 0
          ELSE calculate RoofShapeFactor as (35 -Pitch) / 20
          ENDIF
       Fine:
          IF Pitch is less than 21 THEN RoofShapeFactor = 1
          ELSEIF Pitch is greater than 35 THEN RoofShapeFactor = 0
          ELSE calculate RoofShapeFactor as (35 -Pitch) / 15
          ENDIF
    ENDCASE

    Pass Out: RoofShapeFactor
ENDFUNCTION

CALL FailLoad with Longspan, Typical_load, RoofCondit RETURNING new FailLoad field in
BuildingPointFile
CALL RSF with RoofPitch and TephraType of Coarse or Fine as appropriate RETURNING new
RoofShapeFactor field in BuildingPointFile
CALCULATE new TephraLoad field in BuildingPointFile as RasterValue times
RoofShapeFactor
CALCULATE new FailFraction field in BuildingPointFile as TephraLoad divided by FailLoad

IF FailFraction is greater than 10 THEN set FailFraction to 10
// Ensures datapoints are symbolised consistently

DISPLAY on map, with value of FailFraction symbolised with SymbologyFile
END
```

# Appendix E

## Building survey on La Palma during the 2021 eruption

Appendix E1 contains results of a visual survey of 47 buildings from 1–3 December 2021, covering building type, roof material and pitch, building condition and damage. The buildings in Jedey, Las Manchas, Tacande, Tajuya and La Laguna had all been affected by tephra fall and were all within ~ 5 km of the source. Survey locations (1-6) are shown in Figure E-1. Tephra thicknesses were measured on the ground and on roofs (Table E-1) and tephra samples were taken on the ground in Las Manchas to estimate the bulk density of tephra deposits. Survey results are shown in tables E-2–E-5 and Figs. E-2–E-5. Wider views of the eruption are shown in Fig. E-6.

Appendix E2 details the key findings from the survey which were shared with Instituto Geológico y Minero de España (IGME) colleagues.

Appendix E3 shows my observations of a thin metal sheet roof in Tacande that was on the point of collapse.

## E1 Building survey
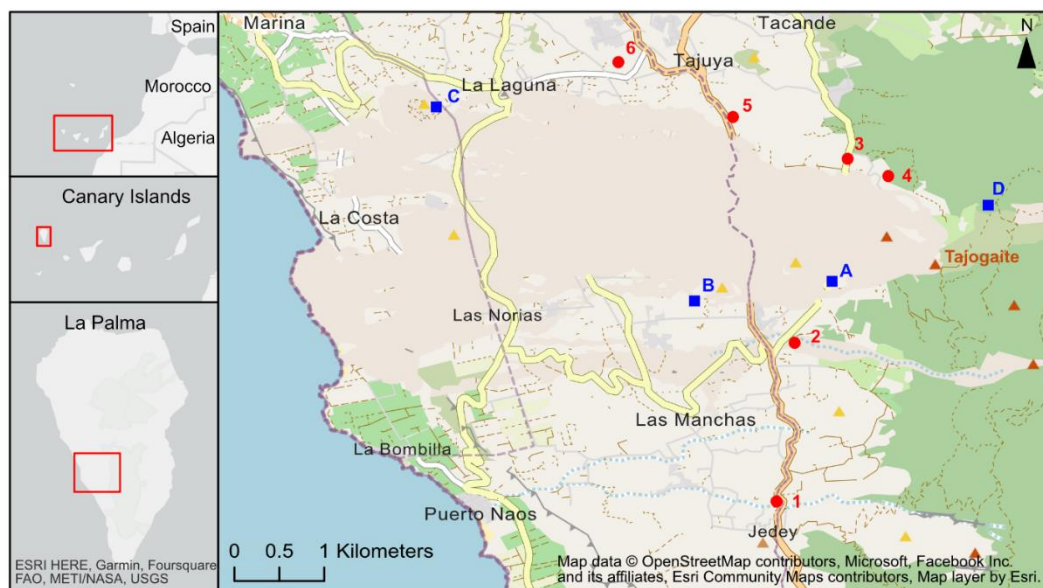


**Fig. E-1:** Locations of buildings surveyed from 1–3 December 2021 to identify impact of tephra fall on roofs. 1: Jedey, 2: Las Manchas, 3 and 4: Tacande, 5: Tajuya, 6: La Laguna. A–D indicate viewpoints shown in Fig. E-6

**Table E-1**: Tephra thicknesses measured by IGME and during this survey.

| Location | Thickness (cm) | Detail |
|---|---|---|
| Jedey | 20 | Maximum thickness on the ground measured by IGME |
| Las Manchas | 21 | Maximum thickness on the ground measured by IGME close to M1* |
| La Laguna church | 0.6 | Thickness on the ground measured by IGME on 27 October 2021 |
| IGME checkpoint near M12* (ground) | 97.7 | Tephra thicknesses on the ground or on roofs, measured during this survey |
| T10* (roof) | 26 | |
| T12* (roof) | 54 | |
| T13* (roof) | 101 (drifted) | |
| Tajuya (ground) | 5–7 | |
| La Laguna church | 2–3 (drifted) | |

* Building locations are shown in Figs E-3–E-5

| Building | Building type | Roof type | Roof pitch (°) | Condition | Damage |
|---|---|---|---|---|---|
| J1 | House | Tile | 10 | Good | No visible damage |
| J2 | House | Tile | Upper: 20 Lower: 13 | Good | No visible damage |
| J3 | House | Chipboard/ tiles | 30 | Poor | Roof collapse |
| J4 | House | Tile | 30 | Poor | Roof bending |
| J5 | House | Tile | 30 | Poor | Roof bending |
| J6 | House | Concrete | 0 | Good | No visible damage |
| J7 | House | Tile | 10 | Good | No visible damage |
| J8 Viveres Lala | House | Tile | 20 | Good | No visible damage |

**Table E-2**: Building survey in Jedey (building locations shown in Fig. E-2). Fire brigades were clearing house roofs.

| Building | Building type | Roof type | Roof pitch (°) | Condition | Damage |
|---|---|---|---|---|---|
| M1 Aperitivo | Low strength structure | Metal sheet | 0 | ? | Roof collapse |
| M2 | House | Tile/ metal sheet | Tile: 35 Metal: 8 | Good | No visible damage (Metal sheet does not appear to have been cleared) |
| M3 | House | Concrete | 0 | Good | No visible damage |
| M4 | Outbuilding | Metal sheet | 20 | ? | Roof collapse |
| M5 | House with outbuildings | Tile/ Fibre cement | Tile: 35 Fib. cem.: 20 | Good | No visible damage (roofs cleared) |
| M6 | House | Tile | 35 | Good | No visible damage |
| M7 | Awning with metal pole supports | Fabric | ? | ? | Fabric intact but metal supports buckled |
| M8 | Outbuilding | Metal sheet | ? | ? | Partial roof collapse |
| M9 | Low strength structure | Metal sheet | ? | ? | Roof collapse |
| M10 | Agricultural building | Tile | 35 | Good | No damage |

**Table E-3**: Building survey in Las Manchas (building locations shown in Fig. E-3). Fire brigades were clearing house roofs.

| Building | Building type | Roof type | Roof pitch (°) | Condition | Damage |
|---|---|---|---|---|---|
| M11 | Outbuilding | Tile | 20 | ? | Roof collapse |
| M12 Terrero Municipal Federico Simón | Wrestling Arena | Metal sheet | 0 | ? | Partial roof collapse |
| M13 | Awning with metal pole supports | Fabric | ? | ? | Fabric intact but metal supports buckled |
| M14 | Outbuilding | Fibre cement on metal girder | 0 | ? | Roof collapse – metal girder failed at joint |
| M15 | House | Concrete | 0 | Good | No visible damage |
| M16 | Outbuilding | Tile | 30 | Good | No visible damage |
| M17 | Outbuilding | Metal sheet | 10 | Poor | Roof collapse |
| M18 | Log shed | Fibre cement | 5 | Poor | Partial roof collapse |
| M19 | Summerhouse | Metal sheet | 5 | Poor | Roof collapse |
| M20 | Outbuildings | Tile/metal sheet | 30 | Poor | Roof collapse |

**Table E-3** continued

| Building | Building type | Roof type | Roof pitch (°) | Condition | Damage |
|---|---|---|---|---|---|
| T1 | Outbuilding | Metal sheet | 0 | ? | Roof bending |
| T2 | House | Tile | Apex: 35 Overhang: 20 | Good | Roof does not appear to have been cleared. Tephra sliding on steeper part, build-up on shallower part |
| T3 | House | Concrete/Tile | Concrete: 0 | Good | No visible damage |
| T4 | House | Tile | 30 | Good | No visible damage |
| T5 | Outbuilding | Fibre cement | 5 | Good | No visible damage |
| T6 | House | Concrete | 0 | Good | No visible damage |
| T7 | Porch with metal | Metal sheet | 0 | ? | Roof collapse |
| T8 | House | Glass roof light | 0 | ? | Roof collapse |
| T9 | Outbuilding | Metal sheet | 2 | Good | No visible damage |
| T10 | Outbuilding | Metal sheet | 0 | Good | Bending of metal sheet |
| T11 | Outbuilding | Metal sheet | 8 | Good | No visible damage |
| T12 | Farm | Metal sheet | 0 | Good/Poor | Part of roof intact, part collapsed, some bending of metal sheet |
| T13 | House | Tile | Apex: 30 Overhang: 10 | ? | No visible damage |

**Table E-4:** Building survey in Tacande (building locations shown in Figs. E-4 and E-5).

| Building | Building type | Roof type | Roof pitch (°) | Condition | Damage |
|----------|---------------|-----------|----------------|-----------|--------|
| Tj1 | House | Tile | 20 | Good | No visible damage |
| Tj2 | Awning on metal supports | Fabric | ? | ? | Collapse of structure |
| Tj3 | House | Tile | 30 | Good | No visible damage |
| Tj4 | House | Tile<br>Concrete (garage) | Tile: Apex: 30<br>Overhang: 10<br>Concrete: 0 | Good | No visible damage |
| Tj5 | House | Concrete | 0 | Good | No visible damage |
| L1 | Greenhouses | Plastic sheeting | 1 | Good | Some collapsed, some bending under ash load, some intact. Ash washed inside by rain – through seams in sheeting. |

**Table E-5**: Building survey in Tajuya and La Laguna (building locations shown in Fig. E-5).
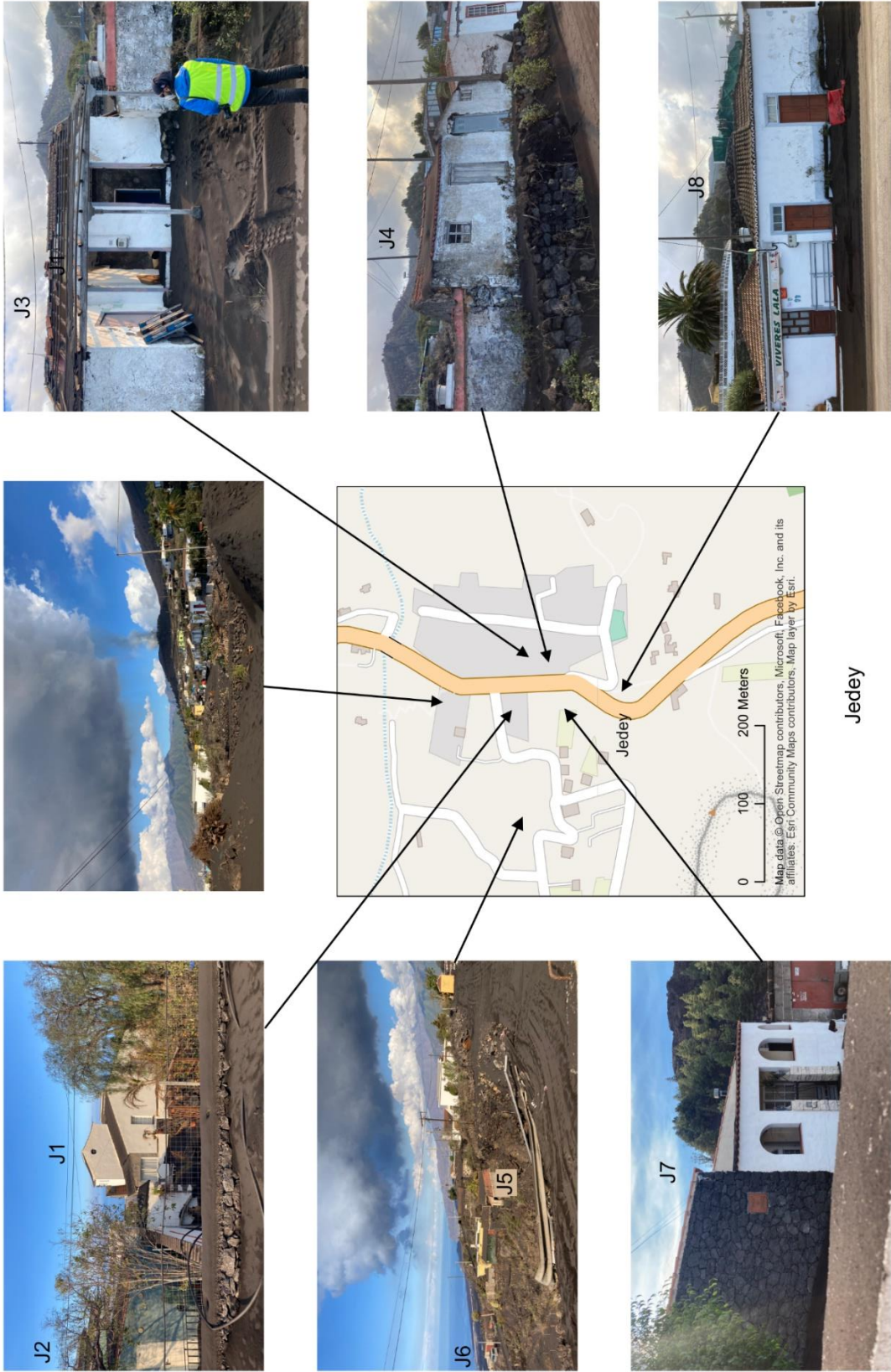
**Fig. E-2:** Buildings surveyed in Jedey

**Fig. E-3:** Buildings surveyed in Las Manchas

**Fig. E-3**: Buildings surveyed in Las Manchas (cont'd)

**Fig. E-4:** Buildings surveyed in Tacande

**Fig. E-5:** Buildings surveyed in Tacande, Tajuya and La Laguna

**Fig. E-6:** Viewpoints of eruption. Arrows on the map indicate direction of view

## E2 Key findings from the survey

1. House roofs mainly appeared undamaged. Many had been cleared of tephra by emergency crews, but some traditional tile roofs appeared sound, even under large deposit depth (T13).

2. Deposits had not slid on flat or low-pitched roofs (< 15 °) (T9, T11).

3. There was some evidence of tephra drifting and sliding on tile roofs (T2), but tephra only slid down the steep part of the roof (~ 35 ° pitch) and not over the shallower edge (~ 20 °).

4. The long span metal sheet roof of the wrestling arena in Las Manchas (M12) had partially collapsed, while nearby houses appeared undamaged.  Maximum tephra depth nearby was measured at 98 cm, although roof failure was reported to have occurred several weeks earlier.

5. Roofs had collapsed on weaker structures (eg. outbuildings, summerhouses, porches). These mainly had metal or fibre cement sheet (uralite) roofs. It was not possible to generalise the failure mechanism, as in some cases it appeared that the structure has failed and in others the roof material had failed.

6. In La Laguna, some of the greenhouses (covered in plastic sheet) failed under the tephra load (L1). A local farmer explained that rain had also washed tephra inside the greenhouses through seams in the sheeting, leading to failure of the banana crop. Maximum tephra depth measured at La Laguna church was 3 cm, but this is likely to be an overestimate as the deposit had drifted.

7. In Tacande, the metal sheet roof on outbuilding T10 was buckled, but not completely failed, and the deposit was undisturbed, indicating that this is close to the tephra depth for failure (Fig. E-7). We measured the deposit thickness as 12 cm ash above 14 cm lapilli.

8. Tephra bulk density was estimated at 1460–1680 kg m$^{-3}$. When oven dried the density of the deposit sample reduced by ~ 10 % (1335 – 1535 kg m$^{-3}$), suggesting the in-situ deposit may have drained. Grain density (measured in the IGME laboratory) was 2400–2700 kg m$^{-3}$.

These findings have been presented to IGME.

## E3 Collapse loads

The thin metal sheet roof of building T10 was on the point of failure (Fig. E-7a and b) under a 26 cm thick deposit (Fig. E-7c and d). Our estimated deposit density of 1460–1680 kg m$^{-3}$ suggests a collapse load of 3.7–4.3 kPa.



**Fig. E-7:** Outbuilding T10 in Tacande (location shown in Fig. E-4) showing a) and b) Buckled metal sheet roofing, c) and d) Tephra deposit on the roof